Characterizing the Evolution of a Restoring Salt Marsh Landscape with Low Altitude Aerial Imagery and Photogrammetric Techniques

by
Samantha Lewis

A Thesis Submitted to
Saint Mary's University, Halifax, Nova Scotia
In Partial Fulfillment of the Requirements for
The Degree of Master of Science in Applied Science.

March, 2022
Halifax, Nova Scotia

Approved:	Dr. Danika van Proosdij Supervisor Department of Geography and Environmental Studies
Approved:	Dr. Jeremy Lundholm Supervisory Committee Member Department of Biology
Approved:	Dr. Jason Rhinelander Supervisory Committee Member Division of Engineering
Approved:	Tony Bowron Supervisory Committee Member Department of Environmental Science
Approved:	Dr. Jonathan Dale External Examiner School of Energy, Construction and Environment, Coventry University
Date:	March 16, 2022

Abstract

Characterizing the Evolution of a Restoring Salt Marsh Landscape with Low Altitude Aerial Imagery and Photogrammetric Techniques

By Samantha Lewis

In Nova Scotia, Canada, managed realignment, a form of nature-based adaptation to the effects of climate change, is being used to restore natural salt marsh systems which provide many benefits including coastal erosion protection and vital habitat. This study utilized remotely piloted aircraft systems equipped with real-time kinematic (RTK) positioning corrections to monitor and measure morphodynamic changes at a managed realignment site in the Bay of Fundy with resolutions and accuracies not achievable with traditional methods. Sedimentation patterns and channel network evolution were analyzed using remote sensing and GIS techniques. Results show strong seasonal signals in the morphological evolution of the site, and variations in sedimentation patterns and channel characteristics between areas with and without relic agricultural features. RTK positioning functionality improved achievable product accuracies and increased the magnitude of measurable change in sedimentation analyses, and hyperspatial resolutions allowed for the mapping of embryonic channel features.

Keywords: Climate Change, Sea Level Rise, Nature-based Adaptation, Managed Realignment, Salt Marsh, Remotely Piloted Aircraft Systems, GIS, Photogrammetry

March 16, 2022

Acknowledgements

The completion of this thesis would not have been possible without the support, guidance and encouragement of many individuals throughout my research journey at Saint Mary's University. Firstly, I would like to thank my supervisor, Dr. Danika van Proosdij, who not only acted as an academic mentor, but provided more emotional support and encouragement than a graduate student could ask for. I would also like to thank my entire supervisory committee, Dr. Jeremy Lunholm, Tony Bowron, and Dr. Jason Rhinelander for providing me with welcomed ideas, advice and feedback on my work. Thanks to everyone CB Wetlands and Environmental Specialists, for supporting my educational journey and providing me with industry insight into salt marsh restoration, as well as helping me with fieldwork. Special thanks to Greg Baker from the SMU Maritime Provinces Spatial Analysis Research Centre, for being my GIS and remote sensing guru. I would also like to acknowledge the many fellow students and colleagues who helped out during my field work adventures or chatted with me in the lab, including Reyhan Akyol, Graeme Matheson, Brandon Champagne, Megan Elliot, Maka Ngulube, Riccardo Brunetta, and Wesley Weatherbee. To my friends and family, thank you for having patience with me throughout this process, and to my partner, Nathan Crowell, thank you for your consistent willingness to brainstorm and unconditional support.

Table of Contents

List of Figures

List of Tables

List of Equations

Chapter 1: Introduction

1.1 Research Context

Some of the most significant issues society is facing today are the adverse effects of climate change. For coastal communities around the world, sea level rise (SLR) is a major threat and combined with increased storm surge and storm frequency will contribute to the increasing risks of coastal erosion, flooding, and inundation of low-lying landscapes, property and infrastructure (IPCC, 2013; Bush et al., 2019). In Nova Scotia, Canada, subsidence, the gradual lowering of an area of land, will cause sea level to rise more significantly than in other parts of the country, with a current forecasted relative sea level rise increase of 1 m by 2100 (Bush et al., 2019). This, combined with the fact that a large percentage of the population resides on or near the coast, means that property and infrastructure are particularly and increasingly at risk of damage in Nova Scotia.

One of the more common defenses against SLR globally is the use of earthen barriers called dykes. Dykes are a hard defence structure that act as a physical barrier between saline ocean water and low-lying areas upland of the structure. Acadian settlers historically constructed dykes in Nova Scotia to convert natural salt marsh systems into fertile agricultural land. There are 241 km of dykes being used as coastal barriers in the province which protect approximately 20,000 ha of property, agricultural land, and infrastructure (van Proosdij et al., 2013) worth over $300 million (Kevin Bekkers, 2017 as cited in Matheson, 2020). To continue to provide protection to low-lying areas and infrastructure, many of these dykes need to be maintained and/or repaired regularly. However, maintenance and repair activities, which may include adding rock armoring, topping the dyke to raise its elevation, or widening the dyke, are costly and sometimes physically unfeasible (van Proosdij and Page, 2012).

A series of approaches called Nature-based Adaptation (NBA) involve the use of vegetation and other natural materials to create or restore natural ecosystems and their processes, and combat some of the projected effects of climate change such as coastal erosion and storm surge (Costanza et al., 1997; Faivre et al., 2017). This research will focus on one specific method of NBA called Managed Realignment (MR). MR involves redesigning an existing dyke structure by shifting it inland (usually while also reducing its length to decrease costs in future maintenance) and reintroducing tidal flow to an area of current agricultural dykeland (French, 2006). The reintroduction of tidal flow allows for the potential re-establishment of a salt marsh in front of the new dyke (Figure 1.1), otherwise known as a foreshore marsh, which provides protection from coastal erosion by means of wave attenuation (Costanza et al., 2008), as well as several valuable ecosystem services and anthropogenic benefits, including vital habitat and carbon storage. Additionally, salt marshes' ability to increase surface elevation with rising sea levels (Friedrichs & Perry, 2001; Kirwan et al., 2016) may allow for long term protection of coastal infrastructure with the increasing effects of climate change.

Topographical differences between natural salt marshes and managed realignment restoration sites, such as the presence of remnant agricultural features, may significantly alter the evolution trajectory of such sites (MacDonald et al., 2010). The early monitoring of new marsh development in a managed realignment context will allow for a better understanding of these differences and aid in our ability to design and implement MR projects for long-term protection of coastal infrastructure and other environmental benefits. Salt marsh formation and evolution occur at varying spatial (Horne et al., 2013) and temporal (van Proosdij et al., 2006a,b) scales. Quantifying landscape changes that accurately model such a dynamic system requires repeat surveys with varying resolution and precision, as well as varying technologies and survey

methods. Since traditional survey types require human interaction with the environment (e.g., footprints) which disrupt and may influence salt marsh evolution, data collection itself can negatively impact the measurement of natural processes. Also, traditional methods to quantify landscape change require significant time and manual input, which are not appropriate when working with a large number of repeat surveys.

Remote sensing techniques such as the use of Remotely Piloted Aircraft Systems (RPAS), otherwise known as Unmanned Aerial Vehicles (UAVs), may offer a unique opportunity for monitoring the morphodynamic processes of coastal wetlands while reducing some of these issues. Only recent studies have begun to utilize RPAS technology for measuring surface elevation change and drainage network initiation and development in salt marsh and mud flat environments (Jaud et al., 2016; Kalacska et al., 2017; Dale et al., 2018, 2020; Matheson, 2020; Brunetta et al., 2021), allowing surveying at higher spatial resolutions than achievable with traditional survey methods. Further research using these technologies, as well as more recent advancements such as the integration of Real-Time Kinematic (RTK) positioning systems, may greatly increase our capabilities of measuring high resolution phenomenon in complex, sensitive environments such as MR sites. This study applies recent advancements in RPAS technology to monitor and measure the morphodynamic evolution of a restoring MR site. Elevation models derived from RPAS aerial imagery and Structure from Motion (SfM) processing techniques are used to examine the spatial and temporal patterns of channel network morphology and sedimentation within the study site. Additionally, the application of RPAS with RTK functionality for these types of environmental monitoring is assessed, and limitations identified to make recommendations for future projects.

1.2 Natural Salt Marsh Ecosystems

Salt marshes are coastal wetland ecosystems that occur within the intertidal zone and are regularly inundated by ocean water. They are found in low-energy, temperate zones (Allen and Pye, 1992; Adam 2011) and are colonized by halophytic vegetation species that are adapted to tolerate inundation by saline water (Pratolongo et al., 2019). Multiple studies have identified a decline in salt marsh coverage globally (Zedler and Kercher, 2005; Lotze et al., 2006), and it is estimated that up to 87% of global wetlands have been lost since 1700 (Ramsar Convention on Wetlands, 2018). Since they provide several valuable ecosystem services including fish habitat and support of fisheries (Boesch and Turner, 1984; MacKenzie and Dionne, 2008; Barbier et al., 2011); carbon sequestration and storage (Mayor and Hicks, 2009; Wollenberg et al., 2018); and coastal protection and flood risk reduction via wave attenuation and water storage (Mitsch and Gosselink, 2000; Möller et al., 2014), this loss has significant implications on ecosystems, industry and the global effects of climate change.

Salt marshes are sinks for sediment suspended in incoming tidal waters and freshwater runoff from uplands (Davidson-Arnott et al., 2002), and can be either dominated by allochtonous sediment supply or organically produced material within the marsh, called minerogenic and organogenic marshes, respectively (Allen, 2000). Salt marsh vegetation survival is limited by inundation frequency and duration (Reed, 1990), and generally salt marsh vegetation does not survive below the mean tide level in any given area (McKee and Mendelssohn, 1989). Therefore, salt marsh establishment and extent are limited by tidal flat or marsh surface elevation. Two aspects of salt marsh morphology are investigated in this research: sediment dynamics and drainage network evolution.

1.2.1 Sediment Dynamics

The processes involved in natural salt marsh establishment and evolution have been studied for decades and over time researchers have gained an understanding of the complex interactions of sediment, hydrology, vegetation, and other variables that drive salt marsh morphodynamics (Allen & Pye, 1992; Allen, 2000; Friedrichs, 2001). A graphic representation of these variables is shown in Figure 1.1, and highlights the interactions of these variables within varying temporal scales. Spatial patterns of sedimentation are a result of complex interactions between a variety of factors that can be subdivided within two categories: the availability of sediment, and the opportunity for sediment to be deposited (van Proosdij et al., 2006a). More specifically, sediment deposition rates and spatial patterns have been related to suspended sediment characteristics (Kranck, 1975; Allen and Pye, 1992), suspended sediment concentration (Reed et al., 1999; Friedrichs and Perry, 2001; Boyd et al., 2017; Poirier et al., 2017), water velocity (Davidson-Arnott et al., 2002; van Proosdij et al., 2006b; Poirier et al., 2017), inundation time (Leonard, 1997; French and Spencer, 1993), vegetation presence (Leonard, 1997; Christiansen et al., 2000; Temmerman et al., 2005; Coulombier et al., 2012) and ice rafting (Gordon and Desplanque, 1983; van Proosdij et al., 2006b, Argow et al., 2011). In temperate environments, such as the Bay of Fundy, many of these factors are seasonal in nature, causing seasonal variation is sedimentation patterns (van Proosdij et al., 2006b; Spencer et al., 2012).

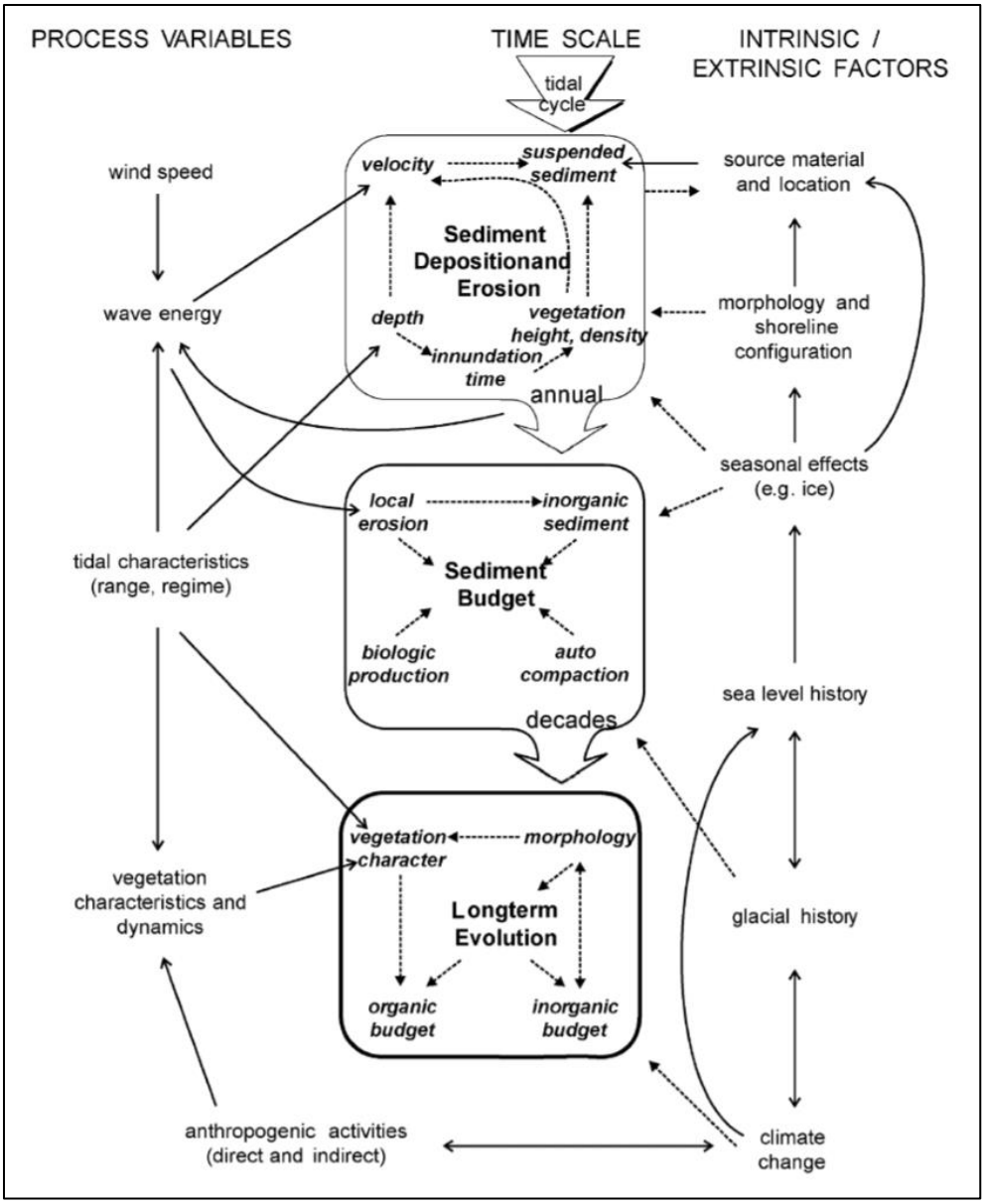

Figure 1.1. *The variables driving tidal salt marsh establishment and evolution, and their corresponding timescales (van Proosdij, 2001). Reproduced with permission from Dr. Danika van Proosdij.*

The variables affecting the availability of sediment to a salt marsh are suspended sediment concentration, distance of travel from source and wave activity (turbulence in the water column and water velocity) (van Proosdij et al., 2006a). These variables not only alter the availability of sediment, but also interact with one another in complex ways. Suspended sediment is strongly impacted by the sediment source. Sources of allochtonous sediment include

discharge from river catchments, eroding coastal cliffs and material from the seafloor (Allen, 2000). Source material will determine composition and grain size of the suspended sediment, which will affect the ability of that sediment to stay suspended in the water column and the distance from source it can travel before settling. Larger particles will settle out of the water column more quickly, while smaller particles such as clays, will stay in suspension and are more readily transported to marsh surfaces (Allen and Pye, 1992). This relationship differs in situations where sediment particles aggregate into flocs and settle out of the water column faster due to their aggregated size (Kranck, 1975).

Within a salt marsh, suspended sediment concentrations vary over the tidal cycle, with higher concentrations occurring during periods of increased water velocity (Allen, 2000; van Proosdij et al, 2006b; Poirier et al., 2017). Suspended sediment concentrations have also been shown to decrease over the course of a tidal cycle, from flood to ebb tide, due to settling (Davidson-Arnott et al., 2002). Seasonal trends have been identified by examining suspended sediment concentrations over larger temporal scales. In the Bay of Fundy, suspended sediment concentrations are higher in the winter (Poirier et al., 2017). This seasonality is in part due to wave activity. Increases in wave activity and water velocity tend to stir up sediments, increasing suspended sediment concentrations in incoming tidal waters (Davidson-Arnott et al., 2002; van Proosdij et al., 2006a; Yang et al., 2007). Wave activity increases in the winter due to an increase in storm event occurrences and a decrease in the wave attenuating effect of vegetation when die back occurs (Tao et al., 2014).

Sediment accretion patterns within a salt marsh are also governed by the opportunity for deposition of material on the marsh surface. The opportunity for deposition is affected by many interconnected, spatially and temporally variable controls: inundation time, topography, water

flow vectors, velocity and waves, suspended sediment concentration, vegetation and ice (Gordon and Desplanque, 1983; Christiansen et al., 2000; Davidson-Arnott et al., 2002; van Proosdij et al., 2006a,b). In temperate environments, accretion has been shown to be seasonal, with higher rates of accretion occurring over winter (van Proosdij et al., 2006b; Spencer et al., 2012), and this seasonality can also be seen in the temporal variations of accretion controls.

Inundation time is one important component of salt marsh hydrodynamics that is controlled by tidal flow and topography. Generally, sediment deposition during a single tidal cycle will increase with increased inundation time (Leonard, 1997) as well as water depth, which is a function of inundation time (French and Spencer, 1993). However, some studies have shown no significant correlation between sediment deposition and inundation time (van Proosdij et al., 2006b). More variation is introduced in locations where tidal regimes are semidiurnal, such as the Bay of Fundy (Davidson-Arnott et al., 2002), and inundation time varies with the changing tidal range.

Water flow speeds and vectors within a salt marsh are controlled by multiple interacting variables including topography, stage, wind and waves (Davidson-Arnott et al., 2002). During the flood phase of the tidal cycle, velocities are higher, and flow is restricted to the tidal channels. Once water levels exceed bankful conditions (water overtops the channel edges), the water velocity decreases as it flows over the larger area of the marsh surface. The reverse occurs on the ebb tide, when water velocities are low until water levels are restricted to the tidal channels and velocities increase once more (Davidson-Arnott et al., 2002; Friedrichs and Perry, 2001). The general relationship between water velocity and sediment deposition is an increase in deposition with a decrease in water velocity. Less turbulence and wave energy in the water column allow for settling of suspended sediments and deposition on the marsh surface or within

channels (Davidson-Arnott et al., 2002; Friedrichs and Perry, 2001). It has also been found that increased wave activity may cause spatial variation in sediment deposition patterns by increasing deposition in the upper marsh relative to the lower marsh (van Proosdij et al., 2006b).

An increase in suspended sediment concentration has been linked to increased sediment deposition (Friedrichs and Perry, 2001). However, Poirier et al. (2017) found that in a Bay of Fundy marsh system with very high suspended sediment concentrations, there was increased deposition within the marsh creek as suspended sediment concentration increased, but not a significant increase in deposition on the marsh surface. This indicates that the relationship between suspended sediment concentration and deposition may be spatially variable in some circumstances. Poirier et al. (2017) hypothesized that this variability was caused by high amounts of flocculation resulting in very fast deposition of materials in the creek, therefore reducing the availability of material for deposition on the marsh surface.

The role of vegetation in sediment accretion patterns is generally accepted as vegetation presence being a driver of sediment settling and deposition (Allen, 2000; Friedrichs and Perry, 2001). Vegetation presents two separate opportunities for the deposition of material on the marsh surface: physical and chemical. The first opportunity is based on the physical structure of the vegetation. Vegetation presence increases friction in the water column, which reduces flow velocities within the vegetation canopy and attenuates waves (Christiansen et al., 2000; Coulombier et al., 2012). This effect is increased with taller, rigid vegetation, and greater biomass/density (Temmerman et al., 2005b; Leonard, 1997; Neumeier and Amos, 2006). As discussed earlier, reduced wave action and current velocities allows for greater amounts of sediment settling and deposition. Below ground root structures also play a role, by increasing bed-shear strength and preventing erosion and resuspension of sediment (Reef et al., 2018).

In theory, water velocity reduction by vegetation structures should have a significant correlation with sediment deposition. However, multiple field studies have been completed in which results did not show a strong relationship between vegetation height, biomass or density with sediment deposition or the sediment budget (Reef et al., 2018; Moskalski and Sommerfield, 2012). In one study in the Bay of Fundy, a measure of vegetation roughness was found to be positively correlated with sediment deposition during rough conditions, but this relationship was not identifiable in calm conditions (van Proosdij et al., 2006b). It has also been found that in some areas of low density or patchy vegetation cover such as in the salt marsh pioneer zone or along the marsh edge, vegetation can enhance scour and erosion rates rather than decrease them (Temmerman et al., 2007; Feagin et al., 2009; Widdows et al., 2008). These examples illustrate the complexity of interactions between controlling variables, and their variability from marsh to marsh. The second opportunity for deposition of material by vegetation presence is chemical in nature. Some salt marsh vegetation species have adapted to the saline environment by secreting salt. The increase in salinity surrounding plant structures may increase sediment flocculation and therefore deposition (Jeffries et al., 1977).

The effect of vegetation on sediment deposition is seasonal. In temperate environments, salt marsh vegetation undergoes significant seasonal variation, and has little above ground presence during winter due to die back and damage from ice (Watkinson and Davy, 1985; Coulombier et al., 2012). The effects of vegetation on current velocities and sediment deposition are highest at the end of the growing season when biomass is at its maximum (van Proosdij et al., 2006b; Coulombier et al., 2012). Due to this seasonality, when assessing the effect of vegetation on sediment deposition, it is necessary to focus on a seasonal or tidal cycle time scale.

Despite the expected effect of increased sediment deposition due to vegetation presence in the growing season, temperate marshes have been shown to have higher rates of sediment accretion over the winter than during vegetated seasons (van Proosdij et al., 2006b; Spencer et al., 2012). This trend has been linked to an increase in suspended sediment concentrations over the winter (Friedrichs and Perry, 2001), but additionally, winter conditions such as ice can create different opportunities for tidal wetland expansion within the marsh system. Sediments and vegetation matter can be carried onto the marsh surface during flood tides by ice rafts, which provide a significant opportunity for sediment deposition (Gordon and Desplanque, 1983; van Proosdij et al., 2006b; Rabinowitz et al., 2022). As ice forms on marsh, mud flat or creek surfaces, layers of sediment up to 15cm thick may freeze onto the bottom of the ice (Gordon and Desplanque, 1983). During ice break up, blocks of ice with this frozen layer of sediment attached, are lifted and transported on incoming tides and then stranded on ebb tides (Gordon and Desplanque, 1983). As temperatures increase in the spring, the ice rafts melt, and the attached sediment is deposited on the marsh surface. These processes are a form of secondary redistribution of sediment in the coastal zone, meaning that sediment is moved from one area of the marsh to another (Argow et al., 2011). This is also the case for vegetation. When ice forms over vegetated surfaces, there is potential for vegetation to adhere to the ice, allowing for the transport of root structures to different areas of the marsh (Dionne, 1989; Rabinowitz et al., 2022). Although some studies have been completed to assess the importance of ice rafts in the sediment budget of specific tidal salt marshes, few have attempted to quantify this input, and the variables affecting ice raft formation, distribution on the marsh, and sediment load are not fully understood (Argow et al., 2011; Rabinowitz et al., 2022).

1.2.2 Drainage Networks

Drainage networks act as circulatory systems for salt marsh environments, transporting water, organic materials, sediment, nutrients, and pollutants in and out of wetlands (Perillo, 2019). They are very important in salt marsh function, even in coastal environments with minimal tidal influence. Channels provide a place for reproduction, refuge, and growth of juveniles for coastal and marine species, as well as a method of transport to and from the open ocean (Perillo, 2019). Drainage networks are one of the primary features to develop in a coastal wetland environment and are often the most dynamic and sensitive to changes in environmental characteristics due to their high energy nature (Perillo, 2019). Currently, the factors that influence the origin of drainage network features are relatively unknown (Perillo, 2009), although there have been many studies to model drainage network initiation (e.g., D'Alpaos et al., 2010; Fagherazzi et al., 2012; Vandenbruwaene et al., 2012b; Zhou et al., 2014).

In the evolution of natural salt marshes, drainage networks are usually inherited from the previously existing tidal mud flat (Eisma, 1997). Channels will go through an initial deepening and enlarging phase (D'Alpaos et al., 2006) determined by the concentration of sheet flow and bed shear stress causing erosion (Whitehouse et al., 2000), and as the salt marsh platform continues to increase in elevation as it matures, the channel banks become steeper and the channels deeper (D'Alpaos et al., 2005). Vandenbruwaene et al. (2012a) conducted a study that observed changes in channel drainage density and channel width over time in a natural salt marsh that evolved from a bare tidal flat in the Scheldt estuary in Europe and determined that drainage density was heavily influenced by vegetation establishment. The site saw an increase in drainage density as pioneer vegetation patches established, with vegetation patches helping to route flow and encourage erosion of channels. The opportunity to study salt marsh channel initiation and development in an empirical scenario is uncommon, so most data on these

processes come from numerical modelling techniques (e.g., D'Alpaos et al., 2005). This research therefore will provide empirical insight into early development of embryonic creek systems in an MR setting.

1.3 Managed Realignment and Tidal Wetland Restoration

NBA methods are being utilized as a method of climate change adaptation against effects such as SLR and coastal erosion (Doswald et al., 2014). They are often multi-beneficial, having additional positive influences other than climate change adaptation, such as the creation of habitat, carbon storage, or recreation (Faivre et al., 2017) and they can have lower costs when compared to traditional coastal protection methods such as hard defences (Koch et al., 2009; Borsje et al., 2011; Temmerman et al., 2013; Reguero et al., 2018). MR is a type of NBA that involves wetland restoration and utilizes the benefits of the restored wetland for the protection of the new/realigned infrastructure. A diagram outlining this process is displayed in Figure 1.2

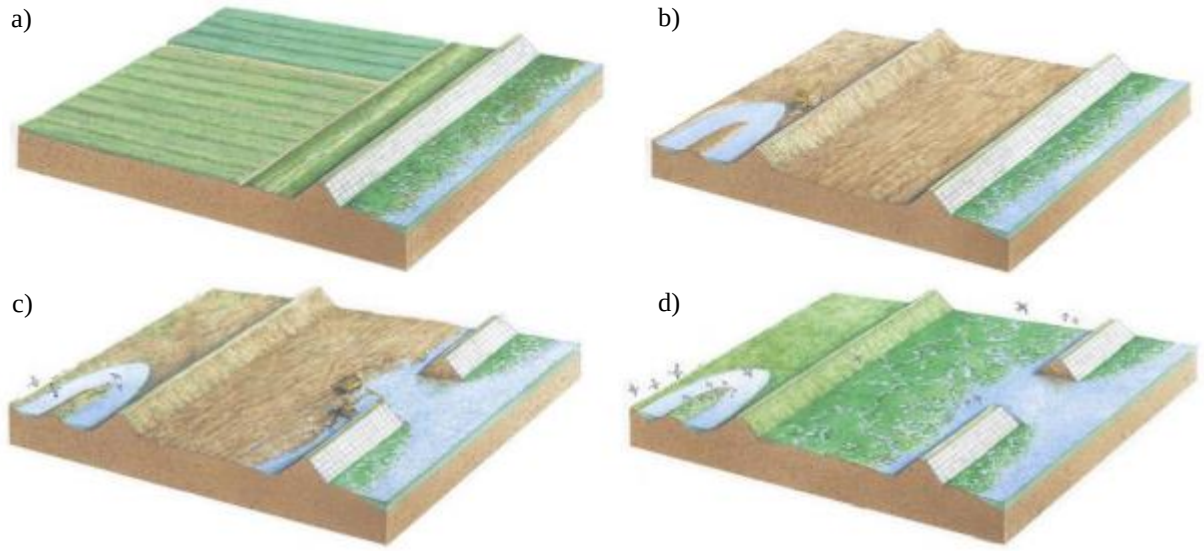

Figure 1.2. Managed realignment process, which includes: a) an existing agricultural dyke with minimal foreshore marsh; b) construction of a new dyke that has been pulled back; c) breaching of the original dyke to reintroduce tidal flow to the restoration area; d) growth of a restored salt marsh that will provide coastal protection to the new dyke as well as numerous ecological benefits (TransCoastal Adaptations: Centre for Nature-Based Solutions, 2019). Reproduced with permission from Dr. Danika van Proosdij.

1.3.1 Sediment Dynamics in Restoration Sites

Although there are multiple salt marsh restoration projects currently taking place in Eastern Canada (Bowron et al., 2012; Wollenberg et al., 2018), the geomorphological and biological processes associated with MR in macrotidal environments with extremely high suspended sediment concentrations such as the Bay of Fundy, and particularly the transformation of former agricultural landscapes to tidal salt marshes, have been infrequently documented in peer-reviewed literature. While research has recently been conducted on the evolution of MR sites (Dale et al., 2018; Brunetta et al., 2019; Virgin et al., 2020), the between site variation in environmental characteristics means that extensive research in a variety of different environments is required to better understand the complex processes and evolutionary trajectories of the tidal wetland landscape. It can be assumed that patterns of sedimentation in MR and restoration sites will be influenced by the complex interaction of multiple variables, similar to processes in natural salt marshes, but that the unique topographical and biological characteristics due to relic agricultural land use, such as the presence of drainage ditches, dales and crowns, and compaction will affect the interactions of such variables and resulting sedimentation patterns.

Since salt marsh vegetation establishment is dependent on tidal flat surface elevation, research on MR restoration sites often investigates the rate of sediment deposition and amount of time required for a tidal flat surface to reach an elevation that is condusive to vegetation establishment and survival. At a microtidal MR site in the Netherlands, Brunetta et al. (2019) measured sedimentation rates on a newly created tidal flat to be 6-7 $cm \cdot yr^{-1}$ and estimated that it would be a further 8-10 years before salt marsh vegetation would establish. Both the starting elevation of the surface relative to the tidal frame, and the rate of sedimentation were controls on this time estimate. In the Bay of Fundy Canada, the Aulac MR project had a mean sediment

deposition of 18.3 ± 3.8 cm in the eastern portion of the site in the first year, and colonization of *Sporobolis alterniflorus* (previously *Spartina alterniflora*) within 2-5 years (Virgin et al., 2020). Sediment deposition values at that restoration site were higher than in a nearby reference salt marsh which had higher starting surface elevations than the restoration site (Virgin et al., 2020), highlighting a significant difference between sedimentation patterns in MR sites compared to natual sites. However, Vandenbruwaene et al. (2011) found that sedimentation patterns in high marsh areas of a restoration site with a controlled reduced tide were similar to those in high marsh areas of a natural marsh reference site. Vandenbruwaene et al. (2011) determined that the most significant vairable affecting sedimentation was mean water depth.

In addition to sedimentation patterns, sediment characteristics in MR and resotration sites have also been examined. A study by Kadiri et al. (2011) compared sediment characteristics in a restored salt marsh and mud flat to those in a natural reference site, and found that while sediments in the restored and natural mud flats had similar characteristics, there were differences in sediment characteristics of the natural marsh and restored marsh. Other morphological characteristics can vary bewteen restoration sites and natural sites, such as the rate of foreshore progradation. An extreme example was found by Friess et al. (2012), when they measured progradation (seward expansion) of a foreshore marsh prior to and post MR, which increased from 3.8 $m \cdot yr^{-1}$ prior, to 21.3 $m \cdot y^{-1}$ post restoration. These variations in sedimentation, sediment characteristics and morphology between natural and restored salt marshes should also lead to variations in the evolution and development of tidal channel networks (drainage networks) in a restoration setting.

1.3.2 Drainage Networks in Restoration Sites

Studies have shown that drainage networks in MR/restoration sites tend to vary in topographic parameters when compared to natural salt marshes (Vandenbruwaene et al., 2012b; Lawrence et al., 2018). A study in the Scheldt estuary in Europe by Vandenbruwaene et al. (2012b) showed that newly formed channels in a 4-year post constructed marsh had lower drainage densities and cross-sectional areas than a nearby natural marsh. Similarly, Lawrence et al. (2018) found that in multiple MR sites in the UK there were fewer creeks and the sites were topographically more similar to coastal agricultural sites than natural marshes. The MR sites in this study also had less vertical surface variation and a higher potential for water accumulation than natural sites. A study by MacDonald et al. (2010) in the Bay of Fundy, Canada, found that salt marshes with a history of agricultural use (storm breached more than 50 years prior to the study) had drainage systems that integrated agricultural drainage ditches and were generally less sinuous than salt marshes with no agricultural history. However, these sites had a comparable drainage densities to the reference saltmarshes with no agricultural history, which may indicate that drainage networks in restored salt marshes may reach comparable densities to natural marshes over a sufficient period of time (in this case, > 50 years), and that other studies show a disparity between drainage densities in restored and natural marshes because the studies were conducted relatively early in the restoration trajectory.

Fewer studies exist that focus on embryonic channel development in salt marsh restoration sites, possibly due to the difficulties involved in measuring and monitoring embryonic channels using traditional methods. It has been suggested that tidal channel development in these sites is related to the antecedent landscape history and the presence of features such as drainage ditches and plough lines (French and Stoddart, 1992), which may be incorporated into the developing drainage network and maintained for long time periods or permanently (e.g., Bowron et al.,

2011; MacDonald et al., 2010). Additionally, sub terranean features of the pre-existing landscape may influence channel development, as proposed by Dale et al. (2018) who utilized RPAS and SfM to monitor embryonic channel evolution at an MR site in the UK and found that the primary creek formation mechanism was the collapse of sub-surface piping. This thesis aims to increase the knowledge base of embryonic channel evolution in MR scenarios.

1.4 Applications of Remotely Piloted Aircraft Systems and Structure from Motion

In recent years, RPAS technology has become more affordable and accessible to the general public, with advancements in flight control and sensor technology allowing for detailed and accurate scientific data collection (Hugenholtz et al., 2012). They offer advantages over other remote sensing imagery and elevation data capturing techniques (manned aircraft surveys, satellites and lidar) such as frequent data collection, high spatial resolution and affordability (Klemas, 2015; Ventura et al., 2017). Consumer-grade RPAS are most often equipped with adequate geolocation technology for manual control of the aircraft and maintaining correct positioning and heading during automated flight plans. Images of the ground surface collected during these flights are processed via SfM, an algorithmic process in which matching points between overlapping photographs are identified and utilized to determine the 3D geometry of features/landscapes. From this geometry, orthomosaics (merged imagery), 3D point clouds and Digital Surface Models (DSMs) are produced. Ground Control Points (GCPs) are used to georeference these products (Eltner et al., 2016), and a well distributed GCP network with at least 4 GCPs has been shown to result in higher horizontal and vertical accuracy of SfM products (Wolf et al., 2000; Tonkin and Midgley, 2016; Raczynski, 2017).

Recent advancements in RPAS technology have introduced survey-grade geolocation capabilities. New RPAS models have been outfitted with differential GNSS (dGNSS) equipment

(RTK) to significantly increase the accuracy of geolocation data during RPAS surveys. This precise positioning information can be integrated into the photogrammetric process, allowing for higher accuracy in photogrammetric products, and a potential reduction in the number of GCPs required during surveys (Taddia et al., 2019). Reducing GCPs in a salt marsh environment is highly advantageous. Firstly, when working in a tidal environment, the site is only accessible and not flooded for certain periods of time. Surveys must be completed within a tide-window to ensure full collection of data before inundation, and full retrieval of deployed equipment such as GCPs. RPAS surveys allow for the collection of data in otherwise inaccessible environments (Casella et al., 2017). Secondly, salt marsh evolution and ecomorphodynamics can be influenced by human interactions, such as footprints in marsh sediments (Kalacska, et al., 2017). By reducing the amount of travelling through the site required (by deploying fewer GCPs), natural process will remain less altered.

Since dGNSS technology on RPAS is fairly new, there have been few studies to assess accuracy improvements and the capacity for GCP reduction. One such study by Taddia et al. (2019) determined that if using a DJI Phantom 4 RTK RPAS, GCPs could be reduced to one single deployed target per survey, while retaining product accuracy at comparable levels to a full set of well distributed GCPs. However, there has been evidence to the contrary that a full deployment of GCPs showed significantly higher accuracy regardless of dGNSS integration (Forlani et al., 2018). This discrepancy in results may be due to variations in equipment (different RPAS in each study), as well as survey landscape. It is clear that more studies should be completed to determine the capabilities of this new technology in geomorphological analyses.

Assessing the accuracy of SfM-derived products can be conducted using validation data and is generally completed as either point to raster (point validation data compared to raster

products), raster to raster (raster validation data compared to raster products) or point to point (point validation data compared to point products) (Carrivick et al., 2016). The most commonly used method is point to raster, specifically the calculation of a Root Mean Square Error ($RMSE_z$) from the differences between point validation elevation data and SfM-derived surfaces (Tsutsui et al., 2007; Carrivick et al., 2016; Bui et al., 2018). This method is problematic however, as it provides one error estimation value for an entire DSM and assumes that errors in SfM-derived surfaces are random (pairwise uncorrelated). It is known that errors in SfM DSMs are actually higher in areas of high surface homogeneity (mud, shadows, water) (Eltner et al., 2016) and high vertical relief and are therefore spatially autocorrelated and non-random (Jaud et al., 2016). Applying RPAS technologies and SfM in tidal areas such as salt marshes and coastal restoration sites also poses an environmental challenge, as the presence of water can cause issues with point matching in the photogrammetric process and increase noise in data products (Jaud et al., 2016).

Multiple recent studies have begun to assess the applicability of RPAS as a monitoring tool in coastal systems. Kalacska et al. (2017) used a small RPAS to measure topography in a salt marsh site and determined that RPAS elevation models were able to detect finer scale topographic details and features such as small channels at a higher resolution compared to aerial lidar. Zhu et al. (2019) utilized repeat RPAS surveys to monitor the spatial and temporal evolution of *Sporobolis alterniflorus* colonies in Chinese coastal wetlands. MR sites have also been studied using RPAS technologies, with a study by Dale et al. (2018) looking at embryonic creek systems, and studies by Brunetta et al. (2019) and Dale et al. (2020) looking at surface elevation change over time. Dale et al. (2018) determined that the agreement between differential GPS validation data and RPAS DSMs was suitable, and that RPAS are an appropriate tool for studying embryonic creek development at resolutions not achievable with traditional methods.

1.5 DEMs of Difference

The utilization of multitemporal DEMs for erosion and deposition estimates is a common technique as it provides benefits over traditional, interpolated point-based surveys, including reduction of error (Cavalli et al., 2017). The process involves subtracting two DEMs of the same area, collected at different times, to calculate surface elevation change between the two data collection dates and results in a DEM of Difference (DoD) raster (Milan et al., 2011). While commonly accepted as more accurate than traditional techniques, several studies have stressed that an assessment of DEM uncertainty and error propagation is required to quantify the reliability of the output DoD (Lane et al., 2003; Wheaton et al., 2010). Additionally, DoDs may be used to calculate volumetric change between surfaces (Lane et al., 2003; Tsutsui et al., 2007; Haas et al., 2016; Brunetta et al., 2019; Matheson, 2020; Vecchi et al., 2021), and additional volumetric uncertainty estimations may be conducted (Taylor, 1997). This includes the calculation of an absolute volumetric uncertainty of a particular DoD using the individual $RMSE_z$ values from input DEMs. Lane et al. (2003) proposed a formula for absolute volumetric uncertainty that adds the DoD errors in quadrature and has been used in recent geomorphological studies with RPAS and SfM techniques (Haas et al., 2016; Xiang et al., 2018). This technique, however, was developed for older elevation model creation methods such as total station and dGNSS surveys in which errors are randomly distributed in the data. Since errors in SfM surfaces are higher in areas of high vertical relief, homogeneity, and shadows, they are spatially correlated and not random in nature (Jaud et al., 2016). Therefore, the Lane et al. (2003) equation may not be appropriate for SfM surfaces and is expected to be an underestimate of volumetric uncertainty (Matheson, 2020). A more appropriate volumetric uncertainty equation for SfM surfaces was proposed by Taylor (1997), which assumes that errors are not pairwise uncorrelated.

A commonly used approach for quantifying significant change in a DoD is the application of a Level of Detection (LoD), which is based on the accuracy of input DEMs (Wheaton et al, 2010; Hugenholtz et al, 2013). The application of an LoD is a method that helps avoid propagating error in volumetric change calculations by applying a high level of scrutiny to DoD values, and only incorporating values of significant change (Hugenholtz et al., 2016; Cavalli et al., 2017). LoDs have recently been applied to RPAS and SfM datasets to determine volumetric change a variety of environments including an iron ore mine (Haas et al., 2016), a gravel riverbed (Lane et al., 2003), a salt marsh restoration site (Brunetta et al., 2021), and in borrow pits[1] in the Bay of Fundy, Canada (Matheson, 2020). Previous studies in salt marsh environments, including Matheson (2020) and Brunetta et al. (2021), have used RPAS with consumer-grade positioning systems, and resulting $RMSE_z$ values ranged between 3.1-6 cm (Brunetta et al., 2021) and 4.1-15.6cm (Matheson, 2020). It is expected that utilizing an RPAS equipped with survey-grade positioning will decrease the $RMSE_z$ of SfM elevation models, and therefore reduce the LoD which will then reduce amount of excluded data from volumetric calculations.

1.6 Purpose and Objectives

The overarching objective of this research is to utilize new advancements in RPAS technology to measure the spatial and temporal patterns of the morphological evolution of a restoring salt marsh landscape. Specifically, this research aims to delineate developing drainage networks and calculate surface elevation and volumetric change within the study site, and by incorporating multi-temporal datasets, identify patterns in these measurements over time. By

[1] Also known as “clay pits”, borrow pits are elongated pits, often parallel to the dyke, that are used to pull materials for dyke construction (Karle and Bartholomä, 2008).

conducting these analyses, this research will contribute to the current scientific knowledgebase of the evolution trajectory of restoring salt marsh landscapes. It will provide additional insights into the influence of high suspended sediment concentrations, hyper tidal regime, and antecedent landscape history of agricultural use. Additionally, this research aims to determine the applicability and limitations of RTK-enabled RPAS and SfM techniques for these types of environmental monitoring, and to develop repeatable methodologies for future research. These objectives will be addressed by investigating the following research questions:

1) What are the characteristics of the developing channel networks within the site, and how do they change throughout the study period?
2) What are the spatial and temporal patterns of surface elevation and volumetric change within the study site, and are these patterns seasonal in nature?
3) Is there a correlation between surface elevation change and starting elevation or proximity to channel?
4) Does the antecedent landscape history influence sedimentation and channel evolution patterns? Do sedimentation and channel evolution patterns vary between the borrow pit and other areas of the site?
5) Are RTK RPAS and SfM technologies appropriate for measuring surface elevation/volumetric change as well as delineating channels at a hyperspatial scale in a recently restored MR site? What are the limitations of these techniques?

Chapter 2: Study Site

This research was conducted at the Converse dyke realignment and salt marsh restoration site, located within the Cumberland Basin in the Upper Bay of Fundy, Canada. The Cumberland Basin Estuary covers 118 km^2 and approximately 2/3 of this area is occupied by salt marshes and mud flats (van Proosdij et al., 2006a) (Figure 2.1). Salt marshes in this region are exposed to semi-diurnal macro-tidal conditions, with a tidal range of 12-14 m (Davidson-Arnott et al., 2002), seasonally variable, high suspended sediment concentrations ranging from 0.05 $g \cdot l^{-1}$ to 4.0 $g \cdot l^{-1}$ (Amos et al., 1991), and temperate weather conditions, with ice and snow present for at least 3 months of the year (van Proosdij et al., 2006b). Concentrations within tidal rivers of the Upper Bay can exceed 70 $g \cdot l^{-1}$ near the turbidity maximum and are dominated by fluid mud (Purcell, 2021). Salt marshes in the Cumberland basin are minerogenic, with surface elevation increases resulting primarily through sediment deposition rather than below ground biomass accumulation. Suspended sediments within the basin range from fine to coarse silt (van Proosdij et al., 1999).

The study site runs along the eastern side of the mouth of the Missaguash River, which is one of multiple large tidal rivers that run through the greater Tantramar marsh system and acts as the Nova Scotia and New Brunswick border. The original dyke protecting this marshland was experiencing extensive erosion, so the site was chosen for an MR and restoration project (Bowron et al., 2021) part of the larger *Making Room for Wetlands*[2] initiative, funded by the Department of Fisheries and Oceans Canada's Coastal Restoration Fund (CRF). This project involved the removal of approximately 420 m length of eroding dyke and backfilling the removed materials into the drainage ditch inland of the original dyke to a surface elevation of ~5.9 m CGVD2013, to bring the surface to the elevation of the natural foreshore marsh.

[2] https://www.transcoastaladaptations.com/making-room-for-wetlands

Additionally, 150 m of new dyke was constructed to a minimum elevation of ~7.2 m CGVD2013 using materials from the old dyke where possible and supplementing materials from adjacent upland areas. This included the creation of a drainage outlet (referred to as the main channel mouth) connecting the inner ditch to the main river channel, decommissioning the existing aboiteau, and the creation of a borrow pit in front of the new dyke (Figure 2.2) from which materials were excavated and used in construction of the new dyke.

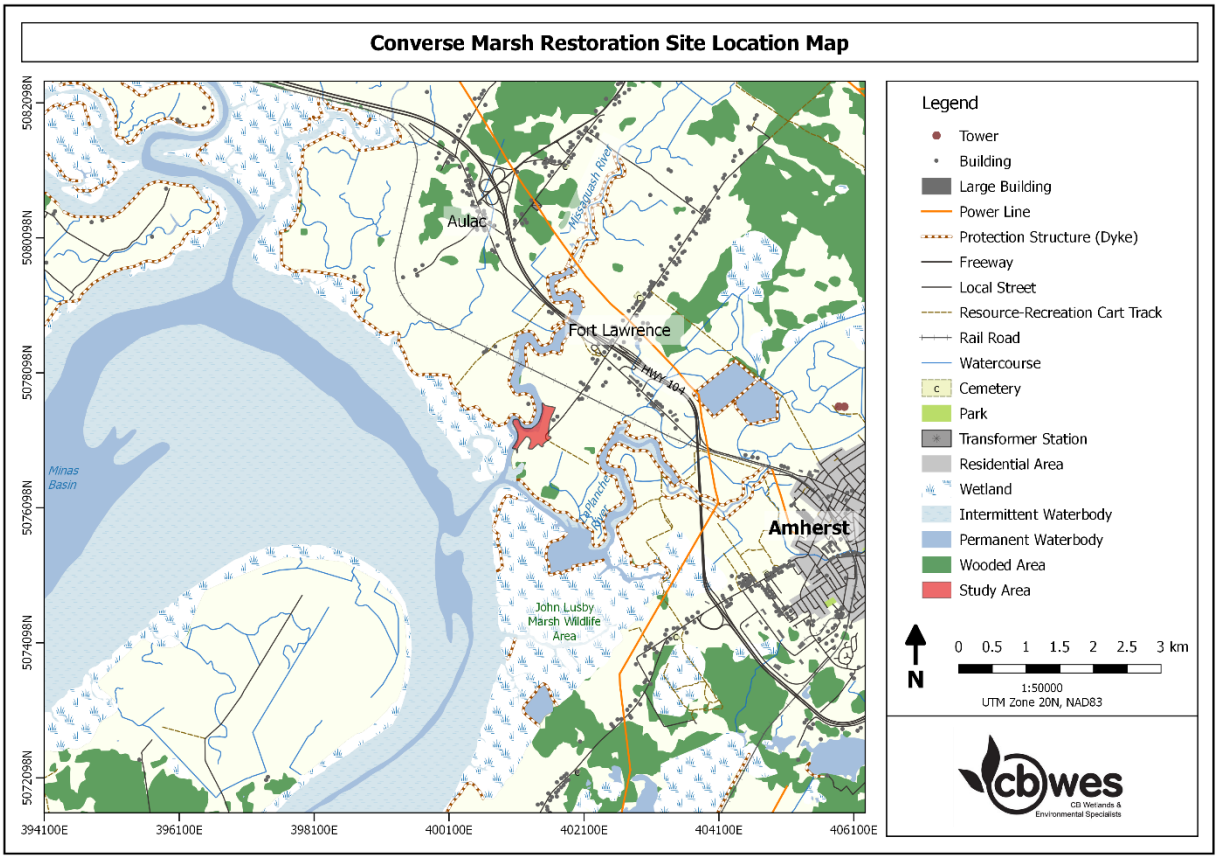

Figure 2.1. Cumberland Basin and surrounding area (Bowron et al., 2021). Reproduced with permission from Tony Bowron.

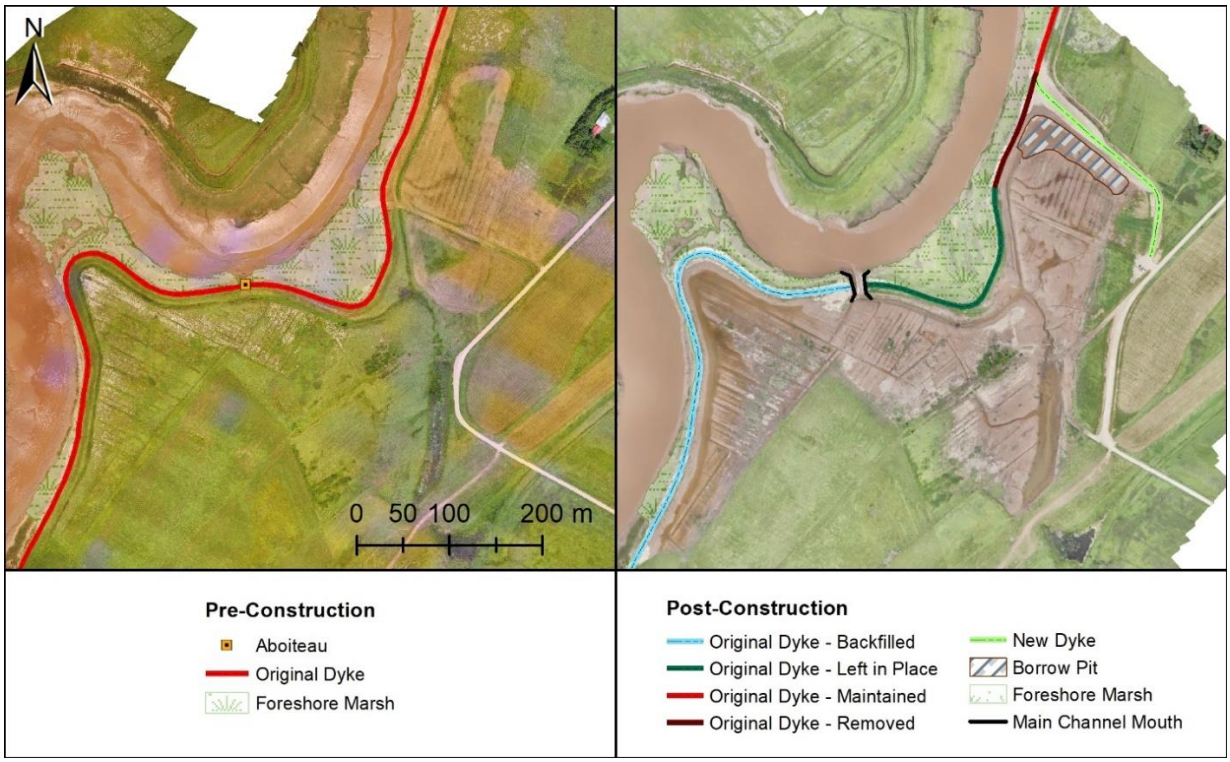

Figure 2.2. Pre-construction (July 2018) and post-construction (August 2019) configurations at the Converse restoration site.

To act as an additional upland tidal barrier, the Fort Lawrence Road was shifted slightly and upgraded to a minimum elevation of ~7.2 m CGVD2013 (Bowron et al., 2021). These activities were completed by December 21, 2018, when the final breach and first tidal flow into the site occurred. Total restored area for this site was 15.4 ha (Bowron et al., 2021). As part of the restoration project's ongoing monitoring program, geospatial data on hydrology, sediments, and vegetation have been collected at the Converse restoration site since 2017 and include pre-restoration baseline conditions.

Topography on the site is strongly influenced by its antecedent landscape history. Relic agricultural ditches cover most of the site, excluding the borrow pit where sediment was excavated and the remaining surface was flattened and graded (Figure 2.3), as well as a freshwater stream area in the southeastern corner of the site. There are also some remnants of

natural salt marsh channels that pre-date the site's agricultural history located south of the borrow pit (northeast section of the site). Hydrological flow onto the site is restricted by the main channel mouth on most high tides, which can be visualized in the flood map displayed in Figure 2.4. Velocities through the channel mouth area are high and can reach 0.6 $m \cdot s^{-1}$ during spring tide conditions (Bowron et al., 2021). Larger spring tides allow for overmarsh flow into the site in areas where the dyke was levelled/backfilled at peak water levels (Figure 2.4). Maximum recorded water level for the 2020 season was 7.1 m CGVD2013 as recorded with a Hobo Level Logger within the Missiguash River. Recorded water levels as well as precipitation for the same period, are shown in Figure 2.5. Ice formed within the Cobequid Bay and Missiguash River during the winter are carried into the site via the main channel mouth during spring tides and are deposited (Figure 2.6), potentially carrying in sediment loads from elsewhere in the system (Argow et al., 2011).

Figure 2.3. Converse restoration site borrow pit excavation prior to site breach. Imagery collected with a DJI Phantom 3 RPAS on September 24, 2018.

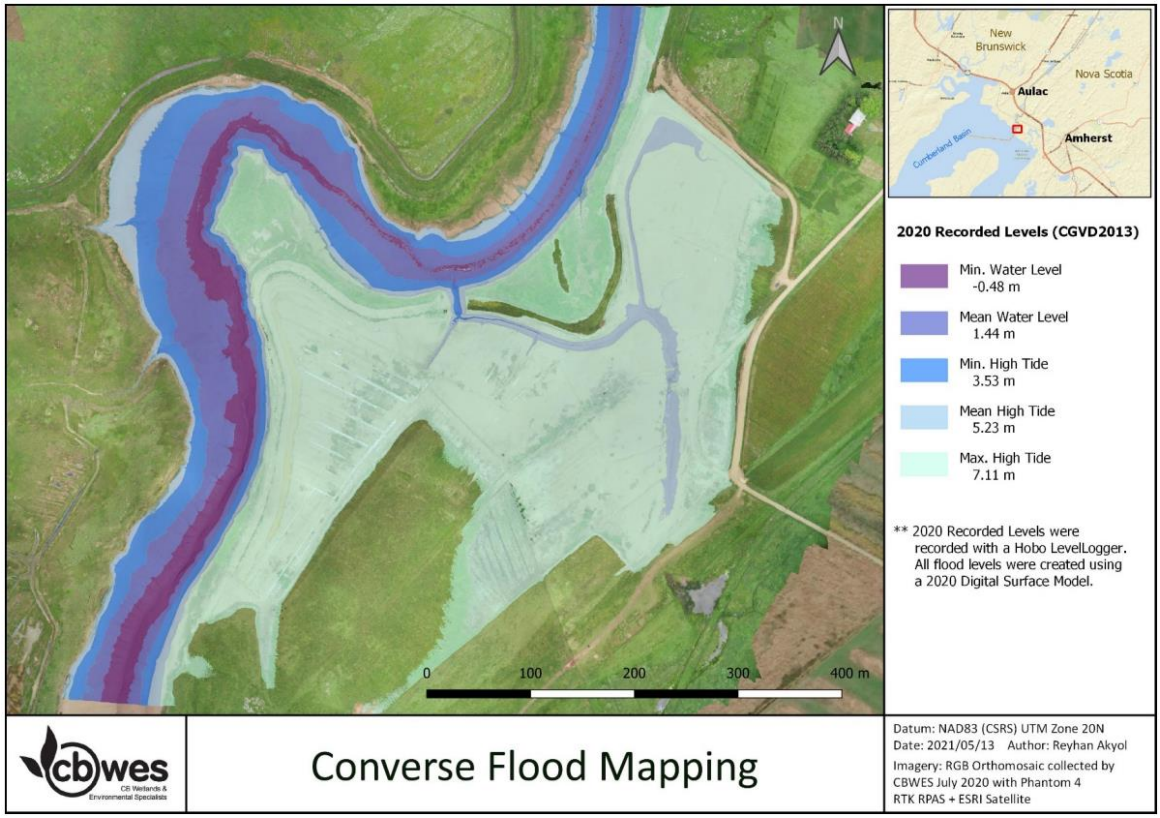

Figure 2.4. Flood map for Converse restoration site, from 2020 river logger flood statistics (Bowron et al., 2021). Reproduced with permission from Tony Bowron.

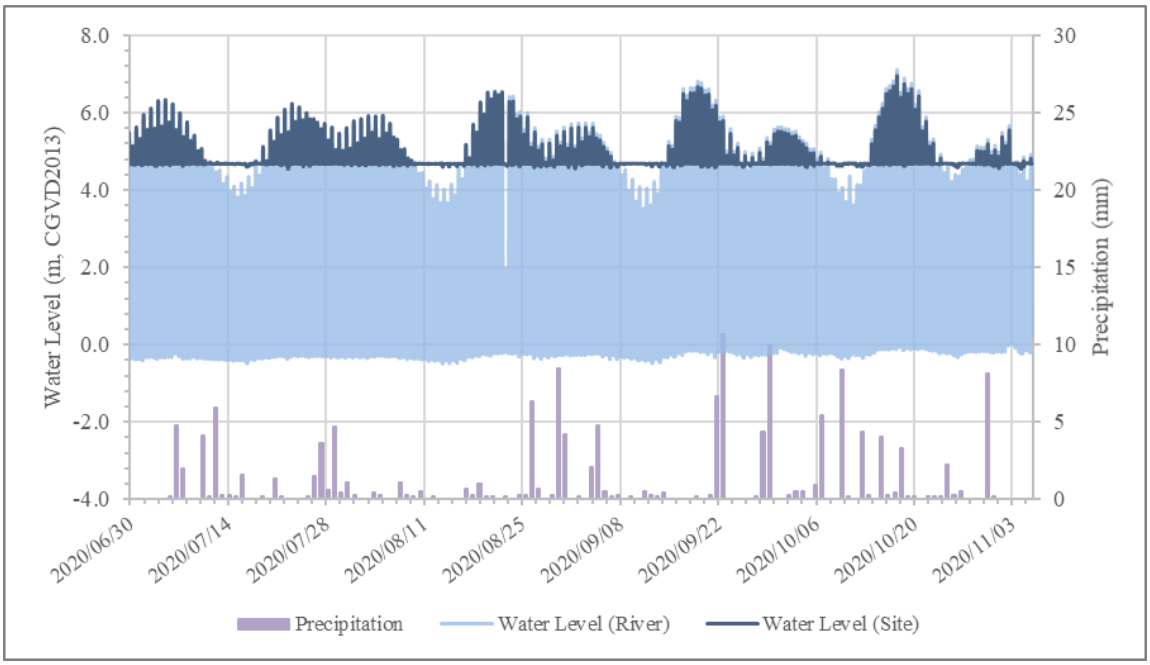

Figure 2.5. Water levels in the Converse River and restoration site with precipitation from Nappan Auto, NS Climate Data Station (Bowron et al., 2021). Reproduced with permission from Tony Bowron.

Figure 2.6. Ice blocks within the Converse restoration site in February 2020.

Measurements of surface elevation change and sediment accretion at the study site were collected from 2018-2020 as part of the project monitoring program. Results showed that both sediment accretion and subsurface processes were contributing to surface elevation change (Bowron et al., 2020). Sediment accretion between 2018-2019, measured using marker horizons, ranged from 0.02-7.82 cm (mean of 2.48 cm ± 2.0 cm), and generally decreased with increasing elevation (Bowron et al., 2020). Accretion values confirm that sediments are being imported to the restoration site surface (Bowron et al., 2020). Sediment characteristics measured between August and November 2020, showed that the mean grain size of marsh surface sediments ranged from 5 µm to 18 µm and these sediments were classified as fine to coarse silt. Suspended sediment concentrations measured at the site in the 2020 field season during spring tide conditions showed seasonal variability, with concentrations ranging from 80.0-857.6 $mg \cdot l^{-1}$ in August and 289.0-2062.5 $mg \cdot l^{-1}$ in November (Figure 2.7). Concentrations varied over the high tide collection period in both collections, but were generally higher in November than August, and tide height was determined as the significant predictor variable for these results (Elliott, 2022).

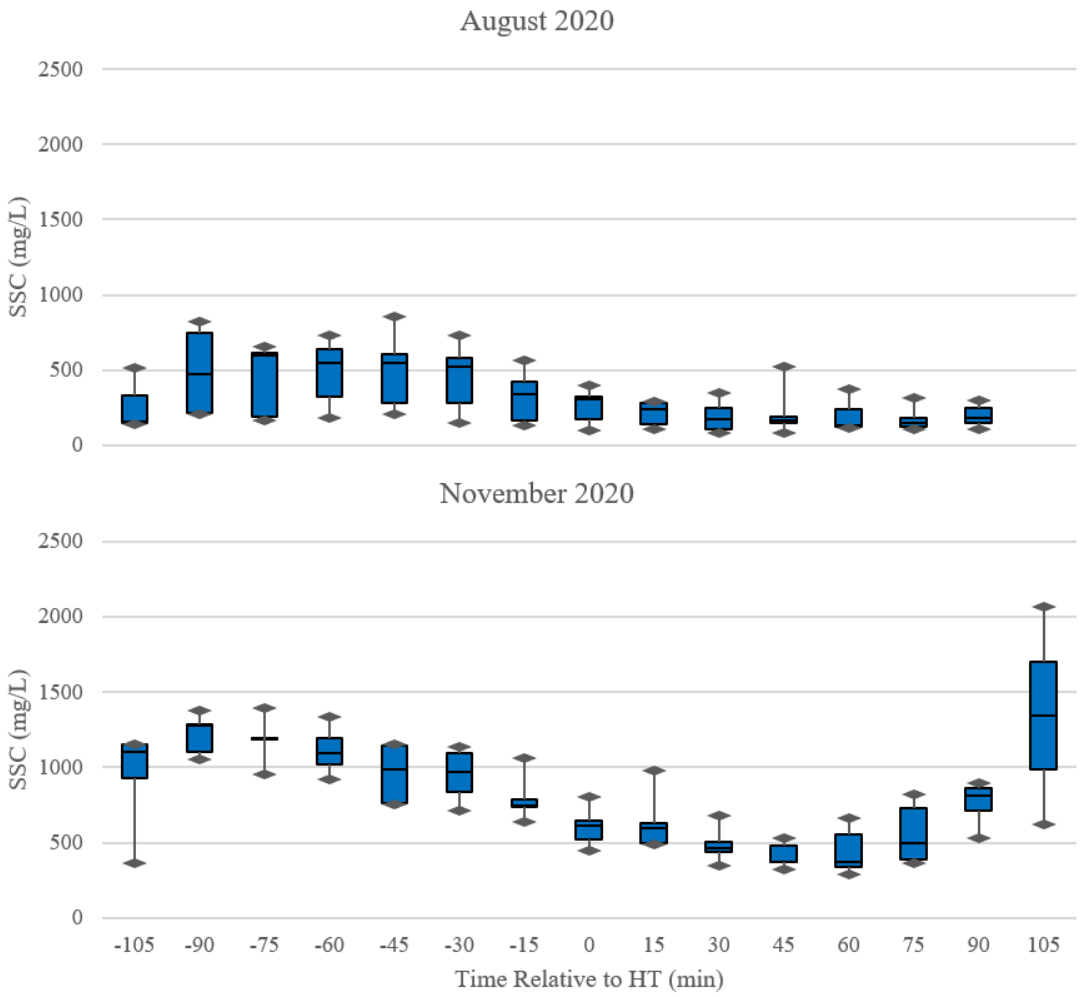

Figure 2.7. Suspended sediment concentrations measured at the Converse restoration site during the 2020 field season with an ISCO water sampler. Measurements were conducted around multiple spring high tides (Elliott, 2022) Reproduced with permission from Megan Elliott.

Chapter 3: Methods

Spatial and temporal patterns of channel network evolution and sedimentation at the Converse restoration site were determined using multi-temporal surveys with an RPAS. Imagery was photogrammetrically processed using SfM software to produce orthomosaics and DSMs for further analyses. GIS software was used to create models of surface elevation change between surveys, calculate volumetric change in areas of interest, delineate and characterize channel networks, and examine change in those networks over time. Additional analyses were conducted with R to determine correlation between surface elevation change, elevation, and proximity to channel networks. Results were also examined to determine the applicability of RTK-enabled RPAS technologies for measuring and monitoring the morphological evolution of MR sites at high spatial scales. Detailed methods are described in the following sections.

3.1 Data Collection

Low altitude RPAS surveys were conducted with a DJI Phantom 4 RTK quadcopter (Figure 3.1a). This aircraft was chosen because it is equipped with RTK GNSS capabilities, providing survey-grade geolocation data for collected imagery. Increased image positioning accuracy from the RTK theoretically increases accuracy in photogrammetric processing and resulting data products and has been shown to reduce the required number of GCPs which are required for data georeferencing (Taddia et al., 2019). The aircraft system included a controller for piloting with built-in flight planning software and a heads-up display with flight details and image transmission from the aircraft.

Aerial imagery was collected between November 2019 and May 2021, and details on all collections are listed in Table 3.1. Required conditions for flight safety and image quality included low wind (less than 36 km/h at flight altitude) (DJI, 2020), no precipitation, and

sufficient daylight levels. For planning purposes, these conditions were assessed prior to field deployments using UAV Forecast (https://www.uavforecast.com/) and SpotWX (https://spotwx.com/) web applications. Tidal conditions also limited flight windows, with all flights being conducted around low tide to maximise the amount of exposed sediment and minimize the amount of water within the survey area. Water reduces visibility (and therefore measurement) of sediment surfaces and increases noise and error in SfM-derived elevation models by causing improper point matching during the photogrammetric process (Jaud et al., 2016).

Two separate flights were conducted during each survey. The first was flown at an altitude of 120 m Above Ground Level (AGL), the regulated maximum altitude for RPAS flights in Canada (400', 122 m) without a Special Flight Operations Certificate (Transport Canada, 2019), to allow for full coverage of the study site (Figure 3.2) in a timely manner. For this flight, the camera was positioned at a nadir angle, meaning that its line of site was perpendicular to the ground surface, or pointing straight down, which is the most commonly used and preferred method in environmental mapping (Griffiths et al., 2019). To examine a few key areas of interest within the study site in greater resolution and detail, the second flight was flown at a reduced altitude of 65 m, which resulted in an increased Ground Sample Distance (GSD), and covered a smaller target area of the site that included the borrow pit, channel mouth, and the channel that connects both features (Figure 3.2). A reduced flight altitude has been shown to increase data accuracy (Raczynski, 2017), and in this study, may improve our ability to measure smaller changes in areas of interest. Additionally, this flight was conducted with an oblique camera angle of 10˚ from nadir. The oblique camera angle may allow for vertical structures such as channel

banks to be picked up more accurately in the imagery compared to a nadir camera angle and has been shown to increase final product accuracy in SfM processing (Taddia et al., 2019).

Each flight was planned with DJI flight planning software (on the DJI Phantom 4 RTK flight controller) and the same plan was used for all flights of each type when possible (in some instances, settings were modified to account for varying collection conditions). Both flight plans had an image side overlap of 60%, and front overlap of 80%, and images were collected based on time intervals (calculated automatically by the flight software using aircraft speed to ensure consistent image overlap throughout the flight). Due to aircraft malfunction during some collections, images were not collected by the aircraft (image dropping) in small sections of the flight plans. To account for this missing data, the aircraft was manually flown in these areas and images were collected by the pilot. The RPAS was connected to SmartNet NS via a cellular network to provide the RTK survey-grade positioning for each collected image.

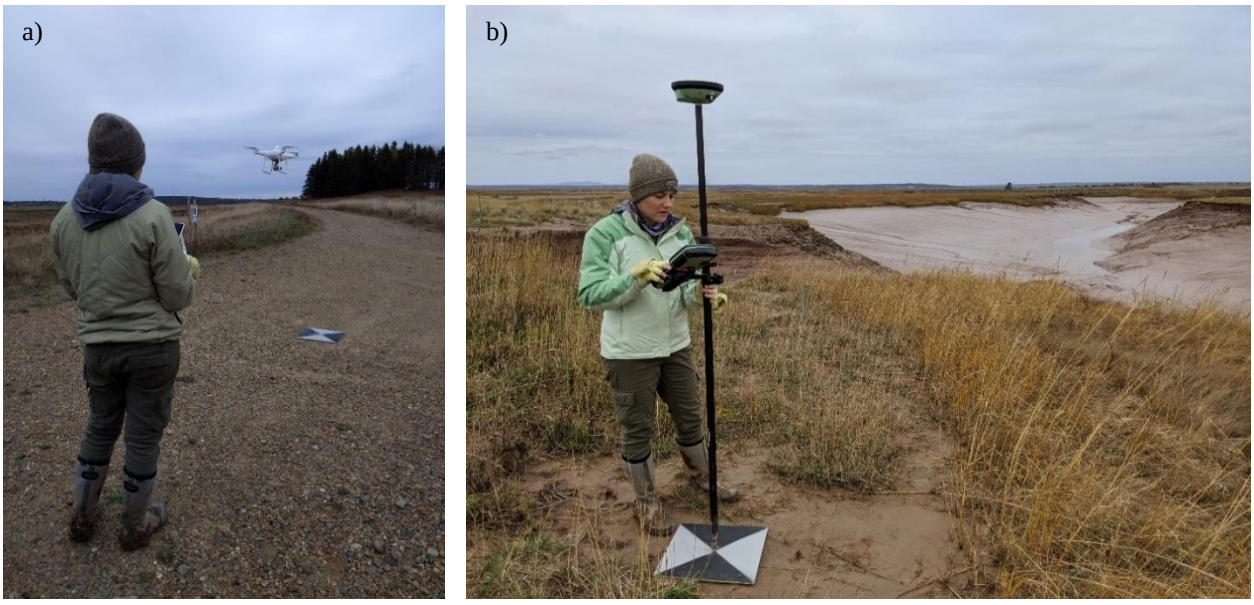

Figure 3.1. a) DJI Phantom 4 RTK taking off for an aerial survey at the Converse restoration site and pilot. b) Collection of a GCP position with a Leica GS14 GNSS with RTK corrections. Both activities were conducted at the Converse restoration site on November 8, 2020.

Table 3.1. Flight plan and environmental conditions for all completed aerial surveys of the Converse restoration site.

Date	Coverage	Camera angle (˚)	Altitude (m)	Start time	End time	# Photos collected	Cloud cover	Max ground windspeed (km/h)
2019/11/24	Full site	-90	120	15:10	15:38	357	1/8	7.0
	Target area	-80	65	14:32	15:07	653		
2020/06/01	Full site	-90	120	13:53	14:10	278	6/8	12.8
	Target area	-80	65	14:20	14:55	654		
2020/07/09	Full site	-90	120	10:25	10:43	278	6/8	8.0
	Target area	-80	65	10:54	11:28	657		
2020/08/21	Full site	-90	120	08:46	9:03	279	7/8	5.6
	Target area	-80	65	09:06	9:51	686		
2020/10/05	Full site	-90	120	10:19	10:35	279	7/8	7.0
	Target area	-80	65	10:38	11:15	694		
2020/11/08	Full site	-90	120	11:51	12:08	278	8/8	9.2
	Target area	-80	65	12:12	12:51	664		
2021/05/04	Full site	-90	120	13:10	13:31	278	6/8	2.3
	Target area	-80	65	13:35	14:15	684		

Figure 3.2. Approximate coverage of each flight type, full site (blue polygon) and target area (red polygon) for RPAS aerial surveys of the Converse restoration site. Background imagery collected August 21, 2020 with a DJI Phantom 4 RTK RPAS.

A total of 10 GCPs were deployed throughout the study site prior to each survey with a configuration based on recommendations in the literature (James and Robson, 2012; Tonkin and Midgley, 2016), and their locations were measured with a Leica GS14 RTK GNSS unit (see Figure 3.3 for approximate GCP deployment locations, and Figure 3.1b for an image of GCP position measurement). GCPs were deployed in approximately the same locations for each flight but varied slightly between deployments. These photo-identifiable targets were used to georeference the data products during photogrammetric processing (Eltner et al., 2016). dGNSS points were also collected with the Leica unit on areas of bare ground throughout the study site during survey deployments, to use as vertical validation for elevation data products. Point locations varied between surveys depending on accessible bare ground.

Figure 3.3. Approximate GCP deployment locations at the Converse restoration site for RPAS aerial surveys. GCP locations varied slightly between deployments. Background imagery collected August 21, 2020 with a DJI Phantom 4 RTK RPAS.

3.2 Data Analysis

3.2.1 Photogrammetric Processing

Photogrammetric processing of aerial imagery was conducted with Agisoft Metashape® (Agisoft LLC, Russia). This software is the most commonly used for research purposes (Eltner et al., 2016) and visual comparisons have shown that it can produce more detailed elevation models compared to the other available processing software for this research, Pix4D Mapper (Figure 3.4). A study by Sona et al., (2014) determined that Agisoft Photoscan (software name at time of publication) produced higher quality photogrammetric products than competing software such as Erdas-LPS, EyeDEA and Pix4D. Highest resolution and accuracy settings within Agisoft Metashape® were used for all steps of processing to produce the highest quality/resolution data products possible (Agisoft LLC, 2019). Input imagery was assessed using the "Estimate Image Quality" tool in Agisoft Metashape® prior to processing. This tool estimates an image quality value between 0 and 1 for each image, with lower values corresponding to lower quality. Photos that were identified as having the lowest quality values were visually assessed for quality issues such as blurring from aircraft rotation or movement, and problematic images were removed prior to processing.

A detailed description of Agisoft Metashape®'s tools and processing steps can be found in their user manual (Agisoft LLC, 2019). A general overview of the remaining processing steps, after adding images and assessing quality, used in this research is as follows (with non-default settings listed):

1) Convert image coordinate system to NAD83(CSRS)/UTM Zone 20N + CGVD2013 height
2) Align Photos (Accuracy: Highest)

3) Add GCPs, and manually shift their point locations to match target centers in the imagery
4) Optimize Cameras
5) Build Dense Cloud (Quality: Ultra High, Depth Filtering: Mild)
6) Build DEM (Source data: Dense cloud)
7) Build Orthomosaic (Surface: DEM)

It is important to note that although Agisoft Metshape® references the elevation model as a DEM, since all points from the dense point cloud, including those from vegetation canopy, were used in creating the elevation model, the output product is actually a DSM. Also, georeferencing of the data takes place within steps 2-4, using both RTK corrected image positions (initial photo alignment) and GCP positions (camera optimization) for high quality georeferenced data outputs (Eltner et al., 2016). Following the above steps, both the DSM and orthomosaic for each dataset were exported as TIF files. Data resolution for each file was rounded up to the nearest 5 mm for export. Resulting DSMs were then assessed for accuracy using their respective collected vertical validation points by calculating the vertical offset between validation points and elevation models, and then summarizing those offsets with simple statistics (minimum, maximum, mean absolute error, standard deviation and $RMSE_z$).

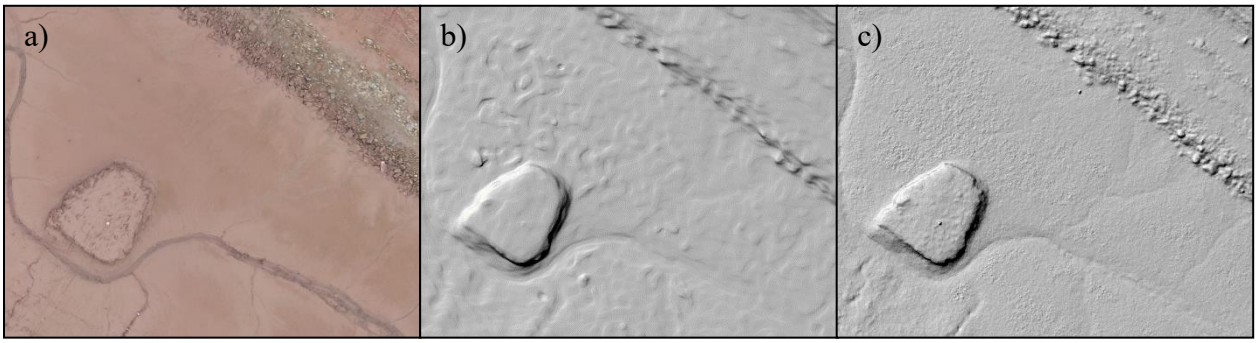

Figure 3.4. a) Imagery, b) hillshade elevation model created by Pix4D Mapper, and c) hillshade elevation model created by Agisoft MetaShape of the Converse restoration site borrow pit. Default settings were used in both SfM processing workflows.

3.2.2 Channel Delineation

Channels were delineated using a semi-automated method that was scripted using Python scripting language and ESRI Arcpy tools. The script can be run within a python IDE program, or from a Command Line on a computer equipped with the relevant software and licenses (ESRI ArcMap or ArcGIS Pro, Spatial Analyst extension, Python 2.7.16), and processes one dataset at a time. The delineation process uses ArcMap's Hydrology toolset, which is commonly used for hydrological analysis of landscapes (Vandenbruwaene et al., 2012; Li et al., 2019). A flow chart of the script's steps is shown in Figure 3.5.

Output DSMs from Agisoft Metashape contain erroneous data around their edges caused by an extrapolation of data beyond the point cloud (edge effects). These areas do not contain valid elevation data and therefore must be removed prior to further processing. An edge clip polygon was manually created by assessing the extent of edge artifacts on all DSMs of both coverages (full site and target area) and determining the minimum extent of clean data. This resulted in two polygons, one for full site datasets and one for target area datasets that would be used to remove erroneous edge artifacts. The full site polygon was further clipped along the centerline of the Missiguash River to remove areas that were not of interest and to reduce processing time in later steps. The first step in the processing script was to clip the input DSM to its corresponding edge clip polygon using the Clip Raster tool. The output from this tool was a "clean" DSM that no longer contained edge artifacts. Further clipping was completed in the next step using an input elevation value. Since only areas within a tidal flooding extent were relevant for channel delineation, a maximum flood extent value of 6.959 m CGVD2013 was derived from Hobo Level Logger data collected within Converse restoration site over the 2019 and 2020 field seasons. This value was the input for a Conditional statement that clipped the input DSM to all areas with an elevation below the maximum flood extent.

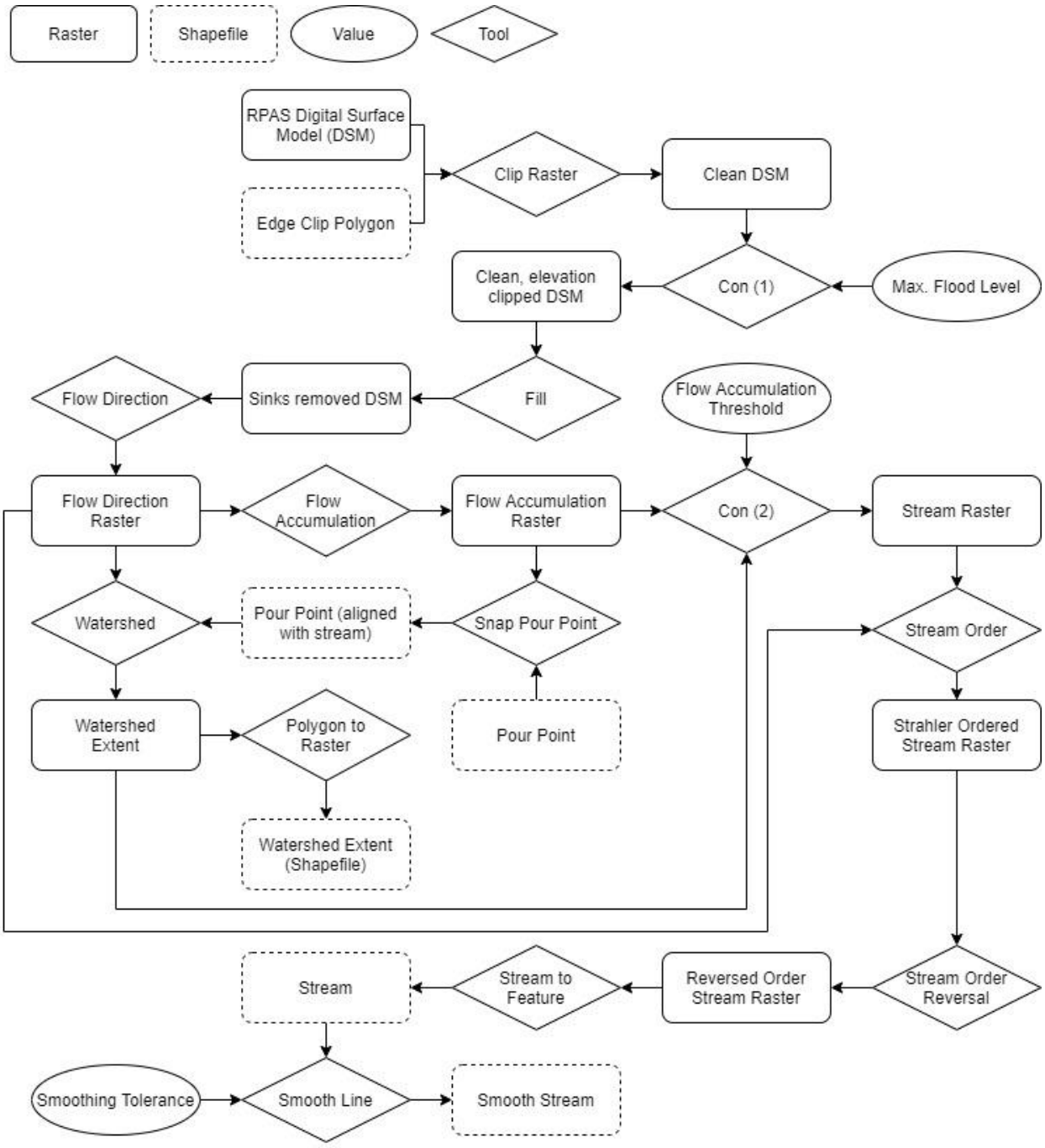

** Con Statements:
(1) If DSM value < Max. Flood Level, output the DSM value (Removes areas of elevation above maximum flood level.)
(2) If Watershed value is not null, and Flow Accumulation value > Flow Accumulation Threshold, output a value of 1 (Removes areas outside of watershed, and returns a value of 1 for any pixel above the Flow Accumulation Threshold. These cells are considered "stream" cells. All other cells are null.)

Figure 3.5. Channel delineation script steps.

After preparing the DSM, tools from the hydrology toolbox were used to begin channel delineation. First, the Fill tool was used to remove sinks in the elevation data that would cause processing failures in future steps. The Flow Direction tool was then run with the clean, filled DSM as an input, to create a raster output of flow direction following the steepest gradient from each cell. The D8 method was used for this tool, meaning that flow direction could only occur from a cell to one of its eight neighboring cells (ESRI, 2020). There are two other flow direction methods that can be used with this tool that allow for more complex direction values, but these flow direction outputs are not compatible with one of the later processing steps that is necessary for stream delineation. The D8 flow direction raster was then used as an input for the Flow Accumulation tool, which output a raster of accumulated flow into each cell. The D8 method was also used for this tool.

Next, a watershed extent was created to limit the output extent to hydrologically relevant areas. Two Pour Points (point feature shapefiles) were manually placed at the appropriate outflow locations for the target area datasets (outflow of eastern channel, at the confluence of eastern and western channels) and the full site datasets (outflow of the main channel, where it reached the river), so that the watershed extents would include the eastern section of the site including borrow pit and eastern channel, and the entire site respectively (Figure 3.6). The corresponding pour point shapefile and flow accumulation raster were used as inputs for the Snap Pour Point tool. This tool shifts an existing pour point feature to align with the cell of highest flow accumulation within a specified distance (ESRI, 2020), in this case 20 cm. The pour point must align with highest accumulated flow for accurate watershed delineation. The Watershed tool was then used, inputting the snapped pour point and flow direction raster, to create a watershed raster in which all cells within the watershed had a value of 1, and all other

cells were null. This raster was then converted to a polygon using the Raster to Polygon tool, for the purpose of being able to easily calculate the watershed area to be used in channel density calculations in later analyses.

Figure 3.6. Manual pour point locations for the full site and target area datasets. Background imagery collected August 21, 2020 with a DJI Phantom 4 RTK RPAS.

The next processing step was to create a stream raster (stream cells with a value of 1, all other cells null) using a Conditional statement that applied a flow accumulation threshold to the flow accumulation raster and clipped the output to the watershed extent. To determine the appropriate flow accumulation value, several different values were tested prior to running the processing script, and their outputs visually assessed. The appropriate amount of channel delineation was defined as having the majority of visible channels delineated, as well as a sufficient number of water flow paths without visible channel definition, referred to as "proto" channels. Initial threshold values were determined based on currently existing methods in the

literature, including mean flow accumulation, and 1% of the maximum flow accumulation (Ozulu & Gökgöz, 2018). The mean flow accumulation value was too low of a threshold and produced a channel delineation with too many channel features to realistically analyze and process the data within the scope of this research. The 1% of the maximum flow accumulation value was too high of a threshold, producing a channel delineation that did not include the majority of visible ("existent") channels. Flow accumulation thresholds between these two values were then tested and examined, and it was determined that a value of 50,000 was appropriate for delineating existent and proto channels within the high spatial resolution (2.0 cm), target area datasets. For the full site datasets with lower spatial resolution (3.5 cm), multiple flow accumulation values were similarly explored, and a value of 120,000 was chosen. Because the resolution of these datasets did not allow for accurate mapping of the smaller water flow path "streams"/embryonic channels, a higher flow accumulation threshold was used to reduce the stream output file to only include larger streams/channels at the full site scale.

After the stream raster had been produced and clipped to the watershed extent, the Stream Order tool was used to apply the Strahler stream ordering method to the stream cells. This is the most commonly used stream ordering method in the literature (Chirol, et al., 2018), and one of two ordering methods available in ArcMap. This method classifies all terminal segments (smallest streams) as stream order 1 and increases the stream order when two segments of the same order meet (Strahler, 1957). This ordering system is problematic in the study of salt marsh evolution, since the development of new terminal channels over time would alter the stream order of larger, consistent channels (Weishar et al., 2005). To overcome this issue, the next step in the script was to reverse the stream order, as presented by Chirol et al. (2018). The following formula was used for stream order reversal:

Equation 1. Stream order based on a reversal of the Strahler ordering system.

$$Order_{Reversed} = Order_{Maximum} - Order_{Strahler} + 1$$

Once the streams were attributed with a reversed Strahler order, the Stream to Feature tool was used to convert the stream raster to a line shapefile. Since the flow direction and flow accumulation rasters were created using pixel data with a smaller resolution than most stream features, the output stream shapefile had a crinkled shape with excess vertices and segments that did not run parallel to the actual channels. Since subsequent processing steps involved the automated drawing of cross-sections perpendicular to stream segments, it was important that stream segments be as close to parallel with actual channels as possible. To reduce the occurrence of cross-sections being drawn non-perpendicularly to actual channels due to variations in the azimuth of the stream segments (see Figure 3.7), the stream shapefile was smoothed using the Smooth Line tool with the Polynomial Approximation with Exponential Kernel (PAEK) method. This method required an input smoothing tolerance to determined how much detail would be retained in the output shapefile. To determine the appropriate smoothing tolerance for the stream shapefile datasets, the tool was run on one test dataset with several different smoothing tolerance values between 0.05 m and 1 m. From visual observation of the results, it was determined that a smoothing tolerance of 0.4 m reduced the "zig-zag" effect of the original shapefile so that the stream segments generally ran parallel to the actual streams, while maintaining a sufficient amount of detail. An example of an original stream shapefile and a smoothed stream shapefile (smoothing tolerance of 0.4 m) can be seen in Figure 3.7.

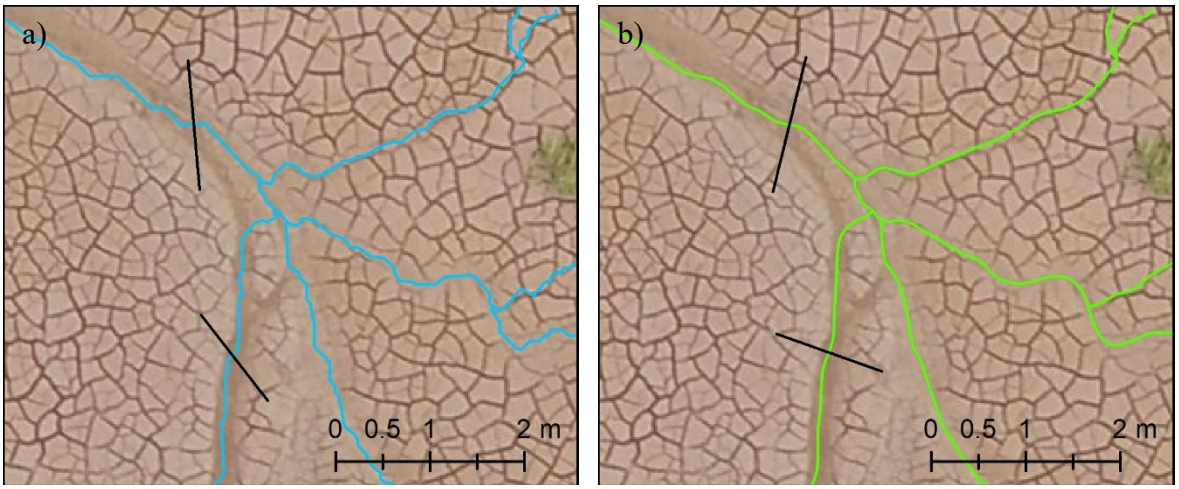

Figure 3.7. a) Original stream shapefile with potential locations and angular positions of cross-sections that are not perpendicular to the actual channels. b) Smoothed stream shapefile (with a smoothing tolerance of 0.4 m) with potential locations and angular positions of cross-sections that are closer to perpendicular to the actual channels.

3.2.3 Channel Classification

A classification of stream segments from the channel delineation output shapefile was required to differentiate between existent channels and proto channels. For the purpose of this research, existent channels were defined as having a cross-sectional depth greater than 2.0 cm along the majority of their length, as well as hydraulic connectivity to another existent channel at their downstream end. Initial classification methods of the August 2020 dataset involved visual analysis of multiple cross-sections along each stream segment using the 3D Analyst tool bar in ArcMap, specifically the Interpolate Line and Profile Graph tools, then manually classifying each segment based on cross-sectional depth. It was determined that this manual technique would be too time consuming and had a significant amount of user bias that could affect the classification results. To resolve these issues, a semi-automated python script was developed to automatically draw cross-sections at regular intervals along all stream segments and classify them based on elevation values along those cross-sections as extracted from the corresponding DSM, using a combination of Arcpy tools and python logic (see Appendix C for script text). The

channel classification script can be described in two separate parts, the first of which involved preparing and creating the stream segments, cross-sections, and points (with elevation values) that would be used to determine segment classification and is summarized as a flow chart in Figure 3.8.

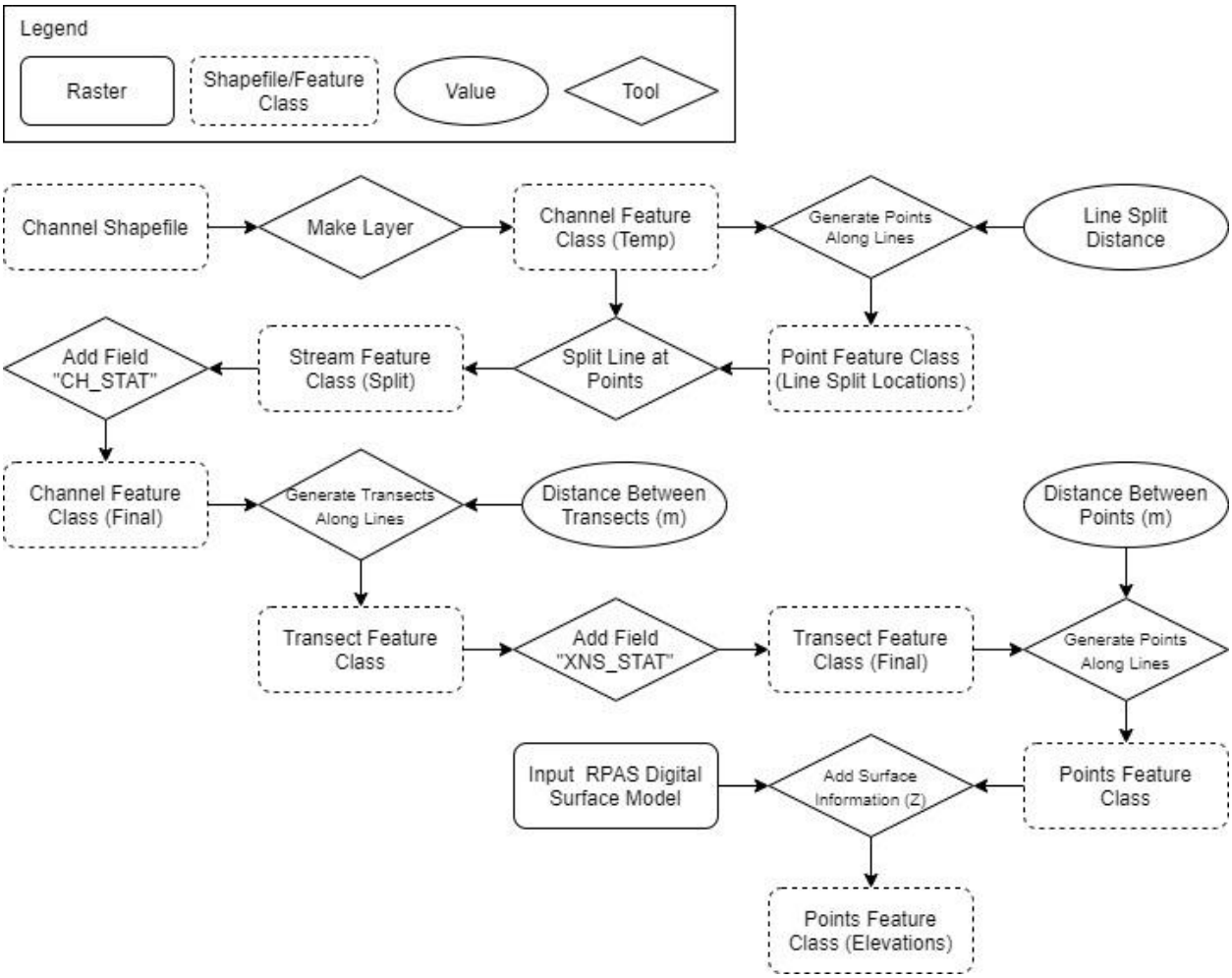

Figure 3.8. Part 1 of the channel classification script steps.

Part 1 of the channel classification script began by creating a file geodatabase (its location and name specified as a script input) to hold intermediate feature classes and the final classified channels, if it did not already exist (this step is not outlined in the summarized flow chart, Figure 3.8). Next, the Make Layer tool was used to convert the delineated channel shapefile into a feature class. During manual classification of the August 2020 dataset, it was

determined that some of the longer channel segments should be split, with a portion of the segment being classified as existent and a portion being classified as proto. To create a similar effect in the automated classification script, channel segments were split at a user defined value so that each new segment could be evaluated independently. This was achieved in the script by running the Generate Points Along Lines tool with the channel feature class as the Input Feature, and the Distance Between Points as 4 m, and then the Split Line at Points tool to split the channel feature class at each point location. This resulted in a new channel feature class in which line segments had a maximum length of 4 m, and segments initially longer than 4 m were divided into multiple segments.

The Add Field tool was then used to add a channel classification field ("CH_STAT") that would be used later to hold the classification result of each segment (branch) of the feature class. Next, cross-sections were generated along all channel segments at a defined value using the Generate Transects Along lines tool. To ensure that segments shorter than the user defined value would have at least 2 associated cross-sections, end points were included. This resulted in all segments having at least 2 cross-sections (start and end points), as well as at regular intervals along their length when applicable. An important note is that the output cross-section shapefile included a field that identified which channel segment each cross-section was associated with. Cross-section length was a user-defined script variable. It was determined during manual classification that morphological variations between channel types in the target area datasets required a variable cross-section length to correctly classify them. For embryonic channels with a small width and relatively dense distribution that had been developing in areas such as the borrow pit, cross-sections were best drawn with a shorter width. This was the case to reduce the occurrence of multiple channels showing up in a single cross-section, as well as the cross-

sections including morphological variations in elevation that were not channel related (eg., banks of the borrow pit). For relic ditch channels and manually constructed channels, cross-sections needed to be wider to include both channel banks. An example of the morphological variation between these two channel types is shown in Figure 3.9. To account for this variation, each channel shapefile (prior to running the channel classification script) was divided into two sections: embryonic channels and relic ditch/large channels (Figure 3.10). These sections were then run through the channel classification script separately. In the full site datasets, since only larger channels had been delineated, all channels were processed together with a single transect length value.

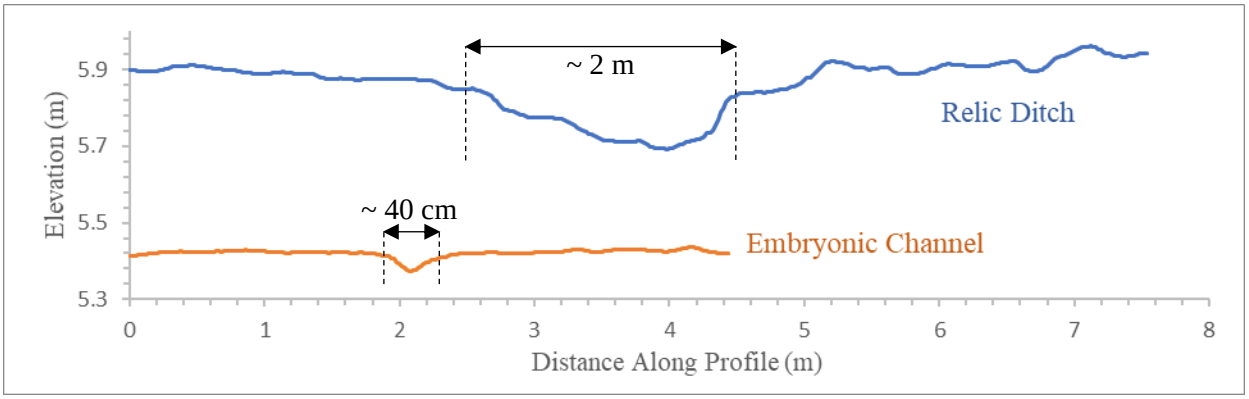

Figure 3.9. Morphological variations between channel types affecting cross-sectional width.

Figure 3.10. Division between embryonic/small channels and relic ditch/large channels as inputs for the channel classification script from the August 2020 target area dataset.

The Add Field tool was then used again, to add a classification field ("XNS_STAT") to the cross-section shapefile which would later hold the results of the classification of each cross-section. Finally, a point feature class was created using the Generate Points Along Lines tool with the cross-section feature class as the Input Feature. Points were generated at a user defined value, and end points were not included. The output point feature class had a field that specified the cross-section that each point was associated with. The Add Surface Information tool was then used to extract corresponding DSM values for each point and add them as a field in the point feature class.

Part 2 of the channel classification script involved a logical assessment of the data that was prepared in Part 1 to classify each channel segment. Since this part of the script was written mainly as a series of python logic statements rather than Arcpy tools, files, and variables, it has been illustrated using a logical statement flow chart in Figure 3.11. The initial step was to use the Arcpy Search Cursor tool to run through the channel segment feature class and create a

list of all individual Branch IDs. For each Branch ID in the list, a Search Cursor was used to find all corresponding Transect IDs from the cross-section feature class and create a list of those Transect IDs. For each Transect ID in the list, the same Search Cursor process was used to create a list of all corresponding points and their elevation values.

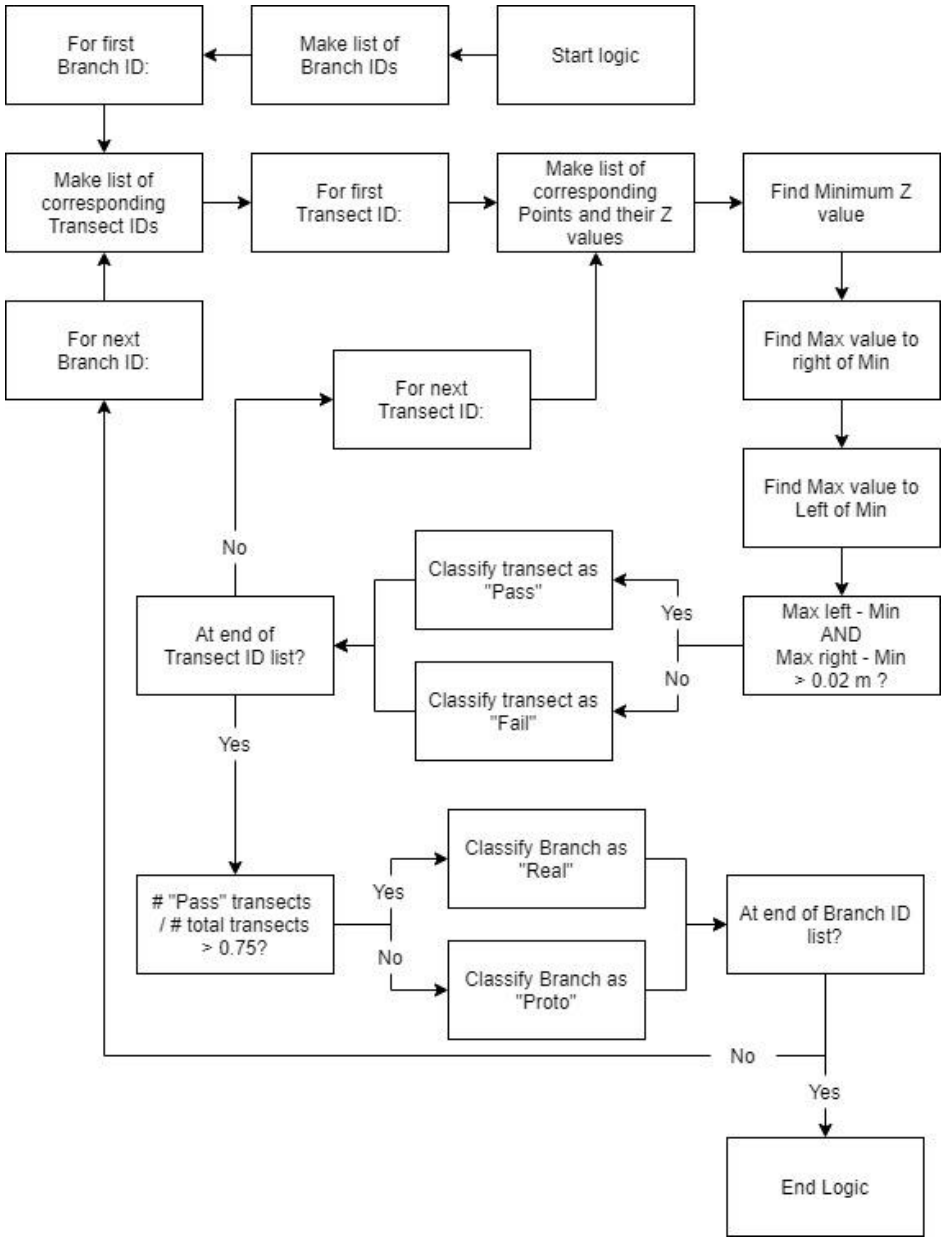

Figure 3.11. Part 2 of the channel classification script steps, presented as a series of logical statements.

From the list of points, the minimum elevation value was identified. This point was considered the thalweg of the channel. It was necessary to find the minimum elevation point from each transect of points to determine the thalweg, rather than the center point (where the transect crossed the delineated channel line) to account for inconsistencies between the channel delineation and actual channel thalweg. In many cases, when the DSM was filled as part of the delineation process, channels were filled in and the resulting delineation ran alongside the filled area rather than along the elevation low point or channel center.

Next, the maximum value to the left of the minimum point was determined (left channel edge), as well as the maximum value to the right of the minimum point (right channel edge). If the difference between the thalweg elevation and both channel edge elevations (channel depth) was greater than 0.02 m, the selected transect was classified as "pass" by editing the "XNS_STAT" field in the cross-section feature class. If the channel depth was less than 0.02 m, or the minimum point was located at either end of the transect, the selected transect was classified as "fail". The same process was then repeated for all Transect IDs associated with the selected Branch ID, until all cross-sections had been classified. At this point, the selected channel segment was assessed by counting the number of transects that had been classified as "pass" and "fail". If more than 50% of the transects were classified as "pass", the channel segment was then classified as "Existent". If not, the channel segment was classified as "Proto". This process, from creating a list of Transect IDs to classifying the individual channel segment, was then completed for all Branch IDs, one at a time. Once the script had completed, the channel segment feature class was fully classified.

To determine the appropriate script settings for the most accurate classification results, the script was run with varying settings on the August 2020 target area dataset. Classification

results from each run were then compared to manual classification results of the same dataset, and a confusion matrix was created for each comparison. To account for the variations in channel morphology, embryonic/small vs relic ditch/large channels, datasets were run through the script and compared to results separately. Total erroneously classified channel length was also calculated for each set of results, and the settings that resulted in the shortest length of erroneously classified channels were chosen for classification of the remaining datasets. Chosen classification settings are stated in Table 3.2.

Table 3.2. Classification script settings chosen for classifying channels in all datasets, determined by comparing script results to a manually classified dataset.

Dataset	Channel Type	Transect Length (m)	Transect Distance (m)	Point Distance (m)	Min. Channel Depth (m)
Target Area	Embryonic/Small	1.000	0.500	0.035	0.020
	Relic Ditch/Large	3.000	0.250	0.050	0.020
Full Site	All	3.000	0.500	0.100	0.020

Since the script classified channels based on channel depth only, incorporating hydraulic connectivity and correcting erroneous classification results were completed manually post-classification. Prior to this, the embryonic and relic ditch feature classes for each dataset were merged and exported as a single shapefile that included all channels in both categories. Manual clean-up of these shapefiles was then completed individually by comparing the results to the corresponding imagery and elevation model. Classified transect feature classes were also examined to determine the cause of erroneous classifications. Classifications were corrected in cases of obvious script malfunction, such as when a single channel had alternating sections of proto and existent classifications (Figure 3.12). Expertise and knowledge of the site was also used to determine the correct classifications in these circumstances.

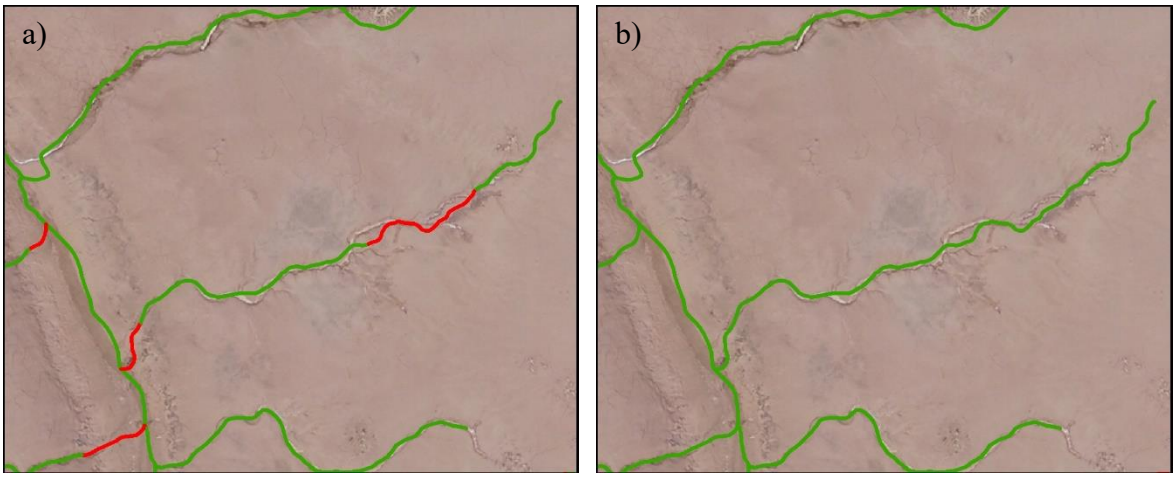

Figure 3.12. a) Channel classification script results containing erroneous classifications and b) manually corrected classification results.

3.2.4 Channel Persistence

Channel persistence was measured to determine if rates of channel persistence between collection dates changed over the course of the study period, and to examine the relationship between channel persistence and classification. Two persistence analyses were conducted, one that determined the rate of persistence of all channel segments regardless of classification from their collection date to all remaining collection dates, and another that calculated the rate of persistence of existent and proto channels from their original collection date to May 4, 2021, as well as their classification in the May 4, 2021 delineation if they did persist.

Both channel persistence analyses were conducted using the Buffer tool and spatial queries in ArcMap with classified channel shapefiles. A buffer shapefile was created for each channel delineation dataset, with a buffer distance of 50 cm for Target Area datasets and 1m for Full Site datasets. The buffer was used in the spatial queries so that small shifts in channel location, caused by natural movement or delineation error would still result in a channel being identified as “persisting” between two collection dates. The general persistence analysis was run using all channel classifications (existent and proto) within each dataset, by selecting channel segments in

the earliest delineation (November 24, 2019) that were "within" the June 1, 2020 buffer shapefile. The length of theses selected channels was determined and converted to a percentage of the total channel length for the initial delineation. The selected "persisting" channels were then used as the input for an additional spatial query, to determine which of these channels were within the buffer shapefile of the subsequent collection date (July 9, 2020), and therefore persisted to that collection date. This process was continued until the percentage of channel length that persisted to May 4, 2021 was determined. The same workflow was followed with the delineated shapefile from each collection date, for both Full Site and Target Area datasets, and resulting values were tabulated.

Additionally, the persistence analysis involving channel classification was conducted to determine differences in persistence between existent and proto channels. This analysis looked only at the persistence of channels from each collection date to the final collection date, May 4, 2021. Channel segments from each collection date in both Full Site and Target Area datasets were selected if they were "within" the buffer polygons for the May 4, 2021 dataset. Length of persisted channel segments was calculated for proto channels that persisted to proto channels, proto channels that persisted to existent channels, proto channels that did not persist, existent channels that persisted to proto channels, existent channels that persisted to existent channels, and existent channels that did not persist, and the resultant values were tabulated.

3.2.5 Drainage Network Characteristics

To compare drainage network evolution over time, total channel length, drainage area and Hortonian drainage density (Equation 2) were calculated for each dataset. Total channel length was calculated by creating a new field in each delineated channel shapefile called "Length", then using the Calculate Geometry tool to populate the field with the length of each

segment. The sum of these values for existent channel segments only was equal to total channel length. Drainage basin area was calculated using the watershed shapefiles that had been created during the channel delineation process. A new field was created in each watershed shapefile called “Area”, and the Calculate Geometry tool was used to calculate the area of each watershed polygon.

Equation 2. Hortonian drainage density where ΣL is total channel length and A is drainage basin area (Horton, 1945).

$$D_d = \frac{\sum L}{A}$$

3.2.6 DEMs of Difference

Seasonal and yearly changes in surface elevation were assessed by calculating DoDs from the photogrammetric elevation models. Significant processing was required to isolate areas of bare ground from the original DSMs (converting DSMs to DEMs of bare ground only) and remove all areas of surface deformation caused by the presence of vegetation, water features and edge effects. These features in the DSM do not accurately represent sediment surface elevations (Carrivick et al., 2016; Jaud et al., 2016; Vecchi et al., 2021) and therefore must be removed prior to DEM subtraction and DoD creation. Additionally, because validation data for each DSM was only collected on bare ground locations, incorporating vegetated or water-filled areas into the DoD analysis would result in an underestimate of vertical error.

Since shapefiles excluding edge effects for each dataset had already been created as part of the channel delineation process, these shapefiles were the starting point for clipping DSMs. In many cases, noisy data additional to the edge effects was present along some edges of the datasets (Figure 3.13a). For the purposes of DoD creation, these areas were also excluded with the edge effect shapefiles to improve data reliability. Areas not of interest in DoD analysis were

also excluded by further manual clipping of the edge effect polygons along the new dyke and gravel access road to the east of the site. To remove water features, they were manually delineated from the orthomosaics in ArcMap at a 1:300 scale, creating a shapefile that contained areas of water coverage for each individual dataset. The Erase tool was then used to cut out the water coverage shapefiles from the edge effect shapefiles, resulting in a polygon for each dataset that excluded areas of noise around the edges of the DSMs, areas north/west of the new dyke and access road, and water features present in the orthomosaics. An example of one such polygon can be seen in Figure 3.13b.

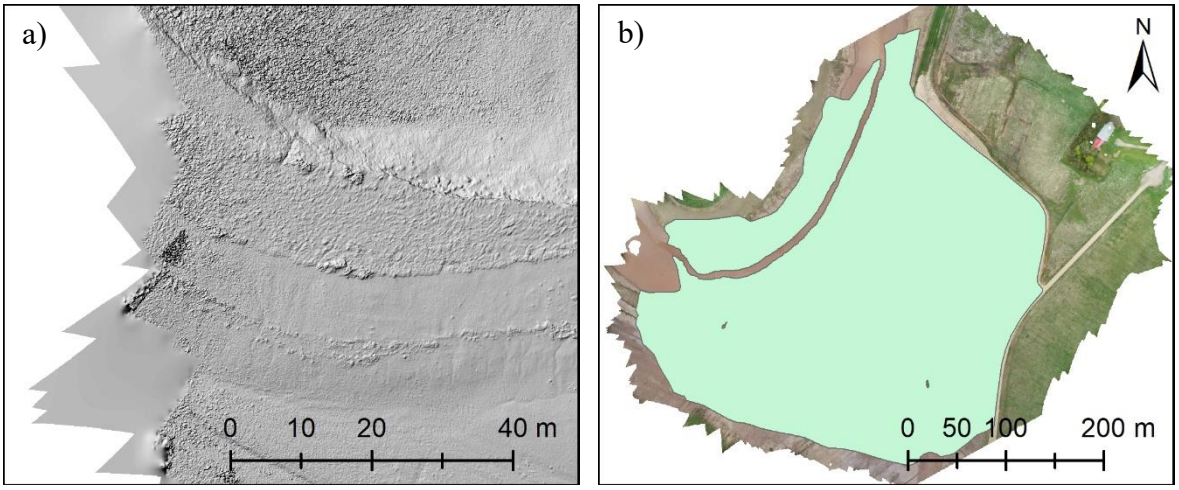

Figure 3.13. a) Hillshade of June 1, 2020 DSM showing DSM edge effect and noisy data extending into the dataset. b) Example of clip polygon excluding edge effects and noisy data, areas outside of the study site, and water coverage. Orthomosaic collected June 1, 2020.

Vegetation was isolated by creating a vegetation mask using a combination of image segmentation, unsupervised classification, and manual editing of the results. It was assumed that the August 2020 dataset would have the maximum extent of vegetation coverage, so the initial vegetation mask was created using this dataset.

Image segmentation was completed in ArcGIS Pro using the Segmentation tool, with a spectral detail of 20.00, spatial detail of 9.00 and minimum segment size of 80. These settings were determined through trial and error, with the goal of reaching the minimum number of

segments while still maintaining enough detail to isolate vegetation. The output of this tool was a 3-band raster, with pixels in each segment sharing an RGB value, and variations in these values between segments (Figure 3.14a). This segmented raster was then classified using the ISO Cluster Unsupervised Classification tool, with 20 classes, minimum class size of 20, and sample interval of 10 (minimum class size and sample interval default values) in ArcMap (Figure 3.14b). The classified raster output was then compared to the original orthomosaic, and each class was assigned as either vegetation (1), sediment (2) or other (3). Classes were assigned based on the majority feature within that class, and when significant overlap occurred between features in a single class, that class was assigned as other (3).

The Reclassify tool was used to convert the original 20 classes into the 3 identified categories (Figure 3.14c). The reclassified raster was converted to a polygon shapefile using the Raster to Polygon tool. Significant manual editing was required to remove areas of sediment from the vegetation class, and vice versa, as well as assign either the vegetation (1) or sediment (2) class to all polygons in the other (3) class. All reclassification edits were completed by comparing the polygons to the orthomosaic imagery.

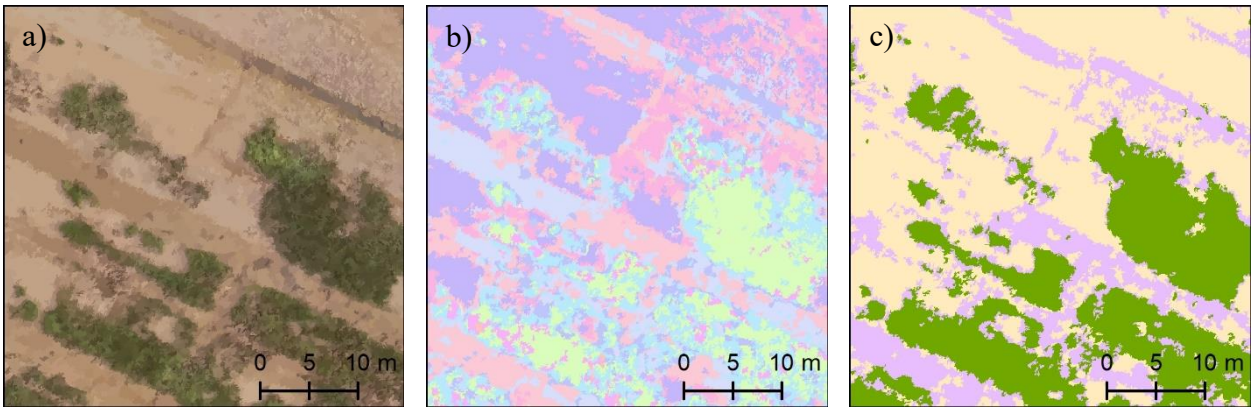

Figure 3.14. a) Segmented raster output from the ArcGIS Pro Segmentation tool with the August 2020 full site orthomosaic. b) Original unsupervised classification results of the segmented raster with 20 random classes. c) Unsupervised classification results reclassified into vegetation (1 – green), sediment (2 – yellow), and other (3 – purple).

After completing the vegetation mask using the August 2020 dataset, it was determined that the October 2020 dataset had a greater vegetation extent, and that further editing of the vegetation mask was required. Further examination of the orthomosaic imagery and DSMs revealed that surface deformation caused by the presence of vegetation had a larger extent than vegetation coverage in the imagery. Since the purpose of the vegetation mask was to remove all surface deformation caused by vegetation, all additional manual edits were completed using a combination of Orthomosaic imagery and DSMs, to account for this variation (Figure 3.15). The mask was edited to include vegetation coverage from the October 2020 dataset, as well as the November 2019 dataset that had some areas of persistent agricultural vegetation that were not present in any of the 2020 datasets. The final vegetation mask was then used to clip vegetation from each of the error/water polygons using the Erase tool, resulting in a final bare ground polygon for each dataset.

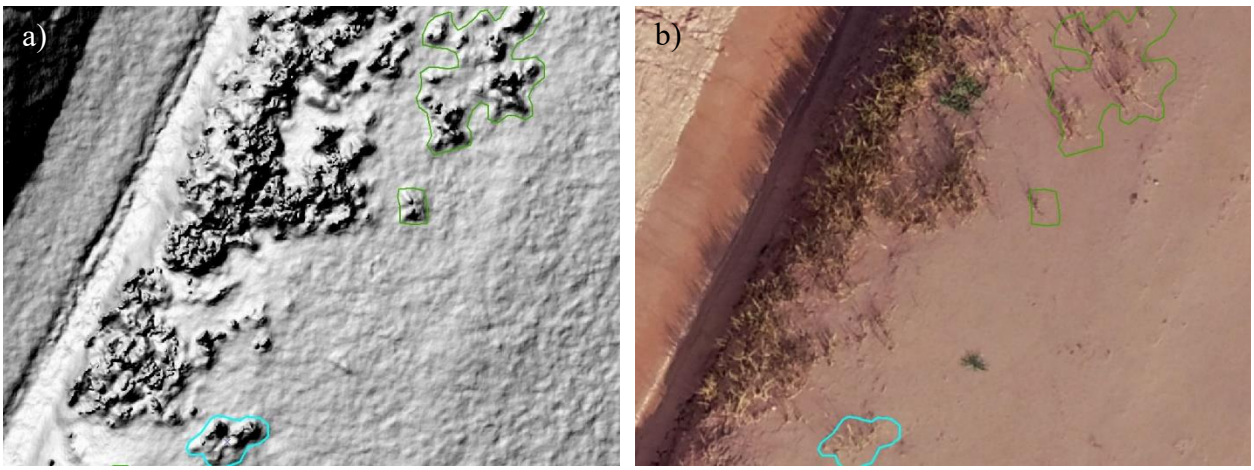

Figure 3.15. a) Example of DSM surface deformation caused by vegetation and shown with a hillshade, compared to b) vegetation presence in the orthomosaic imagery. Vegetation mask polygons are shown by green lines.

For consistency in DoD extents, a minimum extent for both the full site and target area datasets was created by clipping one of the bare ground polygons with all other bare ground polygons. This resulted in two polygons, one for full site datasets and one for target area datasets

that covered bare ground areas which were consistent between all datasets of each coverage type. Each DSM was then clipped to its corresponding (either full site or target area) bare ground polygon using the Clip (Data Management) tool. Resulting DEM rasters were subtracted from one another using the following formula in the Raster Calculator tool to calculate surface elevation change over time per pixel in the raster output, a commonly used methodology for these purposes with RPAS datasets (Turner, 2015; Ierodiaconou, 2016; Matheson, 2020; Brunetta et al., 2021):

Equation 3.3. Digital Elevation Model of Difference (DoD)equation using multitemporal Digital Elevation Models (Addo and Jayson-Quashigah, 2021).

$$\Delta DEM = Z_2 - Z_1$$

In which ΔDEM is the DoD, Z_2 is the more recent DEM and Z_1 is the older DEM. Input DEMs for each DoD determined the time period being represented. DEMs used in DoD creation were selected based on data quality, time periods of interest and the appropriate corresponding survey dates, which are listed in Table 3.4.Two DoDs were created for each time period listed, one with Full Site datasets and one with Target Area datasets.

Table 3.4. List of Input DEMs for DoD creation, and representative DoD time periods.

Input DEM_{new}	Input DEM_{old}	DoD Time Period
Oct 5, 2020	Nov 24, 2019	1-Year
June 1, 2020	Nov 24, 2019	Winter
Oct 5, 2020	June 1, 2020	Growing Season
Aug 21, 2020	June 1, 2020	Spring-Summer
Oct 5, 2020	Aug 21, 2020	Summer-Fall

3.2.7 Volumetric Change Analysis

Volumetric change for each DoD was calculated using the following equation, which has been commonly used in the literature in RPAS and DoD studies:

Equation 3.4. Total volumetric change for a DoD, utilizing the sum of volumetric change per pixel (Gómez-Guitiérrez et al., 2014; Turner et al., 2015; Ierodiaconou et al., 2016).

$$\Delta V = \sum [DoD \times c^2]$$

Where c is cell size and DoD is the vertical change per pixel as calculated in Equation 1. The calculation was conducted in two steps, the first being a multiplication of the DoD by cell size squared (area per pixel). The resulting rasters represented volumetric change per pixel. The Zonal Statistics too, which allows the user to specify an input polygon, was then used to sum all volumetric raster pixels within the specified input polygon. This tool was run twice on each of the target area datasets. Once with the original bare ground polygon for the corresponding volumetric raster that had been split into a river area and a site area, producing total volumetric change sums for the river and site separately, and another with a manually delineated target area polygon that consisted of three polygon extents: the borrow pit, the main channel mouth and the main drainage channels (which included the main channel mouth) (Figure 3.16). For the full site datasets, the Zonal Statistics tool was only run with one input polygon: the corresponding bare ground polygon split into river and site areas.

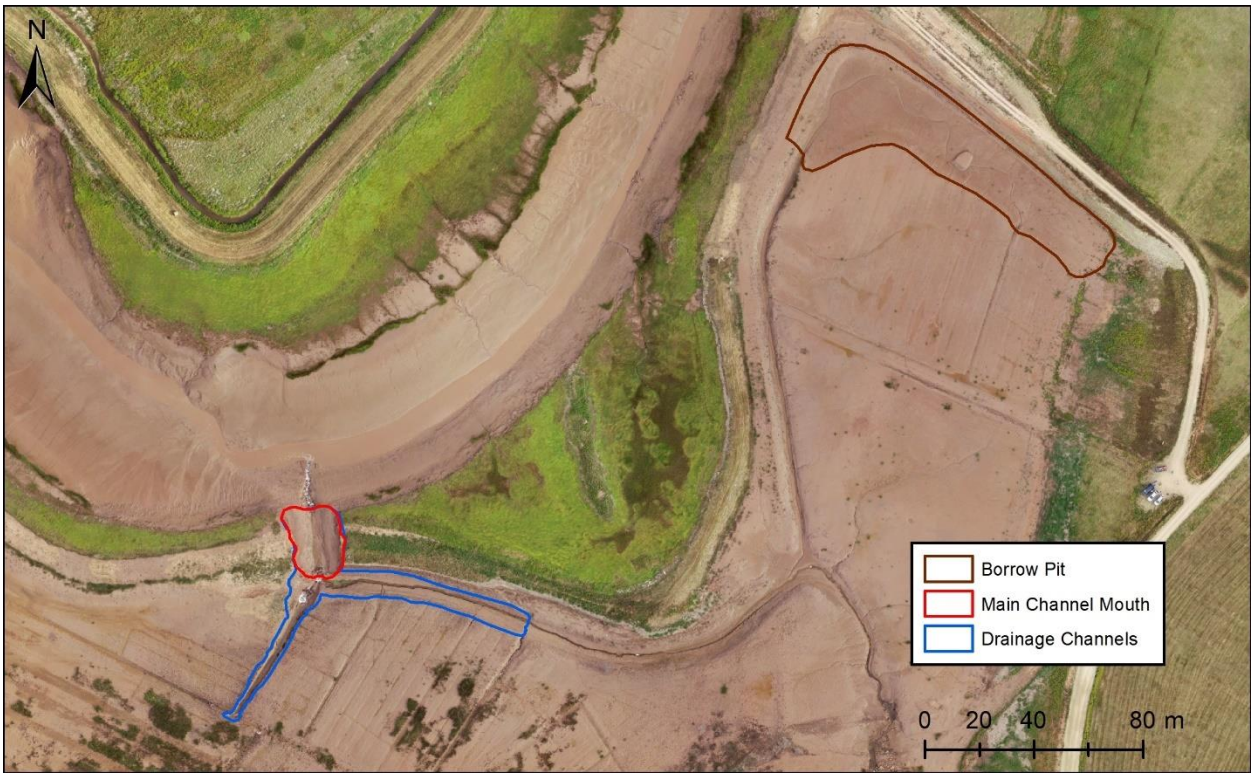

Figure 3.16. Polygon extents used to calculate total volumetric change with the zonal statistics tool for areas of interest within the target area datasets. Note: Main channel mouth area is included in the drainage channels extent.

To account for volumetric uncertainty in the above-mentioned datasets, a Level of Detection (LoD) was applied to all DoDs following the methodology outlined in Matheson (2020). This method of error estimation utilizes the individual DEM $RMSE_z$ values and calculates their propagation into the DoDs using the following equation:

Equation 3.5. DoD uncertainty based on the individual accuracies of incorporated Digital Elevation Models (Brasington et al, 2003; Lane et al, 2003).

$$\delta DoD = \sqrt{(RSME_1)^2 + (RSME_2)^2}$$

Where δDoD is the propagated DoD error and $RSME_{1,2}$ are the vertical RMSE values for the corresponding DEMs. Furthermore, the LoD for each DoD was calculated using the following equation:

Equation 3.6. Level of Detection threshold value for a DoD determined by a statistical coefficient based on desired significance level ("t" value) and the uncertainty between incorporated Digital Elevation Models (Wheaton et al., 2010).

$$LoD = t(\delta DoD)$$

Where LoD is the Level of Detection threshold value and t is a statistical coefficient based on desired significance level (t =1.0 is a 68% confidence interval, t = 1.96 is a 95% confidence interval) (Brasington et al, 2003; Lane et al, 2003; Milan et al, 2011). LoDs were calculated for each DoD using both 68% and 95% confidence intervals, and volumetric change rasters were created incorporating each LoD threshold using the Raster Calculator tool by excluding all pixel values between (-)LoD and (+)LoD. The same procedure as outlined above for calculating total volumetric change was used for each of these volumetric rasters of "significant" change. Although results were calculated using both 68% and 95% confidence intervals, for this study, the majority of DoD and volumetric change results will be presented using a 68% confidence interval, similar to results presented by Brunetta et al. (2021) and Matheson (2020). Due to the nature of morphological changes in some salt marsh restoration sites, where there are often small areas of very high surface elevation loss (eg., erosion of channel mouths), and large areas of very small surface elevation gain (sediment accretion throughout the site), using a 95% confidence interval, while ensuring more confidence in the measured change results, may lead to a substantial loss of data (Brunetta et al., 2021) and a potential skewing of measured morphological change patterns (Matheson, 2020). For comparison, DoD results with a 95% CI will be presented in Appendix H.

Additional to the LoD, maximum volumetric uncertainty was calculated using Taylor's (1997) equation, which assumes that errors are not pairwise correlated and is most appropriate for photogrammetric elevation models due to their known non-random errors (Jaud et al., 2016):

Equation 3.7. Maximum volumetric uncertainty for a corresponding DoD (Taylor, 1997).

$$\sigma_{Vabs} = c^2 \times \delta DoD \times n$$

Where σ_{Vabs} is the absolute volumetric uncertainty of a DoD with n number of cells and cell size c. Another volumetric uncertainty equation proposed by Lane et al. (2003) was used to calculate absolute volumetric uncertainty of the results. This formula however was intended for use with DEMs created using older methods such as total stations and dGNSS points and assumes that vertical errors in surface models are random (Matheson, 2020). While it has been used in this study for comparative purposes, it must be noted that this uncertainty equation may not be appropriate for surface models created with SfM techniques, and is expected to be an underestimate (Matheson, 2020). Additionally, all total volumetric change values were converted to average vertical change per pixel for each area and for all time periods using the following formula:

Equation 3.8. Average vertical change per square meter for a corresponding DoD.

$$\Delta Z_{avg} = \frac{\Delta V}{n \times c^2}$$

Where ΔV is total volumetric change, n is number of cells included in the total volumetric change calculation (variation in cell number based on LoD and confidence interval) and c is cell size.

3.2.8 Raster Correlation

A raster correlation analysis was conducted to determine if spatial patterns of sediment accretion and erosion could be explained by either surface elevation or distance from channel (DFC). DoD rasters were used as the dependent variable to represent sediment accretion and erosion, and DEMs and DFC rasters were used as independent variables. A multiple regression

model was run in R on a subset of raster datapoints to determine the relationships between variables and their significance.

DFC rasters were created by using the Euclidean Distance tool in ArcMap. Prior to this, a shapefile was created for each delineated channel dataset that included only existent channels (proto channels removed). This shapefile was used as the input feature source data in the Euclidean Distance tool, resulting in an output raster with each cell value equalling the distance from that cell to the nearest channel feature. A DFC raster was created for each delineated channel shapefile and was subsequently clipped to its corresponding watershed shapefile (intermediary product in the delineation process) to reduce file size and remove unnecessary data.

To convert raster datasets to a data type that could be analyzed in R, and to create a subset of the raster cells, random points were created, and raster values extracted to them. For the Full Site datasets, an extent shapefile was created from the original DoD clip shapefile that excluded the river, main channel mouth and drainage channels, and borrow pit. The main channel mouth and drainage channel areas were excluded because the controls of sedimentation were likely to be different in these areas. These areas appear to be more heavily influenced by water velocity than surface elevation or distance from channel and would therefore skew results and act as outliers. The borrow pit was excluded because that area was analyzed separately using the Target Area datasets. The Create Random Points tool was used to create a series of points within the input shapefile extent that were randomly distributed. The number of points created was approximately 0.03% of raster cells within the specified extent (n=12,985). Next, the Extract Multi Values from Points tool was used to assign each point a value from all input rasters which are listed in Table 3.1. Additionally, the Add X Y tool was used to extract easting and northing

values to each point. A similar workflow was followed using a shapefile of the borrow pit extent, creating a number of points equalling approximately 0.14% of cells (n=11,683) and extracting data from Target Area rasters.

Table 3.5. Rasters from which data was extracted to randomly generated points for raster correlation analysis (Full Site datasets).

Raster Type	Date/Time Period
DoD	Nov 24, 2019 – Oct 5, 2020 (1-Year) Nov 24, 2019 – Jun 1, 2020 (Winter) June 1, 2020 – Oct 5, 2020 (Growing Season)
DEM	Nov 24, 2019 June 1, 2020
Distance from Channel	Nov 24, 2019 June 1, 2020

For each set of points, three multiple linear regression models were run in R Studio software, one for each of the three DoDs. The models were calculated with the DoDs as the dependent variable, and the starting DEM and DFC rasters (November 24, 2019 for 1-year and winter DoDs, and June 1, 2020 for the growing season DoD) as the independent variables. Both scaled and unscaled versions of each model were calculated. Homogeneity and normality of the datasets was assessed by visually inspecting the residuals of each fitted model. It was determined that a transformation of the independent variables did not noticeably improve residual homogeneity, and therefore no transformations were applied. To determine the RMSE of each predictive model, a cross validation technique was incorporated into the model processing ("caret" package), using 5 folds. This means that the data was divided into 5 subsets and the model run 5 times, each time with a different subset serving as a validation dataset. The RMSE values from each model were then averaged to determine the prediction statistics for the model as a whole. To determine the effect of spatial autocorrelation on the model results, a variance partitioning

workflow was conducted. This workflow incorporated the easting and northing values from each point and calculated the variation in the dependent variable caused by spatial autocorrelation.

Chapter 4: Results

4.1 Photogrammetric Products

A Digital Surface Model (DSM) and orthomosaic were produced from the Structure from Motion (SfM) processing in Agisoft Metashape for each collection date and survey type (Full Site and Target Area). Examples of each are shown in Figures 4.1 and 4.2, and all products are shown in a larger scale format in Appendix D (Full Site) and Appendix E (Target Area). Products were exported from Agisoft Metashape with a Ground Sample Distance (GSD) of 3.5 cm for Full Site datasets and 2 cm for Target Area datasets. Results of the vertical accuracy assessments are outlined in Table 4.1. Vertical offset values between dGNSS validation points and DSMs for all collection dates in the Full Site datasets ranged between -6.7 cm and 5.2 cm and had an average Mean Absolute Error (MAE) of 1.4 cm. In the Target Area datasets, vertical offset values ranged between -5.3 cm and 5.7 cm, and the average MAE was also 1.4 cm. The range in $RMSE_z$ for Full Site and Target Area datasets was 1.3-2.3 cm and 1.3-2.1 cm respectively. Results of a Mann Whitney U test with an alpha value of 0.05 determined that the Full Site and Target Area $RMSE_z$ values were not significantly different.

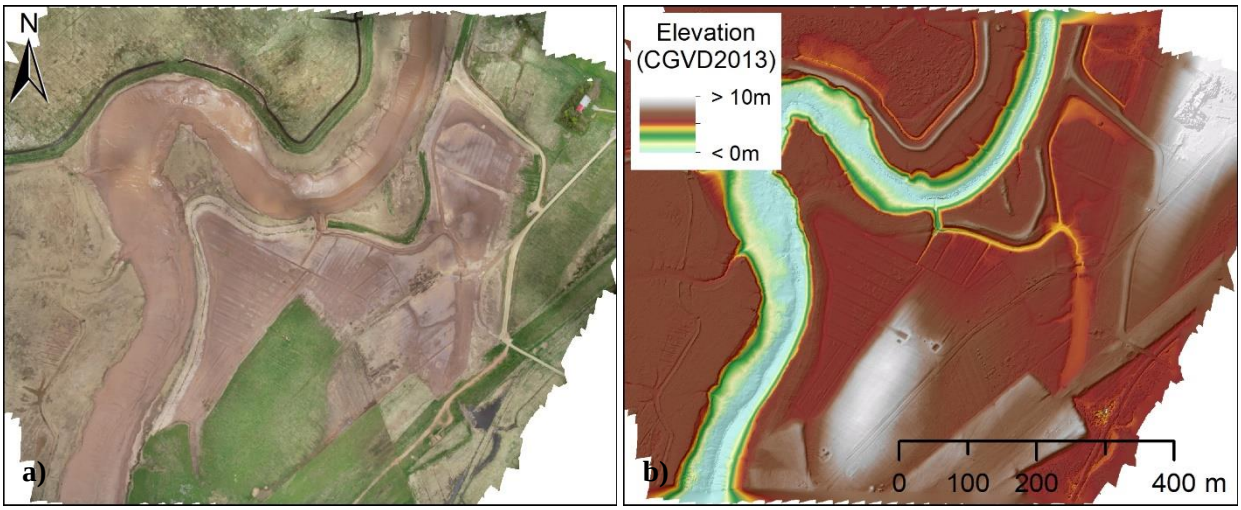

Figure 4.1. a) Orthomosaic and b) Digital Surface model outputs from Agisoft Metashape after Structure from Motion processing of the June 1, 2020 Full Site dataset.

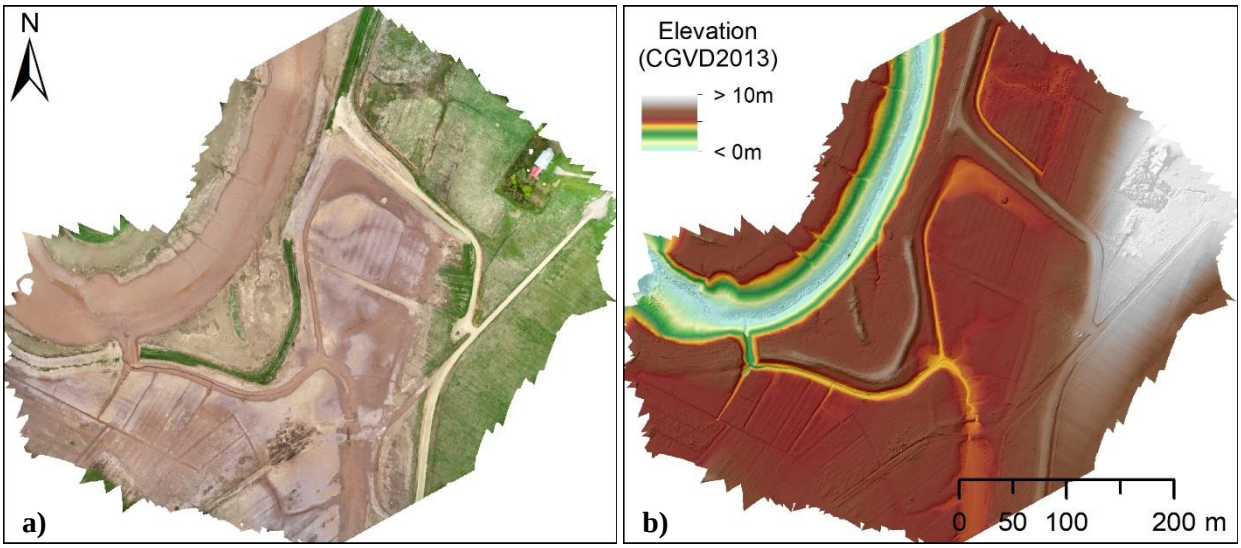

Figure 4.2. a) Orthomosaic and b) Digital Surface Model outputs from Agisoft Metashape after Structure from Motion processing of the June 1, 2020 Target Area dataset.

Table 4.1. Summary of vertical offsets between GNSS validation points and Structure from Motion derived Digital Surface Models.

Collection Date	Area	GSD (cm)	n	Min (cm)	Max (cm)	MAE (cm)	Mean (cm)	SD (cm)	RMSE (cm)
2019-11-24	Full Site	3.5	106	-5.0	4.5	1.1	-0.8	1.6	1.8
	Target	2.0	91	-4.4	5.7	1.5	-0.8	1.6	1.8
2020-06-01	Full Site	3.5	150	-3.7	4.2	1.1	0.2	1.3	1.3
	Target	2.0	134	-3.2	3.2	1.2	-0.9	1.2	1.4
2020-07-09	Full Site	3.5	108	-4.6	3.7	1.2	-0.2	1.5	1.5
	Target	2.0	94	-3.4	2.6	1.2	-0.1	1.5	1.4
2020-08-21	Full Site	3.5	118	-4.5	5.2	1.7	0.5	1.9	1.9
	Target	2.0	105	-3.3	4.3	1.6	0.6	1.9	2.0
2020-10-05	Full Site	3.5	131	-6.7	2.3	1.8	-1.5	1.7	2.3
	Target	2.0	122	-3.9	1.1	1.4	-1.3	1.0	1.7
2020-11-08	Full Site	3.5	110	-3.6	5.2	1.2	-0.7	1.4	1.6
	Target	2.0	101	-4.0	1.8	1.0	-1.0	0.9	1.3
2020-05-04	Full Site	3.5	128	-5.9	1.9	1.4	-1.0	1.5	1.7
	Target	2.0	96	-5.3	5.5	1.8	-0.1	2.1	2.1

4.2 Drainage Network Evolution

4.2.1 Channel Characteristics

Classified channel delineation shapefiles of both Target Area and Full Site datasets are shown in Appendix G, and examples of each are shown in Figures 4.3 and 4.4. Channels were classified as either existent (> 2 cm depth and connected to the rest of the existent channel network) or proto (< 2 cm depth or disconnected from the existent channel network). Target area delineations covered a smaller area due to the extent of input data and position of the pour point, and relatively more channels due to the lower flow accumulation threshold used in the delineation process. In both Full Site and Target Area delineations, channels located in areas with relic drainage ditches tended to follow the ditches and were generally straight with right angles. This differed from channels that developed in areas without relic ditching, such as the borrow pit, as these had a more sinuous shape (Figures 4.3 and 4.4).

Planimetric channel characteristics are outlined in Table 4.2. Hortonian drainage densities of existent channels calculated using total channel length and drainage basin area were higher in the Target Area datasets (avg. of 0.062 m^{-1}) than in Full Site datasets (avg. of 0.043 m^{-1}). When separated by season, drainage densities in both Full Site and Target Area datasets showed a trend of generally lower values in fall (October – November) than in the growing season (June – Aug) (Figure 4.5). This trend was more significant in Target Area datasets than in Full Site datasets. In Full Site datasets, an average of 68.9% of total channel length was classified as existent, while in Target Area datasets, an average of 43.4% of total channel length was classified as existent.

Figure 4.3. Results of the channel delineation of the June 1, 2020 Target Area dataset.

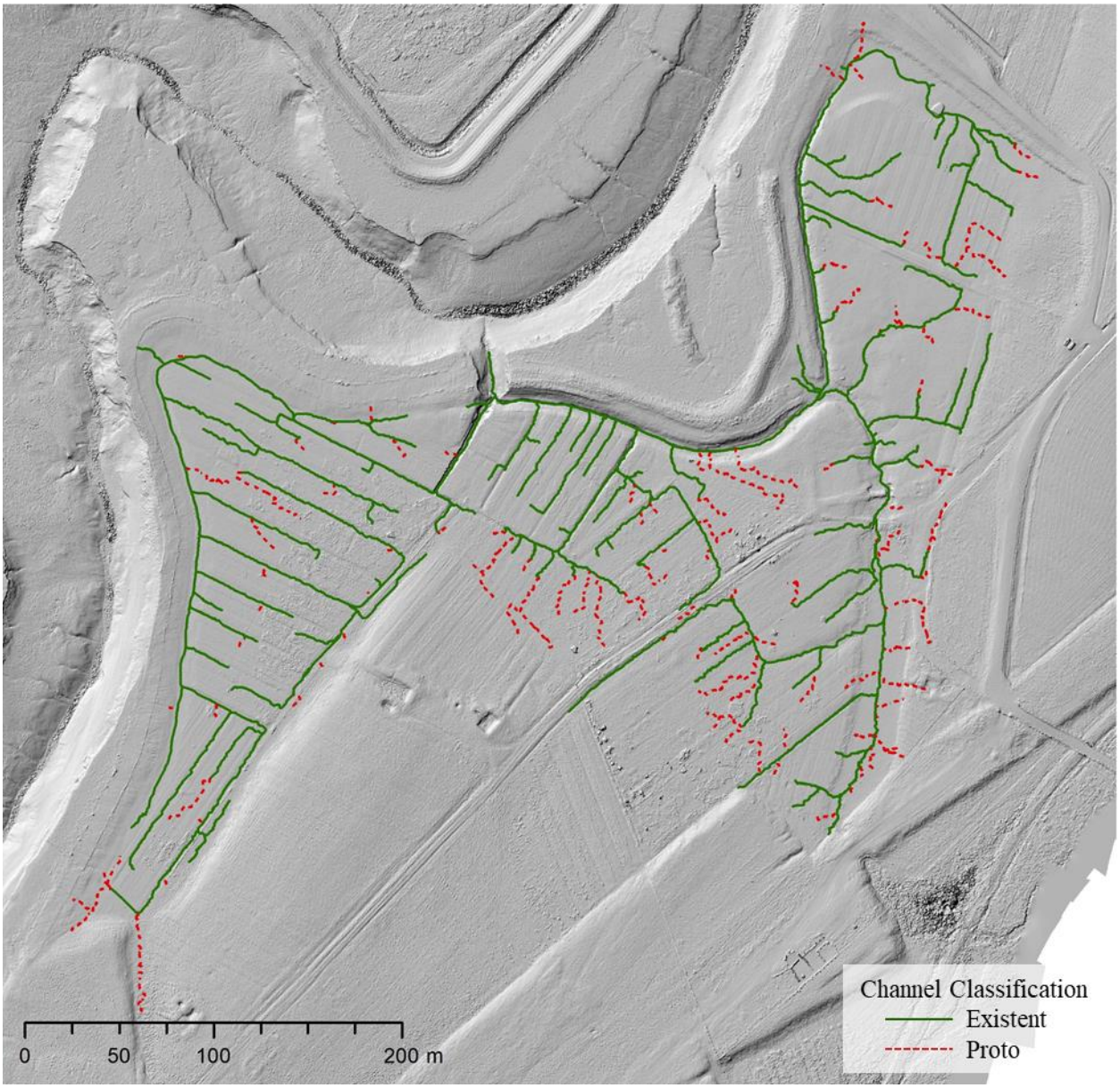

Figure 4.4. Results of the channel delineation of the June 1, 2020 Full Site dataset.

Table 4.2. Channel characteristics of each delineated channel network. Proto channels were not included in total channel length or Hortonian drainage density calculations.

	Date	Total Existent Channel Length (m)	Watershed Area (m^2)	Hortonian Drainage Density (m^{-1})
Target Area	2019/11/24	3063.280	54170.404	0.057
	2020/06/01	3699.839	55914.110	0.066
	2020/07/09	3545.966	53260.406	0.067
	2020/08/21	3492.611	53674.705	0.065
	2020/10/05	3209.672	53964.408	0.059
	2020/11/08	2980.721	54271.307	0.055
	2021/05/04	3654.577	55316.405	0.066
Full Site	2019/11/24	4581.019	116368.020	0.039
	2020/06/01	5304.598	116963.011	0.045
	2020/07/09	5332.183	118386.013	0.045
	2020/08/21	4976.295	116337.026	0.043
	2020/10/05	4817.080	117481.012	0.041
	2020/11/08	5018.004	116195.012	0.043
	2021/05/04	5305.969	116926.013	0.045

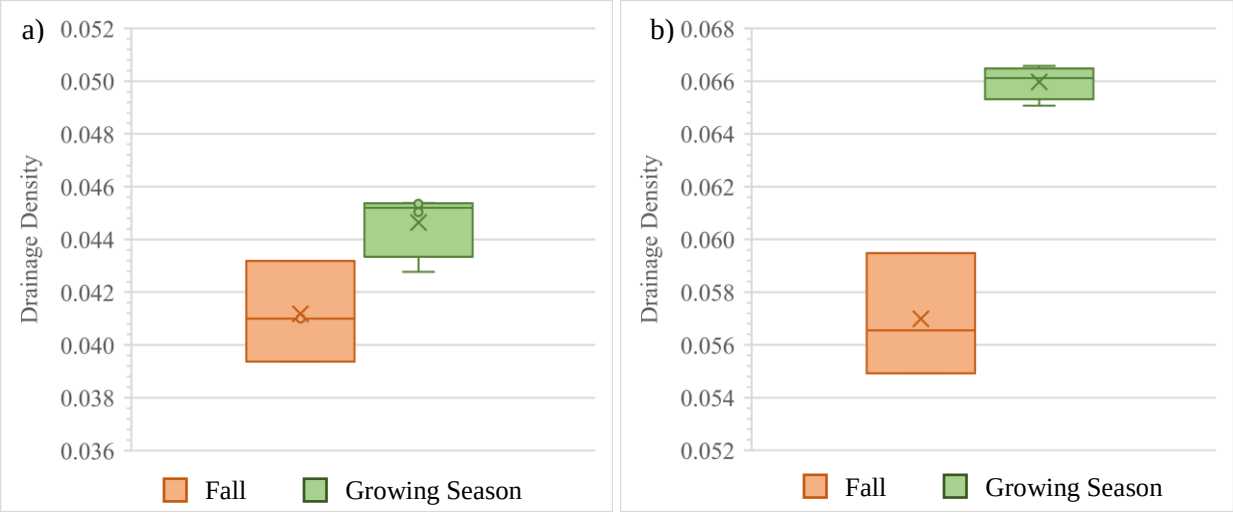

Figure 4.5. Drainage densities grouped by fall vs. growing season collection dates for the a) Full Site datasets, and b) Target Area datasets. Fall datasets were collected from October-November and growing season datasets were collected from June-August.

4.2.2 Channel Persistence

Channel delineations from different collection dates were compared to determine channel persistence within the study site. Results from the general channel persistence analysis, which

looked at how channel segments from each collection date persisted from their collection date through all subsequent collection dates are shown in Table 4.3 for Full Site datasets and Table 4.4 for Target Area datasets. These results showed that for each delineation, approximately half of the total channel length did not persist for the initial time period after the collection date, and in both Full Site and Target Area datasets, the smallest percentage of persistence occurred between November 24, 2019 and June 1, 2020 (45.33% and 35.30% respectively). However, out of the total channel length that persisted through the initial time step for each delineation, the majority of that channel length would then persist to all subsequent collection dates. Specifically, in these circumstances, the rate of persistence for Full Site datasets ranged between 73.27% and 93.51% and averaged 83.98%. Persistence in Target Area datasets was generally lower, and when excluding the initial time step for each delineation, percentages ranged from 65.51% to 87.78% with an average of 77.89%.

Generally, the likelihood of persistence to a particular date was higher in older datasets. For example, the percentage of channel length in the November 24, 2019 Full Site delineation that persisted from November 8, 2020 to May 4, 2021 (86.01%) was higher than the percentage of channel length in the August 21, 2020 Full Site delineation that persisted through the same time period (75.16%). This trend was present in all instances of both Full Site and Target Area datasets and is visualized by the reduction in percentage going from the top of each column to the bottom in Tables 4.3 and 4.4.

Table 4.3. Channel persistence results for Full Site datasets. Percentages were calculated using the length of channels that persisted to the subsequent collection date out of the total length of the initial dataset (left column), then out of those persisting channels, the percentage that persisted to the next collection date for the remaining collection dates.

		Persisted to Date					
		2020/06/01	2020/07/09	2020/08/21	2020/10/05	2020/11/08	2021/05/04
Delineation Collection Date	2019/11/24	45.33%	76.92%	86.12%	93.41%	93.51%	86.01%
	2020/06/01	-	58.80%	78.21%	88.61%	89.84%	84.28%
	2020/07/09	-	-	55.77%	82.13%	88.85%	82.59%
	2020/08/21	-	-	-	60.81%	80.78%	75.16%
	2020/10/05	-	-	-	-	61.34%	73.27%
	2020/11/08	-	-	-	-	-	52.60%

Table 4.4. Channel persistence results for Target Area datasets. Percentages were calculated using the length of channels that persisted to the subsequent collection date out of the total length of the initial dataset (left column), then out of those persisting channels, the percentage that persisted to the next collection date and so on for the remaining collection dates.

		Persisted to Date					
		2020/06/01	2020/07/09	2020/08/21	2020/10/05	2020/11/08	2021/05/04
Delineation Collection Date	2019/11/24	35.30%	75.68%	84.06%	87.21%	87.78%	79.48%
	2020/06/01	-	56.55%	75.08%	81.89%	81.46%	79.09%
	2020/07/09	-	-	56.27%	74.25%	77.80%	75.95%
	2020/08/21	-	-	-	53.06%	70.64%	72.54%
	2020/10/05	-	-	-	-	46.63%	65.51%
	2020/11/08	-	-	-	-	-	41.54%

The classified persistence analysis looked at the percentage length of channels that persisted from the date of collection of each delineation to May 4, 2021, based on the initial channel segment classification as well as the classification of the May 4, 2021 delineations. For each delineation, the percentage length of both proto and existent channels that persisted to either proto or existent channels in the May 4, 2021 dataset was calculated, as well as the percentage

length of each channel classification that did not persist. Results are outlined in Figure 4.6 for Full Site datasets, and Figure 4.7 for Target Area datasets. The results show that proto channels were significantly less likely to persist from their collection date to May 4, 2021 than existent channels, with an average rate of persistence of 13.78% for Full Site datasets and 19.31% for Target Area datasets. Of the total length of proto channels that persisted, an average of 52.87% persisted to proto channel classification in the Full Site datasets, and an average of 65.61% in the Target Area datasets, with the remaining persisting to an existent classification. Existent channel length persistence rates were much higher, with approximately 60% of total length of existent channels persisting to May 4, 2021 in both Full Site and Target Area datasets. Of the total length of existent channels that persisted, on average, 98.39% persisted to existent channel classification in the Full Site datasets, and 93.01% in the Target Area datasets.

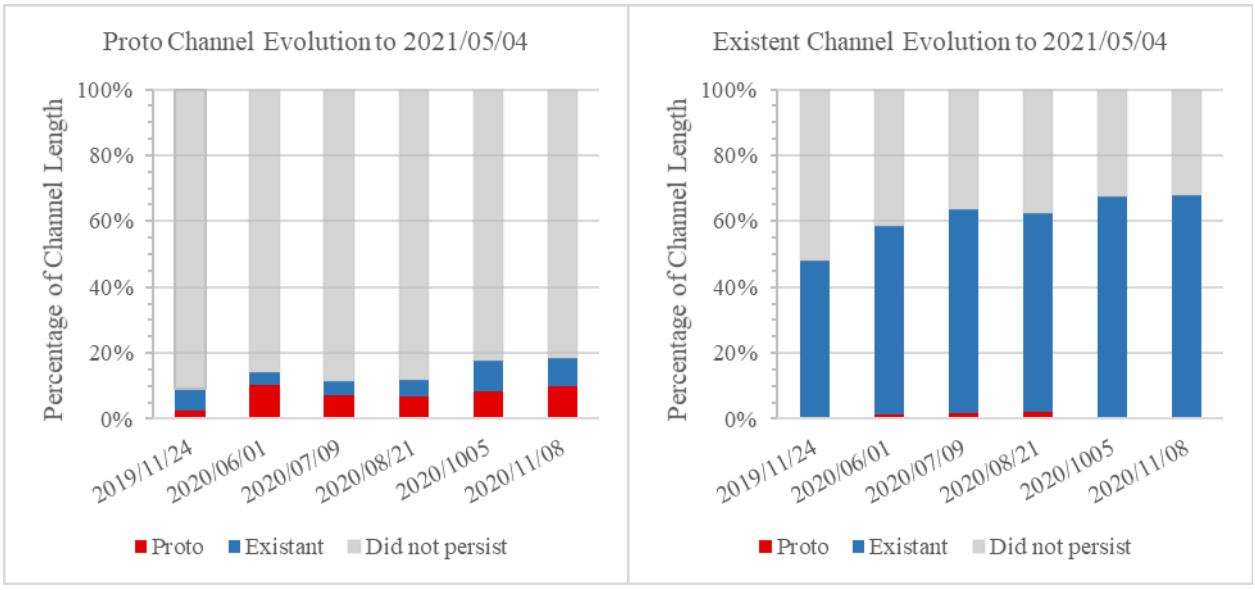

Figure 4.6. Percentages of persistence of channel segments from each initial collection date to May 4, 2021 in Full Site datasets, based on channel segment classification

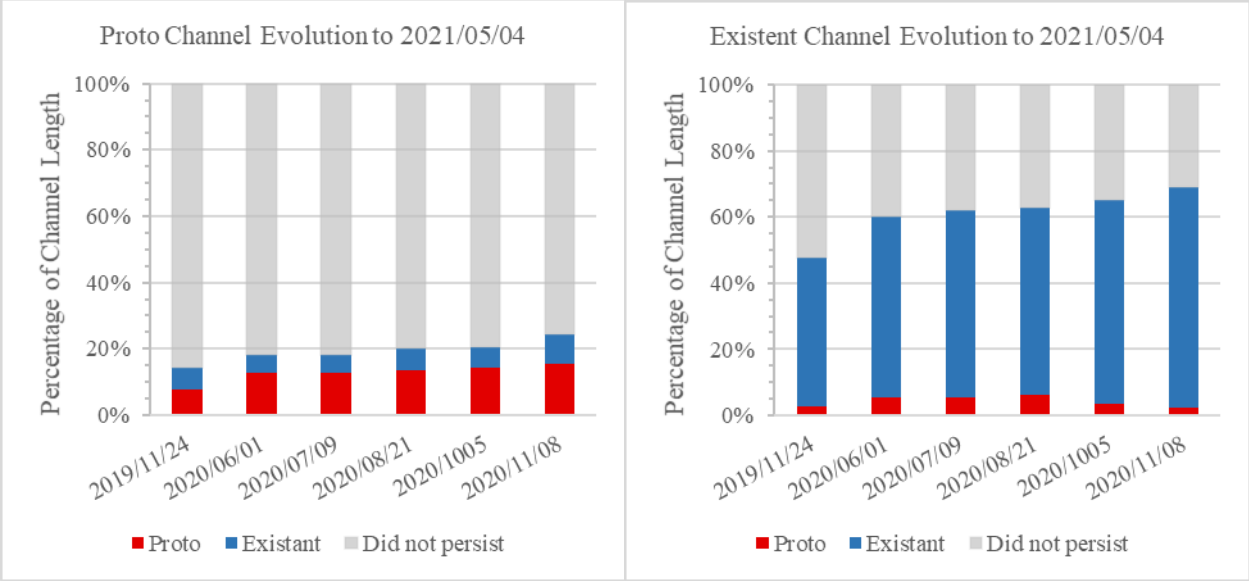

Figure 4.7. Percentages of persistence of channel segments from each initial collection date to May 4, 2021 in Target Area datasets, based on channel segment classification

4.3 DEMs of Difference

DEMs of Difference (DoDs) were created for several time periods with both the Full Site and Target Area datasets. DoD rasters were mapped highlighting an LoD with a 68% confidence interval and are shown in Figures 4.8-4.17. DoD maps with a 95% confidence interval LoD are shown in Appendix H. For the purposes of this research, only DoD data within the site area (excluding the Missaguash River) will be described in these results. The 1-year period (November 24, 2019 – October 5, 2020) DoDs for both Full Site (Figure 4.8) and Target Area (Figure 4.9) datasets show mostly positive surface elevation change in the borrow pit and field area just south of the borrow pit, although the Full Site DoD shows some small areas of negative surface elevation change in the borrow pit as well. The majority of positive values in these areas ranged between the LoD (2.9 cm Full Site and 2.5 cm Target Area) and 10 cm, but there were some small areas of between 10 cm and 50 cm of surface elevation increase in the borrow pit in

both datasets. Also, the pattern of surface elevation change highlights the location of embryonic channels in both datasets.

A marked difference between the 1-year Full Site and Target Area DoDs was a more significant area of negative surface elevation change in the southern area of the Target Area dataset. The Full Site dataset also had some negative surface elevation change in this area, but to a lesser extent. Both DoDs did show a significant loss (> 10 cm) around the main channel mouth and drainage ditches near the main channel mouth. The larger extent of the Full Site DoD showed that the western portion of the site had mostly positive surface elevation change. The percentage of pixels within the LoD was 55% in the1-year Full Site DoD, and 50% in the 1-year Target Area DoD.

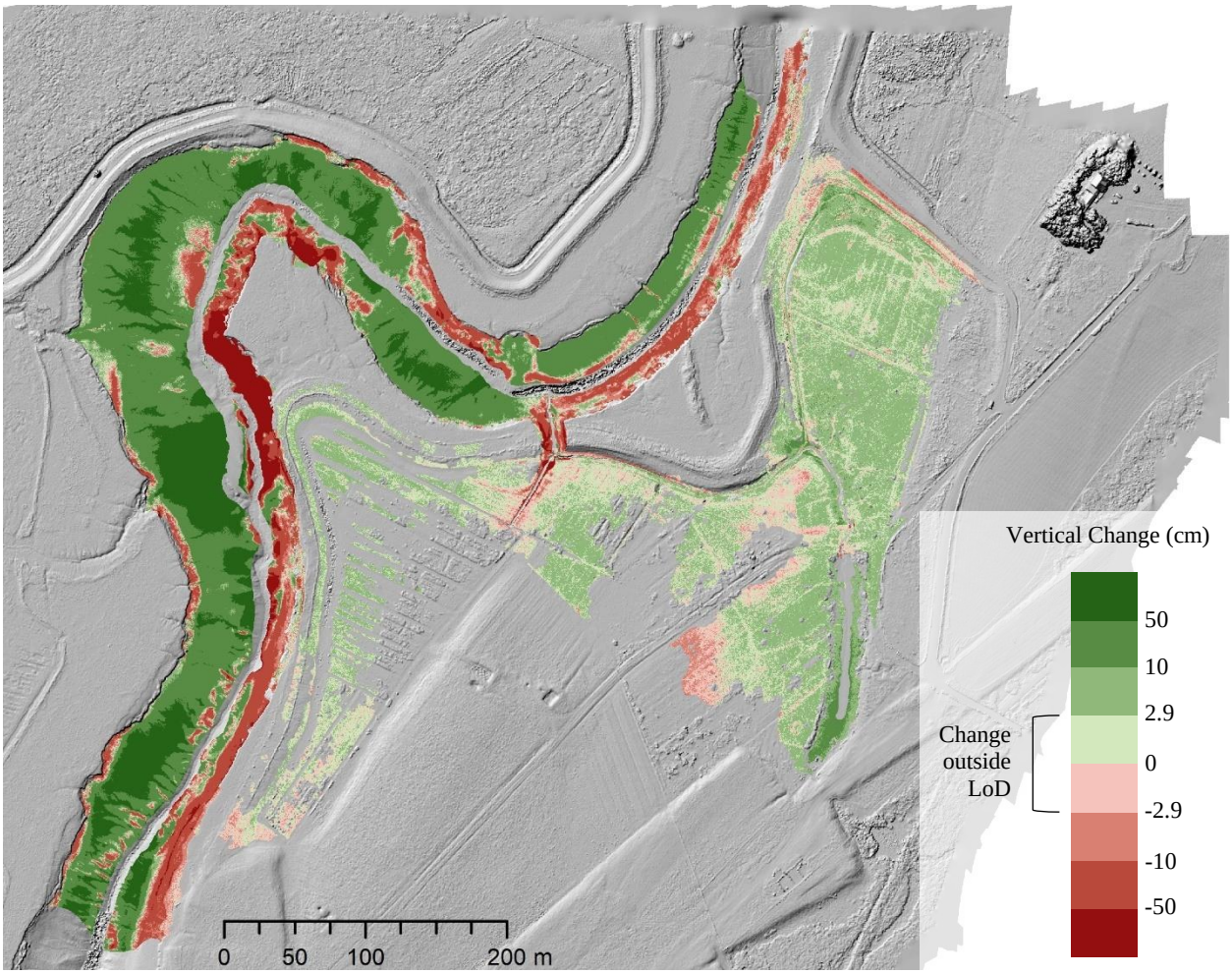

Figure 4.8. DoD raster showing Full Site surface elevation change from November 24, 2019 to October 5, 2020 (1-year). LoD was calculated using a 68% confidence interval. Background is a hillshade of the October 5, 2020 DSM. Percentage of pixels in the site area and river area within LoD are 55% and 94% respectively.

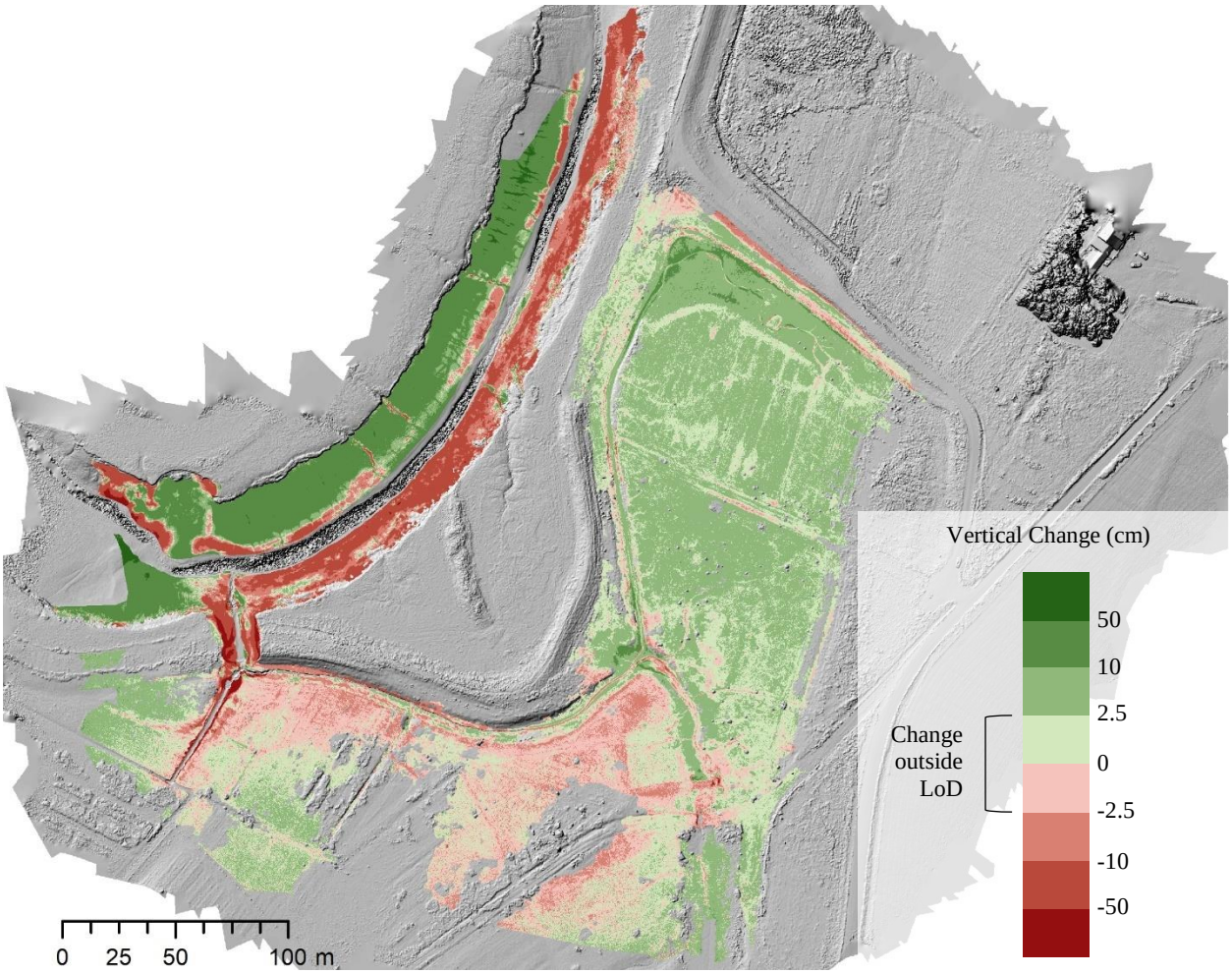

Figure 4.9. DoD raster showing Target Area surface elevation change from November 24, 2019 to October 5, 2020 (1-year). LoD was calculated using a 68% confidence interval. Background is a hillshade of the October 5, 2020 DSM. Percentage of pixels in the site area and river area within LoD are 50% and 91% respectively.

The DoDs representing winter (November 24, 2019 to June 1, 2020) (Figures 4.10 and 4.11) both showed more negative surface elevation change throughout the site compared to the 1-year DoDs, especially in the center area of the site. The Full Site DoD showed more negative surface elevation change surrounding the borrow pit, but both DoDs showed areas of positive surface elevation change within the LoD in the borrow pit. Both the Full Site and Target area datasets had fewer pixels within the LoD compared to the 1-year datasets, with 41% in the Full Site DoD and 42% in the Target Area DoD.

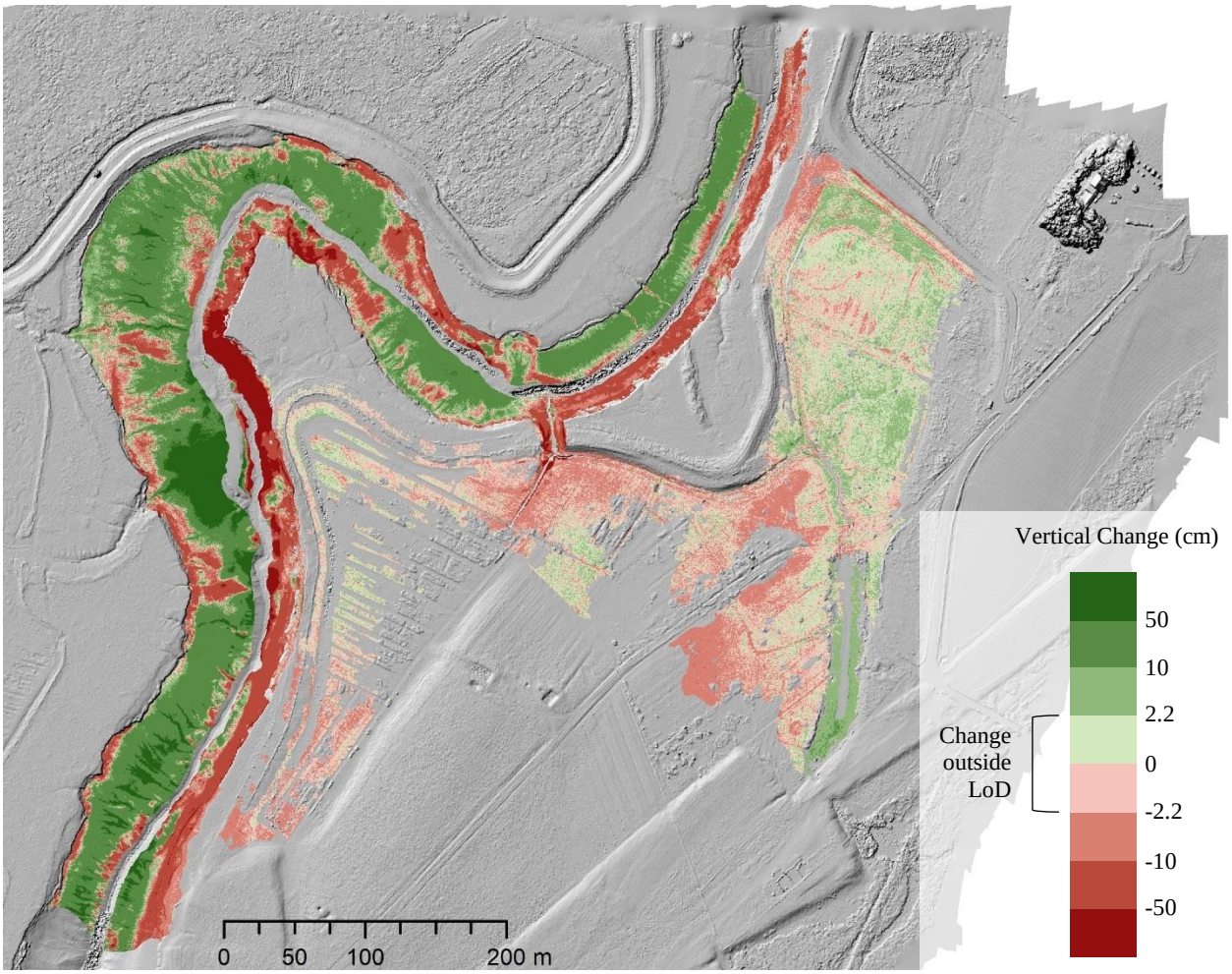

Figure 4.10. DoD raster showing Full Site surface elevation change from November 24, 2019 to June 1, 2020 (winter). LoD was calculated using a 68% confidence interval. Background is a hillshade of the June 1, 2020 DSM. Percentage of pixels in the site area and river area within LoD are 41% and 93% respectively.

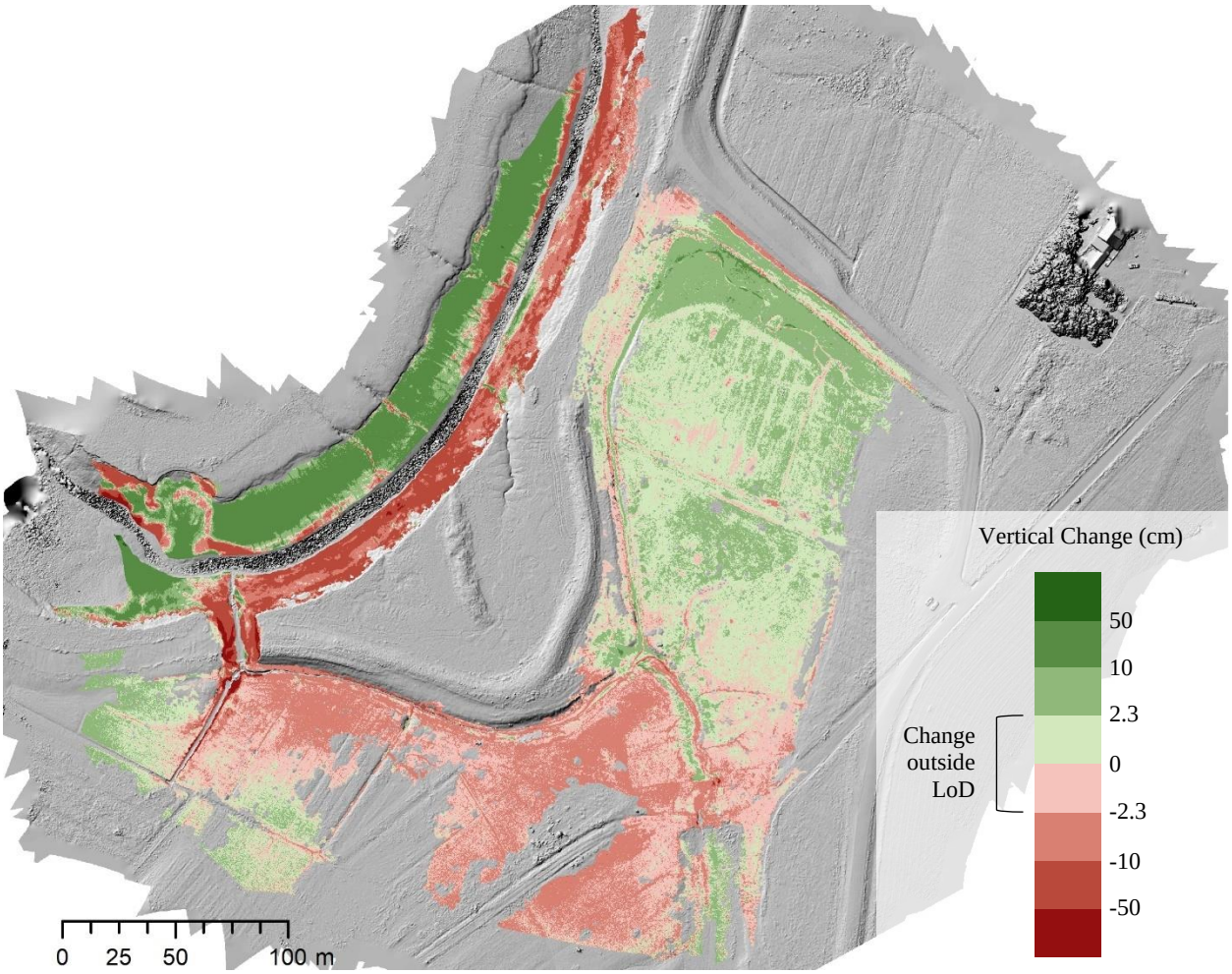

Figure 4.11. DoD raster showing Target Area surface elevation change from November 24, 2019 to June 1, 2020 (winter). LoD was calculated using a 68% confidence interval. Background is a hillshade of the June 1, 2020 DSM. Percentage of pixels in the site area and river area within LoD are 42% and 92% respectively.

The growing season (June 1, 2020 – October5, 2020) DoDs (Figures 4.12and 4.13) were characterized by a majority of positive surface elevation change, and in the Target Area DoD most of this change, as well as most of the negative change, was outside the LoD (-2.2 to 2.2 cm). The percentage of pixels within the LoD in the Full Site and Target Area DoDs was 65% and 31% respectively. Most of the positive surface elevation change in the Target Area DoD that was within the LoD was located around the main drainage ditches, the northwestern corner of the borrow pit, and the freshwater stream area. The Full Site growing season DoD had a generally

even coverage of pixels with values > LoD (-2.6 to 2.6 cm) throughout the site, other than some areas in the borrow pit that had negative surface elevation change, concentrated at the eastern end. This pattern was similar in the Target Area DoD, and in both DoDs these negative values were mostly outside of the LoD.

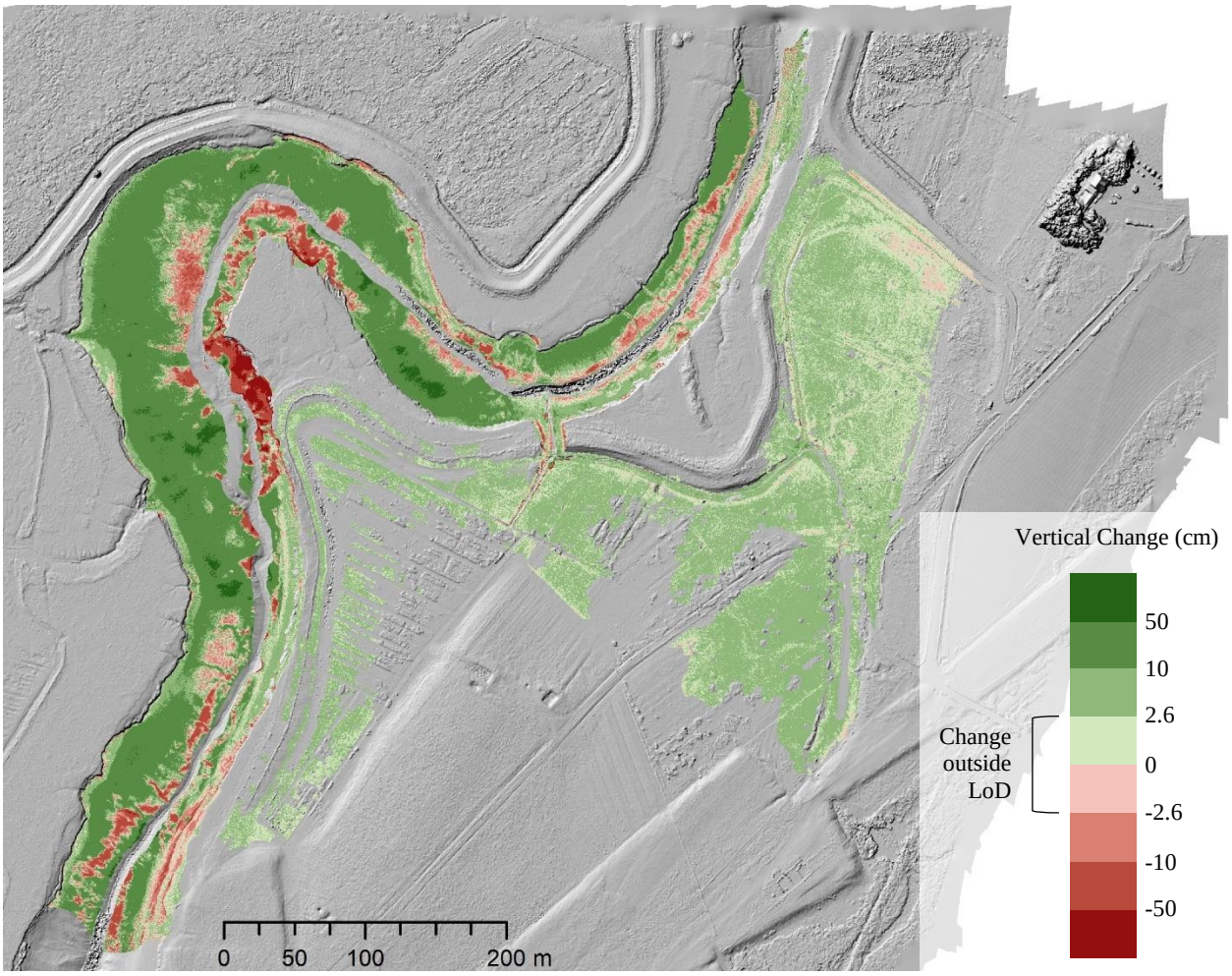

Figure 4.12. DoD raster showing Full Site surface elevation change from June 1, 2020 to October 5, 2020 (growing season). LoD was calculated using a 68% confidence interval. Background is a hillshade of the October 5, 2020 DSM. Percentage of pixels in the site area and river area within LoD are 24% and 84% respectively.

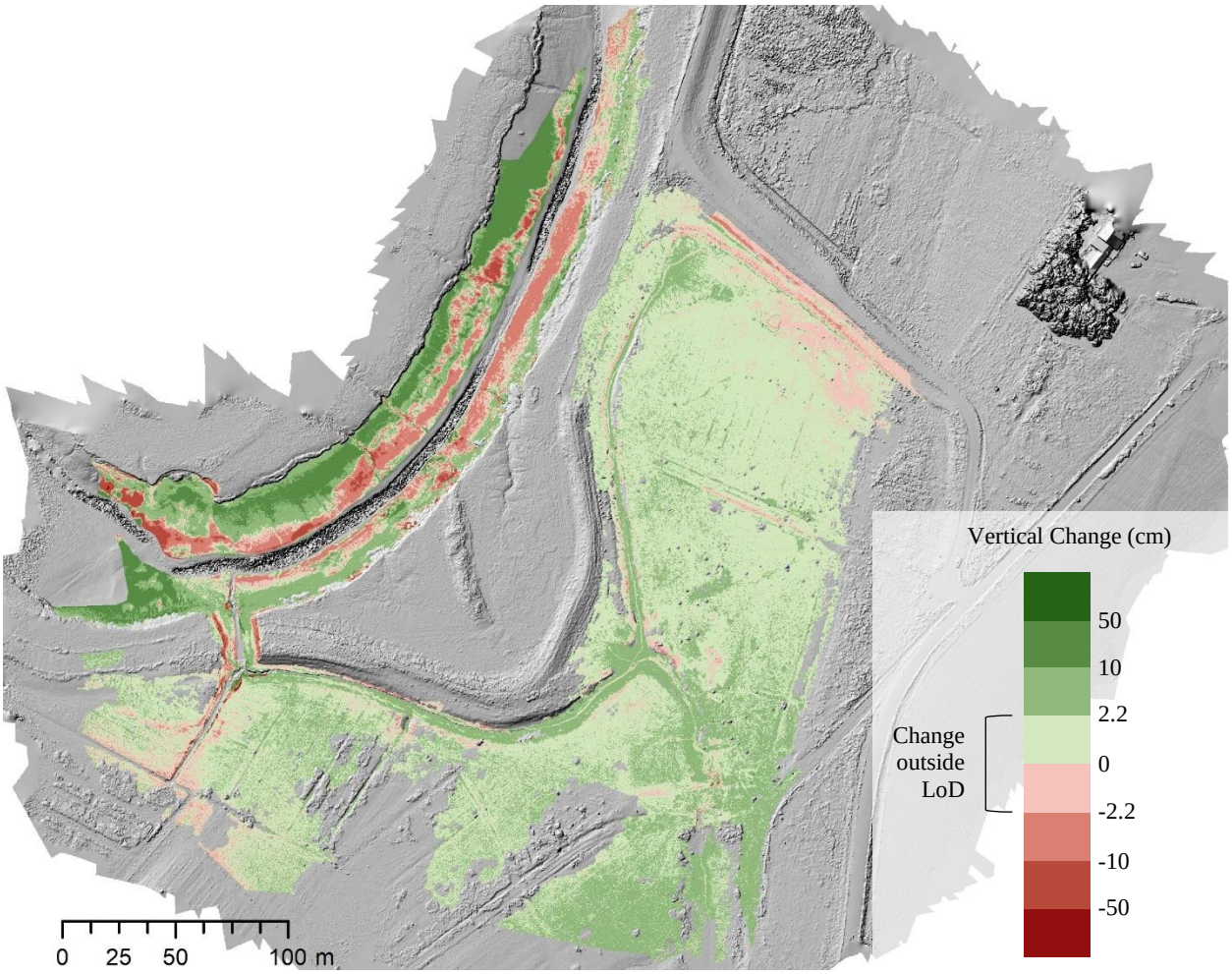

Figure 4.13. DoD raster showing Target Area surface elevation change from June 1, 2020 to October 5, 2020 (growing season). LoD was calculated using a 68% confidence interval. Background is a hillshade of the October 5, 2020 DSM. Percentage of pixels in the site area and river area within LoD are 16% and 67% respectively.

There were some significant differences between Full Site and Target Area DoDs in the spring-summer and summer-fall datasets. Specifically, Target Area DoDs for both time periods (Figures 4.15 and 4.17) showed a pattern of surface elevation change that was more likely to represent a vertical offset between input DEMs in the northern corner of the site than actual surface elevation change. In the spring-summer DoD this is visible as a large area of negative values, and in the summer-fall DoD it is visible as a large area of positive values. Results from the Target Area DoDs for these time periods will not be considered reliable in this study.

Although the Full Site spring-summer (Figure 4.14) and summer-fall (Figure 4.16) DoDs also showed patterns of surface elevation loss and gain respectively in the borrow pit area, the changes vary with topography instead of having a continuous gradient, and appear to be realistic in nature. The Full Site spring-summer DoD was characterized by mostly negative surface elevation change around the borrow pit, field area south of the borrow pit, and freshwater stream area, although most of this change was outside the LoD (< 0 cm and > -2.3 cm). The remainder of the site showed slight positive surface elevation change, with the majority of pixels also having values outside the LoD (> 0 cm and < 2.3 cm). The percentage of pixels in this dataset within the LoD was 24%.

The Full Site summer-fall DoD consisted of mostly positive surface elevation change values within the site, although the majority of these values were outside the LoD (> 0 cm and < 2.3 cm). The total percentage of cells within the LoD in this dataset was 36%. Negative surface elevation change around the main channel mouth and drainage ditches in this DoD was minimal, similar to the spring-summer and growing season DoDs.

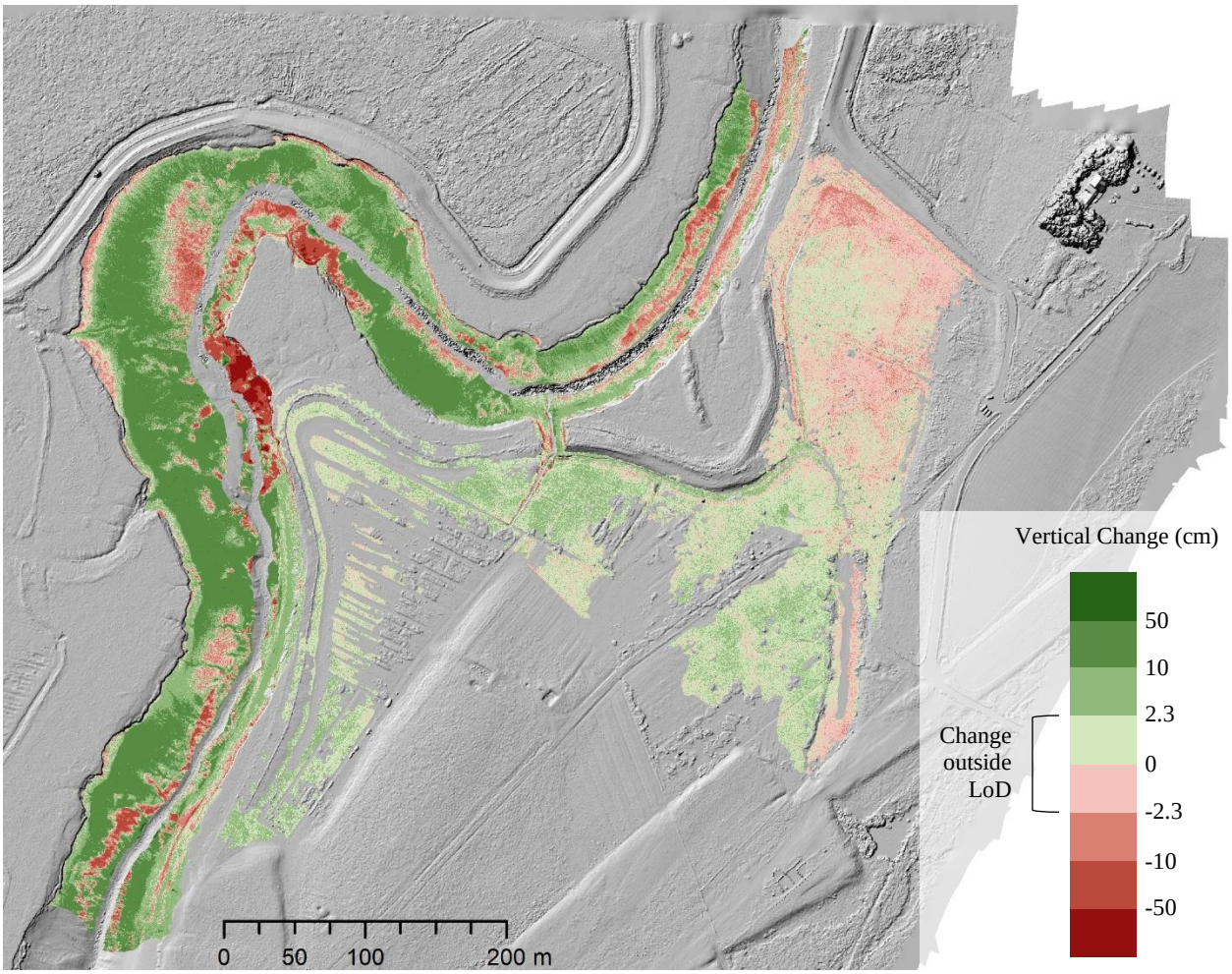

Figure 4.14. DoD raster showing Full Site surface elevation change from June 1, 2020 to August 21, 2020 (spring to summer). LoD was calculated using a 68% confidence interval. Background is a hillshade of the August 21, 2020 DSM. Percentage of pixels in the site area and river area within LoD are 36% and 70% respectively.

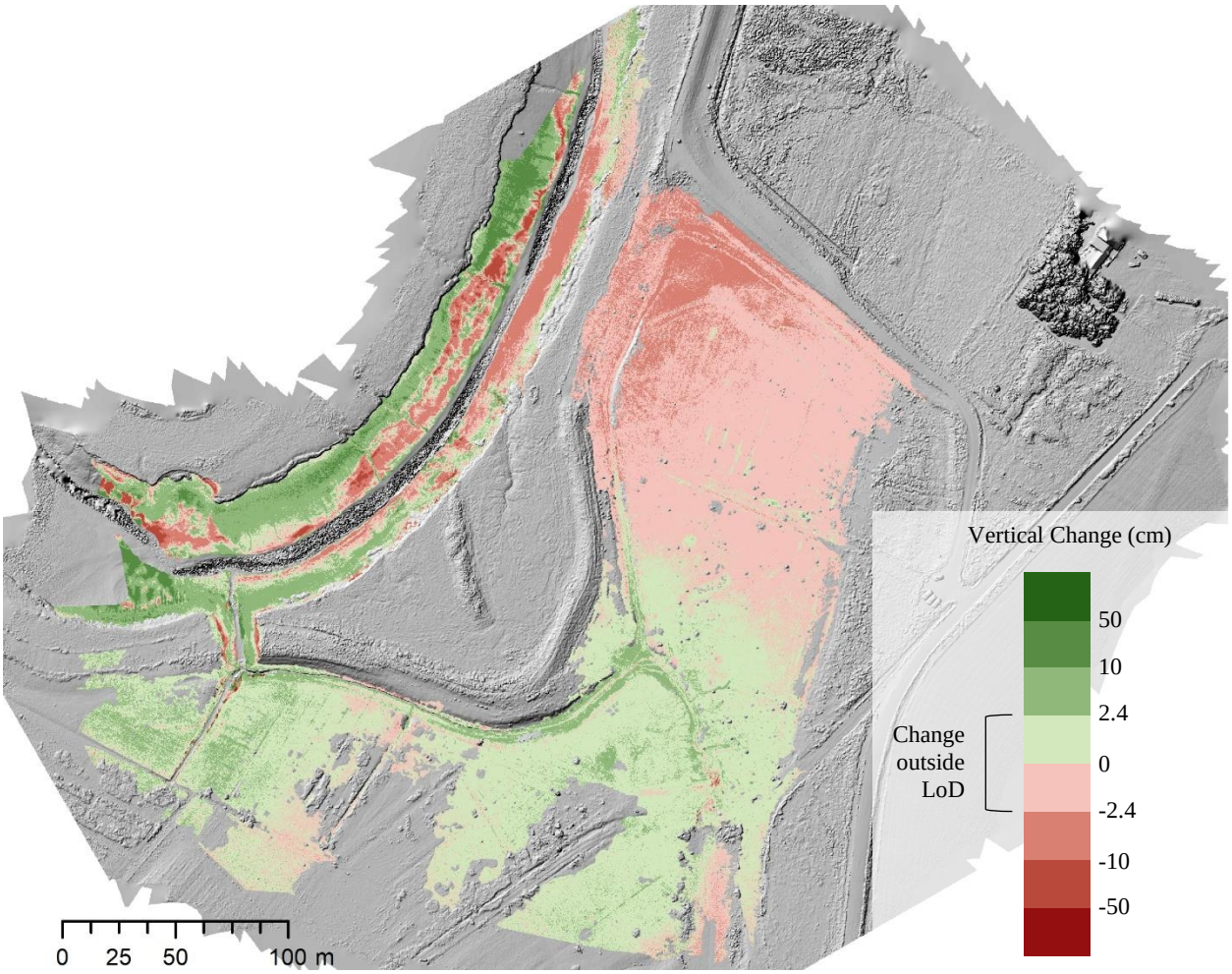

Figure 4.15. DoD raster showing Target Area surface elevation change from June 1, 2020 to August 21, 2020 (spring to summer). LoD was calculated using a 68% confidence interval. Background is a hillshade of the August 21, 2020 DSM. Percentage of pixels in the site area and river area within LoD are 26% and 52% respectively.

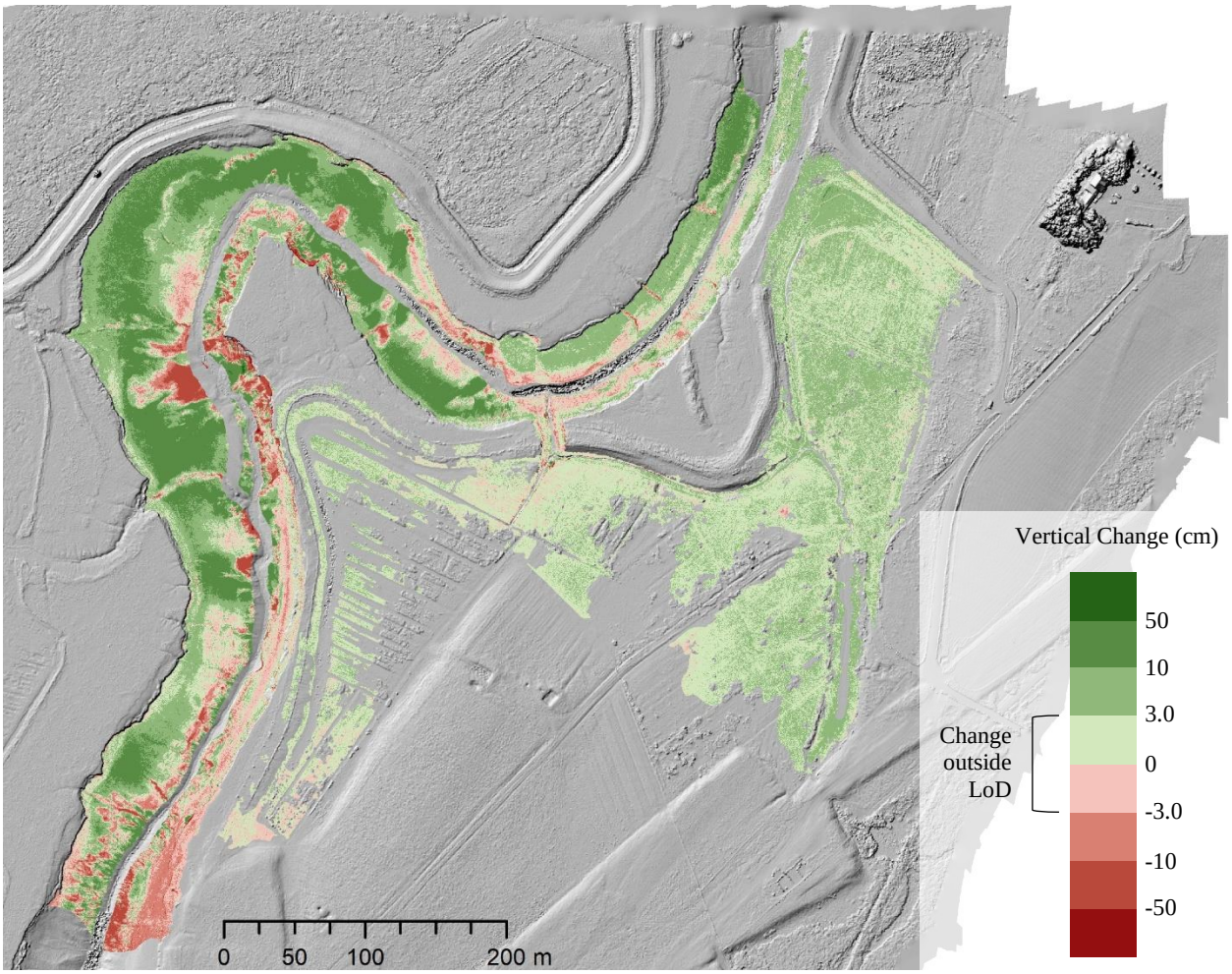

Figure 4.16. DoD raster showing Full Site surface elevation change from August 21, 2020 to October 5, 2020 (summer to fall). LoD was calculated using a 68% confidence interval. Background is a hillshade of the October 5, 2020 DSM.

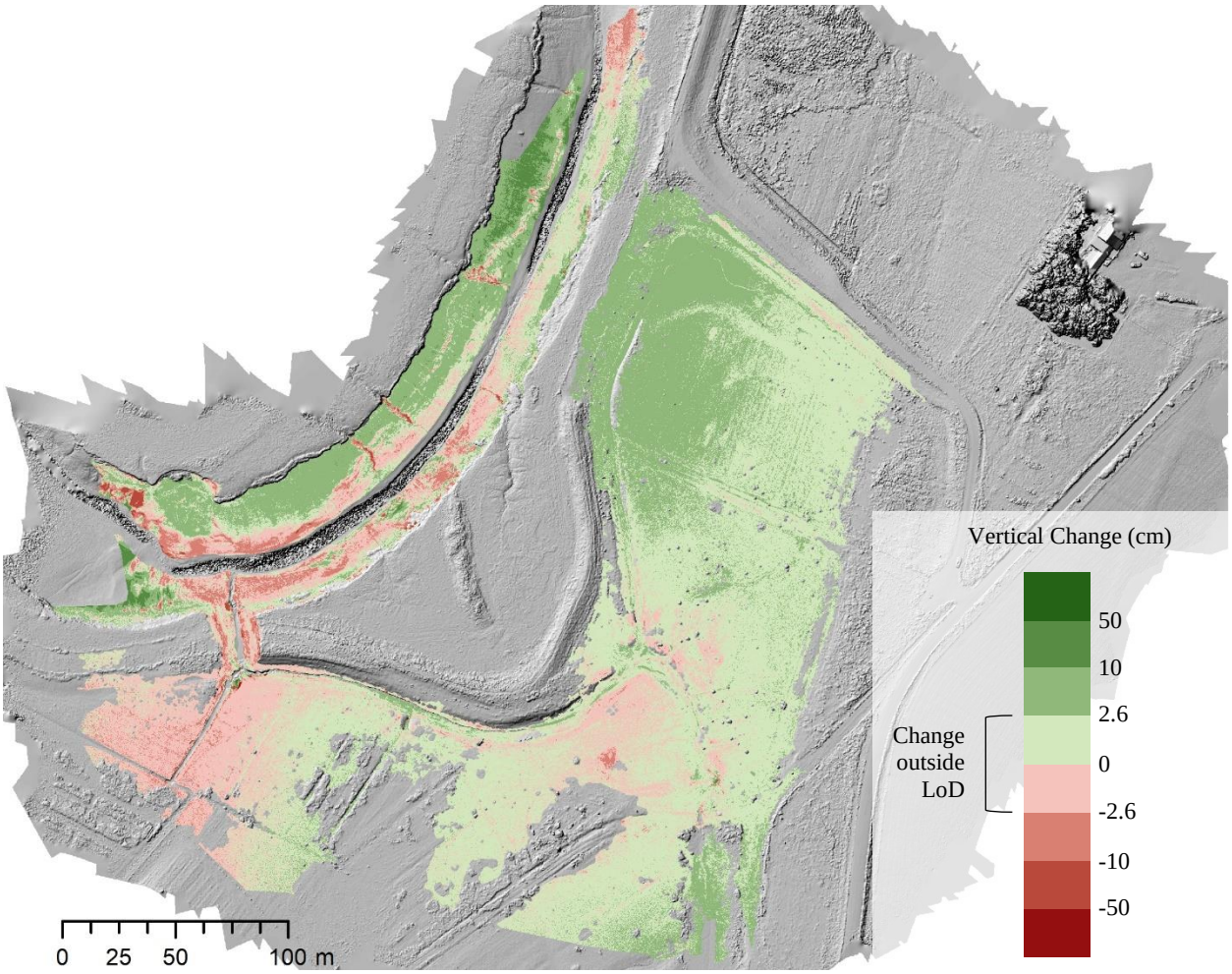

Figure 4.17. DoD raster showing Target Area surface elevation change from August 21, 2020 to October 5, 2020 (summer to fall). LoD was calculated using a 68% confidence interval. Background is a hillshade of the October 5, 2020 DSM.

4.4 Volumetric Change

Total volumetric change in specific areas of the study site was calculated for all DoD rasters and the results are summarized in Tables 4.5-4.7. To compare error estimation methods, results are presented with no LoD, an LoD with a 68% confidence interval (CI), and an LoD with a 95% CI. Total volumetric uncertainties calculated with Equation 3.4 (Taylor, 1997) are also reported for each volumetric change value. All volumetric change results were also reported with the Lane et al. (2003) equation for volumetric uncertainty in Appendix F, Tables F-5 to F-10.

Volumetric change values for the site area of the Full Site datasets for all DoD time periods are outlined in Table 4.5. Total volumetric change for all LoDs were net positive for all time periods excluding winter (November 24, 2019 – June 1, 2020) which was net negative. The maximum volumetric change occurred over the growing season (June 1, 2020 – October 5, 2020) with a value of 1860.8 ± 1528.7 m^3 with no LoD, 1567.1 ± 987.4 m^3 with a 68% CI LoD, and 451.7 ± 204.8 m^3 with a 95% CI LoD. The 1-year, growing season, spring-summer and summer-fall datasets had significantly variable total volumetric change values depending on LoD. However, total volumetric change values for the winter dataset were more comparable at different LoD confidence intervals: -397.6 ± 1285.5 m^3 with no LoD, -389.9 ± 525.1 m^3 with a 68% CI LoD, and -299.4 ± 284.5 m^3 with a 95% CI LoD.

An increased confidence level in the LoD for all time periods generally resulted in a smaller magnitude of measured volumetric change. Total volumetric uncertainty values were relatively large compared to corresponding total volumetric change values, and sometimes exceeded measured volumetric change when no LoD was applied and when 68% CI LoD was applied. Total volumetric uncertainty values for total volumetric change calculated with a 95% CI LoD were all lower than measured change but were still relatively large. Volumetric change results for the river area of the Full Site dataset are shown in Appendix F, Table F-1.

Table 4.5. Results of the volumetric change analysis for the site area of the Full Site datasets using no LoD, an LoD with 68% CI and an LoD with a 98% CI. Volumetric uncertainties were calculated using the Taylor (1997) equation.

Time Frame	No LoD		68% CI			95% CI		
	Total Volumetric Change (m^3)	Average Vertical Change (cm)	LOD (cm)	Total Volumetric Change (m^3)	Average Vertical Change (cm)	LOD (cm)	Total Volumetric Change (m^3)	Average Vertical Change (cm)
2019/11/24 - 2020/10/05 (1-Year)	1464.3 ± 1690.9	2.5 ± 2.9	2.9	1228.0 ± 929.9	3.9 ± 2.9	5.7	418.8 ± 284.5	4.3 ± 2.9
2019/11/24 - 2020/06/01 (Winter)	-397.6 ± 1285.5	-0.7 ± 2.2	2.2	-389.9 ± 525.1	-1.7 ± 2.2	4.4	-299.4 ± 181.4	-3.7 ± 2.2
2020/06/01 - 2020/10/05 (Growing Season)	1860.8 ± 1528.7	3.2 ± 2.6	2.6	1567.1 ± 987.4	4.2 ± 2.6	5.2	451.7 ± 204.8	5.8 ± 2.6
2020/06/01 - 2020/08/21 (Spring – Summer)	430.7 ± 1331.9	0.7 ± 2.3	2.3	273.8 ± 316.4	2.0 ± 2.3	4.5	39.6 ± 32.1	2.8 ± 2.3
2020/08/21 - 2020/10/05 (Summer - Fall)	1429.7 ± 1725.6	2.5 ± 3.0	3.0	865.5 ± 625.6	4.1 ± 3.0	5.8	123.4 ± 58.2	6.3 ± 3.0

Target area datasets were subdivided into 5 specific areas for calculating total volumetric change: site, river, borrow pit, drainage channels and main channel mouth. Since the Target Area DoDs for the spring-summer and summer-fall datasets were determined to be unreliable, their volumetric results will not be discussed. Results for the site area are summarized in Table 4.6, and show a similar trend to the site area in the Full Site datasets. Both 1-year and growing season DoDs had a net positive volumetric change, but the winter DoD had a net negative volumetric change. The highest rate of volumetric change within these time periods varied by LoD. With no LoD, and with a 95% CI LoD, the highest measured volumetric change occurred over the growing season: 666.6 ± 923.1 m^3 and 67.0 ± 39.6 m^3 respectively. However, when an LoD with a 68% CI was applied, the highest amount of volumetric change occurred over the 1-year period: 440.9 ± 522.8 m^3.

Similar to the site area of the Full Site DoDs, there was a large amount of variation within measured total volumetric change between different LoDs confidence intervals, with the least amount of variation occurring in the winter period: -126.3 ± 955.5 m^3 with no LoD, -184.7 ± 397.6 m^3 with a 68% CI LoD, and -163.8 ± 108.3 m^3 with a 95% CI LoD. Volumetric uncertainties for Target Area DoDs were very high and exceeded the measured change values in the majority of results. The river area and problematic datasets (spring-summer, summer-fall) volumetric change results for the Target Area DoDs are reported in Appendix F, Tables F-2 to F-4.

Table 4.6. Results of the volumetric change analysis for the site area of the Target Area datasets using no LoD, an LoD with 68% CI and an LoD with 95% CI. Volumetric uncertainties were calculated using the Taylor (1997) equation.

Time Frame	No LoD		68% CI			95% CI		
	Total Volumetric Change (m^3)	Average Vertical Change (cm)	LOD (cm)	Total Volumetric Change (m^3)	Average Vertical Change (cm)	LOD (cm)	Total Volumetric Change (m^3)	Average Vertical Change (cm)
2019/11/24 - 2020/10/05 (1-Year)	540.4 ± 1040.1	1.3 ± 2.5	2.5	440.9 ± 522.8	2.1 ± 2.5	4.9	46.5 ± 136.3	0.9 ± 2.5
2019/11/24 - 2020/06/01 (Winter)	-126.3 ± 955.5	-0.3 ± 2.3	2.3	-184.7 ± 397.6	-1.1 ± 2.3	4.5	-163.8 ± 108.3	-3.5 ± 2.3
2020/06/01 - 2020/10/05 (Growing Season)	666.6 ± 923.1	1.6 ± 2.2	2.2	369.2 ± 283.6	2.9 ± 2.2	4.3	67.0 ± 39.6	3.7 ± 2.2

Volumetric change values for the borrow pit, main drainage channels and main channel mouth (extents shown in Figure 3.16) are outlined in Table 4.7. Compared to volumetric results from the site, the volumetric uncertainties for these areas of interest were generally smaller relative to measured volumetric change, especially when an LoD was applied (either 68% or 95% CI). Patterns of volume loss or gain varied between the borrow pit and the main drainage channels and main channel mouth. In the borrow pit, all time periods showed net positive volumetric change, and the largest amount of volumetric change occurred over the 1-year period: 174.5 ± 82.9 m^3 with no LoD, 166.9 ± 64.7 m^3 with a 68% CI LoD, and 138.4 ± 43.7 m^3 with a 95% CI LoD.

Seasonal results show that the majority of surface elevation gain in the borrow pit occurred over the winter (146.8 ± 76.2 m^3 with no LoD, 140.4 ± 58.0 m^3 with a 68% CI LoD, and 114.3 ± 38.7 m^3 with a 95% CI LoD). In the drainage channels and main channel mouth, both the 1-year and winter periods had very similar net negative volumetric change values, showing that the majority of change occurred over the winter. The growing season had very small volumetric change values, with the drainage channels net positive with no LoD and a 68% CI LoD, but net negative with a 95% CI LoD, and the main channel mouth net negative at all LoD levels. Total volumetric change values for these datasets did vary with different LoDs, but to a lesser extent than seen in the site area results.

Table 4.7. Results of the volumetric change analysis for areas of interest in Target Area datasets using no LoD, an LoD with 68% CI and an LoD with 95% CI. Volumetric uncertainties were calculated using the Taylor (1997) equation.

Area	Time Frame	No LoD		68% CI			95% CI		
		Total Volumetric Change (m^3)	Average Vertical Change (cm)	LOD (cm)	Total Volumetric Change (m^3)	Average Vertical Change (cm)	LOD (cm)	Total Volumetric Change (m^3)	Average Vertical Change (cm)
Borrow Pit	2019/11/24 - 2020/10/05 (1-Year)	174.5 ± 82.9	5.0 ± 2.5	2.5	166.9 ± 64.7	6.4 ± 2.5	4.9	138.4 ± 43.7	7.9 ± 2.5
	2019/11/24 - 2020/06/01 (Winter)	146.8 ± 76.2	4.4 ± 2.3	2.3	140.4 ± 58.0	5.5 ± 2.3	4.5	114.3 ± 38.7	6.7 ± 2.3
	2020/06/01 - 2020/10/05 (Growing Season)	27.7 ± 73.6	0.8 ± 2.2	2.2	14.7 ± 12.5	2.6 ± 2.2	4.3	0.8 ± 0.5	3.8 ± 2.2
Drainage Channels	2019/11/24 - 2020/10/05 (1-Year)	-103.5 ± 28.4	-9.0 ± 2.5	2.5	-102.3 ± 20.9	-12.2 ± 2.5	4.9	-99.2 ± 16.0	-15.4 ± 2.5
	2019/11/24 - 2020/06/01 (Winter)	-106.2 ± 26.1	-9.3 ± 2.3	2.3	-104.8 ± 22.2	-10.8 ± 2.3	4.5	-98.5 ± 19.2	-11.7 ± 2.3
	2020/06/01 - 2020/10/05 (Growing Season)	3.8 ± 25.2	0.3 ± 2.2	2.2	2.5 ± 14.8	0.4 ± 2.2	4.3	-1.4 ± 8.7	-0.4 ± 2.2
Main Channel Mouth	2019/11/24 - 2020/10/05 (1-Year)	-127.0 ± 9.5	-33.2 ± 2.5	2.5	-126.9 ± 8.7	-36.4 ± 2.5	4.9	-126.6 ± 8.0	-39.3 ± 2.5
	2019/11/24 - 2020/06/01 (Winter)	-125.6 ± 8.7	-32.8 ± 2.3	2.3	-125.5 ± 8.1	-35.1 ± 2.3	4.5	-125.0 ± 7.7	-37.0 ± 2.3
	2020/06/01 - 2020/10/05 (Growing Season)	-1.0 ± 8.4	-0.2 ± 2.2	2.2	-1.5 ± 5.5	-0.6 ± 2.2	4.3	-2.7 ± 3.7	-1.6 ± 2.2

Total volumetric change values were standardized by dividing the total volumetric change by the number of months in each corresponding time period. Monthly volumetric change values are reported in Figures 4.18-4.21. The general trend of monthly volumetric change in the site area for Full Site datasets (Figure 4.18) and Target Area datasets (Figure 4.19) was a negative value during the winter (-64.1 $m^3 \cdot month^{-1}$ and -20.4 $m^3 \cdot month^{-1}$ respectively), increased to positive in the Target Area growing season (159.9 $m^3 \cdot month^{-1}$) and Full Site spring-summer (159.5 $m^3 \cdot month^{-1}$) and summer-fall (953.1 $m^3 \cdot month^{-1}$) periods, and a value between those for the 1 year period (142.2 $m^3 \cdot month^{-1}$ and 52.5 $m^3 \cdot month^{-1}$ respectively).

Target Area borrow pit data sets showed an opposite trend (Figure 4.20), with a peak monthly volumetric change in the winter of 23.7 $m^3 \cdot month^{-1}$, and minimum change over the growing season of 6.7 $m^3 \cdot month^{-1}$. In the main channel mouth area (Figure 4.21), the monthly rates of change were negative over the 1-year (-10.051 $m^3 \cdot month^{-1}$) and winter (17.134 $m^3 \cdot month^{-1}$) periods, but had lower magnitudes than the rates of volumetric gain in the borrow pit for the same time periods. Over the growing season, the rate of change was positive, but with a relatively low magnitude of 0.921 $m^3 \cdot month^{-1}$.

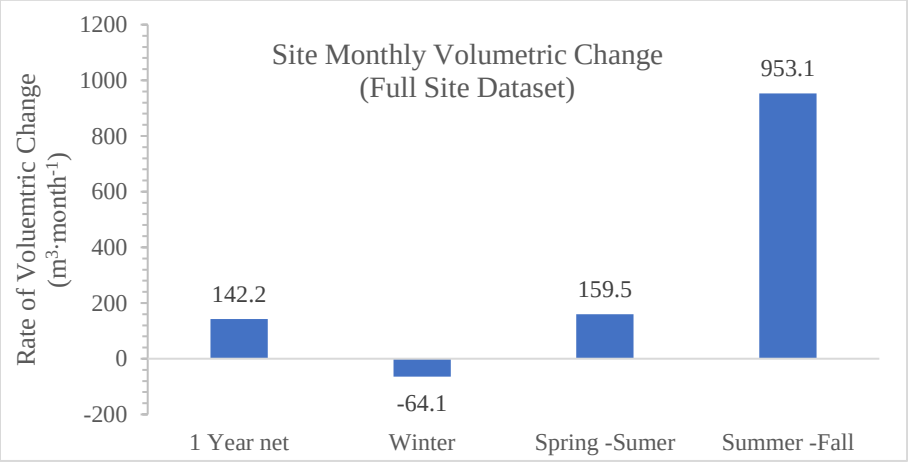

Figure 4.18. Volumetric change per month based on seasonal DoDs for the site area of the Full Site datasets.

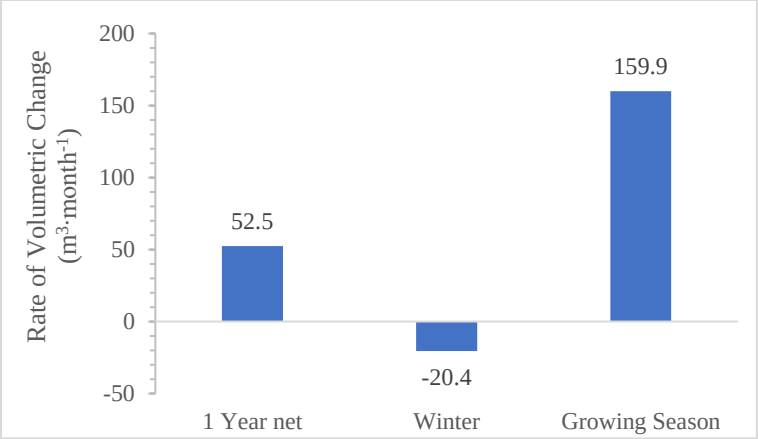

Figure 4.19. Volumetric change per month based on seasonal DoDs for the site area of the Target Area datasets.

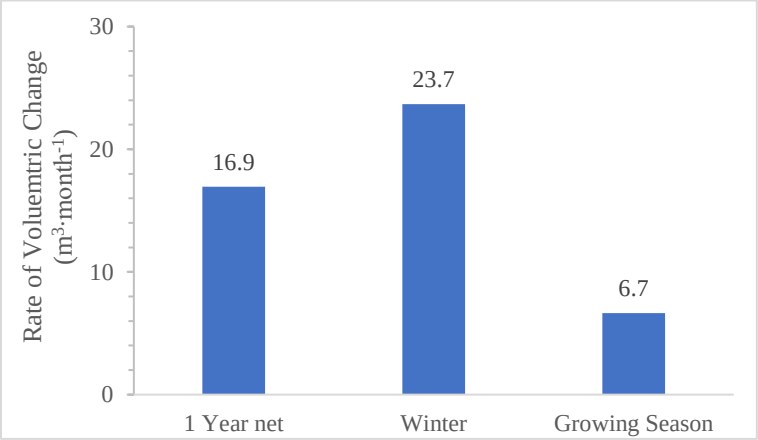

Figure 4.20. Volumetric change per month based on seasonal DoDs for the borrow pit area of the Target Area datasets.

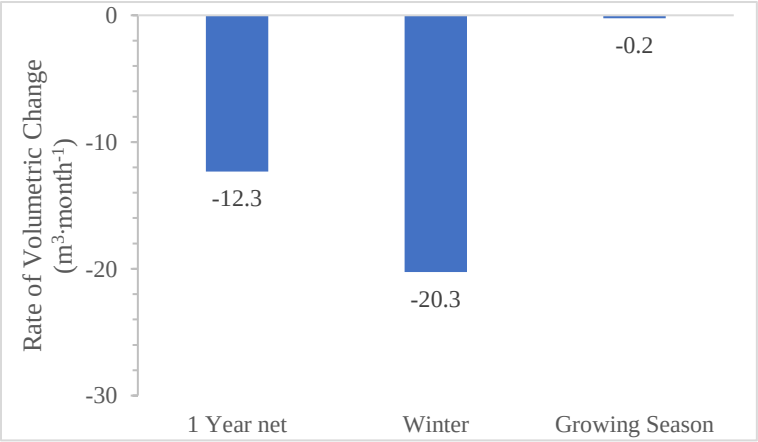

Figure 4.21. Volumetric change per month based on seasonal DoDs for the main channel mouth area of the Target Area datasets.

4.5 Raster Correlation

Multiple linear regression models were calculated in R to predict surface elevation change (DoD rasters) based on starting elevation and distance from channel (DFC). The models were calculated as scaled so that coefficient magnitudes for both independent variables could be directly compared, as well as unscaled, and cross validation was completed to estimate the prediction error of each model. Three time periods for DoD calculation were examined in this analysis: 1-year (November 24, 2019 – October 5, 2020), winter (November 24, 2019 – June 1, 2020), and growing season (June 1, 2020 – October 5, 2020). Results of each multiple linear regression model are presented in Tables 4.8-4.13.

For the 1-year period borrow pit dataset, a significant regression equation was found ($F(3,11679) = 3999$, $p < 2.2 \times 10^{-16}$), with an adjusted R^2 of 0.507 (Table 4.8). The model shows that elevation, DFC, and the interaction effect (elevation * DFC) were significant predictors of surface elevation change, and that the regression equation explained 50.6% of data variance. The regression coefficients show that elevation was negatively correlated with surface elevation change, and DFC was positively correlated, but elevation was approximately 7 times stronger a predictor of surface elevation change. By incorporating the interaction effect, it was determined that the overall effect of DFC on surface elevation change was negative at all elevations, and the overall effect of elevation was negative at all DFC values. The effect of DFC increased in magnitude at higher elevations, and the effect of elevation increased in magnitude at higher DFC values. The RMSE of the model was 2.601×10^{-2}.

The 1-year period full site dataset also had a significant regression equation ($F(3,12981) = 1273$, $p < 2.2 \times 10^{-16}$), with an adjusted R^2 of 0.227 (Table 4.9). In this model, only 22.7% of variance in surface elevation change was explained by elevation, DFC and interaction effect, although all independent variables were significant predictors. The regression coefficients show

that elevation was negatively correlated with surface elevation change, and distance from channel was positively correlated. Elevation was approximately 2.6 times stronger a predictor than DFC, and the interaction effect had a similar magnitude of prediction power as DFC. Incorporation of the interaction effect shows that the overall effect of DFC on surface elevation change was negative at elevations greater than 6.151 m CGVD2013, and positive at elevations below this threshold. The magnitude of this effect was larger at lower elevations than high but did not vary greatly between DEM values. The overall effect of elevation on surface elevation change was negative at all DFC values, and the magnitude of this effect was greatly increased at higher DFC values. The RMSE of the model was 2.705×10^{-2}.

Table 4.8. Multiple linear regression results for surface elevation change in the borrow pit from November 24, 2019 to October 5, 2020 (1-year, Target Area dataset).

	Scaled Coefficient	Unscaled Coefficient	P-Value
Intercept	5.191×10^{-2} (2.491×10^{-4})	0.486 (0.003976)	$<2 \times 10^{-16}$ ***
Elevation	-2.696×10^{-2} (2.506×10^{-4})	-0.08137 (0.0007524)	$<2 \times 10^{-16}$ ***
Distance from Channel	3.522×10^{-3} (2.506×10^{-4})	0.00102 (0.00007423)	$<2 \times 10^{-16}$ ***
Interaction Effect	-1.084×10^{-3} (2.398×10^{-4})	-0.0009681 (0.0002141)	6.2×10^{-6} ***
Adjusted R-squared:	0.507		
No. observations	11679		
RMSE:	2.601×10^{-2}		

Standard errors are reported in parentheses. RMSE calculated using 5-fold cross validation.
*, **, *** indicates significance at the 90%, 95%, and 99% level, respectively.

Table 4.9. Multiple linear regression results for surface elevation change within the study site but excluding main channel mouth, drainage ditches and borrow pit from November 24, 2019 to October 5, 2020 (1-year, Full Site dataset).

	Scaled Coefficient	Unscaled Coefficient	P-Value
Intercept	3.421×10^{-2} (2.724×10^{-4})	0.1314809 (0.0049289)	$<2 \times 10^{-16}$ ***
Elevation	-1.774×10^{-2} (3.102×10^{-4})	-0.0180334 (0.000854)	$<2 \times 10^{-16}$ ***
Distance from Channel	6.733×10^{-3} (3.260×10^{-4})	0.0202884 (0.0006281)	$<2 \times 10^{-16}$ ***
Interaction Effect	-8.757×10^{-3} (2.725×10^{-4})	-0.0032986 (0.0001026)	$<2 \times 10^{-16}$ ***
Adjusted R-squared:	0.227		
No. observations	12981		
RMSE:	2.705×10^{-2}		

Standard errors are reported in parentheses. RMSE calculated using 5-fold cross validation.
*, **, *** indicates significance at the 90%, 95%, and 99% level, respectively.

A significant regression equation was found for both borrow pit and remaining site area datasets over the winter period, ($F(3, 11679) = 2261$, $p < 2.2 \times 10^{-16}$), with an adjusted R^2 of 0.367, and ($F(3, 12981) = 1111$, $p < 2.2 \times 10^{-16}$), with an adjusted R^2 of 0.204 respectively (Table 4.10 and Table 4.11). Both models showed a negative correlation between elevation and surface elevation change, and a positive correlation between DFC and surface elevation change, and all independent variables were significant predictors. In the borrow pit, elevation was a 13.4 times stronger predictor than DFC, and in the remainder of site it was only 2.6 times stronger a predictor. In both datasets, the overall effect of DFC on surface elevation change was negative above a certain elevation threshold (5.661 m CGVD2013 for the borrow pit, 6.098 m CGVD2013 for the site area), and positive below this threshold, although the magnitude of this effect varied minimally with changing elevation values. The effect of elevation on surface elevation change was negative at all DFC values and increased in magnitude at larger DFC values for both datasets, but this increase was more prominent in the site area than the borrow pit. The RMSE of the borrow pit model was 2.547×10^{-2}, and the RMSE of the remaining site area model was 2.622×10^{-2}.

Table 4.10. Multiple linear regression results for surface elevation change in the borrow pit from November 24, 2019 to June 1, 2020 (winter, Target Area dataset).

	Scaled Coefficient	Unscaled Coefficient	P-Value
Intercept	4.389×10^{-2} (2.441×10^{-4})	0.321421 (0.0065551)	$<2 \times 10^{-16}$ ***
Elevation	-1.952×10^{-2} (2.455×10^{-4})	-0.051974 (0.0012324)	$<2 \times 10^{-16}$ ***
Distance from Channel	1.456×10^{-3} (2.455×10^{-4})	0.0085918 (0.0011357)	$<2 \times 10^{-16}$ ***
Interaction Effect	-1.699×10^{-3} (2.349×10^{-4})	-0.0015176 (0.0002097)	4.94×10^{-13} ***
Adjusted R-squared:	0.367		
No. observations	11679		
RMSE:	2.5471×10^{-2}		

Standard errors are reported in parentheses. RMSE calculated using 5-fold cross validation.
*, **, *** indicates significance at the 90%, 95%, and 99% level, respectively.

Table 4.11. Multiple linear regression results for surface elevation change within the study site but excluding main channel mouth, drainage ditches and borrow pit from November 24, 2019 to June 1, 2020 (winter, Full Site dataset).

	Scaled Coefficient	Unscaled Coefficient	P-Value
Intercept	1.117×10^{-3} (2.641×10^{-4})	0.05373 (0.004779)	2.38×10^{-5} ***
Elevation	-1.548×10^{-2} (3.007×10^{-4})	-0.01024 (0.000828)	$<2 \times 10^{-16}$ ***
Distance from Channel	5.959×10^{-3} (3.161×10^{-4})	0.02152 (0.000609)	$<2 \times 10^{-16}$ ***
Interaction Effect	-9.369×10^{-3} (2.642×10^{-4})	-0.003529 (0.00009951)	$<2 \times 10^{-16}$ ***
Adjusted R-squared:	0.204		
No. observations	12981		
RMSE:	2.622×10^{-2}		

Standard errors are reported in parentheses. RMSE calculated using 5-fold cross validation.
*, **, *** indicates significance at the 90%, 95%, and 99% level, respectively.

Model results for the growing season datasets are presented in Table 4.12 and Table 4.13 for the borrow pit and site area respectively. As with all other models, a significant regression equation was found for the borrow pit ($F(3, 11679) = 1573$, $p < 2.2 \times 10^{-16}$), with an adjusted R^2 of 0.288 and the site area ($F(3, 12981) = 57.31$, $p < 2.2 \times 10^{-16}$), with an adjusted R^2 of 0.013. The adjusted R^2 value for the site area growing season model was the lowest out of all the presented models. In both borrow pit and site area models, elevation was negatively correlated with surface elevation change and DFC was positively correlated. However, in the site area dataset, DFC was

not a significant predictor, and in both datasets the interaction effect was a less significant predictor than the independent variables in all other models.

Incorporation of the interaction effect into the overall effect of both independent variables shows that the growing season dataset for both site and borrow pit were unique compared to the other models. In these models, the overall effect of DFC on surface elevation change was positive at all elevations. In the borrow pit, the overall effect of DFC had a higher magnitude at lower elevations, while in the site area it had a higher magnitude at higher elevations. The overall effect of elevation on surface elevation change in the borrow pit was negative at all DFC values, and its magnitude did not vary greatly with different DFC values. Alternatively, the overall effect of elevation on surface elevation change in the site area was negative only when DFC values where less than 23.537 m, and positive when DFC values were above this threshold.

Table 4.12. Multiple linear regression results for surface elevation change in the borrow pit from June 1, 2020 to October5, 2020 (growing season, Target Area dataset).

	Scaled Coefficient	Unscaled Coefficient	P-Value
Intercept	8.338×10^{-3} (1.058×10^{-4})	0.1231 (0.002917)	$<2 \times 10^{-16}$ ***
Elevation	-7.195×10^{-3} (1.057×10^{-4})	-0.02172 (0.0005415)	$<2 \times 10^{-16}$ ***
Distance from Channel	2.191×10^{-3} (1.064×10^{-4})	0.002309 (0.0005427)	$<2 \times 10^{-16}$ ***
Interaction Effect	-3.477×10^{-4} (3.477×10^{-4})	-0.0003132 (0.00009959)	0.00166 **
Adjusted R-squared:	0.288		
No. observations	11679		
RMSE:	1.127×10^{-2}		

Standard errors are reported in parentheses. RMSE calculated using 5-fold cross validation.
*, **, *** indicates significance at the 90%, 95%, and 99% level, respectively.

Table 4.13. Multiple linear regression results for surface elevation change within the study site but excluding main channel mouth, drainage ditches and borrow pit from June 1, 2020 to October5, 2020 (growing season, Full Site dataset).

	Scaled Coefficient	Unscaled Coefficient	P-Value
Intercept	$3.307x10^{-2}$ ($1.722x10^{-4}$)	0.07269 (0.003239)	$<2x10^{-16}$ ***
Elevation	$-1.817x10^{-3}$ ($1.981x10^{-4}$)	-0.006821 (0.0005607)	$<2x10^{-16}$ ***
Distance from Channel	$2.177x10^{-4}$ ($2.096x10^{-4}$)	0.001655 (0.0005005)	0.298815
Interaction Effect	$5.838x10^{-4}$ ($1.645x10^{-4}$)	0.0002898 (0.00008166)	0.000388 **
Adjusted R-squared:	0.011		
No. observations	12981		
RMSE:	$1.735x10^{-2}$		

Standard errors are reported in parentheses. RMSE calculated using 5-fold cross validation.
*, **, *** indicates significance at the 90%, 95%, and 99% level, respectively.

To summarize, the 1-year and winter models showed similar results, with the overall effect of elevation on surface elevation change being negative at all DFC values, but the overall effect of DFC being positive below a certain elevation threshold, and negative above this threshold (excluding the 1-year borrow pit model in which this value was negative at all elevations). Alternatively, the overall effect of DFC on surface elevation change was positive in both growing season models. The overall effect of elevation on surface elevation change was consistently negative in the borrow pit growing season model, but was positive above a certain DFC threshold in the site area model. Adjusted R^2 values were higher in borrow pit models than in full site models, but in both the borrow pit and site area, adjusted R^2 values were highest in the 1-year models and lowest in the growing season models. Generally, in all models, elevation was a stronger predictor of surface elevation change than DFC.

Chapter 5: Discussion

5.1 Drainage Networks

An objective of this research was to determine the characteristics of the developing channel networks within the Converse restoration site and how they changed throughout the study period. Additionally, this research sought to establish how the antecedent landscape history influenced channel evolution patterns. Results of the channel delineation showed a strong seasonal trend in channel density, with fall datasets having lower densities than growing season datasets, a trend not otherwise present in the literature. Comparison of the delineations from multiple collection dates and persistence analyses indicated an early initialization of drainage networks and general stability of these networks throughout the study period. The developing channel network has incorporated relic agricultural features where present, but also some relic natural features, and embryonic channels have developed where the effects of the antecedent landscape history were not present. Further research should be conducted to determine whether these three channel types are evolving differently within the site.

5.1.1 Seasonality of Network Characteristics

The drainage network characteristics highlighted a seasonal pattern in channel evolution. Rather than increase over the duration of the study period as expected, drainage network density peaked in the spring and summer months and was lower in fall in both Full Site and Target Area datasets (Figure 4.5). It is hypothesized that over the winter, channel networks in some areas underwent higher rates of erosion within the channels themselves, while the marsh platform/tidal flats experienced higher rates of deposition, increasing the depth of channels. Water flow pathways that had a depth <2 cm during the fall months, may have developed over the winter to have depths >2 cm, changing their classification from proto channels (fall) to existent channels

(spring), and increasing total existent channel length and therefore Hortonian drainage density. Channel infilling in smaller channels may have occurred over the summer months, causing channel depth to reduce over time and be lowest in fall. An example of a channel that was classified as existent in 2020 and 2021 spring datasets but proto in the 2020 fall dataset is shown in Figure 5.1. This trend can also be visualized in the winter and growing season DoD rasters, and an example of this is shown in Figure 5.2. In this example, two channels that have branched from the main drainage ditch are characterized by erosion in the winter DoD and infilling in the growing season DoD. This trend was not present within all channels however, especially the main drainage ditch, which had infilling over all time periods in areas closer to the borrow pit, and high levels of erosion over all time periods closer to the main channel mouth (see Figures 4.8 to 4.17).

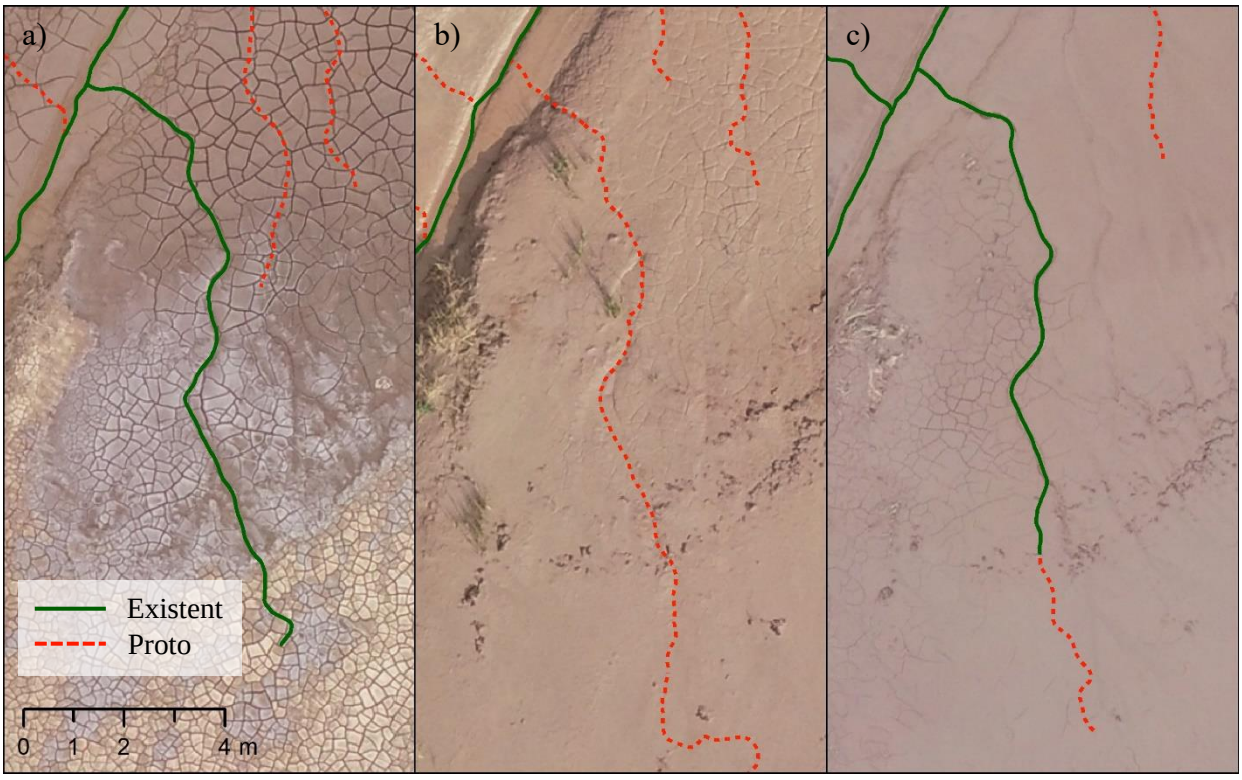

Figure 5.1. Channel classification results for a single channel in a) June 1, 2020 (spring) oblique dataset, b) October5, 2020 (fall) oblique dataset and c) May 4, 2021 (spring) oblique dataset.

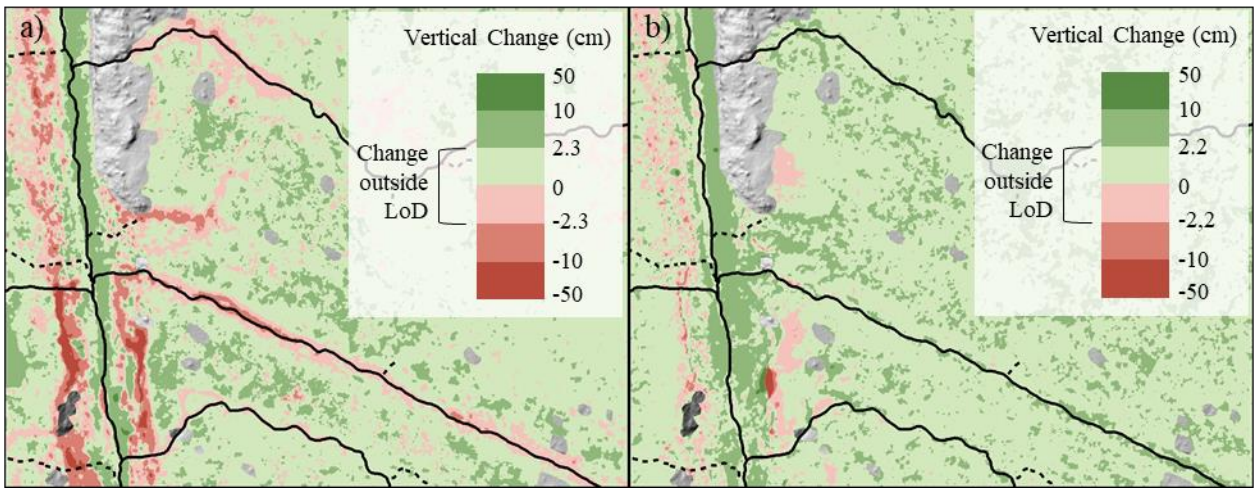

Figure 5.2. a) Winter (November 24, 2019 – June 1, 2020) Target Area DoD showing erosion along existent channels delineated using the June 1, 2020 dataset and b) growing season (June 1, 2020 – October 5, 2020) Target Area DoD showing a lack of erosion along the same channels.

The difference between densities in the fall and the growing season were of a higher magnitude in Target Area datasets than full site datasets (Figure 4.5). This difference is most likely due to the nature of delineated channels in each dataset. During Target Area delineation, a smaller flow accumulation threshold resulted in a delineation with many more smaller water flow pathways (proto channels) and embryonic channels. Since Full Site datasets were processed with a higher flow accumulation threshold, fewer channels, but larger and with more drainage area were delineated. These channels generally had depths greater than 2 cm all year round, and therefore there was less variability in classification results between collection dates.

5.1.2 Early Initialization and Stability

Results of the channel analyses indicate that the site's drainage network was relatively stable throughout the study period, and that the ultimate channel network patterns imprinted within the first year of tidal flow. This result was supported by a qualitative analysis of channel delineations showing general agreement in channel locations, as well as the persistence analysis

(Tables 4.3 and 4.4) which determined that the majority of channels that persisted from their collection date to the subsequent collection date then persisted to all remaining collection dates.

Since the study period for this research began almost one year after the initial introduction of tidal waters to the study site, measurements of channel initialization in the first year of restoration cannot be conducted. However, RPAS data collected during the 2019 field season as part of the site monitoring project and other research activities provided an additional insight into channel evolution. Figure 5.3 shows the borrow pit at three dates prior to the study period, overlaid with the November 24, 2019 channel delineation. There is general alignment between channels present just a few months after the site breach and the delineation, demonstrating that embryonic channels in areas unaffected by relic landscape features established rapidly. This finding agrees with modelling results of D'alpaos et al. (2005) as well as empirical study results by Dale et al. (2018), in which channel networks had begun establishing within an MR site in the UK within 1 year of site breach. However, Dale et al. (2018) determined that channel network initiation was linked to sub surface piping features, a relationship that has not been established at the Converse restoration site.

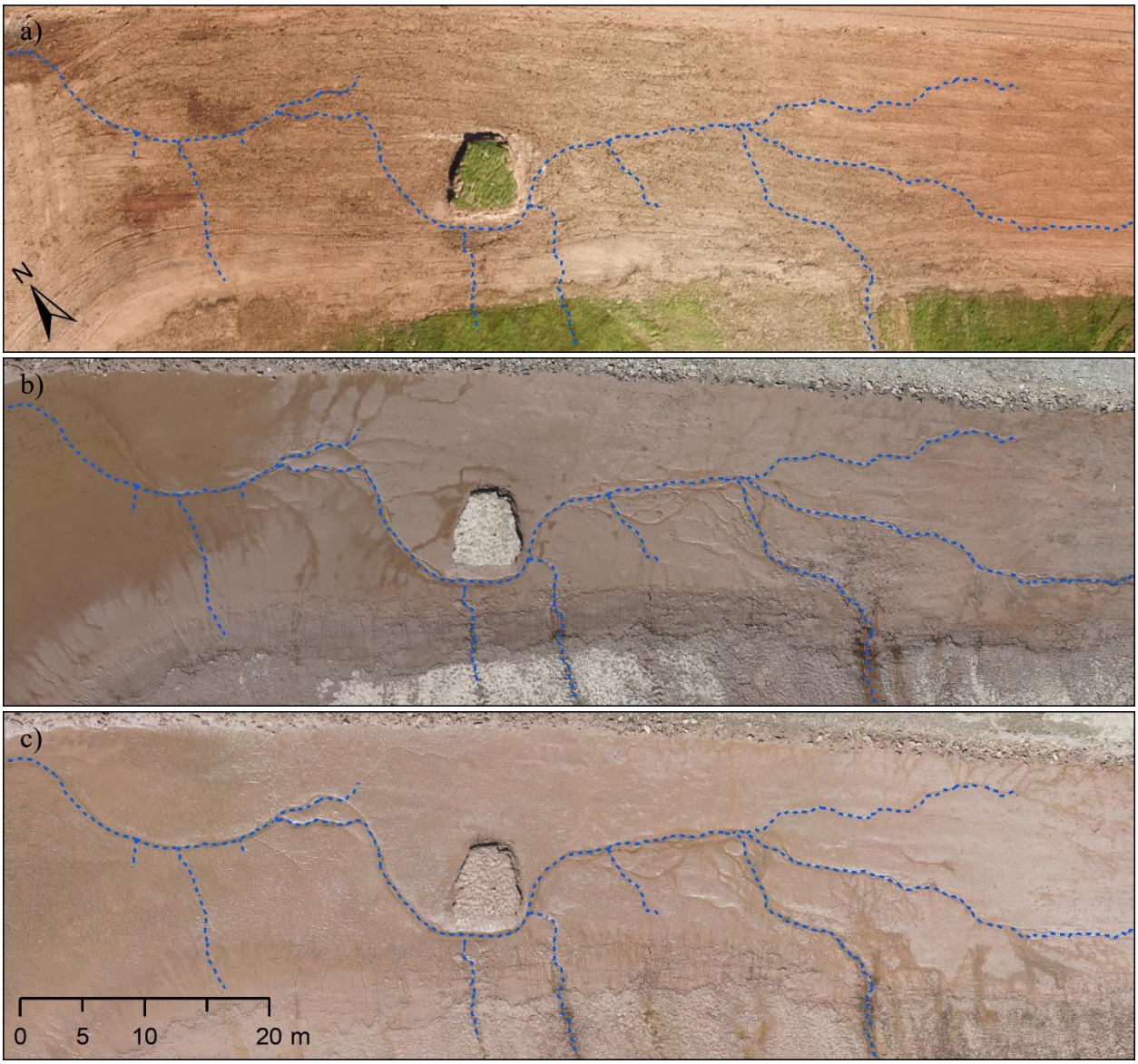

Figure 5.3. November 24, 2019 Target Area channel delineation (dashed blue line) overlaid on supplementary RPAS orthomosaics collected in a) September 2018, prior to the introduction of tidal flow to the site, b) May 2019, 4.5 months after the introduction of tidal flow, and c) August 2019, 8 months after the introduction of tidal flow.

In areas with remnant agricultural ditching, throughout all time periods the channel networks were generally restricted to these ditches and their positions maintained. Differences between collection dates arose from whether or not a ditch was part of the drainage network at that specific time, and in the areas where the drainage ditches connected to the main drainage channel (Figure 5.4). Similar to areas without ditch features, channel establishment was rapid,

and the drainage networks were relatively stable throughout the study period despite some changes over time as referenced. However, one significant area of change between collection dates occurred in the western portion of the site at the pond. Imagery of this area shows that the pond itself drains from multiple locations (Figure 5.5), but since the delineation method used in this study did not allow for multiple flow directions, only one main drainage path was delineated in each dataset. The delineated channel network in each dataset shifted between the north and south drainage path depending on the collection date, with drainage along the south path in the November 8, 2020 and July 9, 2020 datasets, and drainage along the north path in all other datasets. After closer examination of the orthomosaics for all collection dates, it appeared that both drainage paths were functioning throughout the study period, and it is unclear whether this shift in the delineations represents an actual shift in the majority of water flow.

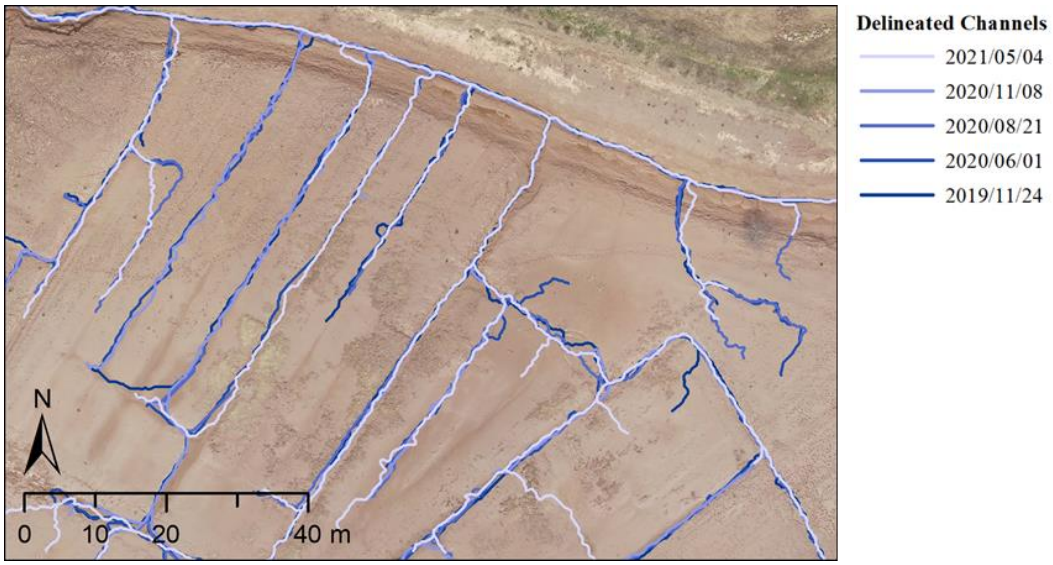

Figure 5.4. Multitemporal channel delineation results (Full Site datasets) in areas of the Converse restoration site with relic agricultural ditches overlaid on the May 4, 2021 orthomosaic.

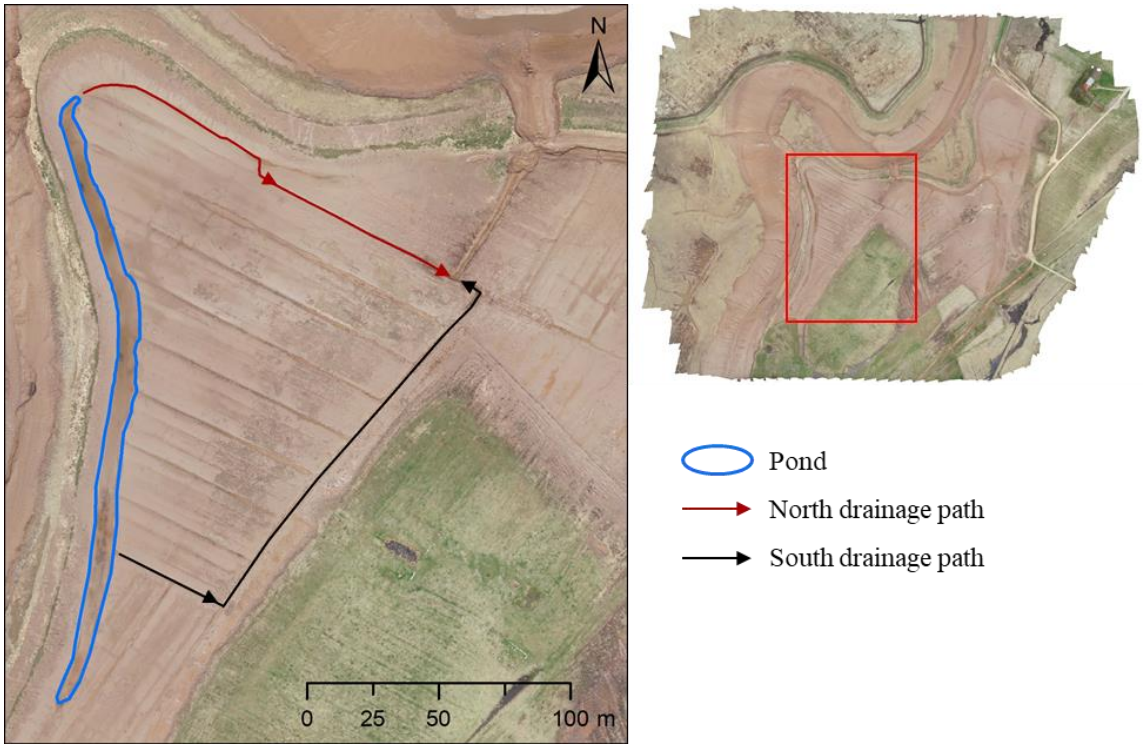

Figure 5.5. Illustration of multiple drainage paths for the pond in the Converse restoration site.

Although the channel networks were generally stable throughout the study period, in areas without relic landscape influence such as the borrow pit, there was a noticeable shift in some channel locations between November 24, 2019 and the remaining collection dates. This shift can be visualized in Figure 5.6, and may indicate that the drainage networks in these areas were still initializing in November 2019. This finding is confirmed in the persistence analysis (Tables 4.3 and 4.4) as the smallest length of channels persisted between November24, 2019 and June 1, 2020 compared to all other time periods.

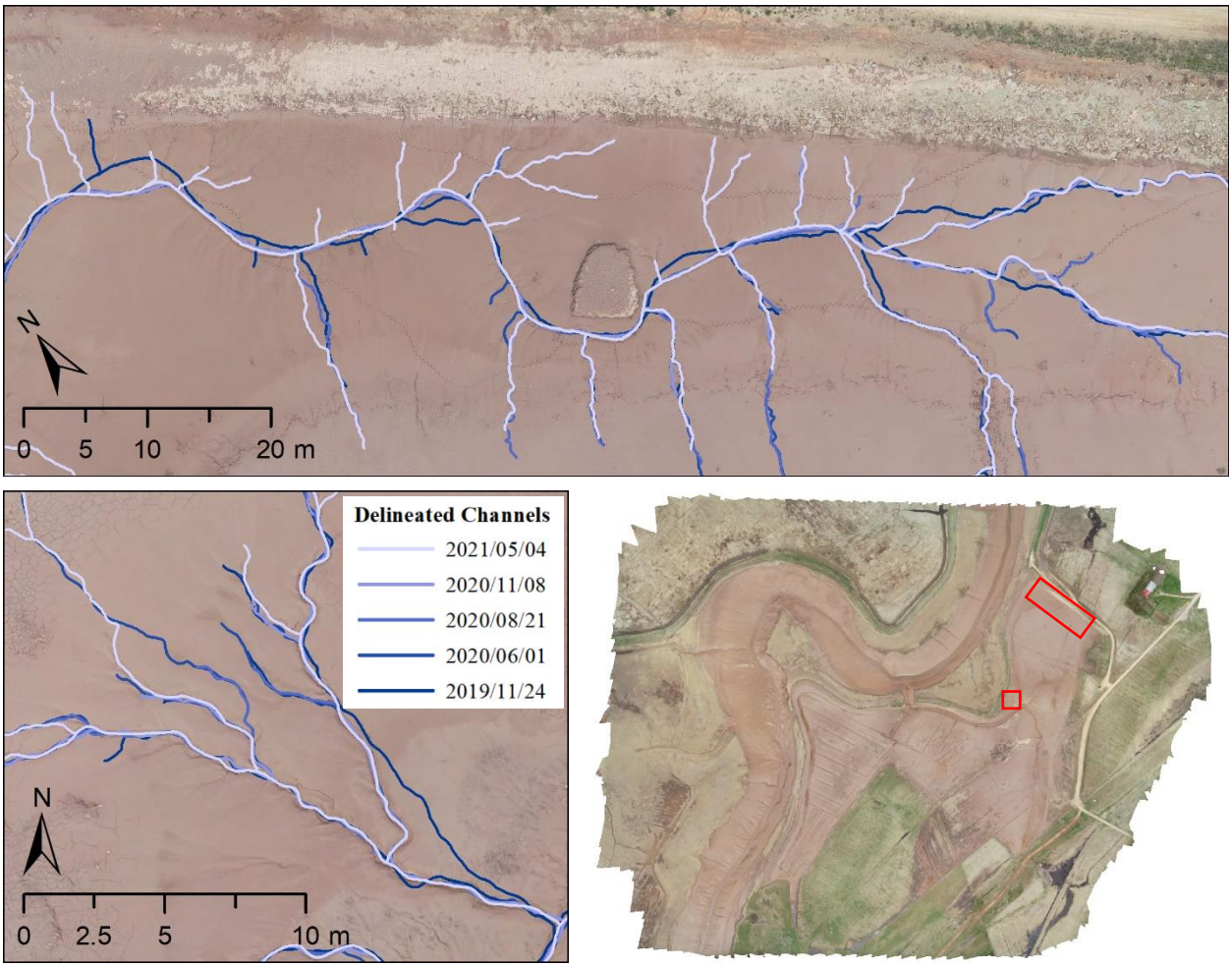

Figure 5.6. Multitemporal channel delineation results (Target Area datasets) in areas of the Converse restoration site without relic agricultural features overlaid on the May 4, 2021 orthomosaic.

In comparing rates of persistence between existent and proto classified channel segments (Figures 4.6 and 4.7), results show that existent channels were more likely to persist to either classification than proto channels, and that the majority of existent channel segments maintained their existent classification. This was expected because proto channels by definition had depths less than 2 cm along the majority of their length and should have been more likely to shift or be affected by sedimentation patterns and surface disturbances such as footprints. However, since proto channels were delineated following routes of steepest elevational gradient, it was expected that these pathways would erode into measurable channels over time, as elevational gradient and

shear stress have been modelled to be the driving factor of channel incision in early tidal network development (D'alpaos et al., 2005). In this study, the average percentage of proto channel segments in all delineations that evolved to existent channel segments in the May 4, 2021 dataset was only 6.46%. This may indicate the importance of factors other than elevational gradient in early channel incision and development, or that the elevation models used in this study for channel delineation had errors that resulted in the misidentification of steepest elevational gradients in areas without existing channel incision.

5.1.3 Effect of the Antecedent Landscape

Delineated channels within the study site (Appendix G) can be divided into three categories: channels developing within relic agricultural/anthropogenic features, channels developing within relic natural features, and embryonic channels developing without the influence of landscape history (Figure 5.7). Each of these channel types were present in both Full Site and Target Area delineations and were maintained between collection dates. In all datasets, relic agricultural ditch features have been incorporated into the site's drainage network, representing the first channel type as previously outlined. These channels are characterized by straight lines and right angles, characteristics that would not normally be present in natural salt marsh channel networks (MacDonald et al., 2010). The incorporation of these features into the site's drainage network agrees with findings from other researchers (French and Stoddart, 1992; MacDonald et al., 2010; Bowron et al., 2011; Lawrence et al., 2018), and if the site follows a similar trajectory as those studied by Macdonald et al. (2010) which are also located in the Bay of Fundy, they may be maintained for another 50 years at least.

However, in one area of the site directly south of the borrow pit, existent channel delineations from the November 24, 2019 and May 4, 2021 Target Area datasets show a slight

reduction in drainage network use of relic agricultural ditching in an area with relic natural drainage features (Figure 5.8), which may indicate a preference in channel characteristics of the site's drainage network, and an infilling of some agricultural ditches. The relic natural drainage features in this area appear to be relic salt marsh channels from before the historic salt marsh landscape was drained and dyked. These channels, along with another main channel branch ~100 m south of this area (see Figure 5.7) are present in all channel delineations.

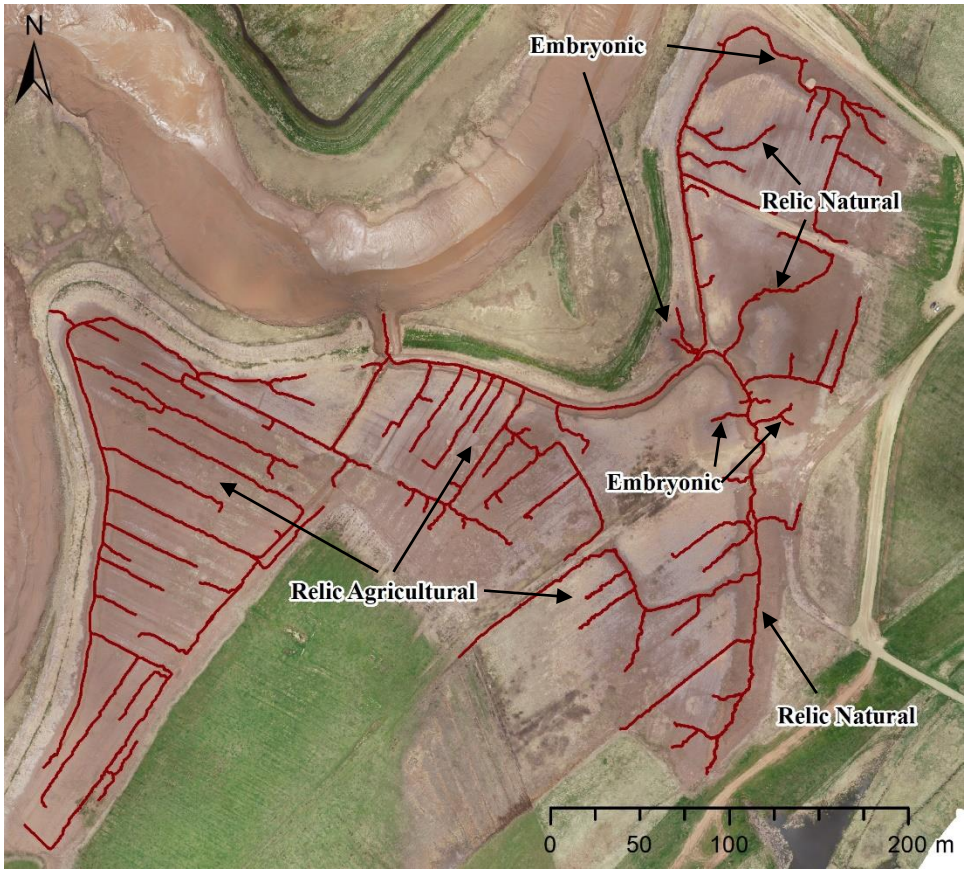

Figure 5.7. June 1, 2020 Full Site existent channel delineation and orthomosaic, labelled with the three distinct channel types present within the site.

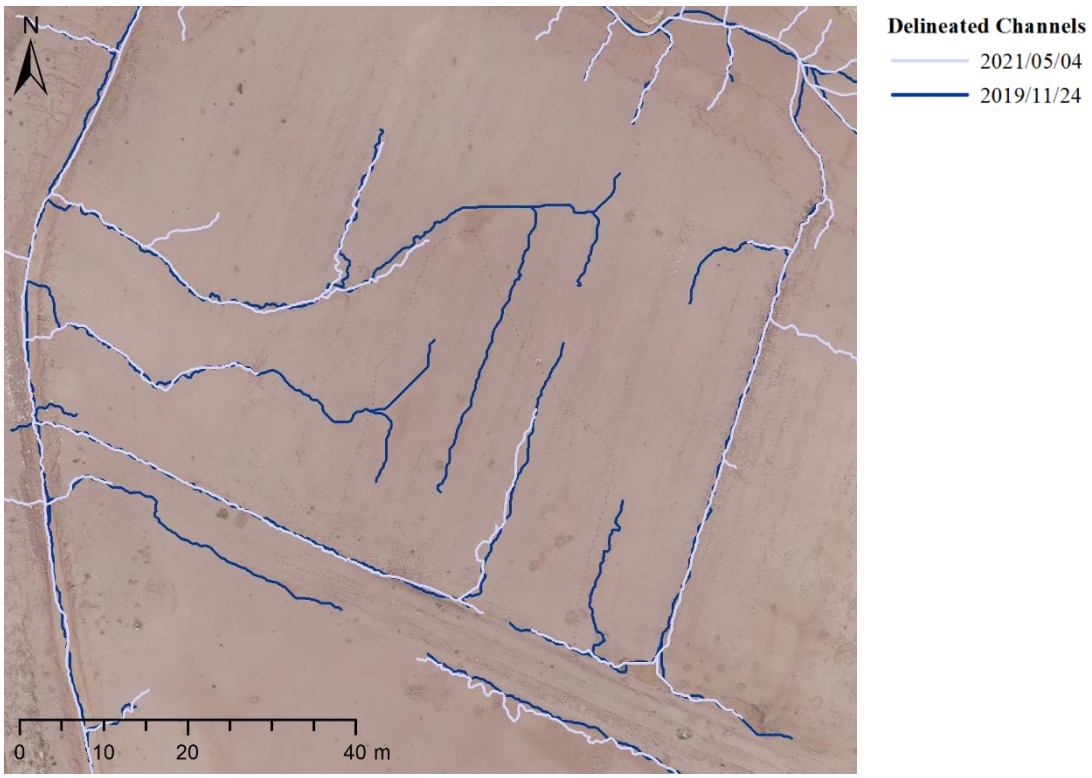

Figure 5.8. November24, 2019 and May 4, 2021 existent channel delineations (Target Area datasets) and May 4, 2021 orthomosaic, highlighting a reduction of drainage network usage of relic agricultural ditching.

The third category of channel within the study site is embryonic channels that have developed in areas without the influence of the landscape history. Specifically, they have mainly developed in three areas of the site as shown in Figure 5.7. These areas, including the borrow pit, were characterized by relatively low elevations at the start of the study period compared to the rest of the site. This agrees with the finding by Vandenbruwaene et al. (2012b), that channel development in a constructed tidal marsh was preferential to areas of lower elevation. RPAS imagery collected prior to site breach (Appendix J, Figure J-3) shows these areas did not have remnant agricultural ditching (originally present in the borrow pit area but removed during excavation), and therefore may have mimicked natural tidal flats in terms of embryonic channel development. The borrow pit may be an example of a methodology for reducing the influence of relic anthropogenic features on drainage network evolution in MR sites, showing that the

removal of the upper layer of agricultural vegetation and sediment in areas with ditch features may encourage a more natural channel network establishment.

5.2 Spatial and Temporal Patterns of Surface Elevation and Volumetric Change

Another of the main research objectives of this thesis was to determine the spatial and temporal patterns of surface elevation and volumetric change within the Converse restoration site. Results showed significant variation in surface elevation and volumetric change between areas of interest (site, borrow pit, main channel mouth), as well as strong seasonal trends. At the site level, the presence of agricultural vegetation beneath a thin layer of sediment may have significantly affected surface elevation change values, resulting in measured sediment loss instead of sediment deposition as expected. In the borrow pit, where agricultural vegetation was not present, surface elevation change was generally net positive, showing an influx of sediment throughout the year, with the highest measured volumetric change occurring over the winter which coincides with expected peak levels of suspended sediment concentrations (Poirier et al., 2017). Sedimentation rates in the borrow pit were comparable to other sites in the Bay of Fundy (Matheson, 2020; Virgin et al., 2020). The main channel mouth was characterized by net erosion (surface elevation decrease) throughout the year, with the highest magnitude of change occurring over the winter. Sediment influx to the borrow pit was higher than sediment loss in the channel mouth over all time periods, indicating that sediment is entering the site from other areas of the system.

5.2.1 Seasonality of Surface Elevation and Volumetric Change

Sedimentation patterns and volumetric change at the Converse restoration site had a strong seasonal signal over the course of the study period, although the trends were not consistent between areas of interest. At the site level, in both Full Site and Target Area datasets, there was a

net loss of surface elevation over the winter, and a net gain over the growing season. This result was unexpected, as increased suspended sediment concentrations in the Bay of Fundy in the winter (Poirier et al., 2017) were expected in increase sediment deposition rates (Friedrichs and Perry, 2001) and surface elevation change. In the borrow pit, all DoD time periods resulted in a net gain of surface elevation, with the highest gain occurring over the winter as expected.

The discrepancy between the site area and borrow pit may be due to variations in surface characteristics. Surfaces in some areas of the site in November 2019 were characterized by remnant agricultural vegetation (grasses) that were covered by a thin layer of sediment. The sediment was not heavy enough to fully compact the vegetation layer, so there were many pockets of air between the actual ground surface and sediments that had been deposited since site breach approximately one year prior. This created false surfaces in some areas of the DSM that were not accounted for in processing. Over the course of the 2019 winter, additional deposited sediment increased compaction forces on the vegetated layer, and air pockets were reduced, which lowered the elevation of the sediment surface as measured in June 2020. In the resulting winter DoD, these areas were characterized by surface elevation loss, but that loss may have been a result of compaction rather than sediment erosion, and those areas may have had significant amounts of sediment deposition. In the borrow pit, where agricultural vegetation had been removed during excavation, deposited sediments caused surface elevation to increase, resulting in the net volumetric gain as calculated for all time periods.

Although the spring-summer and summer-fall Target Area datasets were excluded from further examination due to clear offsets between surfaces, the Full Site DoDs for these time periods did not appear to suffer from the same issues and therefore were investigated. These DoDs and volumetric change results show significant variation in sedimentation patterns

throughout the growing season. While the spring-summer DoD was characterized by a mix of surface elevation loss and gain, with a small net gain, the summer-fall DoD was almost entirely characterized by surface elevation gain, and the rate of volumetric change was approximately 6 times greater than the spring-summer dataset (Figure 4.18). This significant variation may be due to the tidal regime during the growing season (Figure 2.5). Between the August and October surveys, there were a higher number of high tides that exceeded 6.0 m CGVD2013 compared to the June-August time period, meaning that there was more flooding of the site at greater depths and longer inundation times. An increase in these factors have been shown to increase sediment deposition in natural salt marsh systems (French and Spencer, 1993; Leonard, 1997), and this relationship may also be occurring at the Converse restoration site.

5.2.2 Effect of the Antecedent Landscape

The effect of the antecedent agricultural landscape history is clearly displayed when comparing the seasonal patterns of sedimentation in the site area and borrow pit. A large portion of the site was characterized by relic agricultural vegetation that may have significantly altered surface elevation change and volumetric change calculations as earlier described. The borrow pit, which had agricultural vegetation and upper soil layer removed, displayed the opposite sedimentation pattern to the rest of the site, with higher rates of sedimentation occurring over the winter. However, the effect of agricultural vegetation may have only been to mask the actual sedimentation rates occurring on the site, and it is unclear if calculated sedimentation rates would have been more similar between the site and borrow pit if the agricultural vegetation had been removed prior to site breach. Previous work has shown that borrow pit infill rates may be higher than those measured in natural salt marshes or on restoration site marsh platforms (Matheson, 2020), a trend that is supported when comparing the borrow pit and remaining site area

sedimentation rates at the Converse restoration site, although the potential skewing of results by remnant agricultural vegetation compaction must be considered when making these comparisons.

5.2.3 Rate of Sedimentation

Since sedimentation rates throughout the site area were affected by the presence of agricultural vegetation, and the actual amount of sediment accretion can not be directly measured, sedimentation rates in the borrow pit will be used in comparison to other studies. The average vertical rate of change over the 1-year period (second year of restoration) in the borrow pit was 5.0 ± 2.5 cm with no LoD, and 6.4 ± 2.5 cm with an LoD (68% CI). These results were comparable to sediment deposition values collected at the Aulac MR site just north of Converse in the second year of restoration (Virgin et al., 2020), as well as sediment accretion values for the same time period measured at the Converse restoration site using marker horizons (Bowron et al., 2021). Previous work has identified sediment accretion rates in other borrow pits in the Bay of Fundy to vary significantly, ranging from -0.54 $m \cdot y^{-1}$ to 0.18 $m \cdot y^{-1}$ (Matheson, 2020), with results from this study falling within that range.

Comparing the volumetric rate of sediment loss in the main channel mouth (Figure 4.21) to the volumetric rate of sediment gain in the borrow pit (Figure 4.20) over the 1-year, winter and growing season periods shows that there is consistently a larger influx of sediment to the borrow pit alone than is lost from the main channel mouth. This indicates that sediment being deposited in the site is coming from elsewhere in the system as well as areas of erosion within the site, and that erosion of the main channel mouth is not the sole source of sediment for site evolution.

5.3 Correlation Between Surface Elevation Change and Elevation, Proximity to Drainage Network

Multiple linear regression models were calculated to determine the correlation of surface elevation change to elevation and DFC, and to help examine the spatial patterns of sedimentation at the Converse restoration site. Adjusted R^2 values were highest in the 1-year dataset models and lowest in the growing season dataset models, and all borrow pit models had higher adjusted R^2 values than the corresponding site area model for the same time period. Relationships between elevation and DFC may have been more easily identified in the borrow pit due to the generally higher rates of surface elevation change (higher ratio of data above LoD thresholds) than in the site area datasets, as well as a lack of skewed surface elevation change values caused by compaction of agricultural vegetation as seen in other areas of the site.

Results of the models generally agreed that elevation was a much stronger predictor of surface elevation change than DFC. In all models, the elevation coefficient was significant and negative, meaning that as elevation decreased, surface elevation change increased. By incorporating the interaction effect to determine the overall effect of elevation on surface elevation change at varying DFC values, it was determined that the negative coefficient was maintained at all DFC values in all but one model (growing season, site area). Since water depth and inundation time are a function of elevation, this relationship was expected, as it has been shown that an increase in inundation time (increase in depth, decrease in elevation) will increase sediment deposition (Leonard, 1997). However, previous research in the Bay of Fundy and U.S. Mid-Atlantic Coast found no correlation between inundation time (van Proosdij et al., 2006b) or marsh elevation (Boyd et al., 2017) and sediment deposition/accretion.

In both the borrow pit and remaining site area models, the magnitude of the overall effect of elevation on surface elevation change was greater over the winter than the growing season,

indicating seasonality in this relationship. Additionally, aside from in the growing season site area model, higher DFC values resulted in a greater magnitude of the effect of elevation on surface elevation change, indicating that there was a compounding effect of elevation and DFC. At greater distances from channels, a higher surface elevation resulted in less surface elevation change than occurred closer to channels. However, the changing magnitude of this effect depending on DFC was variable between areas. In all borrow pit models, the overall effect of elevation on surface elevation change was only fractionally increased by all DFC values. Alternatively, in the site area 1-year and winter models, the overall effect of elevation on surface elevation change was more than doubled at 5.5 m and 2.9 m from channel respectively. This may indicate that the controls of sediment accretion and erosion differ between the borrow pit and the rest of the study site.

The DFC coefficient was also significant in most of the linear regression models, but of a very small magnitude and positive (Tables 4.8-4.13). However, in the 1-year site area model and both winter models, incorporation of the interaction effect (which had a negative value) changed the sign of the overall effect of DFC to be negative at elevations above a threshold value. It was expected that the effect of DFC on surface elevation change be negative in all scenarios, with higher surface elevation change closer to channel thalwegs, as found by Poirier et al. (2017) at a natural salt marsh in the Bay of Fundy. Results from this research indicate that at lower elevations this relationship is reversed, with lower surface elevation change values closer to channels, which may represent erosion occurring within and around the channels themselves. This trend can be visualized in some of the DoD results (Figure 5.9). The discrepancy in findings between this study and that of Poirier et al. (2017) may be due to channel maturity in both studies. The channel examined by Poirier et al. (2017) was mature, and more than 6 m deep from

channel thalweg to edge, while channels examined within this research included embryonic channels with depths as little as 2 cm. Since the channel network at the Converse restoration site is very early in its establishment and development, erosion along and near the channel thalweg may be more pronounced than in mature channels in a natural salt marsh setting. Additionally, the overall effect of elevation on surface elevation change being greater in magnitude than that of DFC, may indicate that in the early stages of marsh development (such as an early MR restoration site), channels play a less significant role in sediment deposition patterns. This appears to be the case in the borrow pit specifically, since the overall effect of DFC on surface elevation change was relatively low in magnitude, and DFC did not greatly alter the magnitude of the overall effect of elevation.

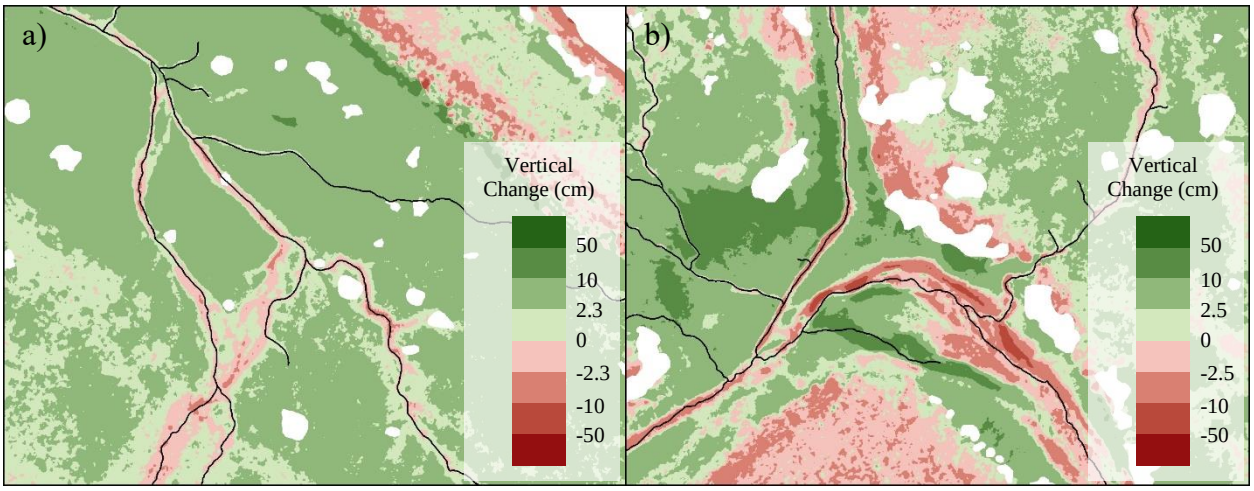

Figure 5.9. a) November 24, 2019 – June 1, 2020 (winter) DoD results within the borrow pit and b) November 24, 2019 – October 5, 2020 (1-year) DoD results at a channel confluence with the June 1, 2020 channel delineation highlighting erosion patterns close to channel thalwegs in areas of low elevation within the Converse restoration site.

Both the borrow pit and site area growing season datasets acted as outliers in the multiple regression results. Most noticeable was the reduced significance of some of the independent variable coefficients, specifically the interaction effects in both models and the DFC coefficient in the site area model. It appears that a reliable relationship between these variables and surface

elevation could not be found to the same level of significance as in the other models. Another non-conforming result was the over all positive effect of DFC on surface elevation change at all elevations within the borrow pit, which directly contradicted the overall negative effect of elevation on surface elevation change, since the relationship between elevation and DFC in this dataset was positive (distance from channel increased as elevation increased). Also, in the site area dataset, the overall effect of elevation on surface elevation change was only negative when DFC was less than 23.537 m, a result not seen in any other models. These findings may indicate that over the growing season, when sediment accretion is expected to be less than over winter or a 1-year period (as was the case in the borrow pit), sediment erosion within and close to channels plays a more significant role in sedimentation patterns than sediment deposition and its usual controls such as elevation (inundation time, depth) or DFC (distance from sediment source) within an early restoration context.

5.4 Applicability of RTK RPAS in Restoration Site Monitoring

This research sought to investigate the applicability of RPAS and SfM technologies and methodologies for delineating salt marsh drainage networks and measuring surface elevation and volumetric change, including the integration of RTK capabilities for improved product accuracy. Results confirmed an increase in elevation model accuracy in this study compared to previous research utilizing aircraft without RTK functionality, and that achieved accuracies may be more dependent on georeferencing data quality than GSD or camera angle when utilizing RTK-enabled aircraft. Produced elevation models allowed for a generally accurate channel delineation, although the presence of vegetation caused some issues. Elevation model $RMSE_z$ values were generally low, and resulted in low LoD values when calculating DoDs, and it was possible to measure changes as small as 2.2 cm with a 68% confidence interval. However, offsets between

some surfaces in one area of the site were not accounted for in LoD calculations, resulting in erroneous DoD values being considered “significant”. Also, volumetric uncertainty values at the site level were very high, indicating that volumetric change values for these datasets were unreliable. It appears that it is more appropriate to conduct DoD and volumetric change analyses in smaller, targeted areas with generally higher levels of expected change (eg. borrow pit and main channel mouth) to achieve reliable volumetric change estimates.

5.4.1 Improved Accuracy with RTK Capabilities

It is expected that with georeferenced SfM elevation models, the absolute vertical accuracy of the model should fall within the accuracy of data used for georeferencing (GCPs and/or camera positioning) but cannot be higher than relative accuracy, which is 1-2x GSD in x and y and 1-3x GSD in z (Matheson, 2020; Pix4D, 2021). In this study, both GCP positions and survey-grade positioning of the aircraft through RTK corrections were used in georeferencing, and therefore the vertical errors of the elevation models should fall within the range in errors of these data. The accuracy of GCP positions for all deployments as measured with a dGNSS system ranged from 0.004-0.007 m (horizontal) and 0.006-0.013 m (vertical). In camera positions for all collected photos, accuracies ranged from 0.011-0.022 m (horizontal) and 0.023-0.039 m (vertical). Since $RMSE_z$ values for all surveys ranged between 1.3-2.3 cm (Table 4.1), it is clear that elevation model errors fall within the range between GCP accuracies and camera position accuracies. However, $RMSE_z$ values are smaller than 1x GSD in all Full Site datasets and are equal to or less than 1x GSD in all but one Target Area dataset (May 4, 2021).

$RMSE_z$ values achieved in this study are comparable to those from other RPAS/SfM studies in the literature with similar spatial resolutions, although they are generally lower. In tidal environments specifically, other researchers have achieved $RMSE_z$ values in datasets with

resolutions between 1.83 and 4 cm ranging from 0.032 m (Dale et al., 2018), 4.1-15.6 cm (Matheson, 2020), 3.1-6 cm (Brunette et al., 2021), and 0.015 m (Taddia et al., 2021). These studies, however, utilized RPAS that are not equipped with survey-grade positioning, and therefore relied solely on GCP deployment to georeference their datasets. In the majority of these studies, $RMSE_z$ values less than GSD were not achieved, which supports the hypothesis that the addition of survey-grade positioning (through RTK capabilities) to the aircraft during the survey allowed for higher accuracies in SfM products. Although RPAS with PPK/RTK capabilities are less common, one comparable study was conducted by Taddia et al. (2018) which used a DJI Phantom 4 RTK RPAS to compare accuracies of datasets with various GCP layouts in conjunction with survey-grade positioning of the aircraft. The $RMSE_z$ value of their 2 cm resolution elevation model when using a well distributed GCP network and a nadir camera angle was 0.020 m, comparable to $RMSE_z$ values produced in this study.

Taddia et al. (2018) also indicated that product accuracies were higher when an oblique camera angle was used for image collection. However, in this thesis, results of a Mann Whitney U test (alpha value of 0.05) comparing the Full Site and Target Area $RMSE_z$ values determined that the two sets of values were not significantly different. Hence, flying at a lower altitude, and with an oblique angle as conducted for Target Area surveys, did not significantly increase DSM accuracies as expected. This finding agrees with a study by Brunetta et al. (2021), in which a reduction in flight altitude and increase in GSD of a series of RPAS surveys did not significantly increase accuracy in SfM elevation products. It may be the case that elevation model accuracy is entirely a function of georeferencing data accuracies and is not significantly affected by GSD or camera angle. Since the validation data in this study was only collected on relatively flat, bare

ground surfaces, it is not clear whether the oblique camera angle used in Target Area surveys increased the accuracy of vertical surfaces in the elevation models.

It is known that the presence of vegetation in DSMs significantly reduces accuracy of surface measurement (Carrivick et al., 2016; Taddia et al., 2021; Vecchi et al., 2021), and it must be noted that the $RMSE_z$ values of surface models in this study were achieved in part because vegetated areas were not included in the validation process or DoD analyses. While removing vegetation from further processing helped to increase data accuracy and reliability, it did not allow for the measurement of surface elevation change related to vegetation presence, and significantly increased manual processing time.

5.4.2 Drainage Network Delineation

The hydrological toolset in ESRI's ArcMap is based off hydrological analyses and processes that were designed for traditional surface models such as lidar, generally with low spatial resolution. Incorporating RPAS data of salt marsh environments into this workflow presented some challenges, including the presence of vegetation and surface depressions. Utilizing a DSM that includes vegetation rather than a DEM with only ground surface elevations results in routing of water flow pathways around vegetated features. While naturally vegetation does provide some resistance to water flow (Christiansen et al., 2000; Coulombier et al., 2012), water can flow through vegetated areas and does so in many areas of the Converse restoration site.

Additionally, in areas where vegetation was growing within a channel, its elevation values cause a "dam" effect during the Fill step of the delineation process (Figure 5.10). The channel upstream of the vegetation is considered a depression, and the area is filled. Channel delineation along these filled areas will then fall along the edge of the fill, rather than the channel

thalweg, creating discrepancies between channel delineation shapefiles and actual channel centers (Figure 5.10). This issue would not exist if utilizing an elevation model without vegetation features, and therefore is a limitation of SfM-derived surfaces for these processing workflows. The same issue occurs in naturally existing depressions in the restoration site surface. Despite these issues, the delineation process utilized in this research produced relatively accurate channel delineations of very small, embryonic channels. The hyperspatial resolution of input datasets aided in these results, and the semi-automated process significantly reduced delineation time compared to a manual delineation technique.

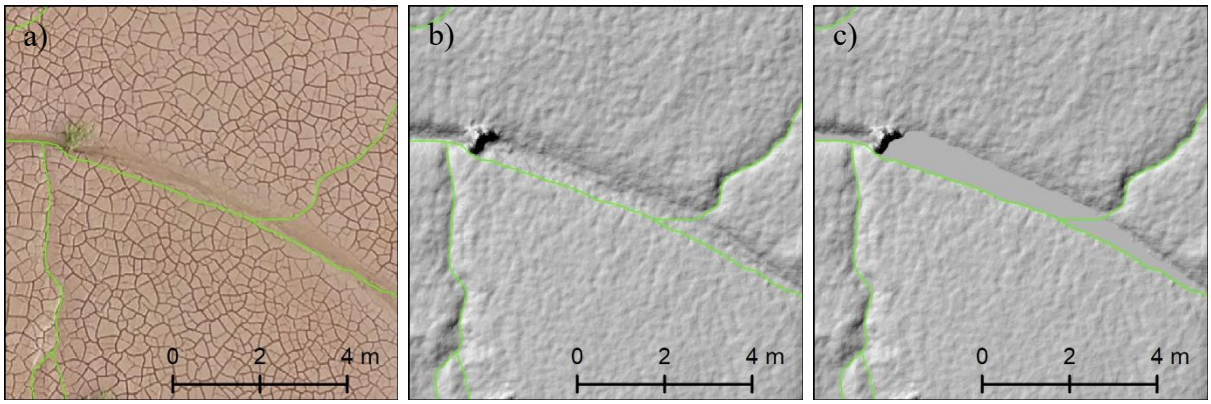

Figure 5.10. Example of channel delineation offset due to vegetation "dams" in the DSM causing filled areas prior to channel delineation. Delineated channel shapefile shown in green compared to a) orthomosaic imagery, b) original DSM, and c) filled DSM from the June 1, 2020 Target Area dataset.

5.4.3 DoD Creation and Volumetric Change Calculations

The $RMSE_z$ values achieved in the collected datasets were relatively low compared to similar studies (Tonkin and Midgley, 2016; Dale et al., 2018; Matheson, 2020), and resulted in comparably low LoD values. It appears that the incorporation of RTK capabilities to RPAS surveys may improve our ability to measure significant surface elevation change at smaller scales than previously achievable, but that the high-level accuracy of data products in this research did not prevent surface offsets to occur and affect some DoD calculations. Furthermore,

RPAS surfaces may not be appropriate for measuring volumetric change at the site level over the time periods examined in this research, as calculated volumetric uncertainty at those scales often exceeded measured volumetric change. It is recommended that future volumetric change calculations in MR sites with similar sedimentation rates be limited to small areas of interest in which expected surface elevation change is significant (eg., majority of cells greater than LoD), such as a borrow pit (area of relatively lower elevation) or channel mouth (area of high erosion) or be conducted over time periods ≥ 1 year. In these circumstances, absolute volumetric uncertainty may be more reasonable compared to total volumetric change, increasing the confidence in change measurements.

The northern section of the spring-summer and summer-fall Target Area DoDs had surface elevation change patterns that did not appear realistic in nature. Examination of the June 1, 2020, August 21, 2020 and October 5, 2020 DSMs (inputs for DoD calculation) determined that in this area there were visible offsets between the surfaces and between two of the surfaces and the validation data (Figure 5.11). Specifically, the June 1, 2020 surface generally matched well with validation data collected throughout the growing season, the August 21, 2020 surface sat a few cm below the validation, and the October 5, 2020 surface sat a few cm above the validation in this area. Since calculated $RMSE_z$ values summarize errors for an entire dataset and are reported as a magnitude of error (no directionality), LoD values calculated for surfaces that have errors in opposite directions from the validation (such as the August and October surfaces) may not accurately determine significant value thresholds. In this example, $RMSE_z$ values for the August and October 2020 datasets were 2.0 cm and 1.7 cm respectively, and the LoD (68% CI) for the calculated DoD between these surfaces was 2.6 cm. This value clearly does not account for differences between the two surfaces that occurred in the northern section of the site of around

~5 cm. This issue was reduced by applying an LoD with a 95% CI but may also be alleviated by utilizing spatially variable error estimates instead of a single value for each surface in future studies (Wheaton et al., 2010; Milan et al., 2011; Cavalli et al., 2017).

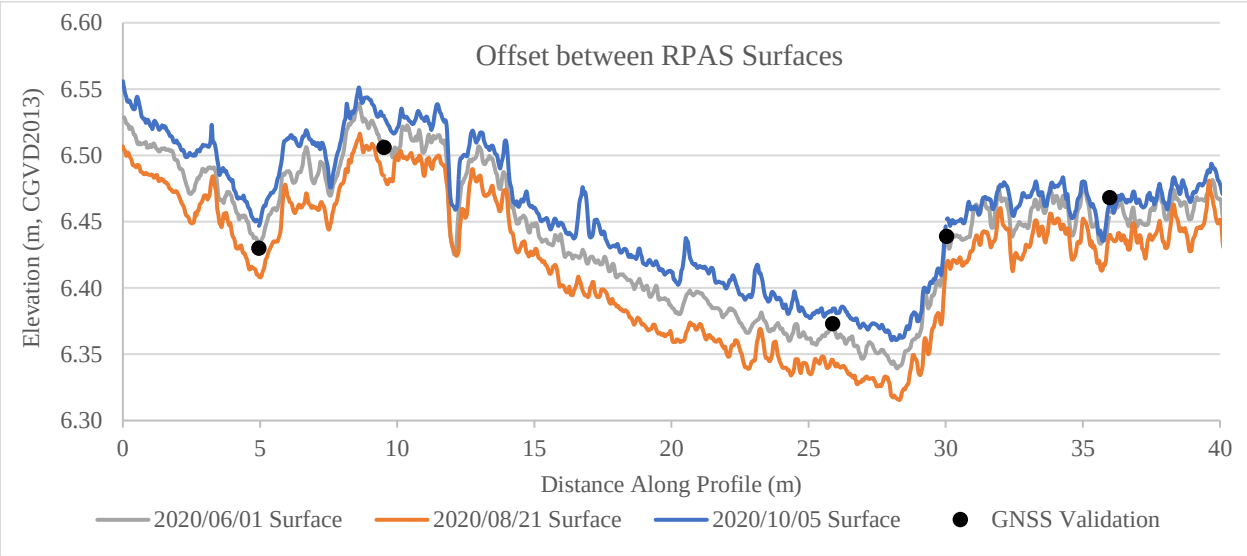

Figure 5.11. Elevation data along cross-section in northern area of the Converse restoration site showing RPAS surface elevations compared to GNSS validation points.

Results of the volumetric change calculations and absolute volumetric error estimations showed that at the site level (in both Full Site and Target Area datasets), total volumetric change was often less than volumetric uncertainty with no LoD and a 68% CI LoD. While this was not the case with the majority of results using the 95% CI LoD, a much smaller percentage of cells were included to calculate total volumetric change (2.4%-14.41% in Full Site datasets and 1.1%-13.1% in Target Area datasets), and surface elevation change over the majority of the site was not significant enough to be measured. Because of this, it appears as though the temporal and spatial scales of the site area DoDs and volumetric change calculations were not appropriate. Alternatively, volumetric change values from areas of interest, such as the borrow pit and main channel mouth were of the majority greater than absolute volumetric uncertainty over the 1-year,

winter and growing season periods, indicating that these techniques may be more appropriate for smaller scale areas where higher rates of change are expected.

An additional concern in conducting DoD analyses to calculate volumetric change is the nature of surface elevation change measurements. Surface elevation change in a salt marsh system is comprised of both above ground and below ground processes. Above ground processes include sediment accretion and erosion, and below ground processes include below ground biomass growth, compaction, and water saturation (Allen, 2000; Paquette et al., 2004). Converting surface elevation change to sediment volumetric change (an above ground process) automatically assumes that below ground processes are negligible. This was not the case, however, at the Converse restoration site, where compaction of agricultural vegetation was identified, and other types of below ground processes may have been occurring.

5.5 Recommendations for Future Research Activities

5.5.1 RPAS Data Collection

Although resolutions and accuracies achieved in this research were relatively high compared to similar studies, there may be adjustments to data collection protocol that could increase the accuracy and reliability of SfM data products. Since DSM vertical accuracy was limited by the accuracy of the data used in georeferencing, and GCP positions had higher vertical accuracies (0.006-0.013 m) than camera positions with an RTK-enabled RPAS (0.023-0.039 m), surface accuracy could potentially be increased by deploying additional GCPs for future surveys. Relying more heavily on a dense GCP network could reduce errors across the DSMs and may limit the issues with surfaces being offset in certain areas and producing erroneous DoD rasters. Although conducting aerial surveys at a lower altitude did not significantly increase surface accuracy, an increase in product resolution may still be beneficial to future research. The high

resolution orthomosaics and surface models produced in this research allowed for detailed mapping of very small embryonic channels and may be used for future research to identify vegetation species, or other tasks that require more detailed imagery.

It is well known that surface homogeneity in imagery causes issues in the tie point matching step of the photogrammetric process (Mancini et al., 2013; Eltner et al., 2016), and salt marsh mud flats are often characterized by a lack of image texture, especially when wet (Jaud et al., 2016). During this research, aerial surveys were conducted during a variety of mud surface conditions, including post significant precipitation and during spring tides when mud surfaces were saturated and lacked texture, and during neap tides after a period of dry weather in which sediments had dried out and cracked. Examination of these datasets showed that aerial surveys conducted while sediments retained cracked features reduced surface homogeneity and significantly reduced instances of erroneous point matching and elevation model noise (Figure 5.12). It is recommended that future surveys be conducted during dry conditions when possible to improve surface reconstruction results and reduce error in SfM products.

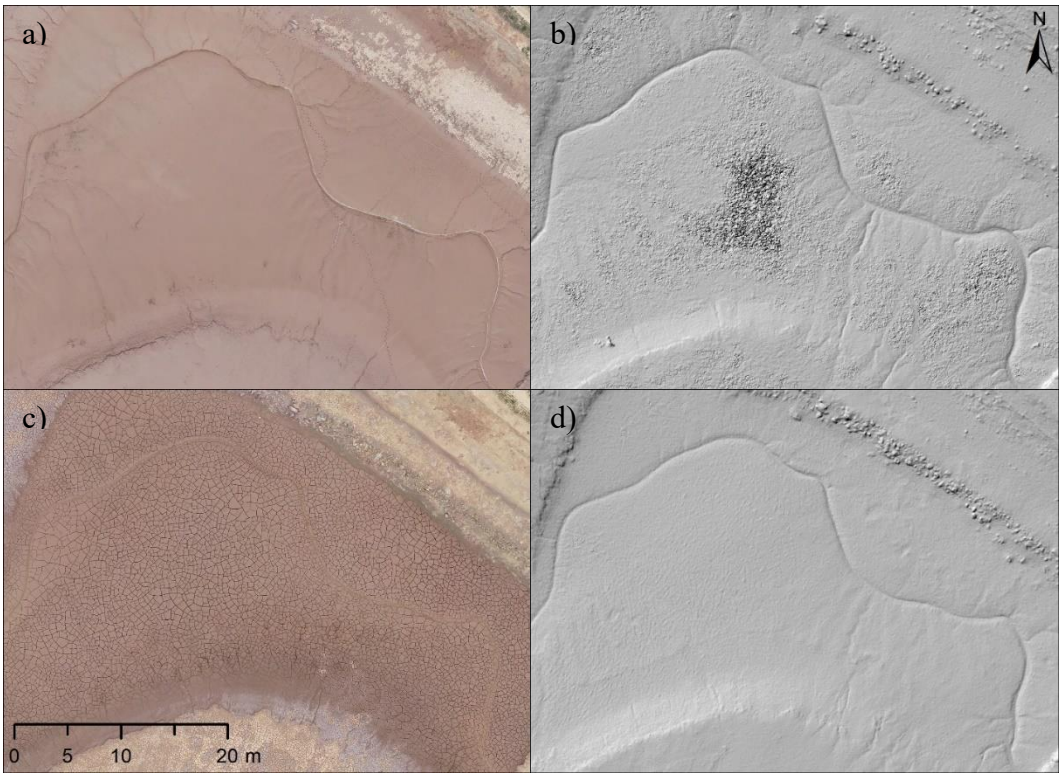

Figure 5.12. May 4, 2021 a) orthomosaic and b) elevation model showing homogenous, wet mud and noisy elevation data resulting from tie point errors in the photogrammetric process compared to June 1, 2020 c) orthomosaic and d) elevation model with cracked mud features.

Continuing these research activities so that a longer study period can be examined would provide further insight into the restoration trajectory. Within this research, the initial fall surface model may not have been an accurate representation of ground elevations due to the presence of agricultural vegetation that created air pockets beneath a thin layer of sediment in some areas of the site. This issue may have affected the validity of volumetric change results for the winter and 1-year periods and speaks to the importance of a reliable initial surface for volumetric analyses. Conducting a similar analysis with new surface models would allow for more accurate representations of surface elevation change, especially for the winter period. Continuing the DoD and volumetric analyses would also inform whether sedimentation rates at the site are slowing down or being maintained.

5.5.2 Data Error Estimation

The DSM error estimation method used in this research was the calculation of a single error value for each surface model. While this approach is generally accepted and utilized in the literature, several studies have recommended the use of spatially variable error estimations (Wheaton et al., 2010; Milan et al., 2011; Cavalli et al., 2017) to better represent non-random, spatially correlated error that is present in SfM elevation models. The application of a spatially variable error estimation method for RPAS datasets in this research may have reduced the issues encountered with directionality of error in some parts of the study site and false surface elevation change measurement. It is recommended that spatially variable error estimation techniques be researched to determine their applicability for RPAS surface models, and if appropriate, incorporated into further DoD and volumetric change analyses.

5.5.3 Channel Delineation Techniques and Analyses

There were noticeable errors in all channel delineations around depressions (caused by ponding water or vegetation "dams") in the surface models, in which channel delineations did not align with channel thalwegs. Since the channel classification technique required the delineations and channel thalwegs to coincide, these offsets also caused issues with classification results that required manual clean up and added significant time to processing. It is recommended that a least-cost path approach be investigated for channel delineation as a potential improved delineation technique, such as the method presented by Melles et al. (2011). A least-cost approach should theoretically not require a "fill" step and may therefore reduce offsets between channel delineations and actual channel thalwegs, consecutively reducing error in classification results. Furthermore, the stream delineation process utilized in this research identified water flow pathways rather than channels, and in both Full Site and Target Area

delineations a classification technique was required to identify existent channels versus proto channels. An alternative method for identifying channels utilizing slope thresholding (Chirol et al., 2018), may alleviate issues in the classification process, and reduce manual input that was required for classification clean up.

Recommendations for additional analyses and research regarding channel delineation and classification results include the investigation of differences in channel characteristics and persistence in the three channel types identified in this research, and cross-sectional analysis. By examining the channel characteristics and persistence of channel types (relic agricultural, relic natural, and embryonic), insight may be gained regarding differences in channel evolution, and a better understanding of drainage network development. Additionally, this research examined planimetric channel characteristics only, and a cross-sectional analysis of channels of interest and/or the three channel types may provide more information about channel evolution on the site, including spatial and temporal patterns of channel infilling/deepening.

Chapter 6: Conclusions

Remote sensing technologies continue to advance at a very fast rate, improving our ability to measure and monitor environmental systems. An RTK-enabled RPAS was utilized in this research along with SfM workflows to conduct multi-temporal aerial surveys of a restoring MR site on the Bay of Fundy, Canada, to measure changes in surface elevation and to map drainage networks. Accuracies of the collected datasets were high compared to results from similar studies in salt marsh systems (Dale et al., 2018; Matheson, 2020; Brunetta et al., 2021; Taddia et al., 2021), allowing for the measurement of fine-scale changes and details within the site. However, caution must be utilized when taking these approaches, as offsets between surfaces can cause erroneous surface elevation change measurements, even when relatively low surface error estimates have been established. Results of DSM accuracy assessments showed no significant increase in accuracy of datasets collected at a reduced altitude (65 m AGL) and with an oblique camera angle, compared to those collected at the legal altitude maximum in Canada (120 m AGL) (Transport Canada, 2019) and with a nadir camera angle. Also, despite the ability to accurately measure surface elevation changes less than 5 cm with collected datasets, conducting volumetric change analyses on the entire site scale over time periods less than 1 year may not be appropriate, and results were more reliable when areas of interest with relatively higher rates of change were examined.

Compaction of remnant agricultural vegetation over the winter most likely skewed volumetric change values at the site level, but the borrow pit, which was excavated prior to site breach, allowed for the analysis of sedimentation patterns without noticeable effects of the antecedent landscape history. Sedimentation rates within the borrow pit were comparable to others reported for MR sites as well as borrow pits specifically in the Bay of Fundy (Matheson, 2020; Virgin et al., 2021; Brunetta et al., 2021). Multiple regression models comparing surface

elevation change to elevation and distance from channel, had higher predictive power (higher adjusted R^2 values) in the borrow pit than in the remaining areas of the site, showing more pronounced sedimentation patterns correlating to tested controls on sediment deposition. Channels developing within the borrow pit were characterized by a sinuous appearance and differed from the majority of channels within the rest of the site that incorporated agricultural ditch features. It appears that the removal of agricultural surface sediments prior to site breach allowed for a morphological evolution that more closely resembled natural salt marsh processes, and this technique could be applied to reduce the impacts of antecedent landscape history on restoration site evolution in the future, although more research is required to determine differences in long-term trajectory within the borrow pit and the remainder of the Converse restoration site.

Sedimentation patterns within the site showed strong seasonal signals as expected. Sedimentation rates in the borrow pit had the highest magnitude over the winter, which may have been due to increased suspended sediment concentrations in the area as measured in previous research (Poirier et al., 2017). Over the growing season, sedimentation rates at the site level showed significant variation, with more positive surface elevation change occurring between August and October, which may have been correlated to an increased frequency of high tides reaching the marsh surface as well as an increase in depth of those tides. The spatial patterns of sedimentation within the borrow pit and remaining areas of the site were more strongly correlated with elevation and distance from channel over the winter compared to the growing season, and elevation was generally a stronger predictor of surface elevation change than distance from channel in all datasets.

Channel density also showed a seasonal signal and was significantly higher in the fall datasets than growing season datasets, rather than increasing over the course of the study period as expected. This indicates that erosive patterns within channel, as well as increased sediment deposition on marsh surfaces may increase channel depth over the winter but infilling during the growing season may reduce embryonic channel depth. Channel networks were found to be relatively stable throughout the study period, and it appears that the fate of the ultimate drainage network patterns imprinted within the first year of tidal flow. Channels within the site were characterized by their formation type, either remnant agricultural, remnant natural, or embryonic.

It is recommended that in future RPAS data collection in salt marsh restoration sites, surveys should be conducted during dry weather and neap tides when possible, to allow the sediment surfaces to dry out and crack, increasing tie point matching in SfM processing and reducing noise and erroneous data in output elevation models. A further increase in accuracy of produced DSMs may be achieved by utilizing a more densely distributed GCP network during aerial surveys, although accuracies achieved in this study were substantially low. While a reduced flight altitude did not significantly reduce DSM error, an increase in resolution allowed for the detailed mapping of very small features such as embryonic channels. It is recommended that in future work, a lower flight altitude may be utilized in target areas when higher resolutions are beneficial (eg., embryonic channel mapping, vegetation species identification).

The time scale of this research of approximately 1-year, represents a small window in the evolution of a salt marsh restoration site, and it is recommended that similar/repeated analyses be conducted at the Converse restoration site over a longer time frame to provide further insight into the long-term restoration trajectory. Additional research should include the investigation of differences in evolution and characteristics of the three channel types identified in this work, as

well as surface elevation and volumetric change analyses. Improvements in data analyses may be made by utilizing spatially variable error estimates of DSMs (Wheaton et al., 2010; Milan et al., 2011; Cavalli et al., 2018), and investigating different channel delineation and classification techniques such as a least-cost path approach (Melles et al., 2011) or slope thresholding (Chirol et al., 2018).

Literature Cited

Adam, P. (2011). Plant Life History Studies in Saltmarsh Ecology. Cambridge: Cambridge University Press, 309–334.

Addo, K.A. and Jayson-Quashigah, P.N. (2021). UAV photogrammetry and 3D reconstruction: application in coastal monitoring. In A. Koubaa and A.T. Azar (Eds.), *Unmanned Aerial Systems: Theoretical Foundation and Applications* (Ch. 7, pp. 157-174). Academic Press. https://doi.org/10.1016/B978-0-12-820276-0.00014-5

Agisoft LLC. (2019). Agisoft Metashape Use Manual: Professional Edition, Version 1.5. https://www.agisoft.com/pdf/metashape_1_5_en.pdf

Allen, J. R. L. and Pye, K. (Eds.). (1992). Saltmarshes: Morphodynamics, conservation and engineering significance. Cambridge, UK: Cambridge University Press. https://doi.org/10.1016/0304-3770(94)90066-3

Allen, J.R.L. (2000). Morphodynamics of Holocene salt marshes: a review sketch from the Atlantic and Southern North Sea coasts of Europe. *Quaternary Science Reviews, 19*(12), 1155-1231. https://doi.org/10.1016/S0277-3791(99)00034-7

Amos, C.L., Tee, K.T., and Zaitlin, B.A. (1991). The post-glacial evolution of Chignecto Bay, Bay of Fundy, and its modern environment of deposition in Clastic Tidal Sedimentology, ed. D.G. Smith, G.E. Reinson, B.A. Zaitlin, and R.A. Rahmani, *Canadian Society of Petroleum Geologists Memoir, 16,* 59-90.

Argow, B.A., Hughes, Z.J. and Fitzgerald, D.M. (2011). Ice raft formation, sediment load, and theoretical potential for ice-rafted sediment influx on northern coastal wetlands. *Continental Shelf Research, 31*(12), 1294-1305. https://doi.org/10.1016/j.csr.2011.05.004

Barbier, E. B., Hacker, S. D., Kennedy, C., Koch, E. W., Stier, A. C., and Silliman, B. R. (2011). The value of estuarine and coastal ecosystem services. *Ecological Monographs, 81*(2), 169–193. https://doi.org/10.1890/10-1510.1

Bleakney, S.J. (2004). The art and science of dyke construction. In *Sods, Soil, and Spades: The Acadians at Grand Pré and Their Dykeland Legacy* (Ch. 5, pp 44-70). Montréal, QC: McGill-Queen's University Press.

Boesch, D. F., and Turner, R. E. (1984). Dependence of fishery species on salt marshes: the role of food and refuge. *Estuaries 7*(4), 460–468. https://doi.org/10.2307/ 1351627

Borsje, B. W., van Wesenbeeck, B. K., Dekker, F., Paalvast, P., Bouma, T. J., van Katwijk, M. M. and de Vries, M.B. (2011). How ecological engineering can serve in coastal protection. *Ecological Engineering, 37*(2), 113–122. https://doi.org/10.1016/j.ecoleng.2010.11.027

Bowron, T., Neatt, N., van Proosdij, D. and Lundholm, J. (2012). Salt marsh tidal restoration in Canada's Maritime provinces. In Roman, C.T., Burdick, D.M. (Eds.), *Tidal Marsh Restoration* (Ch. 13, pp. 191-209). Washington, US: Island Press.

Bowron, T.M., Graham, J., Ellis, K., Kickbush, J, McFadden, C., Poirier, E., Lundholm, J, and van Proosdij, D. (2020). Post-Restoration Monitoring (Year 1) of the Converse Salt Marsh Restoration (NS044) – 2019-20 Summary Report. Prepared for Department of Fisheries and Oceans & Nova Scotia Department of Agriculture. Publication No. 59. Halifax Nova Scotia.

Bowron, T.M., J. Graham, J. Kickbush, K. Ellis, S. Lewis, E. Poirier, J. Lundholm, T. Rabinowitz and D. van Proosdij. (2021). Post-Restoration Monitoring (Year 2) of the Converse Salt Marsh Restoration (NS044) – 2020-21 Technical Report. Prepared for Department of Fisheries and Oceans & Nova Scotia Department of Agriculture. Publication No. 65. Halifax Nova Scotia.

Boyd, B.M., Sommerfield, C.K. and Elsey-Quirk, T. (2017). Hydrogeomorphic influences on salt marsh sediment accumulation and accretion in two estuaries of the U.S. Mid-Atlandtic coast. Marine Geology, 383, 132-145. https://doi.org/10.1016/j.margeo.2016.11.008

Brasington, J., Langham, J., & Rumsby, B. (2003). Methodological sensitivity of morphometric estimates of coarse fluvial sediment transport. *Geomorphology, 53*(3-4), 299-316. https://doi.org/10.1016/S0169-555X(02)00320-3

Brunetta, R., Salvador, J. and Ciavola, P. (2019). Morphological evolution of an intertidal area following a set-back scheme: A case study from the Perkpolder Basin (Netherlands). *Frontiers in Earth Science, 7*, 228. https://doi.org/10.3389/feart.2019.00228

Brunetta, R., Duo, E. and Ciavola, P. (2021). Evaluating Short-Term Tidal Flat Evolution Through UAV Surveys: A Case Study in the Po Delta (Italy). *Remote Sensing, 13*(12), 2322. https://doi.org/10.3390/rs13122322

Bui, D.T., Long, N.Q. and Bui, X. (2018). Lightweight unmanned aerial vehicle and structure-from-motion photogrammetry for generating digital surface model for open-pit coal mine area and its accuracy assessment. In D. Tien Bui, A. Ngoc Do, H.B. Bui and N.D. Hoang (Eds.) *Advances and Applications in Geospatial Technology and Earth Resources* (pp. 17-33). Springer, Cham. https://doi.org/10.1007/978-3-319-68240-2_2

Bush, E., Gillett, N., Watson, E., Fyfe, J., Vogel, F. and Swart, N. (2019). Understanding observed global climate change. In Bush, E. and Lemmen, D.S. (Eds.), *Canada's Changing Climate Report* (Ch. 2, pp. 24-72). Ottawa, ON: Government of Canada.

Cahoon, D.R., Lynch, J.C., Perez, B.C., Segura, B., Holland, R.D., Stelly, C., Stephenson, G. and Hensel, P. (2002). High-precision measurements of wetland sediment elevation: II. The rod surface elevation table. *Journal of Sedimentary Research, 72*(5), 730–733. https://doi.org/10.1306/020702720734

Carrivick, J. L., Smith, M. W., & Quincey, D. J. (2016). *Structure from Motion in the Geosciences*. John Wiley & Sons.

Casella, E., Collin, A., Harris, D. Ferse, S., Bejarano, S., Parravicini, V., Hench, J.L. and Rovere, A. (2017). Mapping coral reefs using consumer-grade drones and structure from motion photogrammetry techniques. *Coral Reefs, 36*, 269–275. https://doi.org/10.1007/s00338-016-1522-0

Cavalli, M., Goldin, B., Comiti, F., Brardinoni, F., and Marchi, L. (2017). Assessment of erosion and deposition in steep mountain basins by differencing sequential digital terrain models. *Geomorphology, 291,* 4-16. https://doi.org/10.1016/j.geomorph.2016.04.009

Chirol, C., Haigh, I.D., Pontee, N., Thompson, C.E. and Gallop, S.L. (2018). Parametrizing tidal creek morphology in mature saltmarshes using semiautomated extraction from lidar. Remote Sensing of Environment, 209, 291-311. https://doi.org/10.1016/j.rse.2017.11.012

Christiansen, T., Wiberg, P.L. and Milligan, T.G. (2000). Flow and sediment transport on a tidal salt marsh surface. *Estuarine, Coastal and Shelf Science, 50*(3), 315-331. https://doi.org/10.1006/ecss.2000.0548

Costanza, R., D'Arge, R., De Groot, R., Farber, S., Grasso, M., Hannon, B., Limburg, K., Naeem, S., O'Neill, R.V., Paruelo, J., Raskin, R.G., Sutton, P. and Van Den Belt, M. (1997). The value of the world's ecosystem services and natural capital. *Nature, 387*(6630), 253. https://doi.org/10.1038/387253a0

Costanza, R., Pérez-Maqueo, O., Martinez, M.L., Sutton, P., Anderson, S.J., Mulder, K. (2008). The value of coastal wetlands for hurricane protection. *Ambio, 37*(4), 241-248. http://www.jstor.org/stable/25547893

Coulombier, T., Neumeier, U. and Bernatchez, P. (2012). Sediment transport in a cold climate salt marsh (St. Lawrence Estuary, Canada), the importance of vegetation and waves. *Estuarine, Coastal and Shelf Science, 101*, 64-75. https://doi.org/10.1016/j.ecss.2012.02.014

Dale, J., Burgess, H.M., Burnside, N.G., Kilkie, P., Nash, D.J. and Cundy, A.B. (2018). The evolution of embryonic creek systems in a recently inundated large open coast managed realignment site. *Anthropocene Coasts, 1,* 16-33. https://doi.org/10.1339/anc-2017-005

Dale, J., Burnside, N.G., Strong, C.J. and Burgess, H. M. (2020). The use of small-Unmanned Aerial Systems for high resolution analysis for intertidal wetland restoration schemes. *Ecological Engineering, 143.* https://doi.org/10.1016/j.ecoleng.2019.105695

D'Alpaos, A., Lanzoni, S., Marani, M., Fagherazzi, S. and Rinaldo, A. (2005). Tidal network ontogeny: Channel initiation and early development. *Journal of Geophysical Research: Earth Surfaces, 110*(F2). https://doi.org/10.1029/2004JF000182

D'Alpaos, A., Lanzoni, S., Mudd, S. M., and Fagherazzi, S. (2006). Modeling the influence of hydroperiod and vegetation on the cross-sectional formation of tidal channels. *Estuarine, Coastal and Shelf Science, 69*(3), 311–324. https://doi.org/10.1016/j.ecss.2006.05.002

D'Alpaos, A., Lanzoni, S., Marani, M. and Rinaldo, A. (2010). On the tidal prism-channel area relations. *Journal of Geophysical Research: Earth Surface, 115*(F1). https://doi.org/10.1029/2008JF001243

Davidson-Arnott, R.G.D., van Proosdij, D., Ollerhead, J. and Schostak, L. (2002). Hydrodynamics and sedimentation in salt marshes: examples from a macrotidal marsh, Bay of Fundy. *Geomorphology, 48*(1), 209-231. https://doi.org/10.1016/S0169-555X(02)00182-4

Dionne, J.C. (1989). An estimate of shore ice action in a *Spartina* tidal marsh, St. Lawrence Estuary, Quebec. *Journal of Coastal Research, 5*(2), 281-293. https://www.jstor.org/stable/4297531

DJI (2020). Phantom 4 RTK: User Manual v2.4. https://dl.djicdn.com/downloads/phantom_4_rtk/20200721/Phantom_4_RTK_User_Manual_v2.4_EN.pdf

Doswald, N., Munroe, R., Roe, D., Giuliani, A., Castelli, I. and Stephens, J. (2014). Effectiveness of ecosystem-based approaches for adaptation: review of the evidence base. Climate and Development, 6(2), 185-201. https://doi.org/10.1080/17565529.2013.867247

Doughty, C.L. and Cavanaugh, K.C. (2019). Mapping coastal wetland biomass from high resolution unmanned aerial vehicle (UAV) imagery. *Remote Sensing, 11*(5). https://doi.org/10.3390/rs11050540

Eisma, D. (1997). Morphology of intertidal areas. In D. Eisma (Ed.), *Intertidal Deposits* (pp. 317-344). Boca Raton, US: CRC Press.

Elliott, M. (2022). *The Connections Between Temporal Variation of Managed Realignment Inlet Conditions and Deposition Variation Across a Restored Marsh Surface.* (Unpublished Masters Thesis in preparation).

Eltner, A., Kaiser, A., Castillo, C., Rock, G., Neugirg, F. and Abellán, A. (2016). Image-based surface reconstruction in geomorphometry - merits, limits and developments. *Earth Surface Dynamics, 4*(2), 359-389. https://doi.org/10.5194/esurf-4-359-2016

ESRI. (2020). *Hydrology toolset.* ArcMap | Documentation. Retrieved from https://desktop.arcgis.com/en/arcmap/latest/tools/spatial-analyst-toolbox/flow-direction.htm

Faivre, N., Fritz, M., Freitas, T., de Boissezon, B., Vandewoestijne, S. (2017). Nature-based solutions in the EU: Innovating with nature to address social, economic and environmental challenges. *Environmental Research, 159*, 509-518. https://doi.org/10.1016/j.envres.2017.08.032

Fagherazzi, S., Kirwan, M. L., Mudd, S. M., Guntenspergen, G. R., Temmerman, S., D'Alpaos, A., van de Koppel, J., Rybczyk, J.M., Reyes, E., Craft, C. and Clough, J. (2012). Numerical models of salt marsh evolution: Ecological, geomorphic, and climatic factors. *Reviews of Geophysics, 50*(1). https://doi.org/10.1029/2011RG000359

Feagin, R.A., Lozada-Bernard, S.M., Ravens, T.M., Möller, I., Yeager, K.M. and Baird, A.H. (2009). Does vegetation prevent wave erosion of salt marsh edges? *Proceedings of the National Academy of Sciences of the United States of America, 106*(25), 10109-10113. https://doi.org/10.1073/pnas.0901297106

Forlani, G., Dall'Asta, E., Diotri, F., Morra di Cella, U., Roncella, R. and Santise, M. (2018). Quality Assessment of DSMs Produced from UAV Flights Georeferenced with On-Board RTK Positioning. *Remote Sensing*, *10*(2), 311. https://doi.org/10.3390/rs10020311

French, P.W. (2006). Managed realignment – The developing story of a comparatively new approach to soft engineering. *Estuarine, Coastal and Shelf Science, 67*(3), 409-423. https://doi.org/10.1016/j.ecss.2005.11.035

French, J. R., & Stoddart, D. R. (1992). Hydrodynamics of salt marsh creek systems: Implications for marsh morphological development and material exchange. *Earth Surface Processes and Landforms*, *17*(3), 235-252. https://doi.org/10.1002/esp.3290170304

French, J.R. and Spencer, T. (1993). Dynamics of sedimentation in a tide dominated backbarrier salt marsh, Norfolk, UK. *Geology*, *110*(3-4), 315-331.

Friedrichs, C.T. and Perry, J.E. (2001). Tidal salt marsh morphodynamics: A synthesis. *Journal of Coastal Research, 27*, 7-37.

Friess, D.A., Spencer, T., Smith, G.M., Möller, I., Brooks, S.M. and Thomson, A.G. (2012). Remote sensing of geomorphological and ecological change in response to saltmarsh

managed realignment, The Wash, UK. International Journal of Applied Earth Observations and Geoinformation, 18, 57-68. https://doi.org/10.1016/j.jag.2012.01.016

Gomez-Gutierrez, A., Schnabel, S., Berenguer-Sempere, F., Lavado-Contador, F. and Rubio-Delgado, J. (2014). Using 3D photo-reconstruction methods to estimate gully headcut erosion. *Catena*, *120*, 91-101. https://doi.org/10.1016/j.catena.2014.04.004

Gordon, D.C. and Desplanque, C. (1983). Dynamics and environmental effects of ice in the Cumberland basin of the Bay of Fundy. *Canadian Journal of Fisheries and Aquatic Sciences, 40*(9), 1331-1342. https://doi.org/10.1139/f83-156

Griffiths, D., Burningham, H., Anderson, K., Westoby, M.J. an James, M.R. (2019). Comparison of pre-and self-calibrated camera calibration models for UAS-derived nadir imagery for a SfM application. *Progress in Physical Geography: Earth and Environment, 43*(2), 215-235. https://doi.org/10.1177/0309133318788964

Haas, F., Hilger, L., Neugirg, F., Umstädter, K., Bretiung, C., Fischer, P., Hilger, P., Heckmann, T., Dusik, J., Kaiser, A., Schmidt, J., Della Seta, M., Rosenkranz, R. and Becht, M. (2016). Quantification and analysis of geomorphic processes on a recultivated iron ore mine on the Italian island of Elba using long-term ground-based lidar and photogrammetric SfM data by a UAV. *Natural Hazards and Earth System Sciences, 16*(5), 1269-1288. https://doi.org/10.5194/nhess-16-1269-2016

Horne, P., Suteanu, C., van Proosdij, D., Baker, G. (2013). Elevation-dependant multiscale analysis of a complex intertidal zone. *Journal of Coastal Research, 29*(3), 631-641.

Horton, R.E. (1945). Erosional development of streams and their drainage basins; hydrophysical approach to quantitative morphology. *Geological Society of America Bulletin*, *56*(3), 275-370. https://doi.org/10.1130/0016-7606(1945)56[275:EDOSAT]2.0.CO;2

Hugenholtz, C.H., Moorman, B.J., Riddell, K. and Whitehead, K. (2012). Small unmanned aircraft systems for remote sensing and Earth science research. Eos, *Transactions of the American Geophysical Union*, *93*(25), 236. https://doi.org/10.1029/2012EO250005

Hugenholtz, C.H., Whitehead, K.B.O., Barchyn, T.E., Moorman, B.J., LeClair, A., Riddell, K. and Hamilton, T. (2013). Geomorphological mapping with a small unmanned aircraft system (sUAS): Feature detection and accuracy assessment of a photogrammetrically-derived digital terrain model. *Geomorphology, 194*, 16-24. https://doi.org/10.1016/j.geomorph.2013.03.023

Hugenholtz, C., Brown, O., Walker, J., Barchyn, T., Nesbit, P., Kucharczyk, M., and Myshak, S. (2016). Spatial accuracy of UAV-derived orthoimagery and topography: Comparing photogrammetric models processed with direct geo-referencing and ground control points. *Geomatica, 70*(1), 21-30. https://doi.org/10.5623/cig2016-102

Ierodiaconou, D., Schimel, A.C.G. and Kennedy, D.M. (2016). A new perspective of storm bite on sandy beaches using Unmanned Aerial Vehicles. Zeitschrift für Geomorphologie, 60(3), 123-137.

IPCC. (2013). Climate Change 2013: The Physical Science Basis. Contribution of Working Group I to the Fifth Assessment Report of the Intergovernmental Panel on Climate Change. Stocker, T.F., Qin, D., Plattner, G.K., Tignor, M., Allen, S.K., Boschung, J., Nauels, A., Xia, Y., Bex, V. and Midgley, P.M. (Eds.). Cambridge, UK and New York, NY, USA: Cambridge University Press. https://doi.org/10.1017/CBO9781107415324

James, M.R. and Robson, S. (2012). Straightforward reconstruction of 3D surfaces and topography with a camera: Accuracy and geoscience application. *Journal of Geophysical Research: Earth Surface, 117*(F3). https://doi.org/10.1029/2011JF002289

Jaud, M., Grasso, F., Le Dantec, N., Verney, R., Delacourt, C., Ammann, D. J., & Grandjean, P. (2016). Potential of UAVs for monitoring mudflat morphodynamics (application to the seine estuary, France). ISPRS International Journal of GeoInformation, 5(4), 50.

Jeffries, R.I., Davy, A.J. and Rudmik, T. (1977). The growth strategies of coastal halophytes. In Jeffries, R.L. and Davy, A.J. (Eds.), *Ecological Processes in Coastal Environments* (pp. 243-268). The First European Ecological Symposium and 19th Symposium of the British Ecological Society Norwhich, 12-16 September, 1977. Oxford, UK: Blackwell Scientific Publications.

Kadiri, M., Spencer, K. L., Heppell, C. M. and Fletcher, P. (2011). Sediment characteristics of a restored saltmarsh and mudflat in a managed realignment scheme in Southeast England. *Hydrobiologia*, *672*(1), 79-89. https://doi.org/10.1007/s10750-011-0755-8

Kalacska, M., Chmura, G.L., Lucanus, O., Bérubé, D. and Arroyo-Mora, J.P. (2017). Structure from motion will revolutionize analyses of tidal wetland landscapes. *Remote Sensing of Environment, 199*, 14-24. https://doi.org/10.1016/j.rse.2017.06.023

Karle, M. and Bartholomä, A. (2008). Salt marsh sediments as natural resources for dike construction—sediment recycling in clay pits. *Senckenbergiana maritima*, *38*(2), 83-92. https://doi.org/10.1007/BF03055283

Kirwan, M. L., Temmerman, S., Skeehan, E. E., Guntenspergen, G. R., and Fagherazzi, S. (2016). Overestimation of marsh vulnerability to sea level rise. *Nature Climate Change, 6*, 253–260. https://doi.org/10.1038/nclimate2909

Klemas, V.V. (2015). Coastal and environmental remote sensing from unmanned aerial vehicles: an overview. *Journal of Coastal Research, 31*(5), 1260–1267. https://doi.org/10.2112/JCOASTRES-D-15-00005.1

Koch, E. W., Barbier, E. B., Silliman, B. R., Reed, D. J., Perillo, G. M., Hacker, S. D., Granek, E.F., Primavera, J.H., Muthiga, N., Polasky, S., Halpern, B.S., Kennedy, C.J., Kappel, C.V. and Wolanski, E. (2009). Non-linearity in ecosystem services: temporal and spatial variability in coastal protection. *Frontiers in Ecology and the Environment, 7*(1), 29–37. https://doi.org/10.1890/ 080126

Kranck, K. (1975). Sediment deposition from flocculated suspensions. *Sedimentology, 22*(1), 111-123. https://doi.org/10.1111/j.1365-3091.1975.tb00286.x

Lane, S.M., Westaway, R.M. and Hicks, D.M. (2003). Estimation of erosion and deposition volumes in a large, gravel-bed, braided river using synoptic remote sensing. *Earth Surface Processes and Landforms*, *28*(3), 249-271. https://doi.org/10.1002/esp.483

Lawrence, P. J., Smith, G. R., Sullivan, M. J. and Mossman, H. L. (2018). Restored saltmarshes lack the topographic diversity found in natural habitat. *Ecological Engineering*, *115*, 58-66. https://doi.org/10.1016/j.ecoleng.2018.02.007

Leonard, L.A. (1997). Controls of sediment transport and deposition in an incised mainland marsh basin, Southeastern North Carolina. *Wetlands, 17*(2), 263-274. https://doi.org/10.1007/BF03161414

Li, Y., Lei, N. and Xiong, Y. (2019). Research on watershed extraction method based on GIS. *IOP Conference Series: Earth and Environmental Science, 300.* https://doi.org/10.88/1755-1315/300/2/022168

Lotze, H.K., Lenihan, H.S., Bourque, B.J., Bradbury, R.H., Cooke, R.G., Kay, M.C., Kidwell, S.M., Kirby, M.X. and Peterson, C.H. (2006). Depletion, Degradation, and Recovery Potential of Estuaries and Coastal Seas. *Science, 312*(5781), 1806-1809.

Lynch, J., Hensel, P. and Cahoon, D. (2015). *The surface elevation table and marker horizon technique: A protocol for monitoring wetland elevation dynamics* (Report NPS/NCBN/NRR—2015/1078). Fort Collins, CO: National Park Service.

MacDonald, G.K., Noel, P.E., van Proosdij, D. and Chmura, G.L. (2010). The legacy of agricultural reclamation on channel and pool networks of Bay of Fundy salt marshes. *Estuaries and Coasts, 33*(1), 151-160. https://doi.org/10.1007/s12237-009-9222-4

MacKenzie, R., and Dionne, M. (2008). Habitat heterogeneity: importance of salt marsh pools and high marsh surfaces to fish production in two Gulf of Maine salt marshes. *Marine Ecology Progress Series, 368*, 217–230. https://doi.org/10.3354/meps 07560

Matheson, G. (2020). *Enhancing dykeland resiliency in a macrotidal estuary*. (Unpublished MSc thesis). Saint Mary's University, Halifax, NS.

Mancini, F., Dubbini, M., Gattelli, M., Stecchi, F., Fabbri, S. and Gabbianelli, G. (2013). Using unmanned aerial vehicles (UAV) for high-resolution reconstruction of topography: The structure from motion approach on coastal environments. *Remote Sensing, 5*(12), 6880-6898. https://doi.org/10.3390/rs5126880

Mayor, J. R., and Hicks, C. E. (2009). Potential impacts of elevated CO2 on plant interactions, sustained growth, and carbon cycling in salt marsh ecosystems. In Silliman, B.R., Grosholz, E.D., and Bertness, M.D. (Eds.), *Human Impacts on Salt Marshes: A Global Perspective* (pp. 207–228). Berkeley, US: University of California Press.

McKee, K. L., & Mendelssohn, I. A. (1989). Response of a freshwater marsh plant community to increased salinity and increased water level. *Aquatic Botany, 34*(4), 301-316. https://doi.org/10.1016/0304-3770(89)90074-0

Melles, S.J., Jones, N.E., Schmidt, B. and Rayfield, B. (2011). A least-cost path approach to stream delineation using lakes as patches and a digital elevation model as the cost surface. *Procedia Environmental Sciences, 7*, 240-245. https://doi.org/10.1016/j.proenv.2011.07.042

Milan, D. J., Heritage, G. L., Large, A. R. and Fuller, I. C. (2011). Filtering spatial error from DEMs: Implications for morphological change estimation. *Geomorphology, 125*(1), 160-171. https://doi.org/10.1016/j.geomorph.2010.09.012

Mitsch, W.J. and Gosselink, J.G. (2000). The value of wetlands: importance of scale and landscape setting. *Ecological Economics, 35*(1), 25-33. https://doi.org/10.1016/S0921-8009(00)00165-8

Möller, I., Kudella, M., Rupprecht, F., Spencer, T., Paul, M., van Wesenbeeck, B.K., Wolters, G., Jensen, K., Bouma, T.J., Miranda-Lange, M. and Schimmels, S. (2014). Wave attenuation over coastal salt marshes under storm surge conditions. *Nature Geoscience, 7*, 727–731. https://doi.org/10.1038/ngeo2251

Moskalski, S.M. and Sommerfield, C.K. (2012) Suspended sediment deposition and trapping efficiency in a Delaware salt marsh. *Geomorphology, 139*, 195-204.

Neumeier, U. and Amos, C.L. (2006). The influence of vegetation on turbulence and flow velocities in European salt-marshes. *Sedimentology, 53*(2), 259-277. https://doi.org/10.1111/j.1365-3091.2006.00772.x

Ozulu, I. and Gökgöz, T. (2018). Examining the stream threshold approaches used in hydrologic analysis. ISPRS International Journal of Geo-Information, 7(6), 201. https://doi.org/10.3390/ijgi7060201

Paquette, C., Sundberg, K.L., Boumans, R.M.J. and Chmura, G.L. (2004). Changes in saltmarsh surface elevation due to variability in evapotranspiration and tidal flooding. *Estuaries, 27*(1), 82-89. https://www.jstor.org/stable/1353492

Perillo, G.M.E. (2009). Tidal courses: classification, origin and functionality. In: G.M.E. Perillo, E. Wolanski, D.R. Cahoon and M.M. Brinson (Eds.), *Coastal Wetlands: An Integrated Ecosystem Approach* (Ch. 6, pp. 185-209). Amsterdam, NL: Elsevier.

Perillo, G.M.E. (2019). Geomorphology of tidal courses and depressions. In: G.M.E. Perillo, E. Wolanski, D.F. Cahoon and C.S. Hopkinson (Eds.), *Coastal Wetlands* (2nd ed.) (Ch. 6, pp. 221-261). Amsterdam, NL: Elsevier. https://doi.org/10.1016/C2018-0-02302-6

Pix4D. (2021). *What is the relative and absolute accuracy of drone mapping.* Pix4D Support. https://support.pix4d.com/hc/en-us/articles/202558889-What-is-the-relative-and-absolute-accuracy-of-drone-mapping

Poirier, E., van Proosdij, D. and Milligan, T.G. (2017). The effect of source suspended sediment concentration on the sediment dynamics of a macrotidal creek and salt marsh. *Continental Shelf Research, 148*, 130-138. https://doi.org/0.1016/j.csr.2017.08.017

Pratolongo, P., Leonardi, N., Kirby, J. R., and Plater, A. (2019). Temperate coastal wetlands. In G. Perillo, E. Wolanski, D. Cahoon, and M. Brinson (Eds.), *Coastal Wetlands* (pp. 105-152). Amsterdam, NL: Elsevier. https://doi.org/10.1016/b978-0-444-63893- 9.00003-4

Purcell, J. (2020). *Application of managed dyke realignment and hydrodynamic modelling for flood mitigation in Truro, Nova Scotia*. (Unpublished MSc thesis). Saint Mary's University, Halifax, NS.

Rabinowitz, T.R.M., Greene, L., Glogowski, A. D., Bowron, T., van Proosdij, D., and Lundholm, J.T. (2022). Hitchhiking halophytes in wrack and sediment-laden ice blocks contribute to tidal marsh development in the Upper Bay of Fundy. *Wetlands Ecology and Management*, 1-14. https://doi.org/10.1007/s11273-022-09867-3

Raczynski, R. J. (2017). *Accuracy analysis of products obtained from UAV-borne photogrammetry influenced by various flight parameters* (Master's thesis). Norwegian University of Science and Technology, Trondheim, Norway.

Ramsar Convention on Wetlands. (2018). Global Wetland Outlook: State of the World's Wetlands and their Services to People. Gland, Switzerland: Ramsar Convention Secretariat.

Reed, D.J. (1990). The impact of sea-level rise on coastal salt marshes. *Progress in Physical Geography*, *14*(4), 465-481. https://doi.org/10.1177/030913339001400403

Reed, D.J., Spencer, T., Murray, A.L., French, J.R. and Leonard, L. (1999). Marsh surface sediment deposition and the role of tidal creeks. *Journal of Coastal Conservation, 5*(1), 81-90. https://doi.org/10.1007/BF02802742

Reef, R., Schuerch, M., Christie, E.K., Möller, I. and Spencer, T. (2018). The effect of vegetation height and biomass on the sediment budget of a European saltmarsh. *Estuarine, Coastal and Shelf Science, 202*, 125-133. https://doi.org/10.1016/j.ecss.2017.12.016

Reguero, B.G., Beck, M.W., Bresch, D.N., Calil, J. and Meliane, I. (2018). Comparing the cost effectiveness of nature-based and coastal adaptation: A case study from the Gulf Coast of the United States. PLoS ONE, 13(4). https://doi.org/10.1371/journal.pone.0192132

Sona, G., Pinto, L., Pagliari, D., Passoni, D. and Gini, R. (2014). Experimental analysis of different software packages for orientation and digital surface modelling from UAV images. *Easrth Science Informatics, 7*(2), 97-107. https://doi.org/10.1007/s12145-013-0142-2

Spencer, T., Friess, D., Möller, I., Brown, S., Garbutt, R. and French, J. (2012). Surface elevation change in natural and re-created intertidal habitats, eastern England, UK, with particular reference to Freiston Shore. *Wetland Ecology and Management, 20*(1), 9-33. https://doi.org/10.1007/s11273-011-9238-y

Strahler, A.N. (1957). Quantitative analysis of watershed geomorphology. *Transactions-American Geophysical Union, 38*(6), 913-920. https://doi.org/10.1029/tr038i006p00913

Taddia, Y., Stecchi, F. and Pellegrinelli, A. (2019). Using DJI Phantom 4 drone for topographic mapping of coastal areas. *The international Archives of the Photogrammetry, Remote Sensing and Spatial Information Science, XLII-2-W13,* 625-630. https://doi.org/10.5194/isprs-archives-XLII-2-W13-625-2019

Taddia, Y., Pellegrinelli, A., Corbau, C., Franchi, G., Staver, L.W., Stevenson, J.C. and Nardin, W. (2021). High-resolution monitoring of tidal systems using UAV: A case study on Poplar Island, MD (USA). *Remote Sensing, 13*(7), 1364. https://doi.org/10.3390/rs13071364

Tao, J., Hill, P.S., Mulligan, R.P. and Smith, P.C. (2014). Seasonal variability of total suspended matter in Minas Basin, Bay of Fundy. *Estuarine, Coastal and Shelf Science, 151*, 169-180. https://doi.org/10.1016/j.ecss.2014.10.005

Taylor, J. (1997). *Introduction to Error Analysis, the Study of Uncertainties in Physical Measurements.* New York: University Science Books.

Temmerman, S., Bouma, T.J., Govers, G., Wang, Z.B., de Vries, M.B. and Herman, P.M.J. (2005). Impact of vegetation on flow routing and sedimentation patterns: Three-dimensional modeling for a tidal marsh. *Journal of Geophysical Research: Earth Surface, 110*(F4). https://doi.org/10.1029/2005JF000301

Temmerman, S., Meire, P., Bouma, T. J., Herman, P. M. J., Ysebaert, T., and De Vriend, H. J. (2013). Ecosystem-based coastal defence in the face of global change. *Nature, 504*(7478), 79–83. 10.1038/nature12859

Tonkin, T. and Midgley, N. (2016). Ground-control networks for image based surface reconstruction: An investigation of optimum survey designs using UAV derived imagery and structure-from-motion photogrammetry. Remote Sensing, 8(9). https://doi.org/10.3390/rs8090786

TransCoastal Adaptations, Centre for Nature Based Solutions. (2019). Managed Realignment; A review of methods, benefits, and challenges. PowerPoint presentation found on TransCoastal Adaptation shared drive.

Transport Canada (2019). Remotely Piloted Aircraft Systems (Section 901.25). *Canadian Aviation Regulartions (SOR/96-433).* https://lois-laws.justice.gc.ca/eng/regulations/SOR-96-433/FullText.html#s-901.11

Tsutsui, K., Rokugawa, S., Nakagawa, H., Miyazaki, S., Cheng, C., Shiraishi, T. and Yang, S. (2007). Detection and volume estimation of large-scale landslides based on elevation-change analysis using DEMs extracted from high-resolution satellite stereo imagery. *IEEE Transactions on Geoscience and Remote Sensing, 45*(6), 1681–1696. https://doi.org/10.1109/TGRS.2007.895209

Turner, D., Lucieer, A., and de Jong, S.M. (2015). Time series analysis of landslide dynamics using an Unmanned Aerial Vehicle (UAV). *Remote Sensing, 7*(2), 1736-1757. https://doi.org/10.3390/rs70201736

Vandenbruwaene, W., Maris, T., Cox, T.J.S., Cahoon, D.R., Meire, P. and Temmerman, (2011). Sedimentation and response to sea-level rise of a restored marsh with reduced tidal exchange: Comparison with a natural tidal marsh. *Geomorphology, 130*(3-4), 115-126. https://doi.org/10.1016/j.geomorph.2011.03.004

Vandenbruwaene, W., Bouma, T.J., Meire, P., Temmerman, S. (2012a). Bio-geomorphic effects on tidal channel evolution: impact of vegetation establishment and tidal prism change. *Earth Surface Processes and Landforms, 38*(2), 122-132. https://doi.org/10.1002/esp.3265

Vandenbruwaene, W., Miere, P., Temmerman, S. (2012b). Formation and evolution of a tidal channel network within a constructed tidal marsh. Geomorphology, 151-152, 114-125. https://doi.org/10.1016/j.geomorph.2012.01.022

van Proosdij, D. (2001). *Spatial and temporal controls on the sediment budget of a macrotidal saltmarsh*. (PhD thesis). The University of Guelph, Guelph, ON.

van Proosdij, D. and Page, S. (2012). Best Management Practices for Climate Change Adaptation in Dykelands: Recommendations for Fundy ACAS Sites. Saint Mary's University, Department of Geography, Halifax, Nova Scotia, Canada.

van Proosdij, D., Davidson-Arnott, R.G.D. and Ollerhead, J. (2006a). Controls on spatial patterns of sediment deposition across a macro-tidal salt marsh surface over single tidal cycles. *Estuarine, Coastal and Shelf Science, 69*(1), 64-86. https://doi.org/10.1016/j.ecss.2006.04.022

van Proosdij, D., Ollerhead, J. and Davidson-Arnott, R.G.D. (2006b). Seasonal and annual variations in the volumetric sediment balance of a macro-tidal salt marsh. *Marine Geology, 225*(1), 103-127. https://doi.org/10.1016/j.margeo.2005.07.009

van Proosdij, D., Perrott, B., and Carroll, K. (2013). Development and application of a geo-temporal atlas for climate change adaptation in Bay of Fundy dykelands. In Conley, D.C., Masselink, G., Russell, P.E. and O'Hare, T.J. (Eds.), Proceedings 12th International Coastal Symposium (Plymouth, England), *Journal of Coastal Research, Special Issue No. 65*, 1069-1074. https://doi.org/10.2112/SI65-181.1

Vecchi, E., Tavasci, L., De Nigris, N. and Gandolfi, S. (2021). GNSS and photogrammetric UAV derived data for coastal monitoring: A case of study in Emilia-Romagna, Italy. *Journal of Marine Science and Engineering, 9*(11), 1194. https://doi.org/10.3390/jmse9111194

Ventura, D., Bonifazi, A., Gravina, M.F. and Ardizzone, G.D. (2017). Unmanned aerial systems (UASs) for environmental monitoring: a review with applications in coastal habitats. In O.D.L. Mejia and J.A.E. Gomez (Eds.), *Aerial Robots - Aerodynamics, Control and Applications* (Ch. 8, pp. 165-184). InTech. http://dx.doi.org/10.5772/intechopen.69598

Virgin, S.D.S, Beck, A.D., Boone, L.K., Dykstra, A.K., Ollerhead, J., Barbeau, M.A. and McLellan, N.R. (2020). A managed realignment in the upper Bay of Fundy: Community dynamics during salt marsh restoration over 8 years in a megatidal, ice-influenced environment. *Ecological Engineering, 149.*

Watkinson, A. and Davy, A. (1985). Population biology of salt marsh and sand dune annuals. *Vegetatio, 62*(1), 487-497. https://doi.org/10.1007/BF00044776

Weishar, L.L., Teal, J.M., Hinkle, R. (2005) Stream order analysis in marsh restoration on Delaware Bay. *Ecological Engineering, 25*(3), 252-259. https://doi.org/10.1016/j.ecoleng.2005.04.003

Wheaton, J.M., Brasington, J., Darby, S.E. and Sear, D.A. (2010). Accounting for uncertainty in DEMs from repeat topographic surveys: improved sediment budgets. *Earth Surface Processes and Landforms: The Journal of the British Geomorphological Research Group, 35*(2), 136-156. https://doi.org/10.1002/esp.1886

Whitehouse, R.J.S., Bassoullet, P., Dyer, K.R., Mitchener, H.J. and Roberts, W. (2000). The influence of bedforms of flow and sediment transport over intertidal mud flats. *Continental Shelf Research, 20*, 1099-1124. https://doi.org/10.1046/S0278-4343(00)00014-5

Widdows, J., Pope, N.D. and Brinsley, M.D. (2008). Effect of *Spartina anglica* stems on near-bed hydrodynamics, sediment erodability and morphological changes on an intertidal mudflat. *Marine Ecology Progress Series, 362*, 45-57.

Wolf, P., DeWitt, B., Wilkinson, B. (2000). Elements of Photogrammetry With Applications in GIS, Columbus. McGraw-Hill Higher Education, OH, USA.

Wollenberg, J.T., Ollerhead, J. and Chmura, G.L. (2018). Rapid carbon accumulation following managed realignment on the Bay of Fundy. *PLoS ONE, 13*(3). https://doi.org/10.1371/journal.pone.0193930

Xiang, J., Chen, J., Sofia, G., Tian, Y. and Tarolli, P. (2018). Open-pit mine geomorphic changes analysis using multi-temporal UAV survey. *Environmental Earth Sciences, 77*(6), 1-18. https://doi.org/10.1007/s12665-018-7383-9

Yang, S.L., Li, P., Gao, A., Zhang, J., Zhang, W.X., and Li, M. (2007). Cyclical variability of suspended sediment concentration over a low-energy tidal flat in Jiaozhou Bay, China: effect of shoaling on wave impact. *Geo-Marine Letters, 27*(5), 345-353. https://doi.org/10.1007/s00367-007-0058-2

Zedler, J.B. and Kercher, S. (2005). Wetland resources: status, trends, ecosystem services, and restorability. *Annual Review of Environment and Resources, 30*, 39-74. https://doi.org/10.1146/annurev.energy.30.050504.144248

Zhou, Z., Stefanon, L., Olabarrieta, M., D'Alpaos, A., Carniello, L., and Coco, G. (2014). Analysis of the drainage density of experimental and modelled tidal networks. *Earth Surface Dynamics*, *2*(1), 105-116. https://doi.org/10.5194/esurf-2-105-2014

Zhu, X., Meng, L., Zhang, Y., Weng, Q. and Morris, J. (2019). Tidal and meteorological influences on the growth of invasive species Spartina alterniflora: Evidence from UAV remote sensing. *Remote Sensing*, *11*(10), 1208. https://doi.org/10.3390/rs11101208

Appendix A - RPAS Data Collection Trouble Shooting

Due to aircraft malfunction during some collections, images were not collected by the aircraft (image dropping) in small sections of the flight plans. This occurred in two different scenarios, one that was not easily identified during collection but did not significantly impact data coverage, and one that interrupted data collection and was therefore easy to identify but required additional photo collection to ensure data coverage. In the first scenario, the aircraft would drop around 5-10 images within the first few minutes of a flight section (most often after changing the aircraft battery mid-collection and resuming the flight plan). Due to a delay on the controller of the displayed number of collected images for the first few minutes of each flight section, it was not possible to identify when this issue was occurring. Since images were collected with a 60% side overlap, dropped photos did not cause significant negative impacts on the collected datasets such as holes.

The second scenario also involved a malfunctioning of the aircraft during data collection but occurred less often. Occasionally during flights, the aircraft would stop collecting images altogether and would not resume image collection unless the aircraft was landed and restarted. To mitigate this issue, the displayed number of images collected on the controller was monitored during all flights. Since it was common for delays to occur between actual image collection and when this number updated on the controller, the issue was identified if the aircraft travelled more than half of a flightline without an increase in the displayed number of collected images. At this point the aircraft would be returned home for a landing and restart. Unfortunately, upon resuming an interrupted flight, the aircraft would continue the flight plan at the point it was interrupted, and not the point at which photo collection stopped. This left significant gaps in image collection. To account for this missing data, the aircraft was manually flown in these areas and images were collected manually

Appendix B - Channel Delineation Script

```
# Name: Channel Delineation
# Description: Delineates stream networks from a Digital Surface Model
# Paste this to command line to run: C:\Python27\ArcGISx6410.7\python.exeD:\SLewis\Thesis
\Scripts\ChannelDelineation.py

# Import system modules and extensions
import sys
sys.path.append("C:\Program Files (x86)\ArcGIS\Desktop10.7\arcpy")
import arcpy, os
from arcpy.sa import *
import arcpy.cartography as CA
arcpy.CheckOutExtension("Spatial")
arcpy.env.overwriteOutput = True

# Input Variables ############################################################

# Input elevation model
inDSM =
r'E:\CON_20210504\SfM_Projects\CON_20210504_R4MS_Obliques.files\Products\CON_2021
0504_R4MS_Obliques_DSM_CGVD2013_2cm.tif'
# Location for output files
output_folder = r'D:\SLewis\Thesis\Processing\ChannelDelineation\20210504_Obliques'
# Max elevation for processing (max flood extent in meters)
elev_max = 6.959
# Input edge effects clip shapefile (covering extent of "good" data without edge effect noise from
SfM)
edge_clip =
r'D:\SLewis\Thesis\Processing\ChannelDelineation\ExtraFiles\CON_Obliques_AllEdge_ForCha
nnelDelin.shp'
# Input pour point for watershed calculation
pour_point =
r'D:\SLewis\Thesis\Processing\ChannelDelineation\ExtraFiles\PourPoint_Obliques.shp'
# Input flow accumulation threshold value (50,000 for Target Area datasets, 120,000 for Full
Site datasets)
flow_acc_thresh = 50000
# Stream order type
stream_ord_type = 'STRAHLER'
# Smoothing output stream features: Input smoothing tolerance value in m, or enter 0 if you do
not want to smooth
smooth_tol = 0.4
```

```
print('Inputs acceptable')

# Set Data Info and Temp Folder ################################################
file_name = str(os.path.basename(inDSM).split('.')[0])
shp_folder = str(output_folder + os.sep + 'Shapefiles')
if not os.path.exists(shp_folder):
    os.makedirs(shp_folder)

print('Shapefile folder: ' + shp_folder)

# Run Tools ####################################################################

# Clip raster to remove edge effects
edgeDSM = output_folder + os.sep + file_name + '_EdgeClipped.tif'
arcpy.management.Clip(
    in_raster = inDSM,
    rectangle = "400814.754 5076836.992 401803.636 5077587.748",
    out_raster = edgeDSM,
    in_template_dataset = edge_clip,
    clipping_geometry = "ClippingGeometry")

print("Edge effects removed")

# Clip Raster to maximum flood extent
elevCon = Con(Raster(edgeDSM) < elev_max, inDSM)

print('Elevation clip successful')

# Fill clipped DSM if the file does not already exist, otherwise, call the file as a raster object for
later use
if not os.path.exists(output_folder + os.sep + file_name + '_Fill.tif'):
    outFill = Fill(elevCon)
    outFill.save(output_folder + os.sep + file_name + '_Fill.tif')
    print ('DSM has been filled')
else:
    outFill = Raster(output_folder + os.sep + file_name + '_Fill.tif')
    print ('Filled DSM already exists')

# Create Flow Direction (defaults to D8 method) raster if the file does not exist, otherwise, call
the file as a raster object for later use
if not os.path.exists (output_folder + os.sep + file_name + '_FlowD.tif'):
    flow_dir = FlowDirection(outFill)
    flow_dir.save(output_folder + os.sep + file_name + '_FlowD.tif')
```

```
    print('Flow direction raster created')
else:
    flow_dir = Raster(output_folder + os.sep + file_name + '_FlowD.tif')
    print ('Flow direction raster already exists')

# Create Flow Accumulation (set to D8 method) raster if the file does not exist, otherwise, call
the file as a raster object for later use
if not os.path.exists (output_folder + os.sep + file_name + '_FlowAcc.tif'):
    flow_acc = FlowAccumulation(
        in_flow_direction_raster = flow_dir,
        in_weight_raster = "",
        data_type = "INTEGER",
        flow_direction_type = "D8")
    flow_acc.save(output_folder + os.sep + file_name + '_FlowAcc.tif')
    print('Flow accumulation raster created')
else:
    flow_acc = Raster(output_folder + os.sep + file_name + '_FlowAcc.tif')
    print ('Flow accumulation raster already exists')

# Snap pour point to stream
SnapPour = SnapPourPoint(in_pour_point_data = pour_point,
                         in_accumulation_raster = flow_acc,
                         snap_distance = 0.2)
print('Pour point snapped to stream cells')

# Create watershed raster for extent if the file does not exist, otherwise, call the file as a raster
object for later use
if not os.path.exists (output_folder + os.sep + file_name + '_Watershed.tif'):
    watershed_extent = Watershed(
        in_flow_direction_raster = flow_dir,
        in_pour_point_data = SnapPour)
    watershed_extent.save(output_folder + os.sep + file_name + '_Watershed.tif')
    watershed_shape = shp_folder + os.sep + file_name + '_Watershed.shp'
    arcpy.conversion.RasterToPolygon(
        in_raster = watershed_extent,
        out_polygon_features = watershed_shape,
        simplify = "NO_SIMPLIFY")
    print('Watershed extent raster and shapefile created')
else:
    watershed_extent = Raster(output_folder + os.sep + file_name + '_Watershed.tif')
    print ('Watershed extent already exists')
```

```
# Clip flow accumulation raster to watershed, and apply a flow accumulation threshold to
determine stream cells (set stream cell values to 1)
stream = Con(watershed_extent, Con(flow_acc > flow_acc_thresh, 1))
print('Accumulation raster clipped to watershed extent, and flow accumulation threshold applied
to create stream raster')

# Add stream order to stream cells
stream_ord_1 = StreamOrder(
    in_stream_raster = stream,
    in_flow_direction_raster = flow_dir,
    order_method = stream_ord_type)
print('Stream order has been added to stream raster')

# Reverse stream order
max_stream_ord = int(arcpy.GetRasterProperties_management(stream_ord_1,
property_type='MAXIMUM').getOutput(0))
stream_ord = max_stream_ord - stream_ord_1 + 1
stream_ord.save(output_folder + os.sep + file_name + '_StreamOppOrd.tif')
print('Stream order has been reversed')

# Create stream shapefile from stream raster
out_stream = (shp_folder + os.sep + file_name + '_Stream.shp')
StreamToFeature(
    in_stream_raster = stream_ord,
    in_flow_direction_raster = flow_dir,
    out_polyline_features = out_stream,
    simplify = 'SIMPLIFY')

# Smooth stream shapefile
if smooth_tol > 0:
    smooth_stream = shp_folder + os.sep + file_name + '_SmoothStream.shp'
    CA.SmoothLine(
        in_features = out_stream,
        out_feature_class = smooth_stream,
        algorithm = "PAEK",
        tolerance = smooth_tol)
print('Final stream shapefile created!')
```

Appendix C - Channel Classification Script

```
# Name: Channel Classification
# Description: Classifies delineated stream segments based on channel depth
# Paste this to command line to run: C:\Progra~1\ArcGIS\Pro\bin\Python\envs\arcgispro-
py3\python.exe D:\SLewis\Thesis\Scripts\Channel_Classification_v0.4_FullSite.py

print("Start Channel Script")

# Import system modules and extensions
import arcpy, os
from arcpy.sa import *

## Define Feature Creation and Extract Elevation Function ############################

def
extract_elevations(instream,segment_length,inelevation,transect_len,transect_dist,point_dist,proc
_workspace):
    print('Extracting cross-section elevations from valid branches')

    # Make layer with stream shapefile
    print("Making branch layer")
    fo_temp_streams = proc_workspace + os.sep + "temp_streams"
    arcpy.MakeFeatureLayer_management(
        in_features = instream,
        out_layer = fo_temp_streams)

    fo_temp_points = proc_workspace + os.sep + "temp_points"
    arcpy.GeneratePointsAlongLines_management(
        Input_Features=fo_temp_streams,
        Output_Feature_Class=fo_temp_points,
        Point_Placement="DISTANCE",
        Distance=segment_length,
        Include_End_Points="NO_END_POINTS")

    fo_streams = proc_workspace + os.sep + "streams"
    arcpy.SplitLineAtPoint_management(
        in_features = fo_temp_streams,
        point_features = fo_temp_points,
        out_feature_class = fo_streams ,
        search_radius = 0.5)

    arcpy.management.AddField(
        in_table = fo_streams,
```

```
    field_name = "CH_STAT",
    field_type = "TEXT")

arcpy.management.AddField(
    in_table = fo_streams,
    field_name = "AVG_DEP",
    field_type = "FLOAT")

arcpy.management.Delete(
    in_data = fo_temp_points
    #{data_type})

print("Branch layer created")

# Generate transects for x-section
print("Making transects")
fo_transects = proc_workspace + os.sep + "transects"
arcpy.management.GenerateTransectsAlongLines(
    in_features = fo_streams,
    out_feature_class = fo_transects,
    interval = transect_dist,
    transect_length = transect_len,
    include_ends = "END_POINTS")

arcpy.management.AlterField(
    in_table = fo_transects,
    field = "ORIG_FID",
    new_field_name = "SEG_ID",
    clear_field_alias = "CLEAR_ALIAS")

arcpy.management.AddField(
    in_table = fo_transects,
    field_name = "XNS_STAT",
    field_type = "TEXT")

arcpy.management.AddField(
    in_table = fo_transects,
    field_name = "XNS_DEP",
    field_type = "FLOAT")

print("Transects created")

# Generate cross-section points along transects
```

```
    print("Making extraction points")
    fo_extraction_points = proc_workspace + os.sep + "extraction_points"
    arcpy.management.GeneratePointsAlongLines(
        Input_Features = fo_transects,
        Output_Feature_Class = fo_extraction_points,
        Point_Placement = "DISTANCE",
        Distance = point_dist)

    print("Extraction points created")
    arcpy.management.AlterField(
        in_table = fo_extraction_points,
        field = "ORIG_FID",
        new_field_name = "XNS_ID",
        clear_field_alias = "CLEAR_ALIAS")

    # Extract elevations to points
    print("Extracting elevations to points")
    arcpy.ddd.AddSurfaceInformation(
        in_feature_class = fo_extraction_points,
        in_surface = inelevation,
        out_property = "Z")

    # Wrap feature generation portion
    t1 = time.time()
    t1 -= t0
    t1 = float(t1)
    print("Elevations extracted")
    return(fo_streams,fo_transects,fo_extraction_points)

## Define Channel Class Decision Function ##########################################

def is_channel(streams,transects,points,min_ch_depth,pass_threshold):
    t2 = time.time()
    print("Assessing channel x-sections")

    # Setup the required field lists
    sc_xns_fields = ['XNS_ID', 'SEG_ID', 'Z']
    uc_xns_fields = ['OBJECTID', 'CH_STAT', 'AVG_DEP']
    uc_tr_fields = ['OBJECTID', 'XNS_STAT', 'XNS_DEP']

    # Get unique SEG_IDs and determine channel status per segment
    vals = [row[0] for row in arcpy.da.SearchCursor(transects, 'SEG_ID')]
    seg_ids = set(vals)
```

```
    br_status_list = []
    xns_status_list = []
    depth_list = []
    for i, seg_id in enumerate(seg_ids):
        print("Assessing Branch: %s (%s of %s)" %(seg_id, i+1,len(seg_ids)))
        # Get unique XNS_IDs
        expression = (u'{0} = {1}'.format(sc_xns_fields[1], seg_id))
        vals = [row[0] for row in arcpy.da.SearchCursor(transects, 'OBJECTID', where_clause =
expression)]
        xns_ids = set(vals)
        fails = 0
        passes = 0
        # Determine cross-section status
        for ii, xns_id in enumerate(xns_ids):
            #print("Measuring X-Section: %s (%s of %s; Pass: %s Fail: %s)" %(xns_id, ii+1,
len(xns_ids), passes, fails))
            expression = (u'{0} = {1}'.format(sc_xns_fields[0], xns_id))
            with arcpy.da.SearchCursor(
                in_table = points,
                field_names = sc_xns_fields,
                where_clause = expression
                ) as sc:
                    elevation = []
                    for srow in sc:
                        elevation.append(srow[2])

                    # We now have a list of elevations and decisions to make
                    xns_status = ""
                    thalweg = min(elevation)
                    thalweg_index = elevation.index(thalweg)
                    l_br = elevation[:thalweg_index]
                    r_br = elevation[thalweg_index:]

                    if len(l_br) > 0 and len(r_br) > 0:
                        xns_depth = min([max(l_br),max(r_br)]) - thalweg
                        depth_list.append(xns_depth)
                        if max(l_br) > (thalweg + min_ch_depth) and max(r_br) > (thalweg +
min_ch_depth):
                            #print("Pass")
                            passes += 1
                            xns_status = "Pass"
                        else:
                            #print("Fail")
```

```
                    fails += 1
                    xns_status = "Fail"
                else:
                    #print("Fail")
                    xns_depth = 0
                    fails += 1
                    xns_status = "Edge"

                xns_status_list.append([xns_id,xns_status,xns_depth])
        average_depth = sum(depth_list)/len(depth_list)
        # Determine the channel code
        ch_status = ""

        # Every segment has at least two transects.
        if passes > 0:
            if passes / (passes+fails) >= pass_threshold:
                ch_status = "Existent"
            else:
                ch_status = "Proto"
        else:
            ch_status = "Proto"

        print("Branch is: %s" %(ch_status))
        br_status_list.append([seg_id,ch_status,average_depth])

    # Update stream with channel status
    for i,r in enumerate(br_status_list):
        seg_id,ch_status,average_depth=r[:]
        print('Updating Branch: %s of %s' %(i+1, len(br_status_list)))
        expression = (u'{0} = {1}'.format(uc_xns_fields[0], seg_id))
        with arcpy.da.UpdateCursor(
            in_table = streams,
            field_names = uc_xns_fields,
            where_clause = expression
            ) as uc:
                for urow in uc:
                    urow[1] = ch_status
                    urow[2] = average_depth
                    uc.updateRow(urow)

    # Update cross-sections with xns status
    for i,r in enumerate(xns_status_list):
        xns_id,xns_status,xns_depth=r[:]
```

```
        print('Updating Cross-section: %s of %s' %(i+1, len(xns_status_list)))
        expression = (u'{0} = {1}'.format("OBJECTID", xns_id))
        with arcpy.da.UpdateCursor(
            in_table = transects,
            field_names = uc_tr_fields,
            where_clause = expression
            ) as uc:
                for urow in uc:
                    urow[1] = xns_status
                    urow[2] = xns_depth
                    uc.updateRow(urow)

    # Wrap branch definitions
    print("Branches defined")

## Define Inputs ###############################################################

# Input delineated channel shapefile
instream =
r"D:\SLewis\Thesis\Processing\ChannelDelineation\20191124_FullSite\Shapefiles\CON_20191
124_P4MS_FullSite_DSM_CGVD2013_35mm_SmoothStream120.shp"
# Input elevation model
inelevation = r"\\sparc7\dvp\archive\RPAS\Converse\2019-11-
24\03_SfM_Projects\CON_20191124_R4MS_FullSite\01_RawProducts\CON_20191124_P4MS
_FullSite_DSM_CGVD2013_35mm.tif"
# Location for output files
output_folder = r"D:\SLewis\Thesis\Processing\ChannelClassification\20191124_FullSite"
# Maximum stream segment length (m)
segment_length = 8
# Total length of each transect (m)
transect_len = 3
# Distance between transects (m)
transect_dist = 0.5
# Distance between points along each transect (m)
point_dist = 0.05
# Minimum acceptable channel depth
min_ch_depth = 0.02
# Pass / fail threshold
pass_threshold = 0.5
# Set Geodatabase
gdb = 'Channel_Definition.gdb'
# Set Data Info and Temp Folder
proc_workspace = str(output_folder + os.sep + gdb)
```

```
## Run Script ##################################################################

# Initialize the workspace
if not os.path.exists(proc_workspace):
    arcpy.management.CreateFileGDB(
        out_folder_path = output_folder,
        out_name = gdb,
        out_version = "CURRENT")
arcpy.env.workspace = proc_workspace
arcpy.env.overwriteOutput = True
arcpy.CheckOutExtension("Spatial")

# Build the required feature classes and extract elevations
streams, transects, points =
extract_elevations(instream,segment_length,inelevation,transect_len,transect_dist,point_dist,proc
_workspace)

# Generate and apply channel classifications
is_channel(streams,transects,points,min_ch_depth,pass_threshold)

# Script finished
print("Channels classified!")
```

Appendix D - Structure from Motion Data Products (Full Site)

Figure D-1. RGB orthomosaic produced by Agisoft Metashape. Imagery data collected with a DJI Phantom 4 RTK RPAS during a full site survey of Converse, November 24, 2019. Resolution is 3.5cm and horizontal RMSE expected to be less than the resolution.

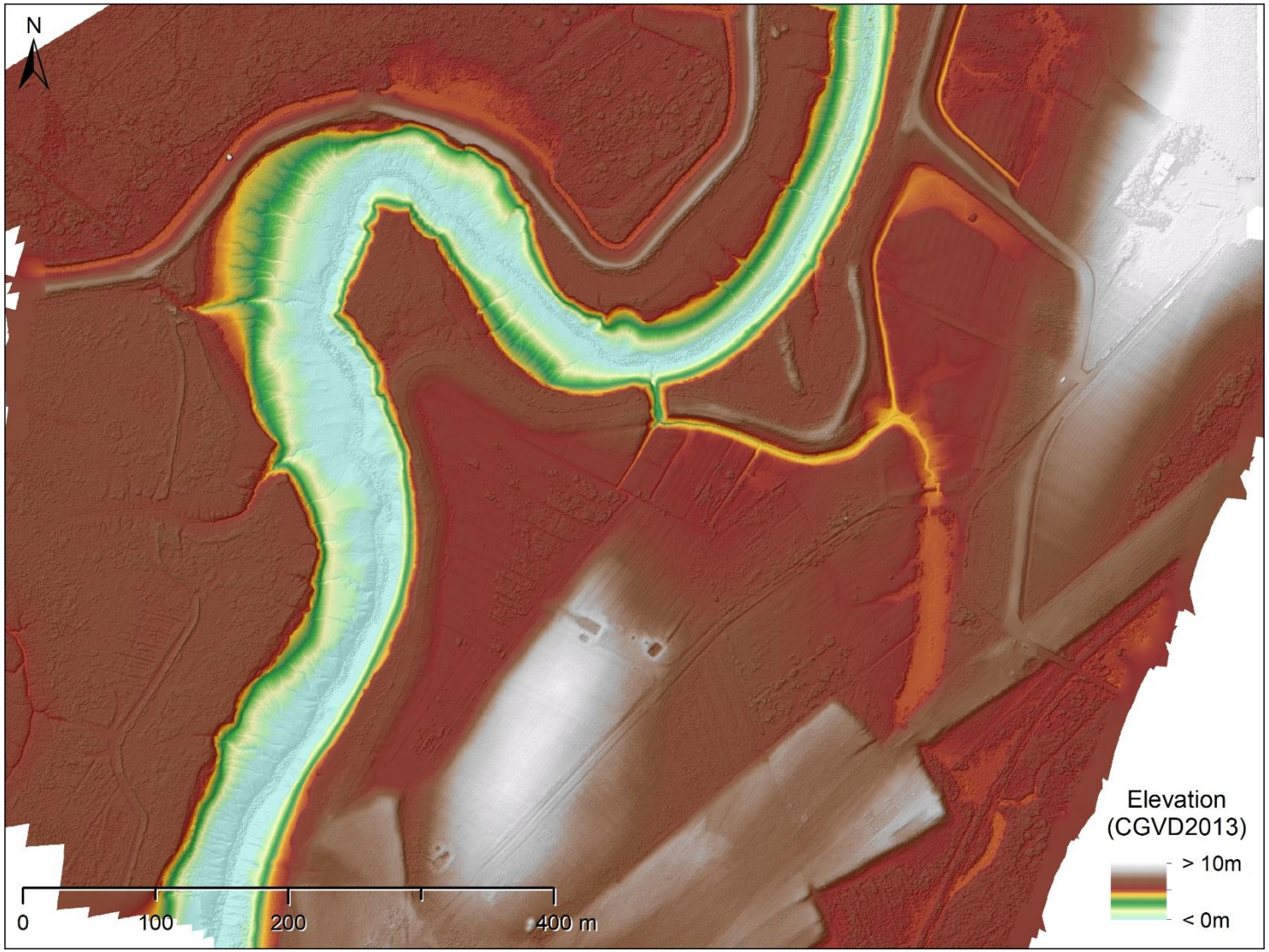

Figure D-2. Elevation model produced by Agisoft Metashape (displayed as a combined colour ramp and hillshade). Imagery data collected with a DJI Phantom 4 RTK RPAS during a full site survey of Converse, November 24, 2019. Resolution is 3.5 cm, and vertical RMSE is 1.8 cm.

Figure D-3. RGB orthomosaic produced by Agisoft Metashape. Imagery data collected with a DJI Phantom 4 RTK RPAS during a full site survey of Converse, June 1, 2020. Resolution is 3.5cm and horizontal RMSE expected to be less than the resolution.

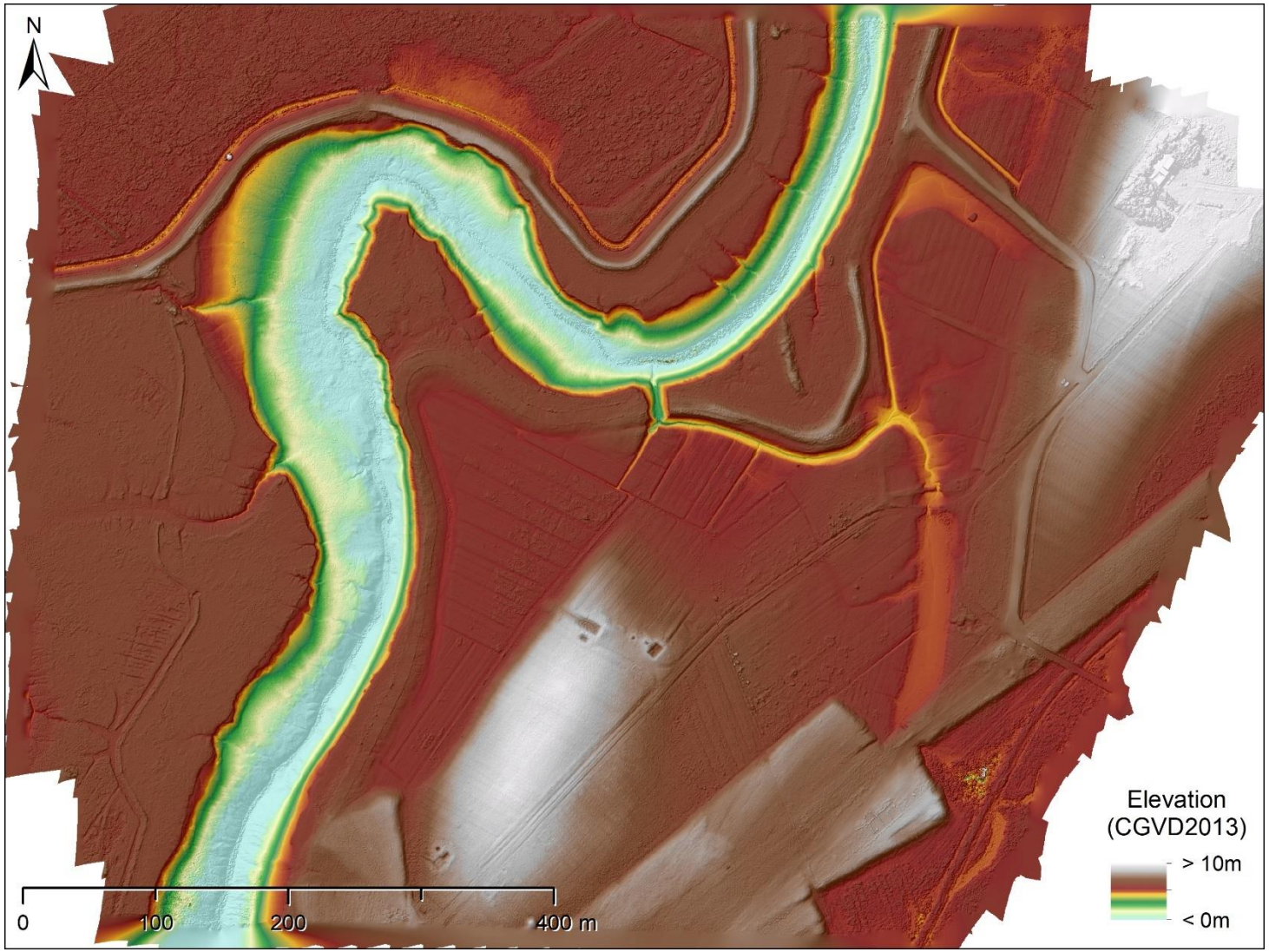

Figure D-4. Elevation model produced by Agisoft Metashape (displayed as a combined colour ramp and hillshade). Imagery data collected with a DJI Phantom 4 RTK RPAS during a full site survey of Converse, June 1, 2020. Resolution is 3.5 cm, and vertical RMSE is 1.3 cm.

Figure D-5. RGB orthomosaic produced by Agisoft Metashape. Imagery data collected with a DJI Phantom 4 RTK RPAS during a full site survey of Converse, July 9, 2020. Resolution is 3.5cm and horizontal RMSE expected to be less than the resolution.

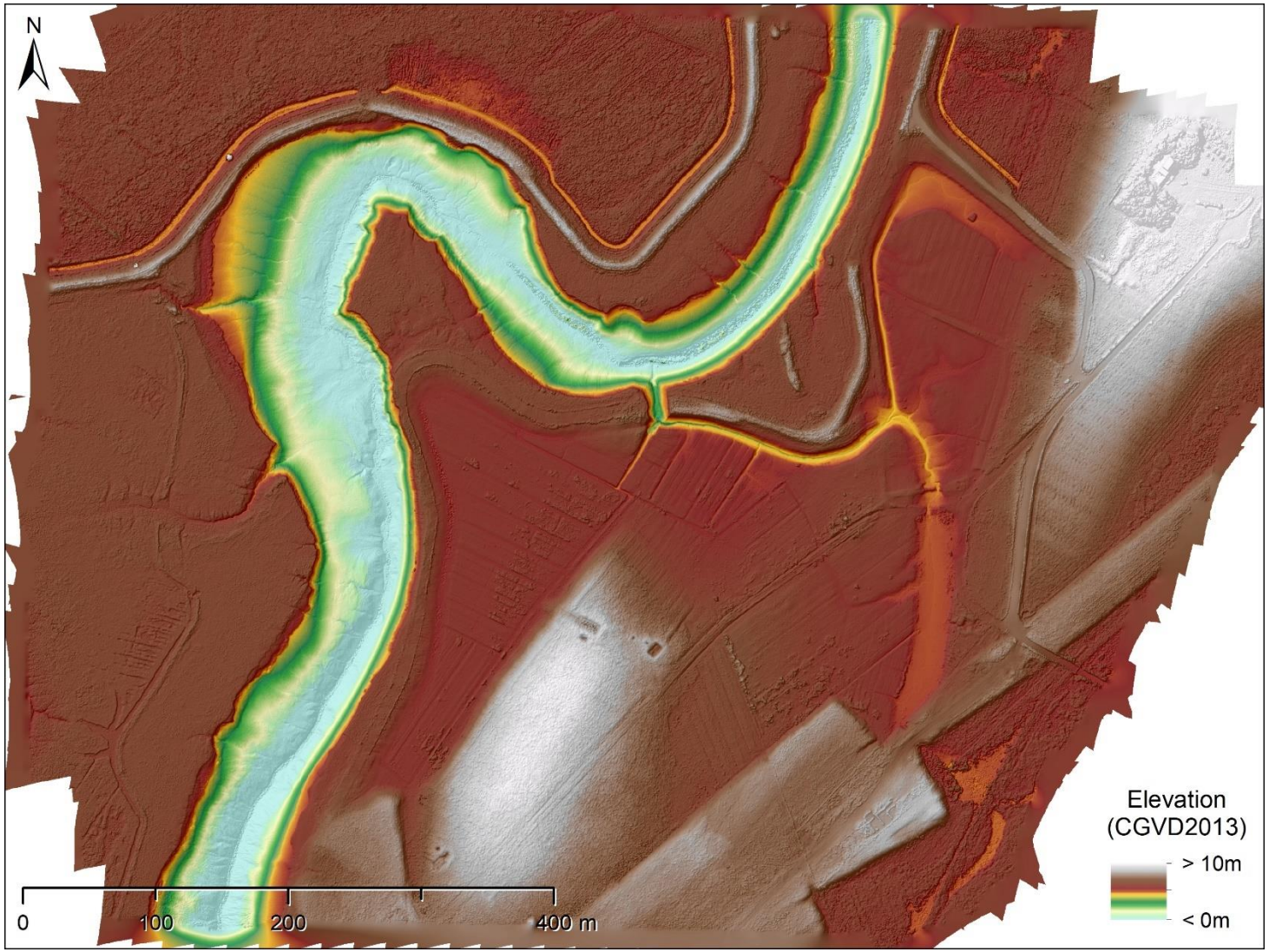

Figure D-6. Elevation model produced by Agisoft Metashape (displayed as a combined colour ramp and hillshade). Imagery data collected with a DJI Phantom 4 RTK RPAS during a full site survey of Converse, July 9, 2020. Resolution is 3.5 cm, and vertical RMSE is 1.5 cm.

Figure D-7. RGB orthomosaic produced by Agisoft Metashape. Imagery data collected with a DJI Phantom 4 RTK RPAS during a full site survey of Converse, August 21, 2020. Resolution is 3.5cm and horizontal RMSE expected to be less than the resolution.

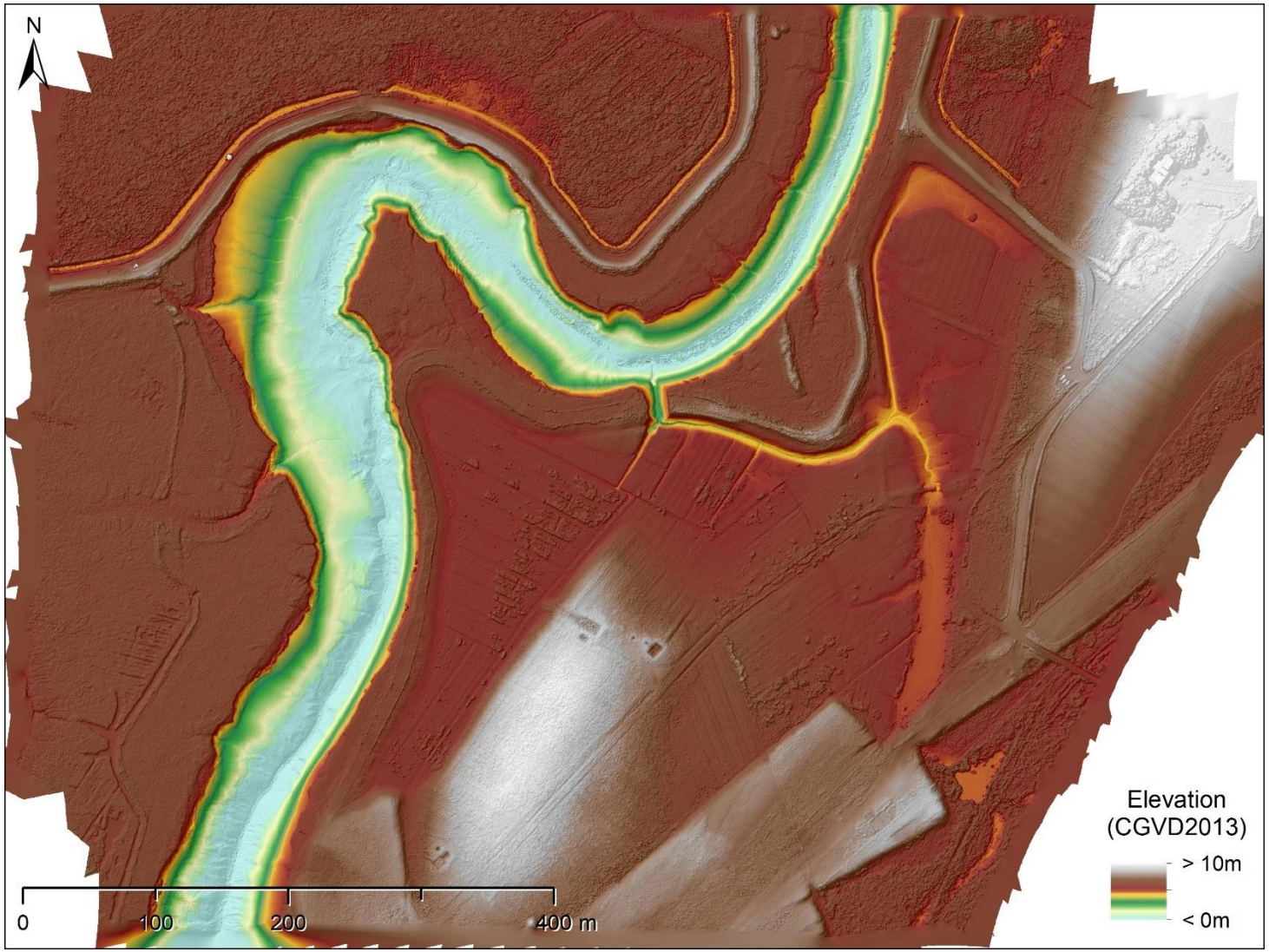

Figure D-8. Elevation model produced by Agisoft Metashape (displayed as a combined colour ramp and hillshade). Imagery data collected with a DJI Phantom 4 RTK RPAS during a full site survey of Converse, August 21, 2020. Resolution is 3.5 cm, and vertical RMSE is 1.9 cm.

Figure D-9. RGB orthomosaic produced by Agisoft Metashape. Imagery data collected with a DJI Phantom 4 RTK RPAS during a full site survey of Converse, October 5, 2020. Resolution is 3.5cm and horizontal RMSE expected to be less than the resolution.

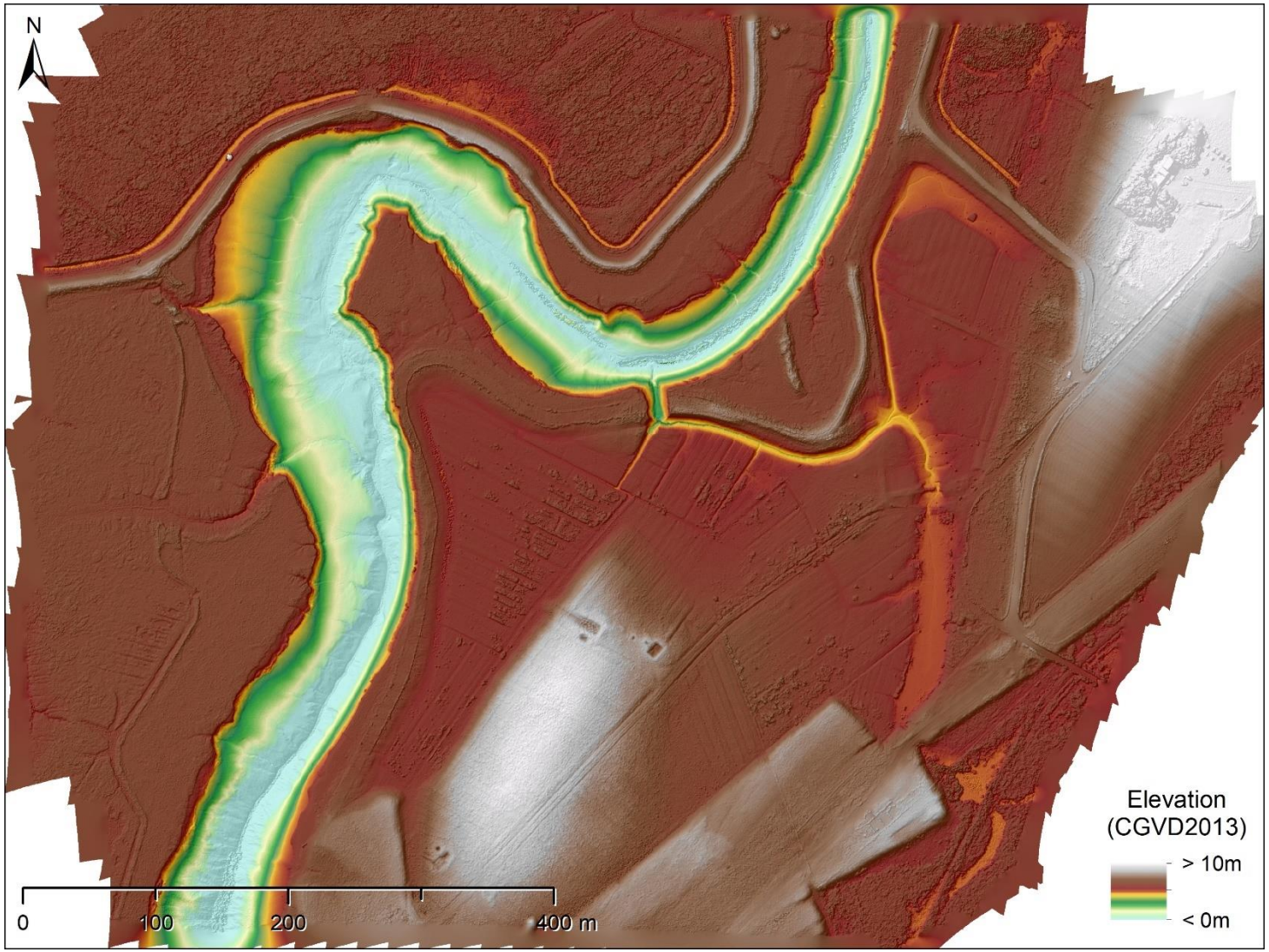

Figure D-10. Elevation model produced by Agisoft Metashape (displayed as a combined colour ramp and hillshade). Imagery data collected with a DJI Phantom 4 RTK RPAS during a full site survey of Converse, October 5, 2020. Resolution is 3.5 cm, and vertical RMSE is 2.3 cm.

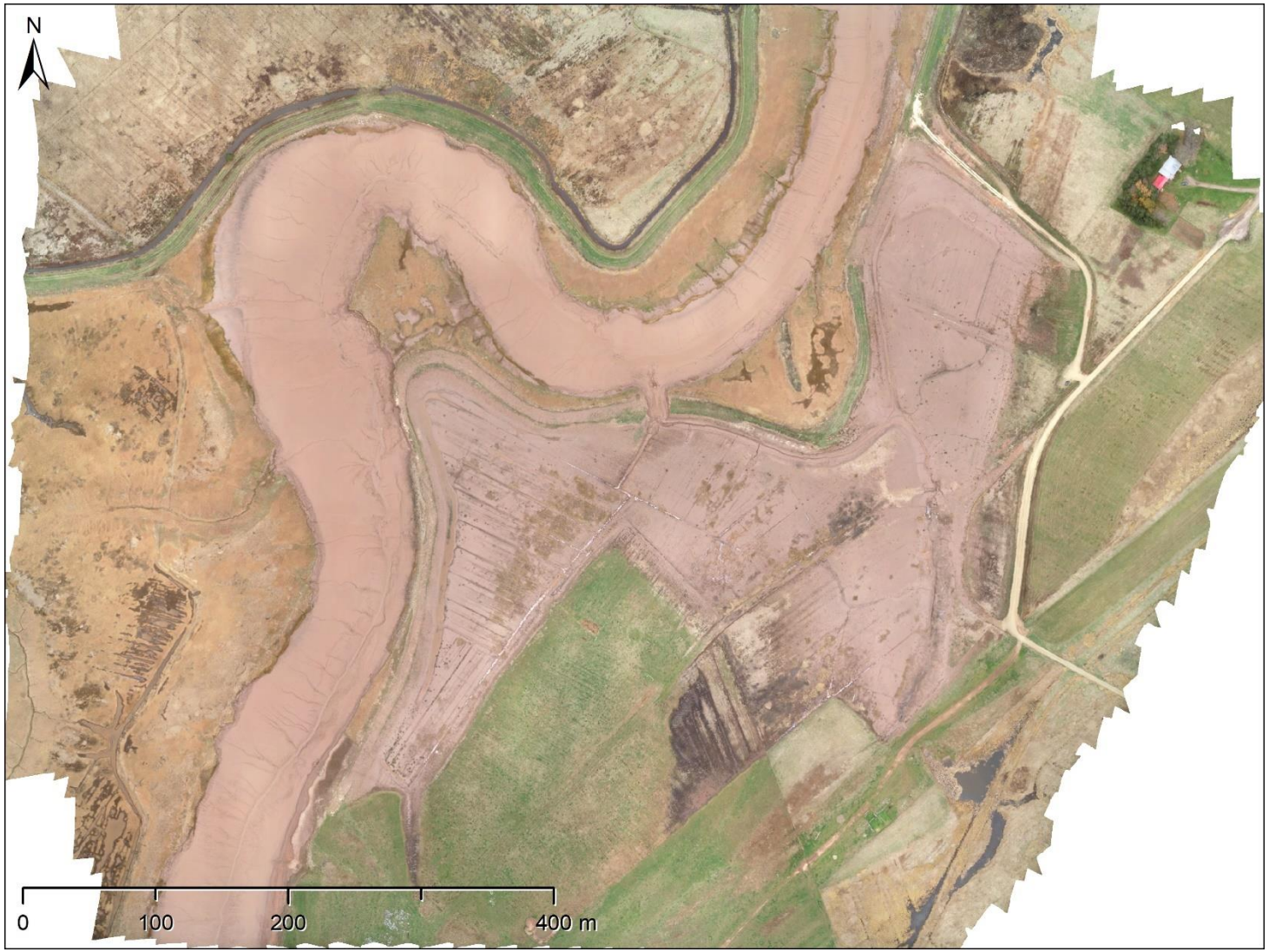

Figure D-11. RGB orthomosaic produced by Agisoft Metashape. Imagery data collected with a DJI Phantom 4 RTK RPAS during a full site survey of Converse, November 8, 2020. Resolution is 3.5cm and horizontal RMSE expected to be less than the resolution.

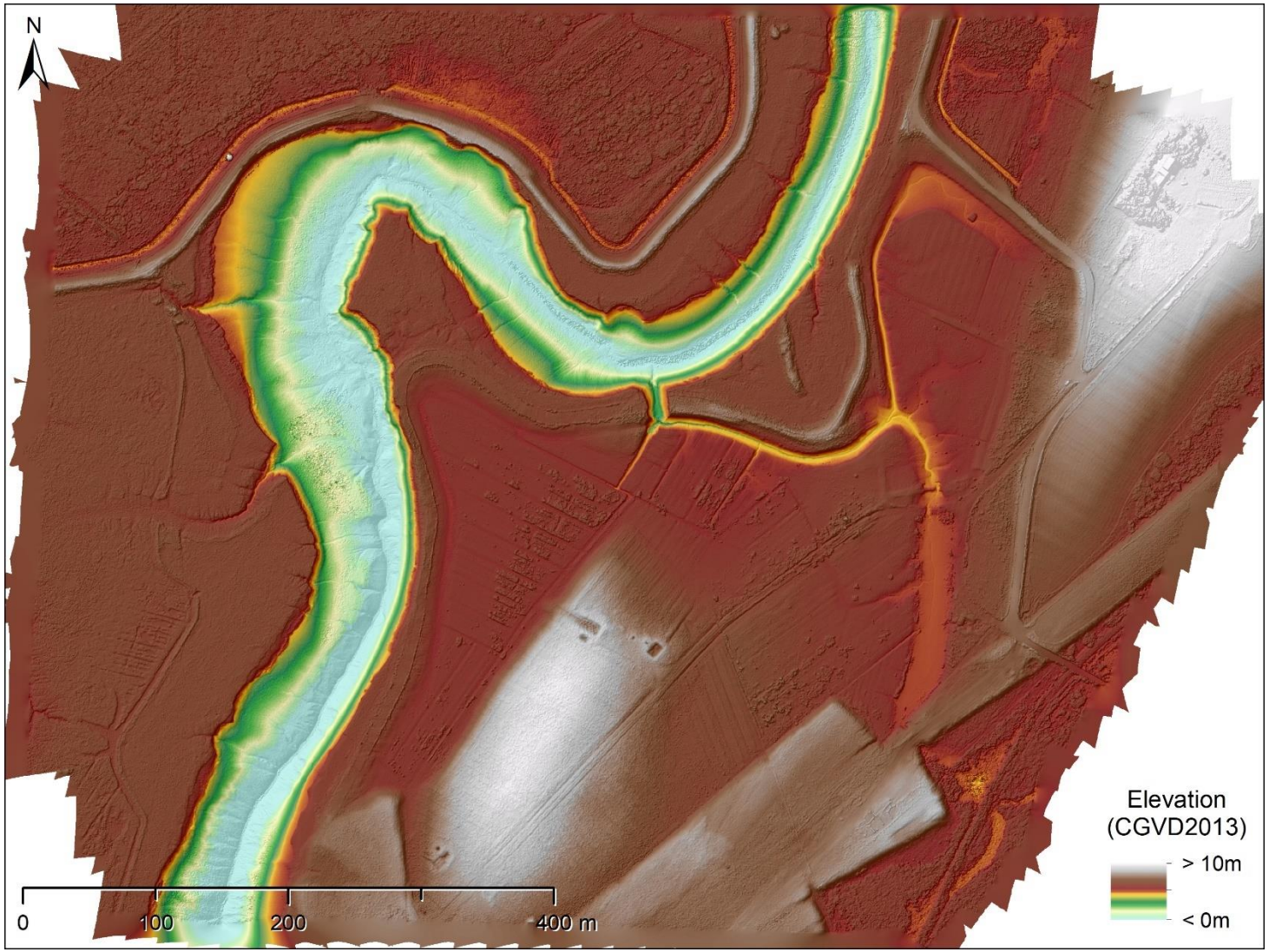

Figure D-12. Elevation model produced by Agisoft Metashape (displayed as a combined colour ramp and hillshade). Imagery data collected with a DJI Phantom 4 RTK RPAS during a full site survey of Converse, November 8, 2020. Resolution is 3.5 cm, and vertical RMSE is 1.6 cm.

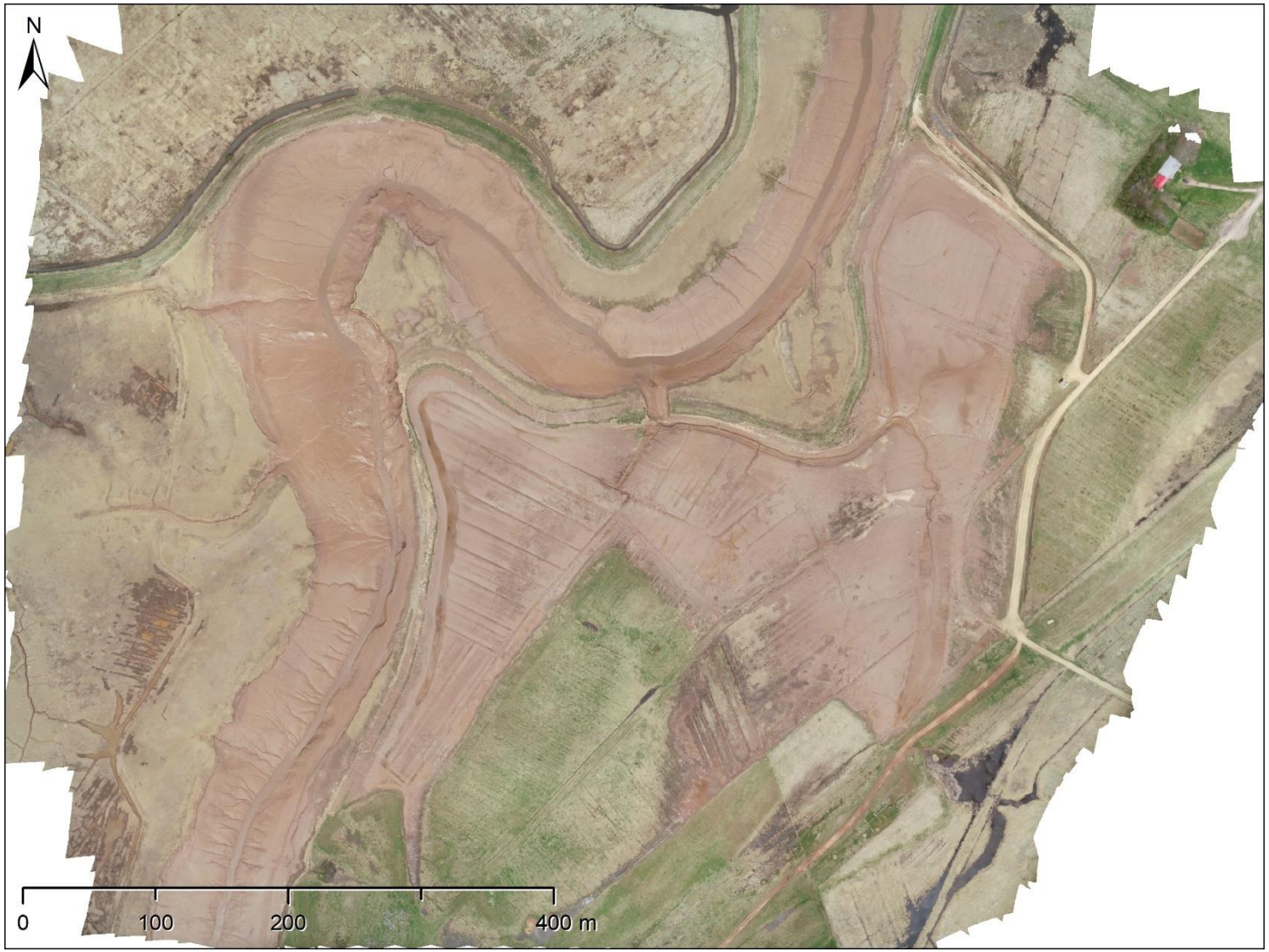

Figure D-13. RGB orthomosaic produced by Agisoft Metashape. Imagery data collected with a DJI Phantom 4 RTK RPAS during a full site survey of Converse, May 4, 2021. Resolution is 3.5cm and horizontal RMSE expected to be less than the resolution.

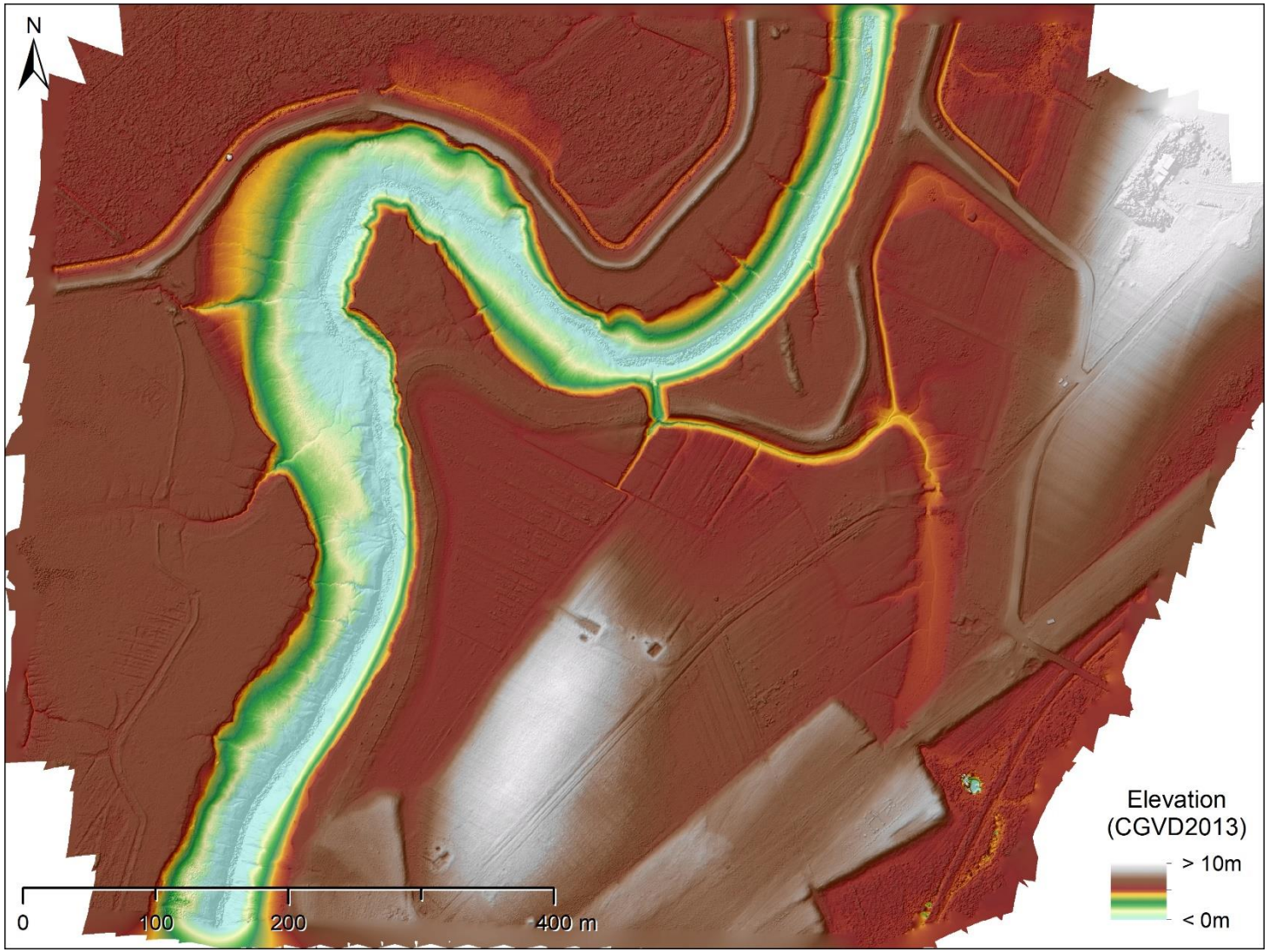

Figure D-14. Elevation model produced by Agisoft Metashape (displayed as a combined colour ramp and hillshade). Imagery data collected with a DJI Phantom 4 RTK RPAS during a full site survey of Converse, May 4, 2021. Resolution is 3.5 cm, and vertical RMSE is 1.7 cm.

Appendix E - Structure from Motion Data Products (Target Area)

Figure E-1. RGB orthomosaic produced by Agisoft Metashape. Imagery data collected with a DJI Phantom 4 RTK RPAS during a target area survey of Converse, November 24, 2019. Resolution is 2 cm and horizontal RMSE expected to be less than the resolution.

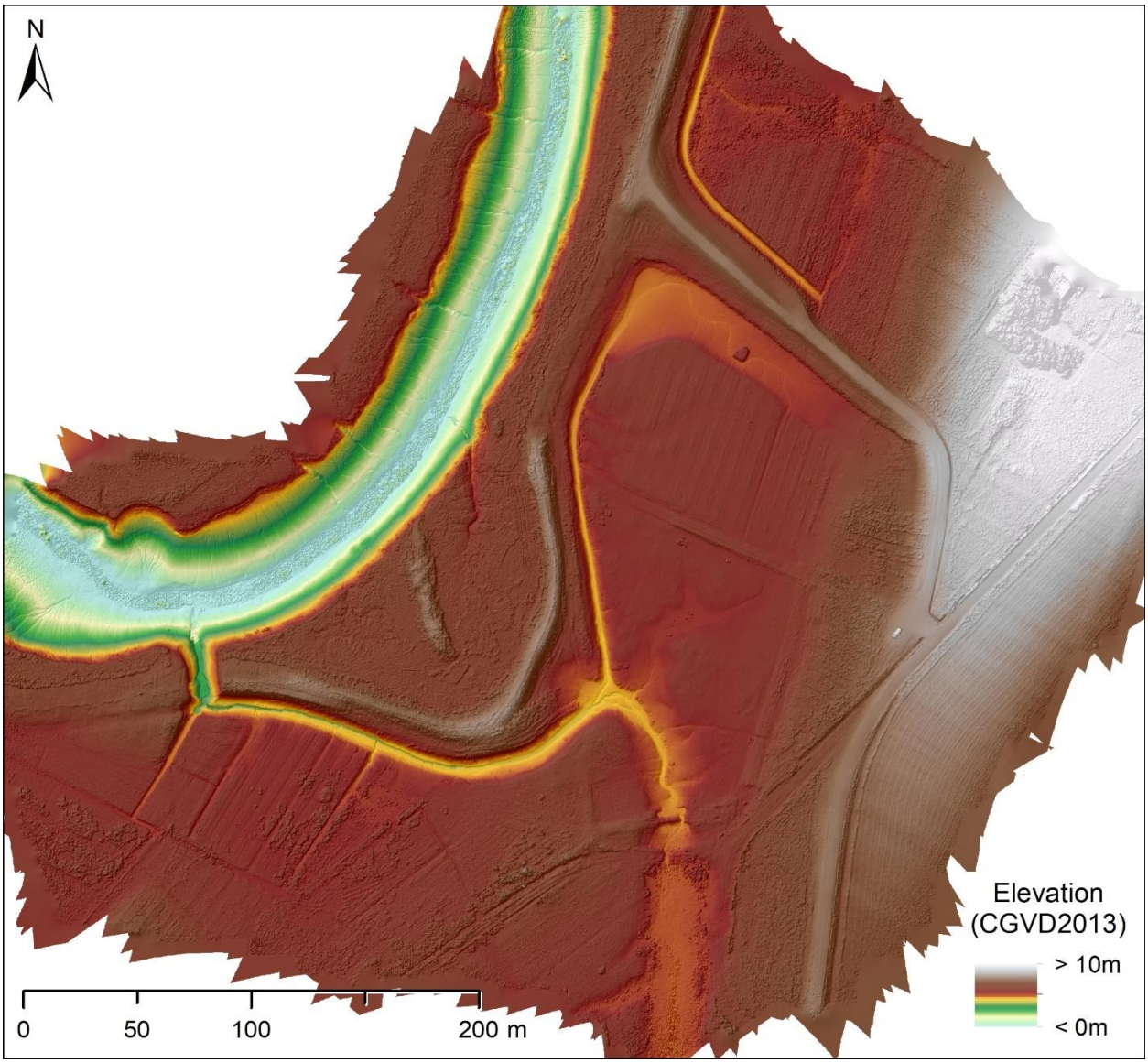

Figure E-2. Elevation model produced by Agisoft Metashape (displayed as a combined colour ramp and hillshade). Imagery data collected with a DJI Phantom 4 RTK RPAS during a target area survey of Converse, November 24, 2019. Resolution is 2 cm, and vertical RMSE is 1.8 cm.

Figure E-3. RGB orthomosaic produced by Agisoft Metashape. Imagery data collected with a DJI Phantom 4 RTK RPAS during a target area survey of Converse, June 1, 2020. Resolution is 2 cm and horizontal RMSE expected to be less than the resolution.

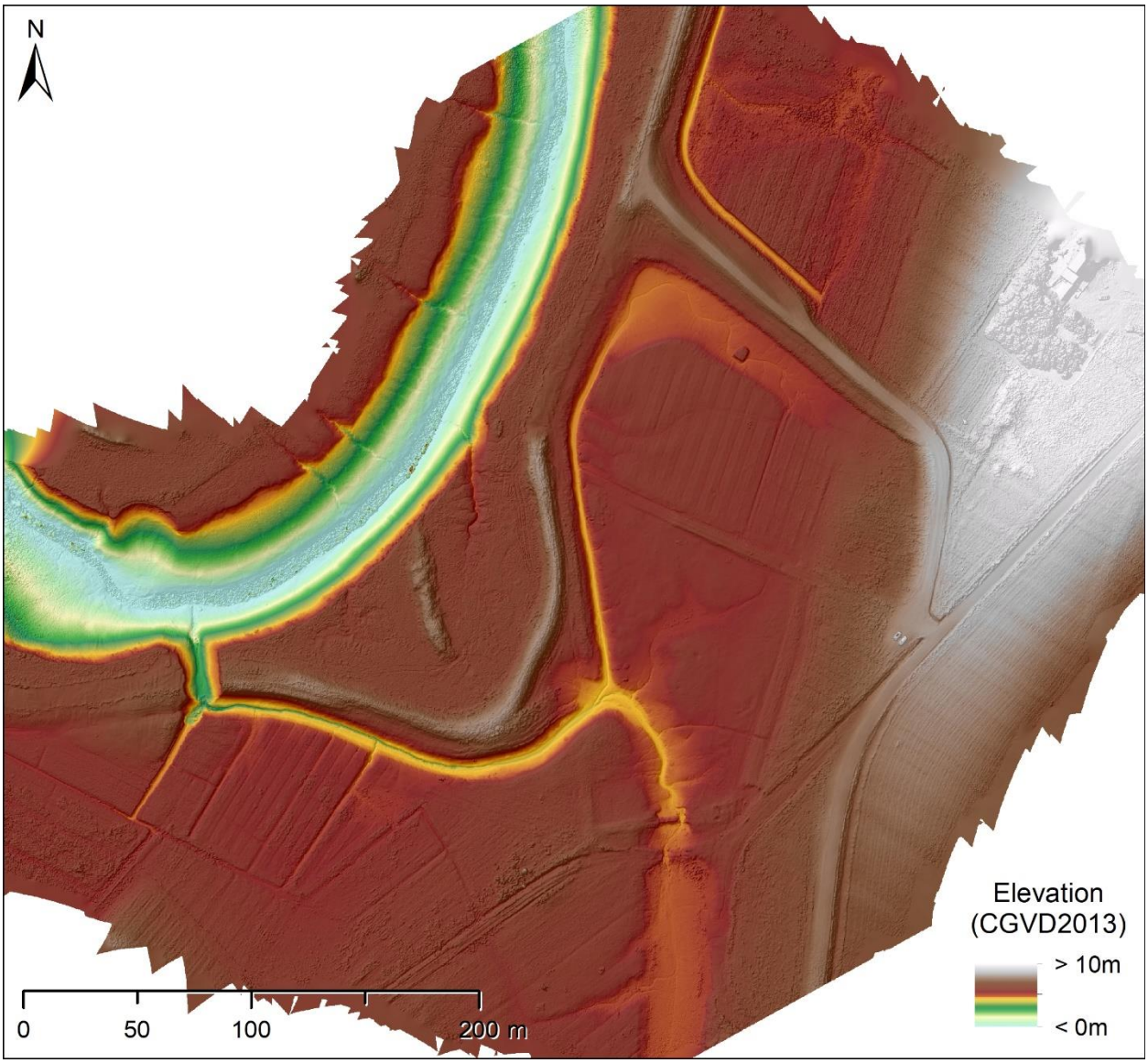

Figure E-4. Elevation model produced by Agisoft Metashape (displayed as a combined colour ramp and hillshade). Imagery data collected with a DJI Phantom 4 RTK RPAS during a target area survey of Converse, June 1, 2020. Resolution is 2 cm, and vertical RMSE is 1.4 cm.

Figure E-5. RGB orthomosaic produced by Agisoft Metashape. Imagery data collected with a DJI Phantom 4 RTK RPAS during a target area survey of Converse, July 9, 2020. Resolution is 2 cm and horizontal RMSE expected to be less than the resolution.

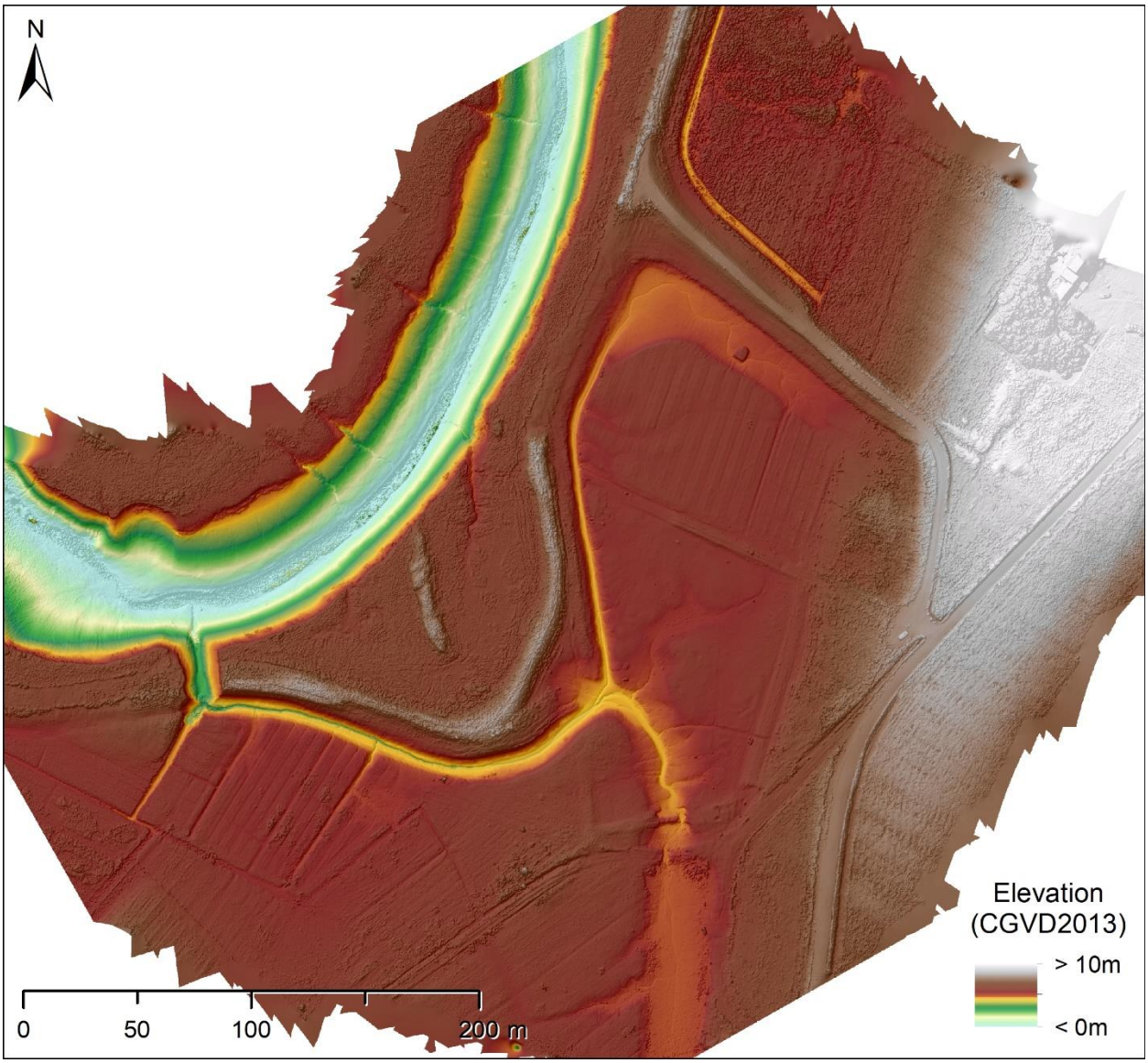

Figure E-6. Elevation model produced by Agisoft Metashape (displayed as a combined colour ramp and hillshade). Imagery data collected with a DJI Phantom 4 RTK RPAS during a target area survey of Converse, July 9, 2020. Resolution is 2 cm, and vertical RMSE is 1.4 cm.

Figure E-7. RGB orthomosaic produced by Agisoft Metashape. Imagery data collected with a DJI Phantom 4 RTK RPAS during a target area survey of Converse, August 21, 2020. Resolution is 2 cm and horizontal RMSE expected to be less than the resolution.

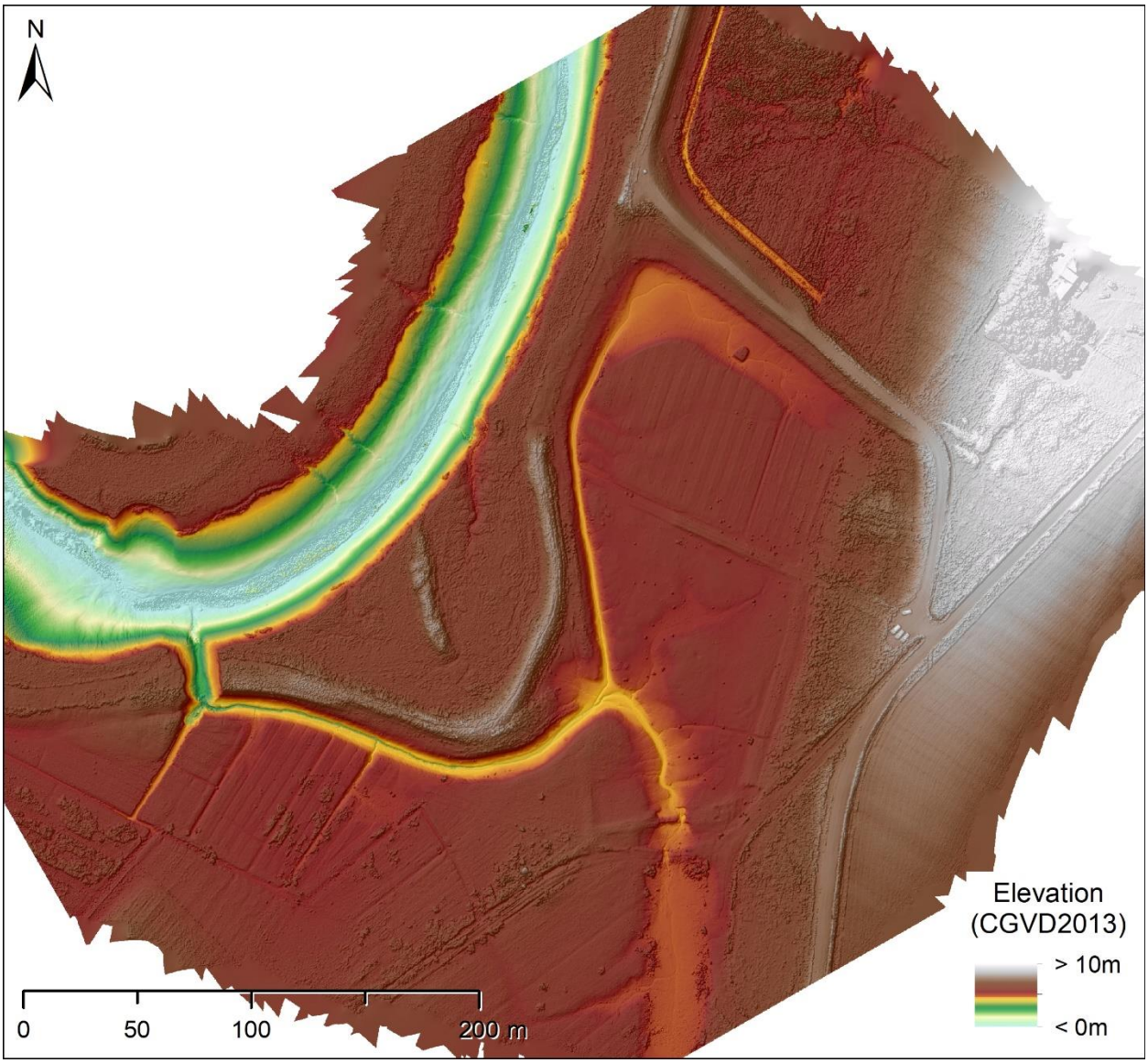

Figure E-8. Elevation model produced by Agisoft Metashape (displayed as a combined colour ramp and hillshade). Imagery data collected with a DJI Phantom 4 RTK RPAS during a target area survey of Converse, August 21, 2020. Resolution is 2 cm, and vertical RMSE is 2.0 cm.

Figure E-9. RGB orthomosaic produced by Agisoft Metashape. Imagery data collected with a DJI Phantom 4 RTK RPAS during a target area survey of Converse, October 5, 2020. Resolution is 2 cm and horizontal RMSE expected to be less than the resolution.

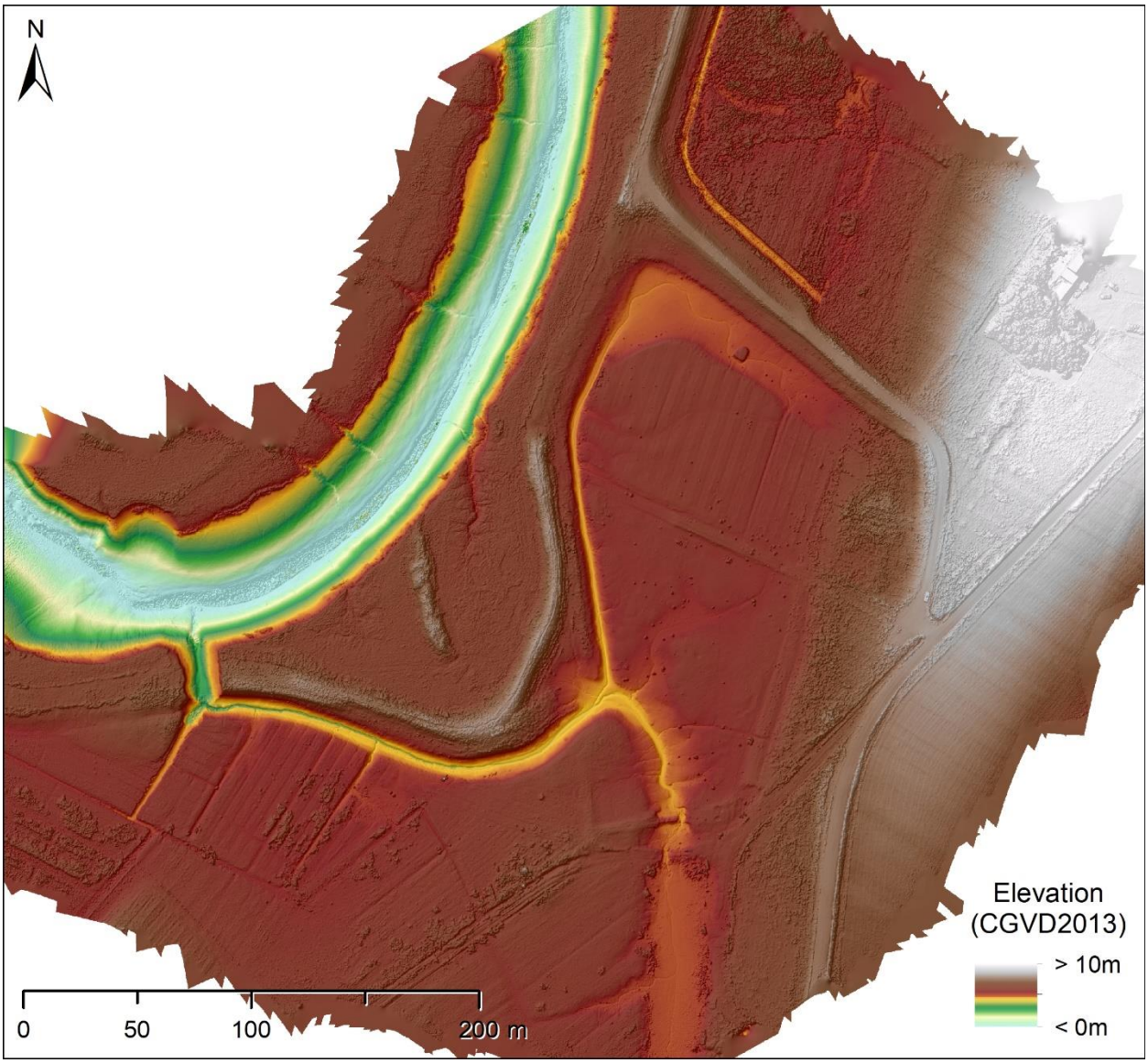

Figure E-10. Elevation model produced by Agisoft Metashape (displayed as a combined colour ramp and hillshade). Imagery data collected with a DJI Phantom 4 RTK RPAS during a target area survey of Converse, October 5, 2020. Resolution is 2 cm, and vertical RMSE is 1.7 cm.

Figure E-11. RGB orthomosaic produced by Agisoft Metashape. Imagery data collected with a DJI Phantom 4 RTK RPAS during a target area survey of Converse, November 8, 2020. Resolution is 2 cm and horizontal RMSE expected to be less than the resolution.

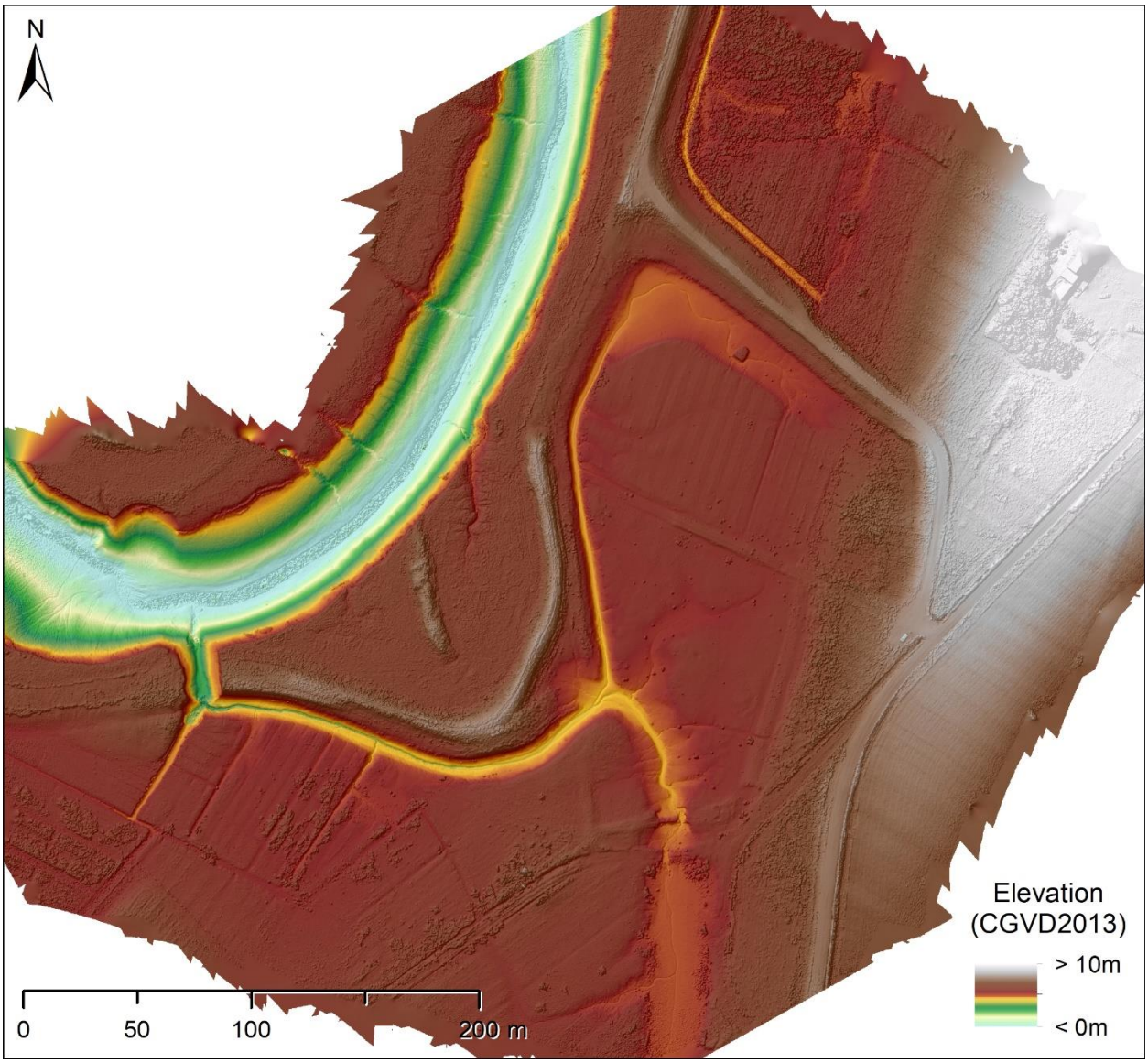

Figure E-12. Elevation model produced by Agisoft Metashape (displayed as a combined colour ramp and hillshade). Imagery data collected with a DJI Phantom 4 RTK RPAS during a target area survey of Converse, November 8, 2020. Resolution is 2 cm, and vertical RMSE is 1.3 cm.

Figure E-13. RGB orthomosaic produced by Agisoft Metashape. Imagery data collected with a DJI Phantom 4 RTK RPAS during a target area survey of Converse, May 4, 2021. Resolution is 2 cm and horizontal RMSE expected to be less than the resolution.

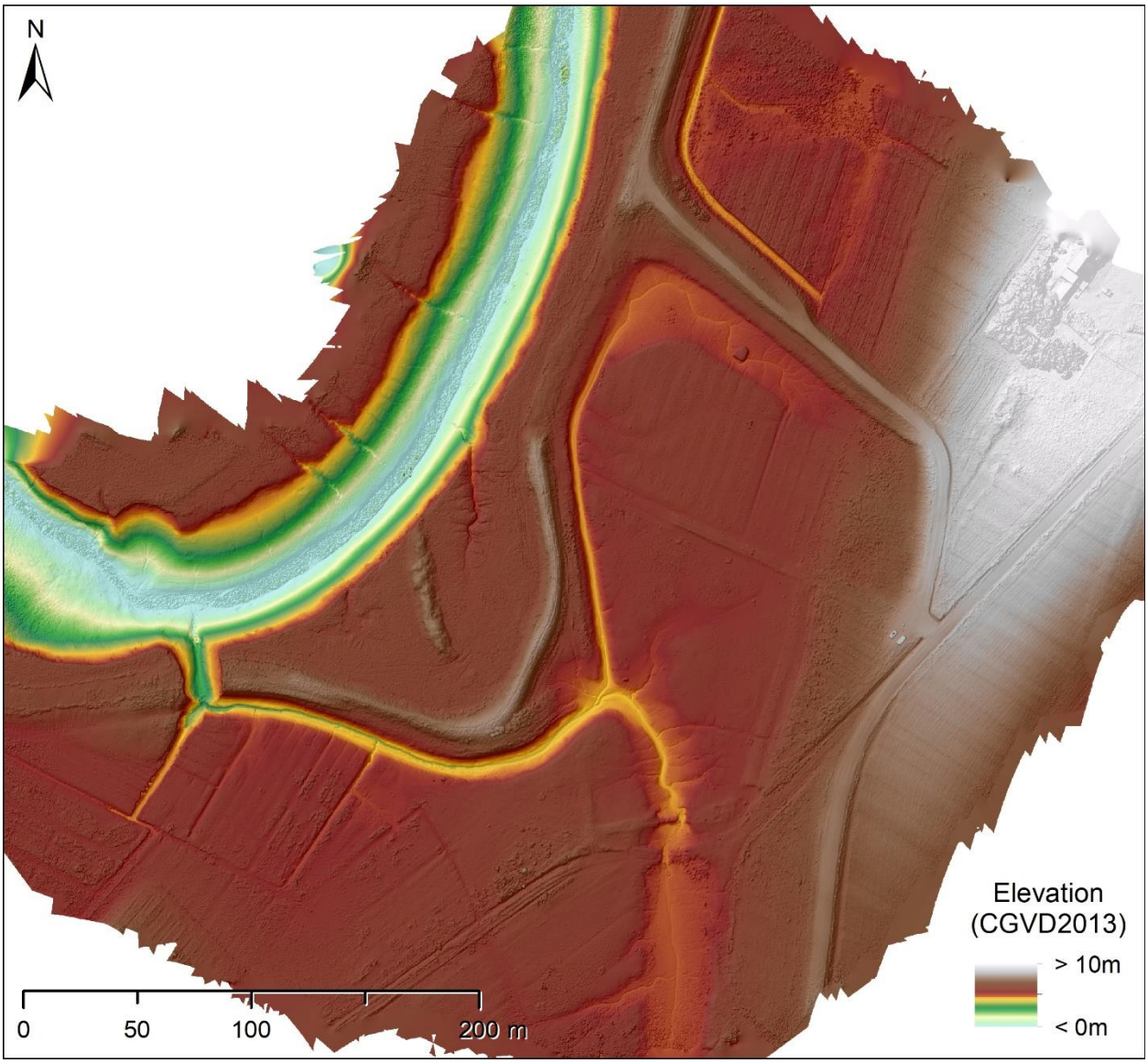

Figure E-14. Elevation model produced by Agisoft Metashape (displayed as a combined colour ramp and hillshade). Imagery data collected with a DJI Phantom 4 RTK RPAS during a target area survey of Converse, May 4, 2021. Resolution is 2 cm, and vertical RMSE is 2.1 cm.

Appendix F - Additional Volumetric Analysis Results

Table F.1 outlines the volumetric change results for the river area of the Full Site datasets. These results varied significantly from the site results in terms of variability of total volumetric change values with differing LoDs. Within the river area, total volumetric change values remained relatively consistent with no LoD, a 68% CI LoD, and a 95% CI LoD. All volumetric changes within the river area were net positive, with the largest change occurring in the 1-year dataset: 12607.9 ± 2137.6 m^3 with no LoD, 12610.5 ± 2000.7 m^3 with a 68% CI LoD, and 12620.3 ± 1877.4 m^3 with a 95% CI LoD.

The river area volumetric change results for the Target Area DoDs are outlined in Table F.2. Trends in these results were very similar to those in the river area of the Full Site DoDs, and all time periods had a net positive volumetric change. The highest amount of total volumetric change occurred over the 1-year period: 908.3 ± 330.6 m^3 with no LoD, 910.0 ± 300.1 m^3 with a 68% CI LoD, and 919.3 ± 273.4 m^3 with a 95% CI LoD. Total volumetric change values did not vary a lot between different LoDs in all time periods, although volumetric uncertainties were relatively high compared to measured change.

Tables F.3 and F.4 show results of the volumetric analyses of the problematic Target Area datasets (spring-summer and summer-fall), and Tables F.5 to F.10 show all results of the volumetric analyses but with the Lane et al. (2003) equation utilized to calculate volumetric uncertainty.

Table F-1. Results of the volumetric change analysis for the river area of the Full Site datasets using no LoD, an LoD with 68% CI and an LoD with 95% CI. Volumetric uncertainties were calculated using the Taylor (1997) equation.

Time Frame	No LoD		68% CI			95% CI		
	Total Volumetric Change (m^3)	Average Vertical Change (cm)	LOD (cm)	Total Volumetric Change (m^3)	Average Vertical Change (cm)	LOD (cm)	Total Volumetric Change (m^3)	Average Vertical Change (cm)
2019/11/24 - 2020/10/05 (1-Year)	12607.9 ± 2137.6	17.2 ± 2.9	2.9	12610.5 ± 2000.7	18.4 ± 2.9	5.7	12620.3 ± 1877.4	19.6 ± 2.9
2019/11/24 - 2020/06/01 (Winter)	4007.7 ± 1625.2	5.5 ± 2.2	2.2	4008.4 ± 1508.2	5.9 ± 2.2	4.4	4015.3 ± 1394.6	6.4 ± 2.2
2020/06/01 - 2020/10/05 (Growing Season)	8599.3 ± 1932.6	11.8 ± 2.6	2.6	8567.6 ± 1670.4	13.5 ± 2.6	5.2	8413.8 ± 1434.2	15.9 ± 2.6
2020/06/01 - 2020/08/21 (Spring – Summer)	5100.8 ± 1683.8	7.0 ± 2.3	2.3	5074.4 ± 1410.3	8.3 ± 2.3	4.5	4939.1 ± 1164.1	9.8 ± 2.3
2020/08/21 - 2020/10/05 (Summer - Fall)	3498.5 ± 2181.5	4.8 ± 3.0	3.0	3343.6 ± 1521.4	6.6 ± 3.0	5.8	3092.2 ± 1067.9	8.6 ± 3.0

*Table F-2. Results of the volumetric change analysis for the river area of the Target Area datasets using no LoD, an LoD with 68% CI and an LoD with 95% CI. Volumetric uncertainties were calculated using the Taylor (1997) equation. * denotes unreliable results.*

Time Frame	No LoD		68% CI			95% CI		
	Total Volumetric Change (m^3)	Average Vertical Change (cm)	LOD (cm)	Total Volumetric Change (m^3)	Average Vertical Change (cm)	LOD (cm)	Total Volumetric Change (m^3)	Average Vertical Change (cm)
2019/11/24 - 2020/10/05 (1-Year)	908.3 ± 330.6	6.8 ± 2.5	2.5	910.0 ± 300.1	7.5 ± 2.5	4.9	919.3 ± 273.4	8.3 ± 2.5
2019/11/24 - 2020/06/01 (Winter)	381.7 ± 304.0	2.9 ± 2.3	2.3	383.8 ± 278.4	3.1 ± 2.3	4.5	393.1 ± 252.0	3.6 ± 2.3
2020/06/01 - 2020/10/05 (Growing Season)	540.7 ± 293.4	4.1 ± 2.2	2.2	538.0 ± 225.2	5.3 ± 2.2	4.3	527.6 ± 166.9	7.0 ± 2.2
2020/06/01 - 2020/08/21 (Spring – Summer)	242.0 ± 325.3*	1.8 ± 2.4*	2.4	237.9 ± 217.3*	2.7 ± 2.4*	4.8	223.2 ± 136.9*	4.0 ± 2.4*
2020/08/21 - 2020/10/05 (Summer - Fall)	284.8 ± 349.7*	2.1 ± 2.6*	2.6	272.1 ± 182.5*	3.9 ± 2.6*	5.1	208.7 ± 88.8*	6.2 ± 2.6*

Table F-3. Results of the volumetric change analysis for the site area of the problematic Target Area datasets using no LoD, an LoD with 68% CI and an LoD with 95% CI. Volumetric uncertainties were calculated using the Taylor (1997) equation. Please note, presented data are considered unreliable due to RPAS surface offsets.

Time Frame	No LoD		68% CI			95% CI		
	Total Volumetric Change (m^3)	Average Vertical Change (cm)	LOD (cm)	Total Volumetric Change (m^3)	Average Vertical Change (cm)	LOD (cm)	Total Volumetric Change (m^3)	Average Vertical Change (cm)
2020/06/01 - 2020/08/21 (Spring – Summer)	55.2 ± 1023.1	0.1 ± 2.4	2.4	12.6 ± 166.8	0.2 ± 2.4	4.8	5.2 ± 11.1	1.2 ± 2.4
2020/08/21 - 2020/10/05 (Summer - Fall)	611.5 ± 1100.1	1.5 ± 2.6	2.6	356.4 ± 288.8	3.2 ± 2.6	5.1	33.5 ± 22.4	3.9 ± 2.6

Table F-4. Results of the volumetric change analysis for areas of interest in problematic Target Area datasets using no LoD, an LoD with 68% CI and an LoD with 95% CI. Volumetric uncertainties were calculated using the Taylor (1997) equation. Please note, presented data are considered unreliable due to RPAS surface offsets.

Area	Time Frame	No LoD		68% CI			95% CI		
		Total Volumetric Change (m^3)	Average Vertical Change (cm)	LOD (cm)	Total Volumetric Change (m^3)	Average Vertical Change (cm)	LOD (cm)	Total Volumetric Change (m^3)	Average Vertical Change (cm)
Borrow Pit	2020/06/01 - 2020/08/21 (Spring – Summer)	-72.6 ± 81.6	-2.1 ± 2.4	2.4	-41.7 ± 31.5	-3.2 ± 2.4	4.8	-1.7 ± 0.8	-5.0 ± 2.4
	2020/08/21 - 2020/10/05 (Summer - Fall)	100.2 ± 87.7	2.9 ± 2.6	2.6	77.4 ± 47.4	4.3 ± 2.6	5.1	24.3 ± 10.9	5.9 ± 2.6
Drainage Channels	2020/06/01 - 2020/08/21 (Spring – Summer)	8.4 ± 28.0	0.6 ± 2.4	2.4	4.6 ± 14.0	0.8 ± 2.4	4.8	-1.5 ± 6.3	-0.6 ± 2.4
	2020/08/21 - 2020/10/05 (Summer - Fall)	-5.5 ± 30.0	-0.4 ± 2.6	2.6	-4.6 ± 7.9	-1.5 ± 2.6	5.1	-5.2 ± 2.7	-5.1 ± 2.6
Main Channel Mouth	2020/06/01 - 2020/08/21 (Spring – Summer)	6.2 ± 9.3	1.4 ± 2.4	2.4	5.3 ± 6.2	2.1 ± 2.4	4.8	3.1 ± 3.9	2.0 ± 2.4
	2020/08/21 - 2020/10/05 (Summer - Fall)	-7.6 ± 10.0	-1.7 ± 2.6	2.6	-6.2 ± 3.3	-5.0 ± 2.6	5.1	-3.7 ± 1.1	-8.6 ± 2.6

Table F-5. Results of the volumetric change analysis for the site area of the Full Site datasets using no LoD, an LoD with 68% CI and an LoD with a 98% CI. Volumetric uncertainties were calculated using the Lane et al. (2003) equation.

Time Frame	No LoD		68% CI			95% CI		
	Total Volumetric Change (m^3)	Average Vertical Change (cm)	LOD (cm)	Total Volumetric Change (m^3)	Average Vertical Change (cm)	LOD (cm)	Total Volumetric Change (m^3)	Average Vertical Change (cm)
2019/11/24 - 2020/10/05 (1-Year)	1464.3 ± 24.6	2.5 ± <0.1	2.9	1228.0 ± 18.2	3.9 ± 0.1	5.7	418.8 ± 10.1	4.3 ± 0.1
2019/11/24 - 2020/06/01 (Winter)	-397.6 ± 18.7	-0.7 ± <0.1	2.2	-389.9 ± 12.0	-1.7 ± 0.1	4.4	-299.4 ± 7.0	-3.7 ± 0.1
2020/06/01 - 2020/10/05 (Growing Season)	1860.8 ± 22.2	3.2 ± <0.1	2.6	1567.1 ± 17.9	4.2 ± 0.1	5.2	451.7 ± 8.1	5.8 ± 0.1
2020/06/01 - 2020/08/21 (Spring – Summer)	430.7 ± 19.4	0.7 ± <0.1	2.3	273.8 ± 9.4	2.0 ± 0.1	4.5	39.6 ± 3.0	2.8 ± 0.2
2020/08/21 - 2020/10/05 (Summer - Fall)	1429.7 ± 25.1	2.5 ± <0.1	3.0	865.5 ± 15.1	4.1 ± 0.1	5.8	123.4 ± 4.6	6.3 ± 0.2

Table F-6. Results of the volumetric change analysis for the river area of the Full Site datasets using no LoD, an LoD with 68% CI and an LoD with 95% CI. Volumetric uncertainties were calculated using the Lane et al. (2003) equation.

Time Frame	No LoD		68% CI			95% CI		
	Total Volumetric Change (m^3)	Average Vertical Change (cm)	LOD (cm)	Total Volumetric Change (m^3)	Average Vertical Change (cm)	LOD (cm)	Total Volumetric Change (m^3)	Average Vertical Change (cm)
2019/11/24 - 2020/10/05 (1-Year)	12607.9 ± 27.7	17.2 ± <0.1	2.9	12610.5 ± 26.8	18.4 ± <0.1	5.7	12620.3 ± 25.9	19.6 ± <0.1
2019/11/24 - 2020/06/01 (Winter)	4007.7 ± 21.0	5.5 ± <0.1	2.2	4008.4 ± 20.3	5.9 ± <0.1	4.4	4015.3 ± 19.5	6.4 ± <0.1
2020/06/01 - 2020/10/05 (Growing Season)	8599.3 ± 25.0	11.8 ± <0.1	2.6	8567.6 ± 23.2	13.5 ± <0.1	5.2	8413.8 ± 21.5	15.5 ± <0.1
2020/06/01 - 2020/08/21 (Spring – Summer)	5100.8 ± 21.8	7.0 ± <0.1	2.3	5074.4 ± 19.9	8.3± <0.1	4.5	4939.1 ± 18.1	9.8 ± <0.1
2020/08/21 - 2020/10/05 (Summer - Fall)	3498.5 ± 28.2	4.8 ± <0.1	3.0	3343.6 ± 23.6	6.6 ± 0.1	5.8	3092.2 ± 19.7	8.6 ± 0.1

*Table F-7. Results of the volumetric change analysis for the site area of the Target Area datasets using no LoD, an LoD with 68% CI and an LoD with 95% CI. Volumetric uncertainties were calculated using the Lane et al. (2003) equation. * denotes unreliable results.*

Time Frame	No LoD		68% CI			95% CI		
	Total Volumetric Change (m^3)	Average Vertical Change (cm)	LOD (cm)	Total Volumetric Change (m^3)	Average Vertical Change (cm)	LOD (cm)	Total Volumetric Change (m^3)	Average Vertical Change (cm)
2019/11/24 - 2020/10/05 (1-Year)	540.4 ± 31.1	1.3 ± 0.1	2.5	440.9 ± 22.1	2.1 ± 0.1	4.9	46.5 ± 11.3	0.9 ± 0.2
2019/11/24 - 2020/06/01 (Winter)	-126.3 ± 28.6	-0.3 ± 0.1	2.3	-184.7 ± 18.4	-1.1 ± 0.1	4.5	-163.8 ± 9.6	-3.5 ± 0.2
2020/06/01 - 2020/10/05 (Growing Season)	666.6 ± 27.6	1.6 ± 0.1	2.2	369.2 ± 15.3	2.9 ± 0.1	4.3	67.0 ± 5.7	3.7 ± 0.3
2020/06/01 - 2020/08/21 (Spring – Summer)	55.2 ± 30.6*	0.1 ± 0.1*	2.4	12.6 ± 12.4*	0.2 ± 0.2*	4.8	5.2 ± 3.2*	1.2 ± 0.7*
2020/08/21 - 2020/10/05 (Summer - Fall)	611.5 ± 32.9*	1.5 ± 0.1*	2.6	356.4 ± 16.9*	3.2 ± 0.2*	5.1	33.5 ± 4.7*	3.9 ± 0.6*

*Table F-8. Results of the volumetric change analysis for the river area of the Target Area datasets using no LoD, an LoD with 68% CI and an LoD with 95% CI. Volumetric uncertainties were calculated using the Lane et al. (2003) equation. * denotes unreliable results.*

Time Frame	No LoD		68% CI			95% CI		
	Total Volumetric Change (m^3)	Average Vertical Change (cm)	LOD (cm)	Total Volumetric Change (m^3)	Average Vertical Change (cm)	LOD (cm)	Total Volumetric Change (m^3)	Average Vertical Change (cm)
2019/11/24 - 2020/10/05 (1-Year)	908.3 ± 17.5	6.8 ± 0.1	2.5	910.0 ± 16.7	7.5 ± 0.1	4.9	919.3 ± 16.0	8.3 ± 0.1
2019/11/24 - 2020/06/01 (Winter)	381.7 ± 16.1	2.9 ± 0.1	2.3	383.8 ± 15.4	3.1 ± 0.1	4.5	393.1 ± 14.7	3.6 ± 0.1
2020/06/01 - 2020/10/05 (Growing Season)	540.7 ± 15.6	4.1 ± 0.1	2.2	538.0 ± 13.6	5.3 ± 0.1	4.3	527.6 ± 11.7	7.0 ± 0.2
2020/06/01 - 2020/08/21 (Spring – Summer)	242.0 ± 17.3*	1.8 ± 0.1*	2.4	237.9 ± 14.1*	2.7 ± 0.2*	4.8	223.2 ± 11.2*	4.0 ± 0.2*
2020/08/21 - 2020/10/05 (Summer - Fall)	284.8 ± 18.6*	2.1 ± 0.1*	2.6	272.1 ± 13.4*	3.9 ± 0.2*	5.1	208.7 ± 9.4*	6.2 ± 0.3*

Table F-9. Results of the volumetric change analysis for areas of interest in Target Area datasets using no LoD, an LoD with 68% CI and an LoD with 95% CI. Volumetric uncertainties were calculated using the Lane et al. (2003) equation.

Area	Time Frame	No LoD		68% CI			95% CI		
		Total Volumetric Change (m^3)	Average Vertical Change (cm)	LOD (cm)	Total Volumetric Change (m^3)	Average Vertical Change (cm)	LOD (cm)	Total Volumetric Change (m^3)	Average Vertical Change (cm)
Borrow Pit	2019/11/24 - 2020/10/05 (1-Year)	174.5 ± 8.8	5.0 ± 0.3	2.5	166.9 ± 7.8	6.4 ± 0.3	4.9	138.436 ± 6.379	7.9 ± 0.4
	2019/11/24 - 2020/06/01 (Winter)	146.8 ± 8.1	4.4 ± 0.2	2.3	140.4 ± 7.0	5.5 ± 0.3	4.5	114.3 ± 5.8	6.7 ± 0.3
	2020/06/01 - 2020/10/05 (Growing Season)	27.7 ± 7.8	0.8 ± 0.2	2.2	14.7 ± 3.2	2.6 ± 0.6	4.3	0.8 ± 0.6	3.8 ± 2.9
Drainage Channels	2019/11/24 - 2020/10/05 (1-Year)	-103.5 ± 5.1	-9.0 ± 0.5	2.5	-102.3 ± 4.0	-12.2 ± 0.5	4.9	-99.2 ± 3.9	-15.4 ± 0.6
	2019/11/24 - 2020/06/01 (Winter)	-106.2 ± 4.7	-9.3 ± 0.4	2.3	-104.8 ± 4.4	-10.8 ± 0.5	4.5	-98.5 ± 4.1	-11.7 ± 0.5
	2020/06/01 - 2020/10/05 (Growing Season)	3.8 ± 4.6	0.3 ± 0.4	2.2	2.5 ± 3.5	0.4 ± 0.5	4.3	-1.4 ± 2.7	-0.4 ± 0.7
Main Channel Mouth	2019/11/24 - 2020/10/05 (1-Year)	-127.0 ± 3.0	-33.2 ± 0.8	2.5	-126.9 ± 2.8	-36.4 ± 0.8	4.9	-126.634 ± 2.726	-39.3 ± 0.9
	2019/11/24 - 2020/06/01 (Winter)	-125.6 ± 2.7	-32.8 ± 0.7	2.3	-125.5 ± 2.6	-35.1 ± 0.7	4.5	-125.0 ± 2.6	-37.0 ± 0.8
	2020/06/01 - 2020/10/05 (Growing Season)	-1.0 ± 2.6	-0.2 ± 0.7	2.2	-1.5 ± 2.1	-0.6 ± 0.9	4.3	-2.7 ± 1.7	-1.6 ± 1.1

Table F-10. Results of the volumetric change analysis for areas of interest in problematic Target Area datasets using no LoD, an LoD with 68% CI and an LoD with 95% CI. Volumetric uncertainties were calculated using the Lane et al. (2003) equation. Please note, presented data are considered unreliable due to RPAS surface offsets.

Area	Time Frame	No LoD		68% CI			95% CI		
		Total Volumetric Change (m^3)	Average Vertical Change (cm)	LOD (cm)	Total Volumetric Change (m^3)	Average Vertical Change (cm)	LOD (cm)	Total Volumetric Change (m^3)	Average Vertical Change (cm)
Borrow Pit	2020/06/01 - 2020/08/21 (Spring – Summer)	-72.6 ± 81.6	-2.1 ± 2.4	2.4	-41.7 ± 31.5	-3.2 ± 2.4	4.8	-1.7 ± 0.8	-5.0 ± 2.4
	2020/08/21 - 2020/10/05 (Summer - Fall)	100.2 ± 87.7	2.9 ± 2.6	2.6	77.4 ± 47.4	4.3 ± 2.6	5.1	24.3 ± 10.9	5.9 ± 2.6
Drainage Channels	2020/06/01 - 2020/08/21 (Spring – Summer)	8.4 ± 28.0	0.6 ± 2.4	2.4	4.6 ± 14.0	0.8 ± 2.4	4.8	-1.5 ± 6.3	-0.6 ± 2.4
	2020/08/21 - 2020/10/05 (Summer - Fall)	-5.5 ± 30.0	-0.4 ± 2.6	2.6	-4.6 ± 7.9	-1.5 ± 2.6	5.1	-5.2 ± 2.7	-5.1 ± 2.6
Main Channel Mouth	2020/06/01 - 2020/08/21 (Spring – Summer)	6.2 ± 9.3	1.4 ± 2.4	2.4	5.3 ± 6.2	2.1 ± 2.4	4.8	3.1 ± 3.9	2.0 ± 2.4
	2020/08/21 - 2020/10/05 (Summer - Fall)	-7.6 ± 10.0	-1.7 ± 2.6	2.6	-6.2 ± 3.3	-5.0 ± 2.6	5.1	-3.7 ± 1.1	-8.6 ± 2.6

Appendix G - Channel Delineation Results

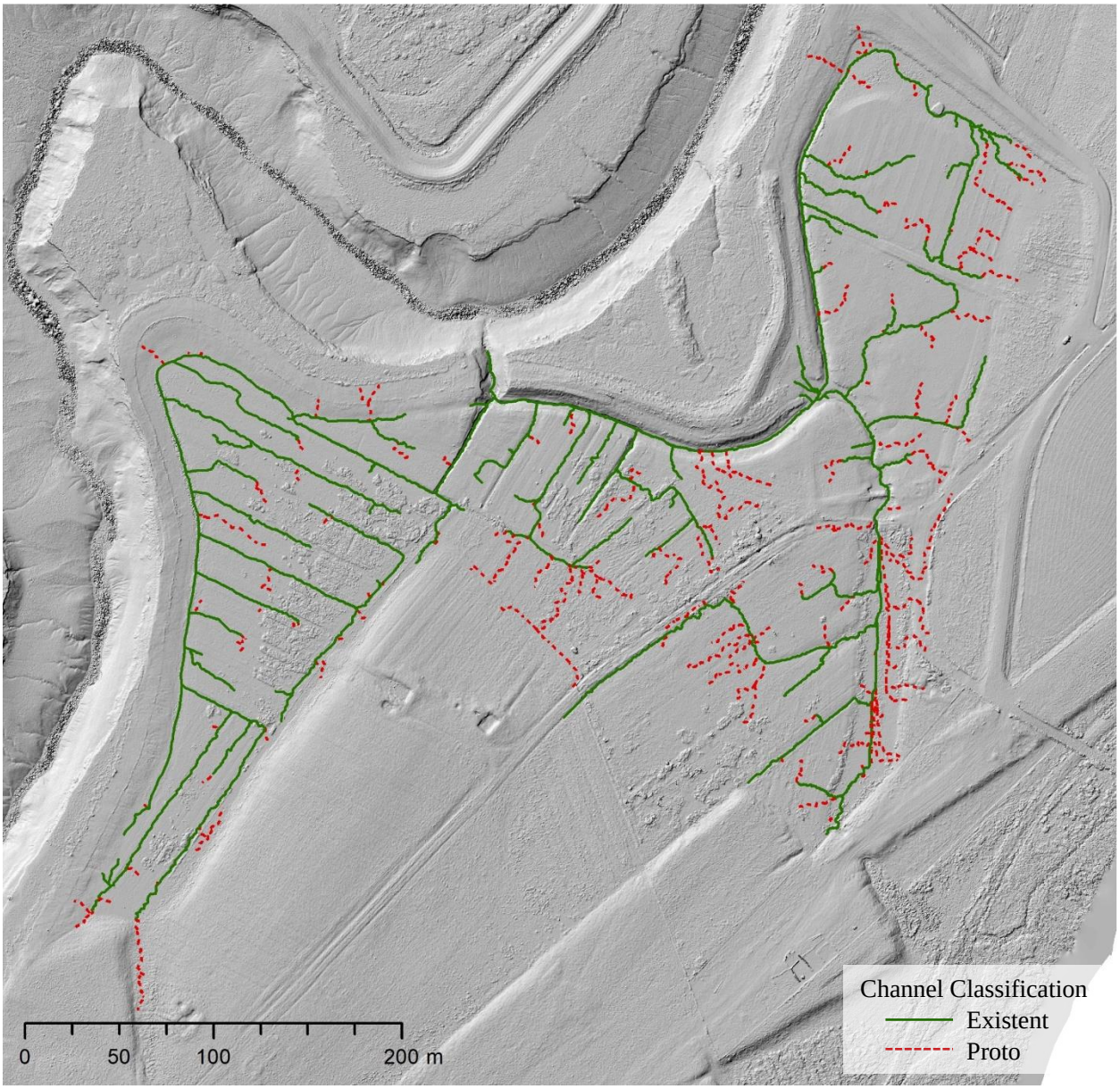

Figure G-1. Results of the channel delineation of the November 24, 2019 Full Site dataset.

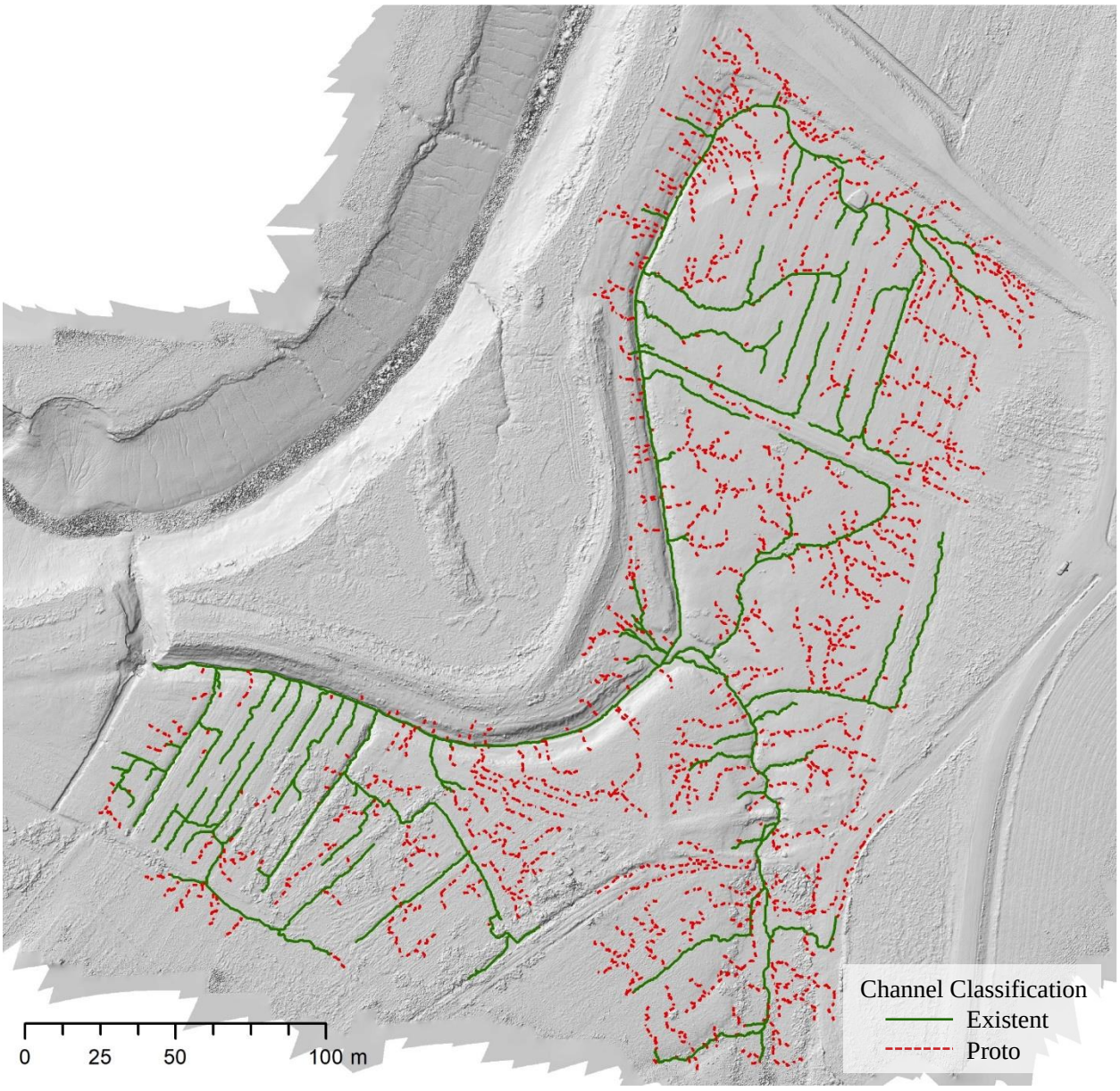

Figure G-2. Results of the channel delineation of the November 24, 2019 Target Area dataset.

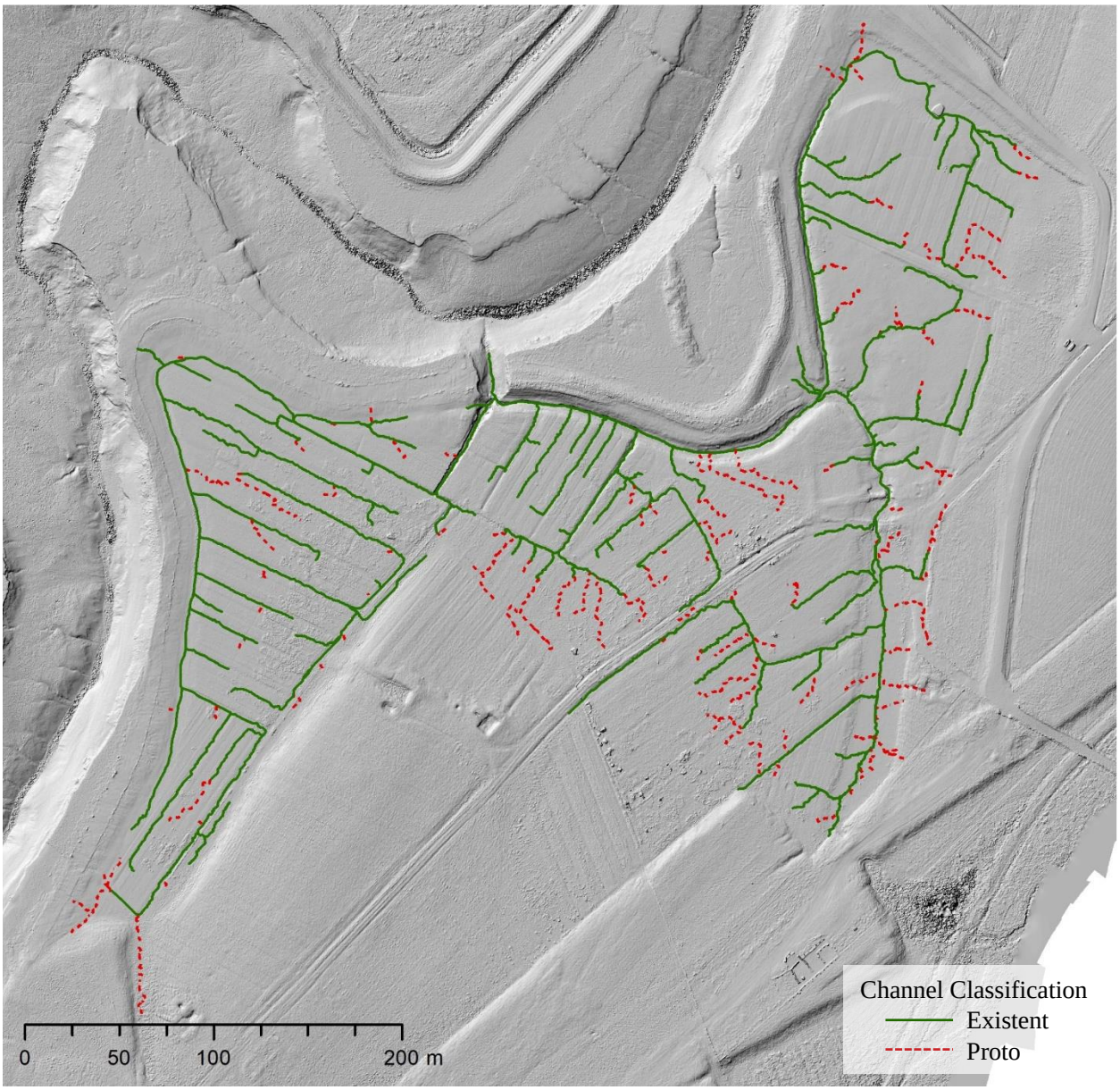

Figure G-3. Results of the channel delineation of the June 1, 2020 Full Site dataset.

Figure G-4. Results of the channel delineation of the June 1, 2020 Target Area dataset.

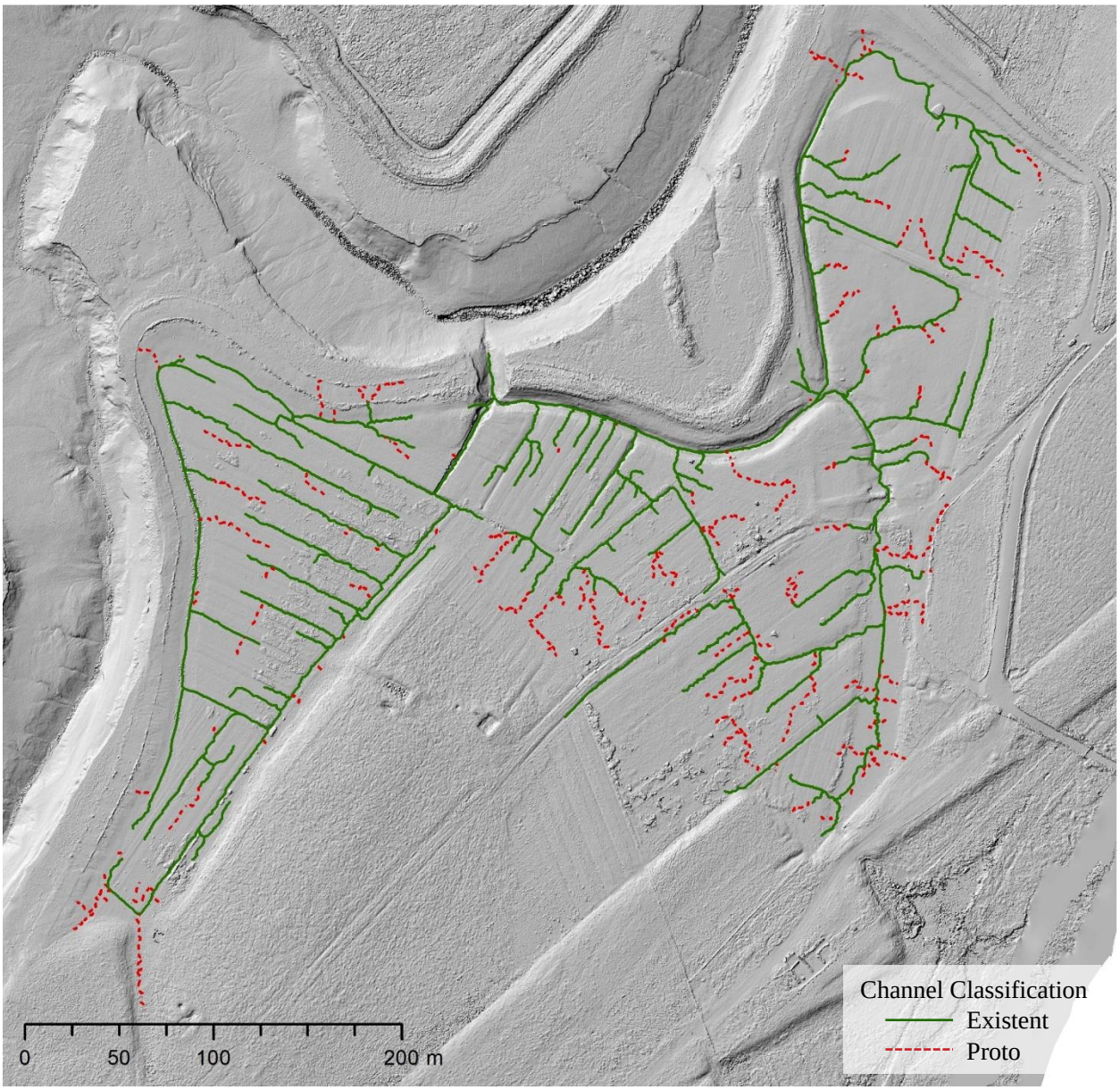

Figure G-5. Results of the channel delineation of the July 9, 2020 Full Site dataset.

Figure G-6. Results of the channel delineation of the July 9, 2020 Target Area dataset.

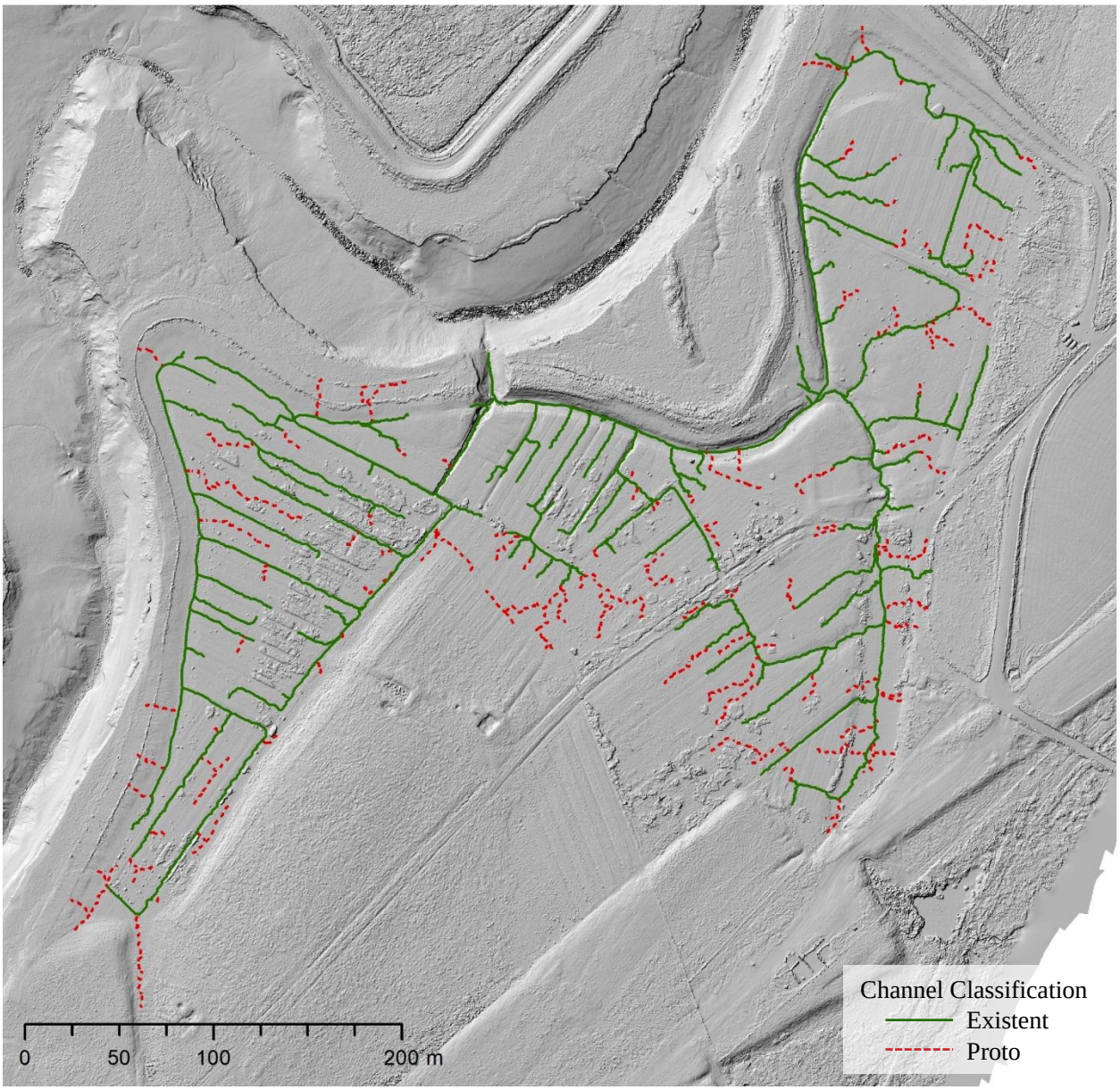

Figure G-7. Results of the channel delineation of the August 21, 2020 Full Site dataset.

Figure G-8. Results of the channel delineation of the August 21, 2020 Target Area dataset.

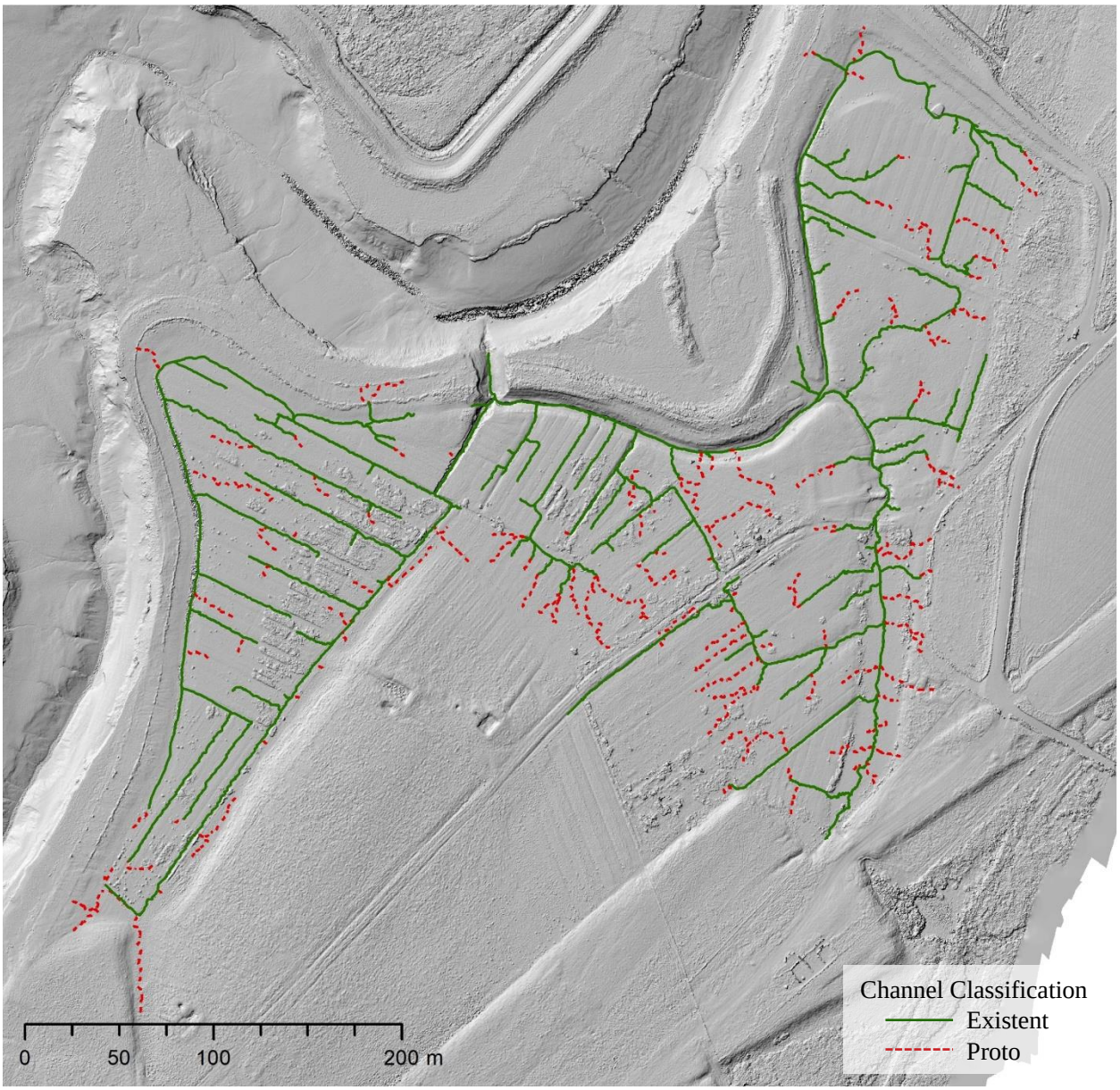

Figure G-9. Results of the channel delineation of the October 5, 2020 Full Site dataset.

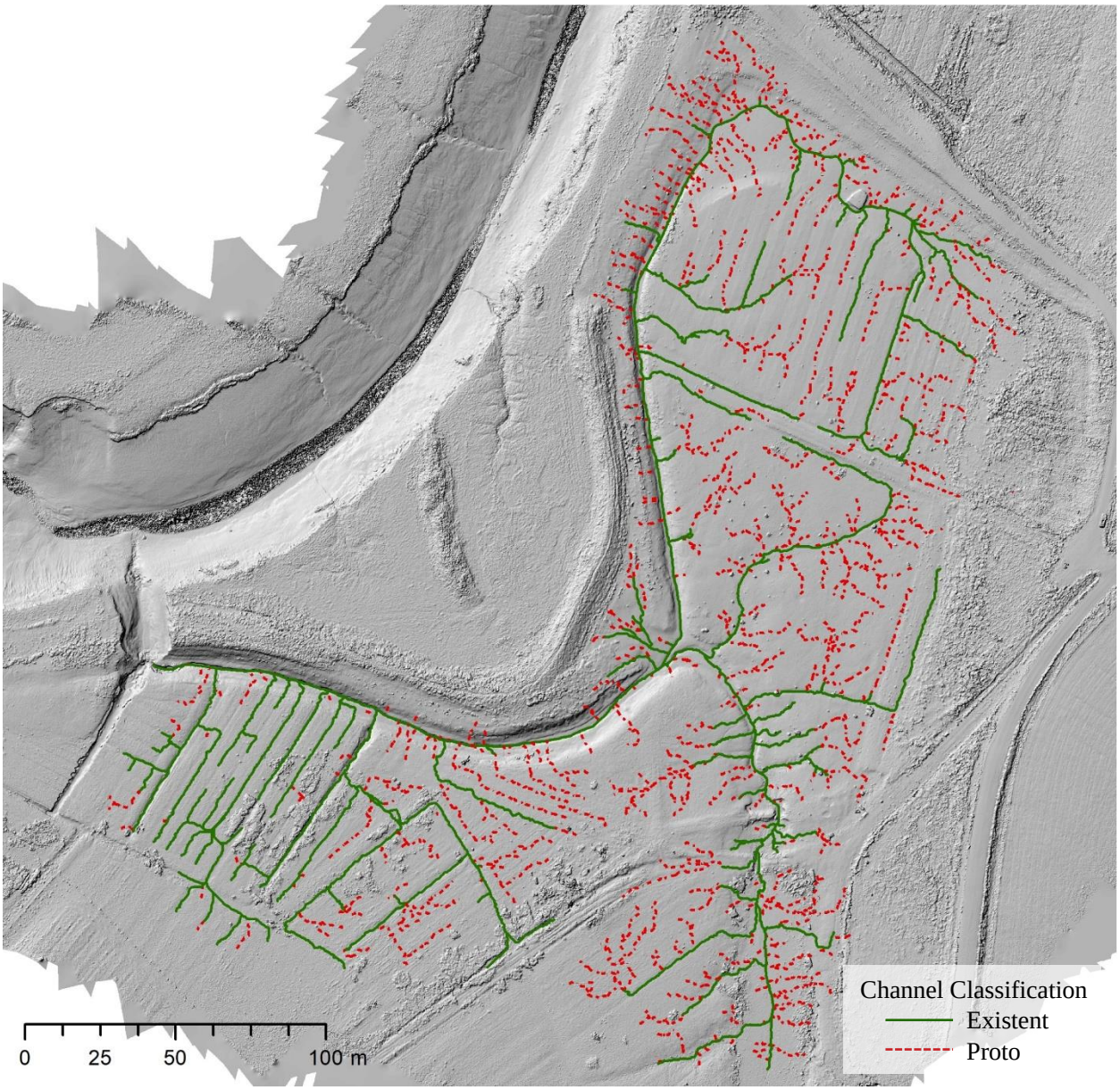

Figure G-10. Results of the channel delineation of the October 5, 2020 Target Area dataset.

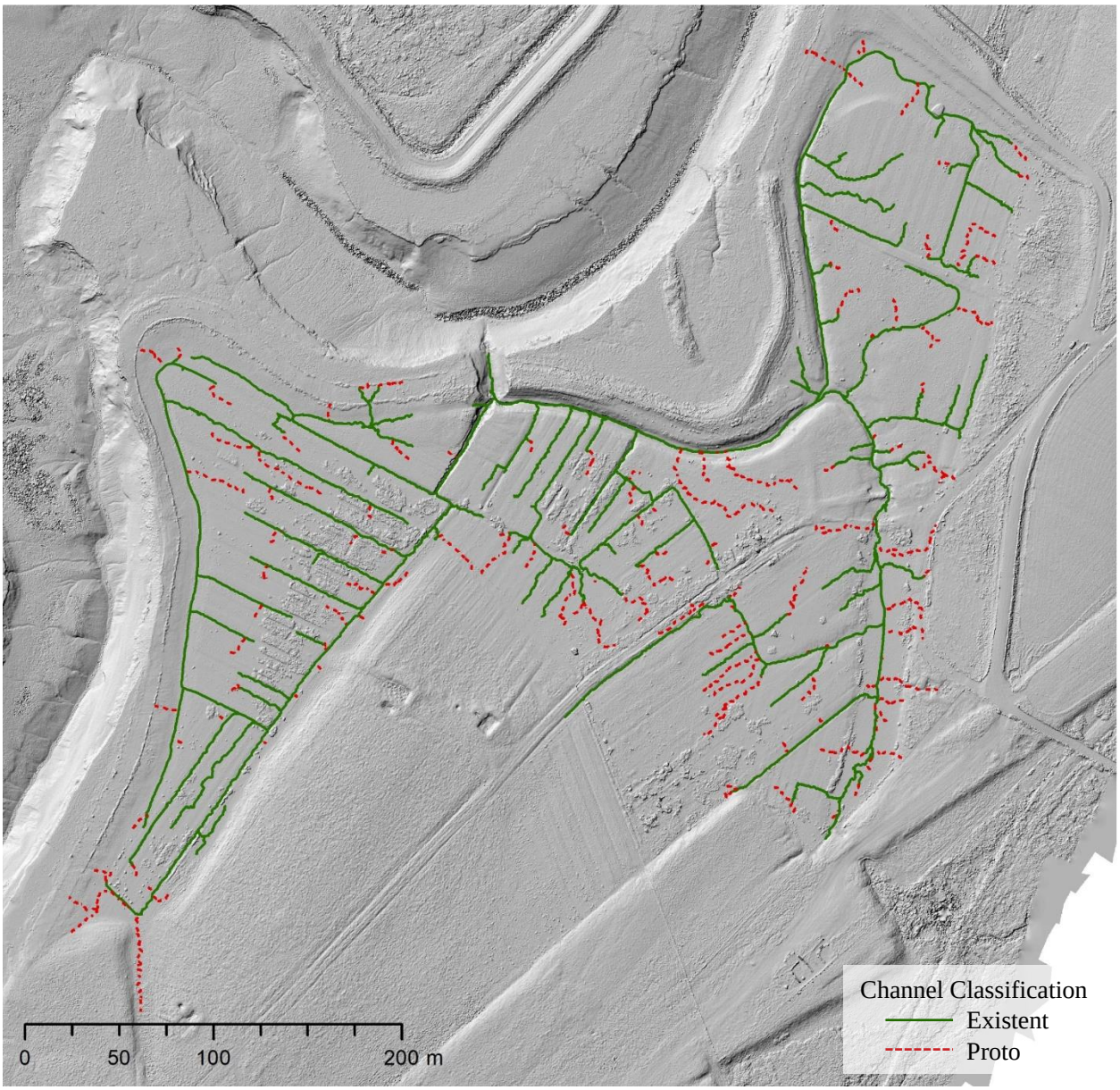

Figure G-11. Results of the channel delineation of the November 8, 2020 Full Site dataset.

.

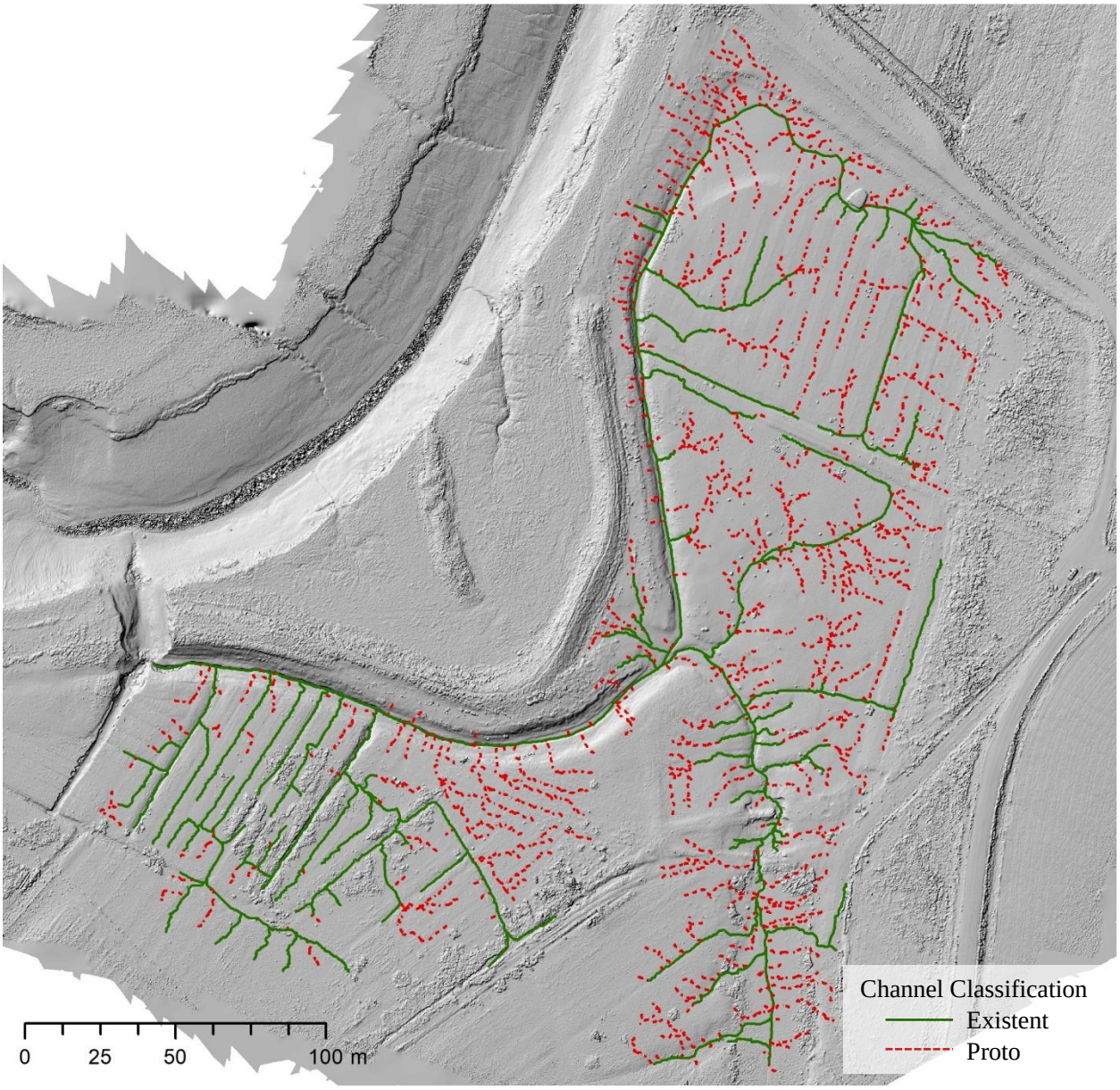

Figure G-12. Results of the channel delineation of the November 8, 2020 Target Area dataset.

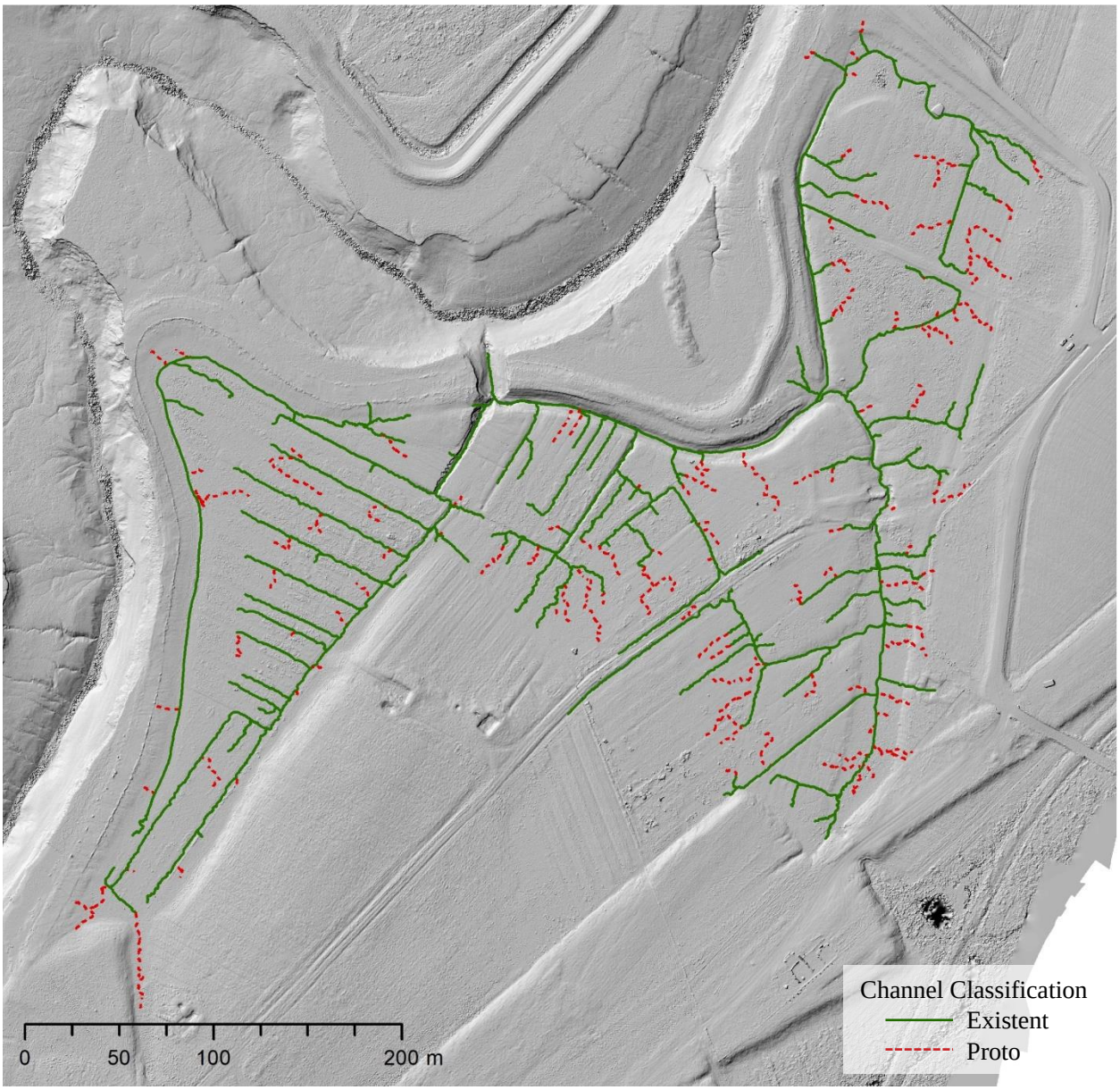

Figure G-13. Results of the channel delineation of the May 4, 2021 Full Site dataset.

Figure G-14. Results of the channel delineation of the May 4, 2021 Target Area dataset.

Appendix H - 95% Confidence Interval Digital Elevation Models of Difference Results

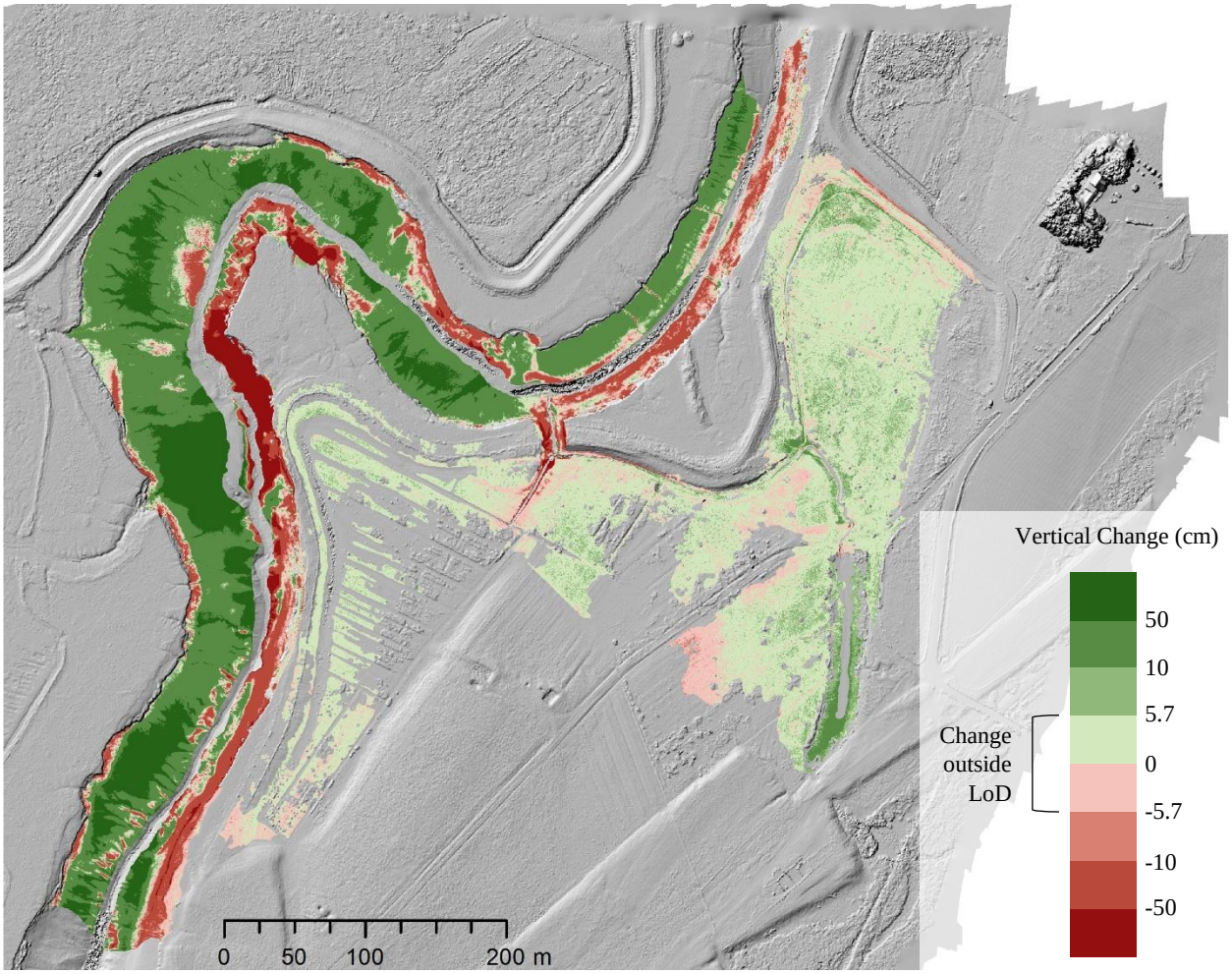

Figure H-1. DEM of Difference raster showing Full Site surface elevation change from November 24, 2019 to October 5, 2020 (1-year). LoD was calculated using a 95% confidence interval. Background is a hillshade of the October 5, 2020 DSM. Percentage of pixels in the site area and river area within LoD are 17% and 88% respectively.

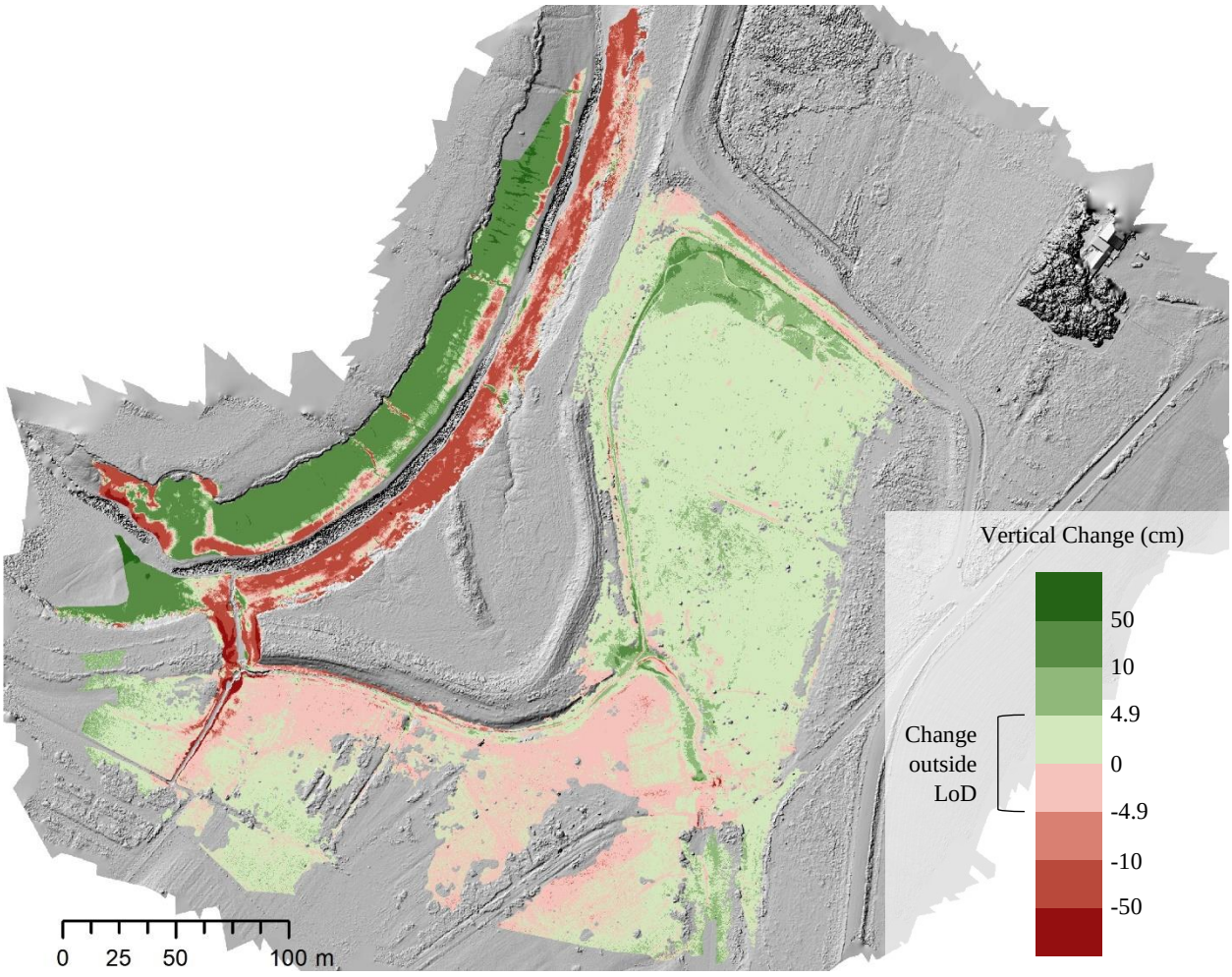

Figure H-2. DEM of Difference raster showing Target Area surface elevation change from November 24, 2019 to October 5, 2020 (1-year). LoD was calculated using a 95% confidence interval. Background is a hillshade of the October 5, 2020 DSM. Percentage of pixels in the site area and river area within LoD are 13% and 83% respectively.

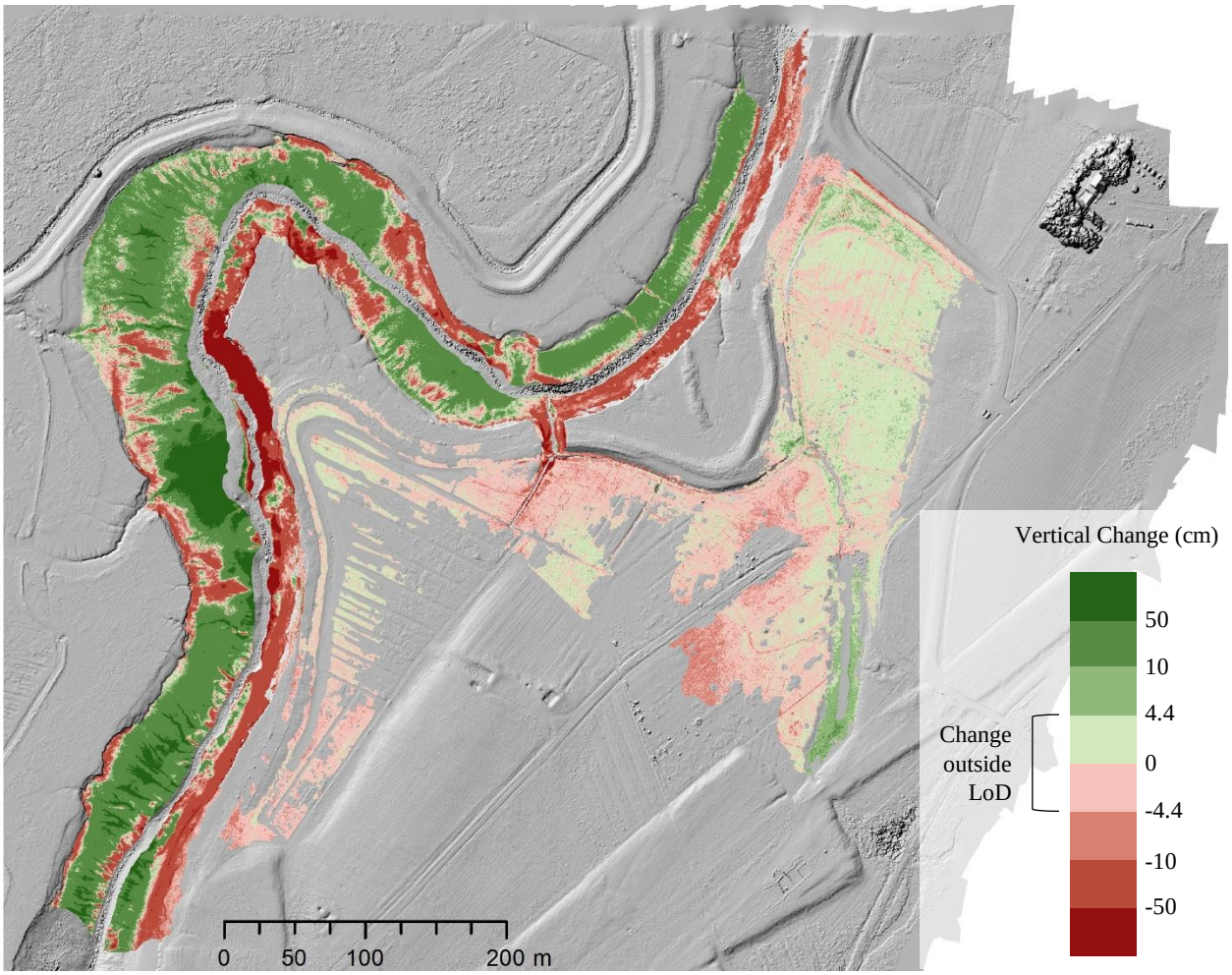

Figure H-3. DEM of Difference raster showing Full Site surface elevation change from November 24, 2019 to June 1, 2020 (winter). LoD was calculated using a 95% confidence interval. Background is a hillshade of the June 1, 2020 DSM. Percentage of pixels in the site area and river area within LoD are 14% and 86% respectively.

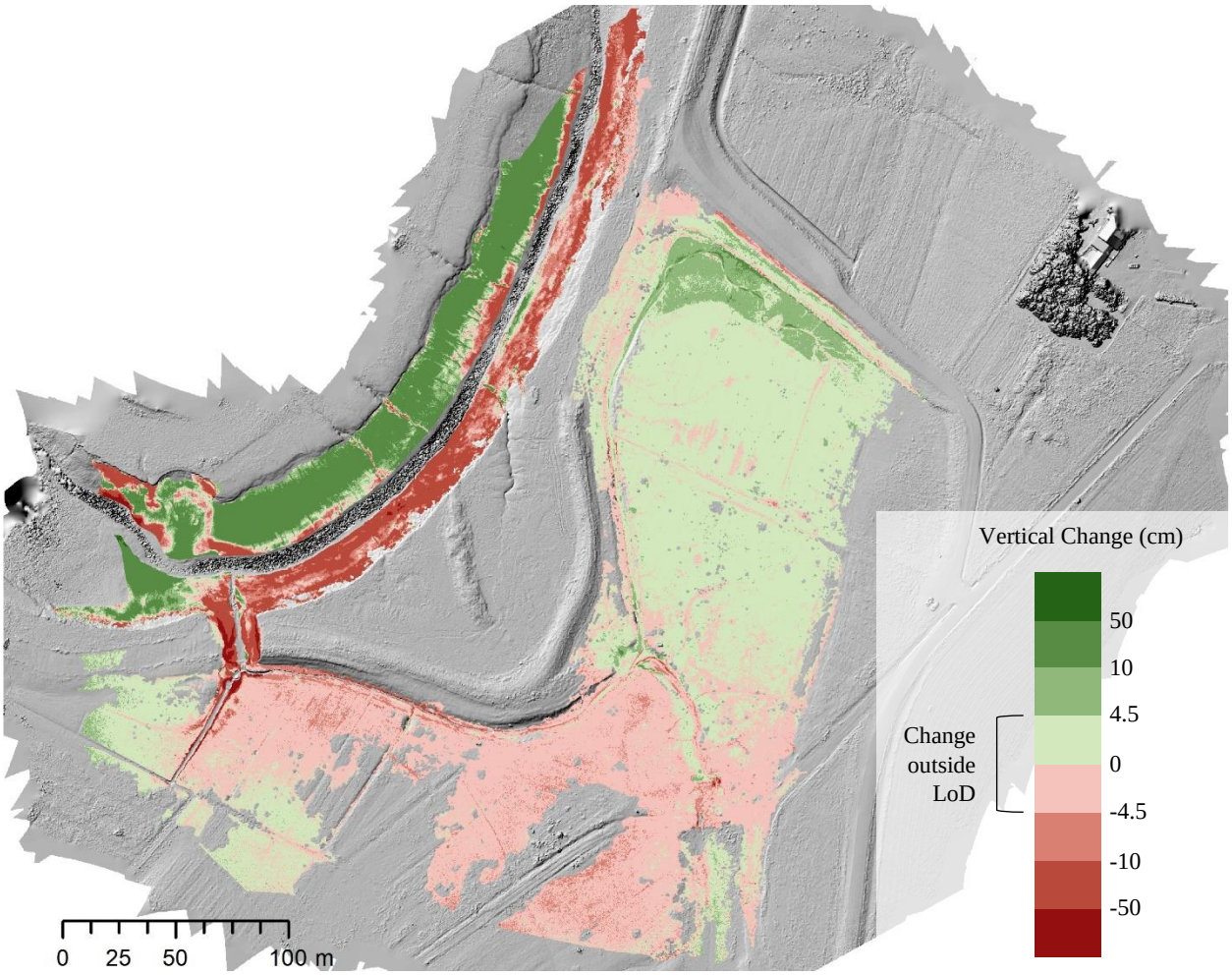

Figure H-4. DEM of Difference raster showing Target Area surface elevation change from November 24, 2019 to June 1, 2020 (winter). LoD was calculated using a 95% confidence interval. Background is a hillshade of the June 1, 2020 DSM. Percentage of pixels in the site area and river area within LoD are 11% and 83% respectively.

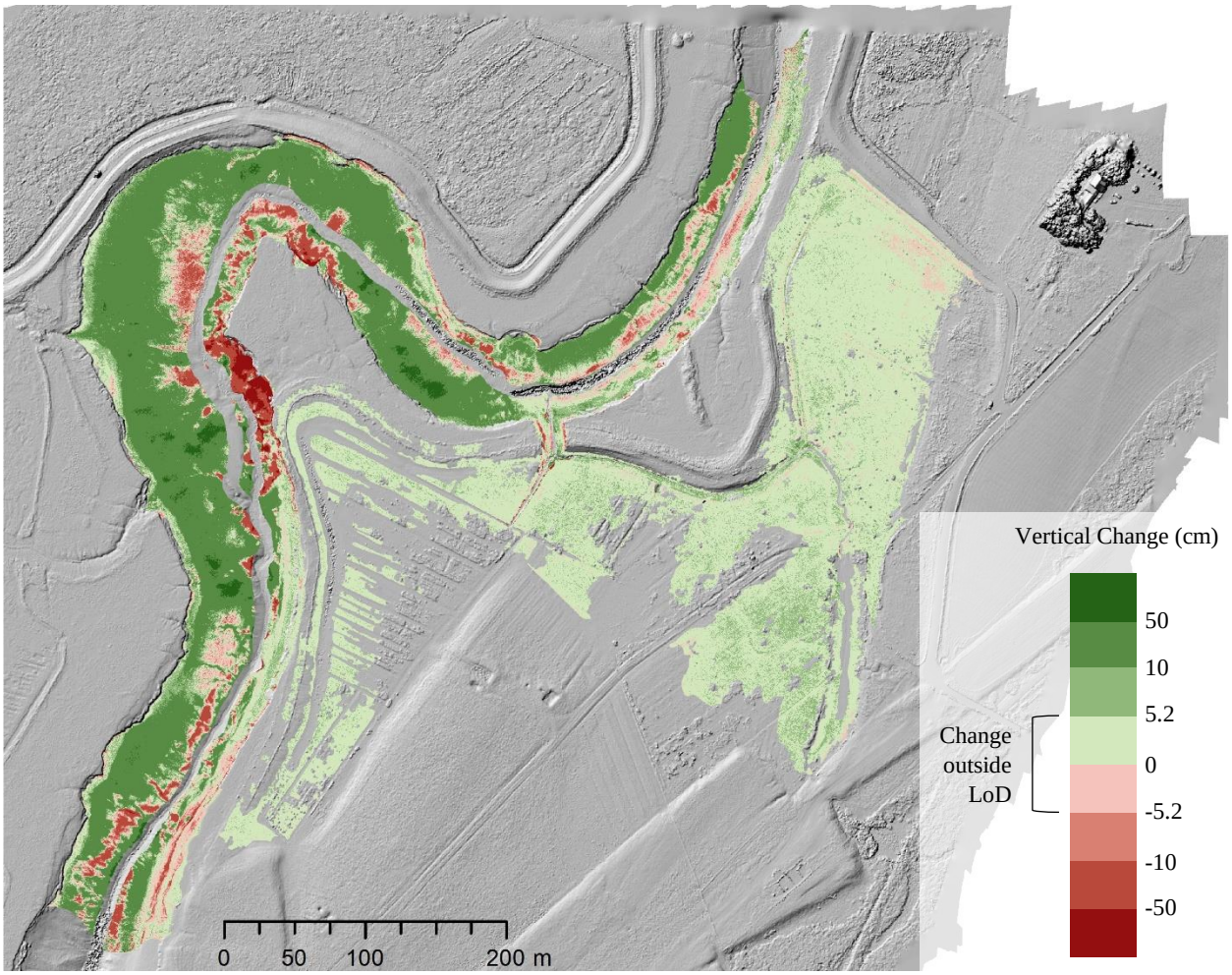

Figure H-5. DEM of Difference raster showing Full Site surface elevation change from June 1, 2020 to October 5, 2020 (growing season). LoD was calculated using a 95% confidence interval. Background is a hillshade of the October 5, 2020 DSM. Percentage of pixels in the site area and river area within LoD are 13% and 74% respectively.

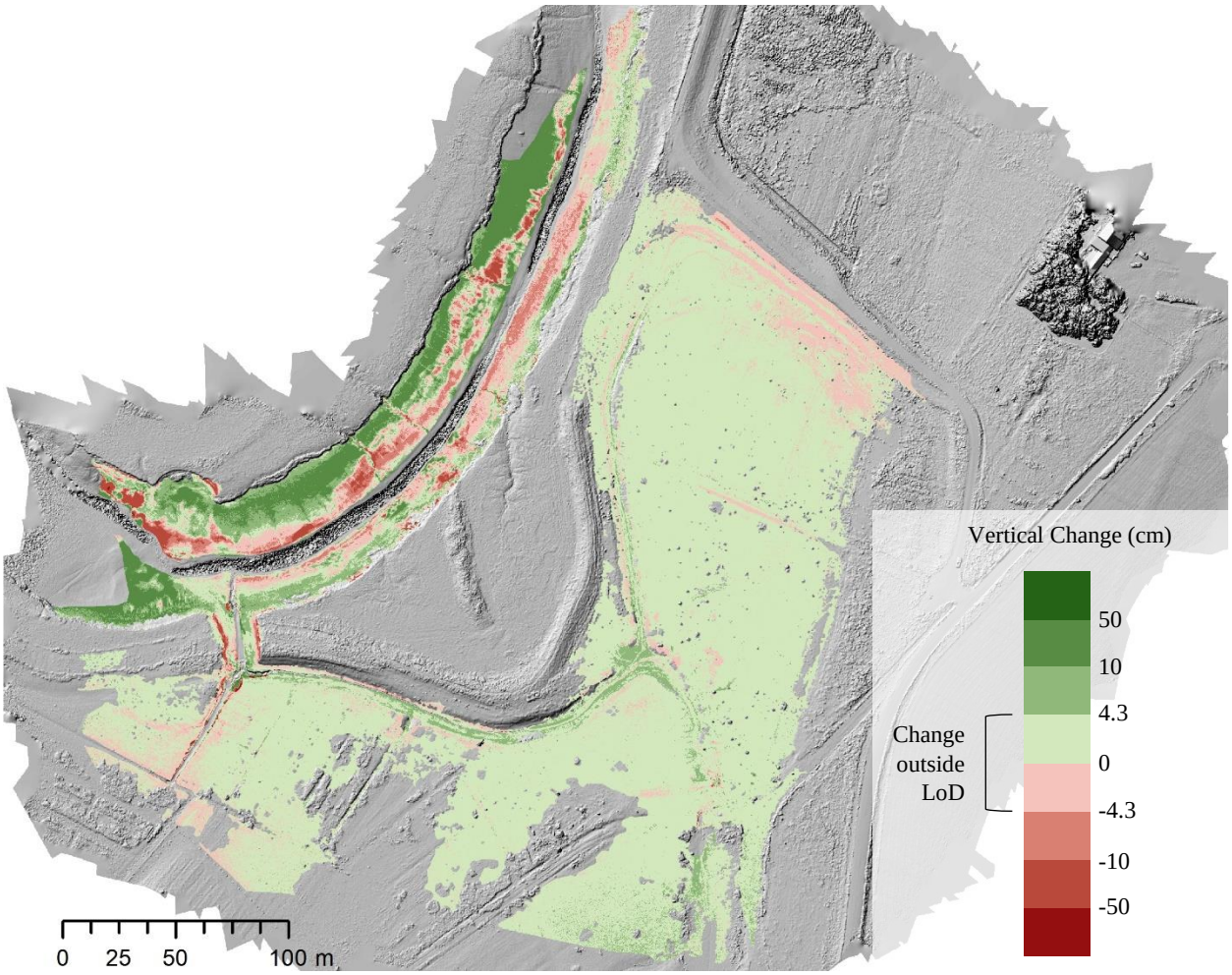

Figure H-6. DEM of Difference raster showing Target Area surface elevation change from June 1, 2020 to October 5, 2020 (growing season). LoD was calculated using a 95% confidence interval. Background is a hillshade of the October 5, 2020 DSM. Percentage of pixels in the site area and river area within LoD are 4% and 57% respectively.

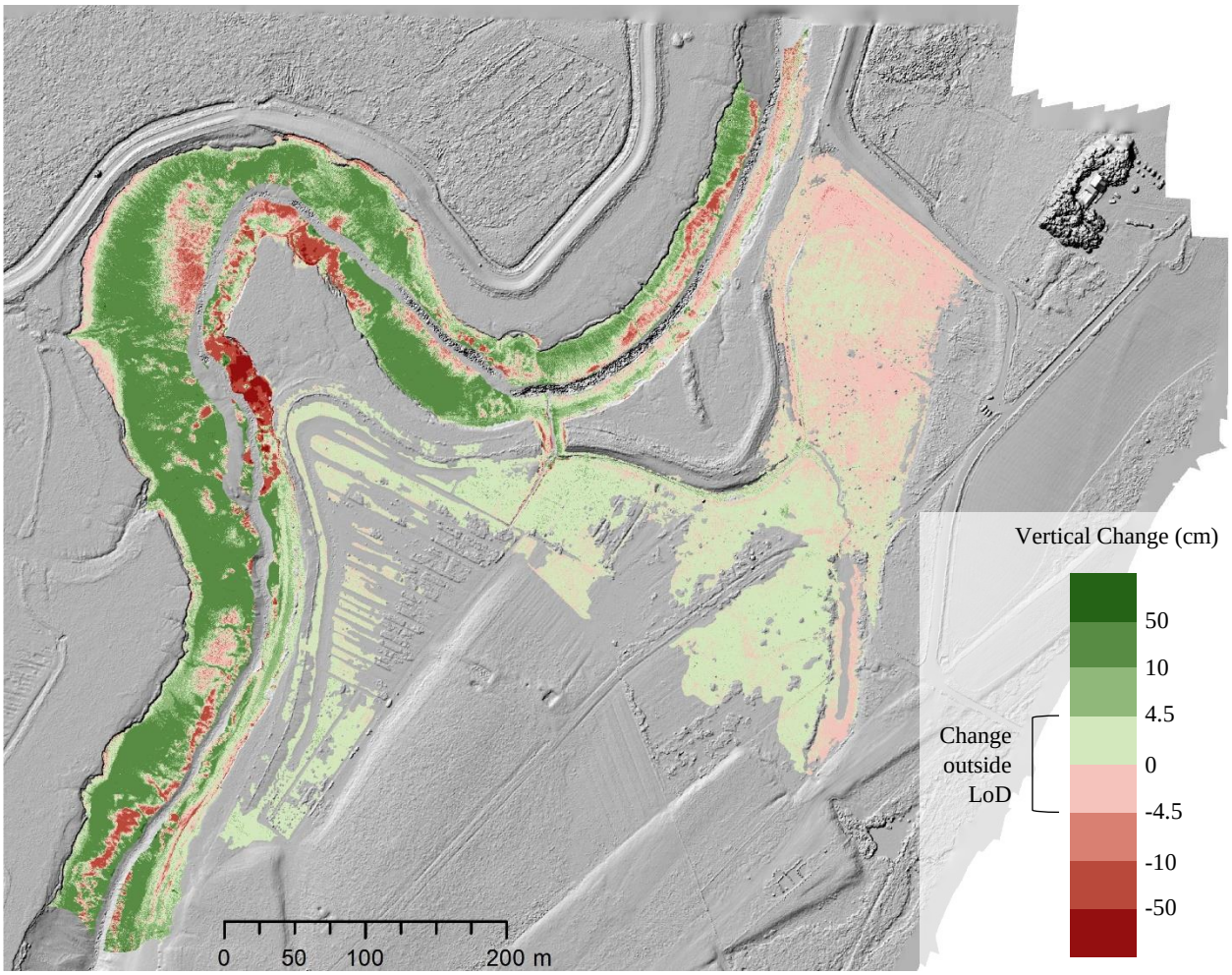

Figure H-7. DEM of Difference raster showing Full Site surface elevation change from June 1, 2020 to August 21, 2020 (spring-summer). LoD was calculated using a 95% confidence interval. Background is a hillshade of the August 21, 2020 DSM. Percentage of pixels in the site area and river area within LoD are 2% and 69% respectively.

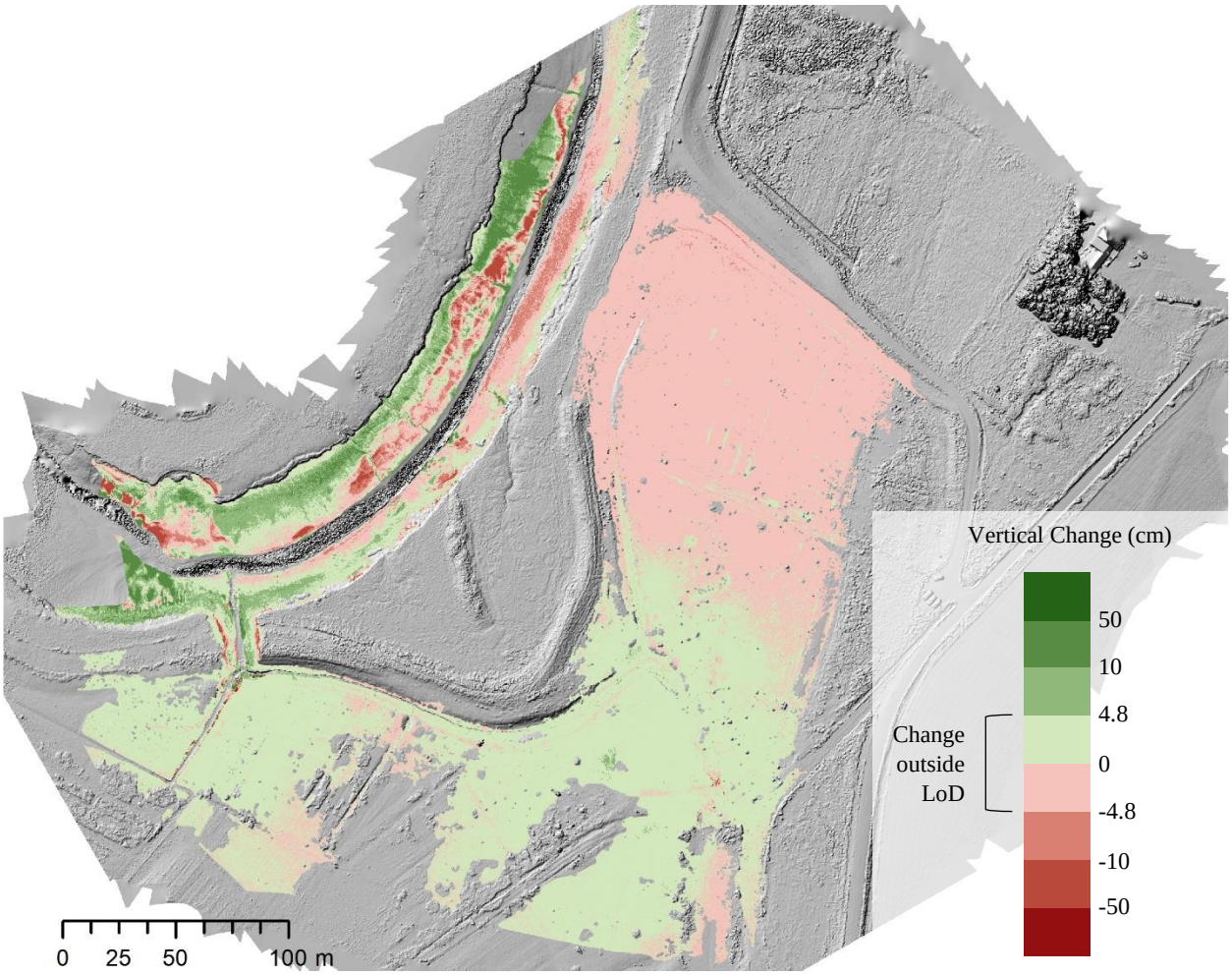

Figure H-8. DEM of Difference raster showing Target Area surface elevation change from June 1, 2020 to August 21, 2020 (spring-summer). LoD was calculated using a 95% confidence interval. Background is a hillshade of the August 21, 2020 DSM. Percentage of pixels in the site area and river area within LoD are 1% and 42% respectively.

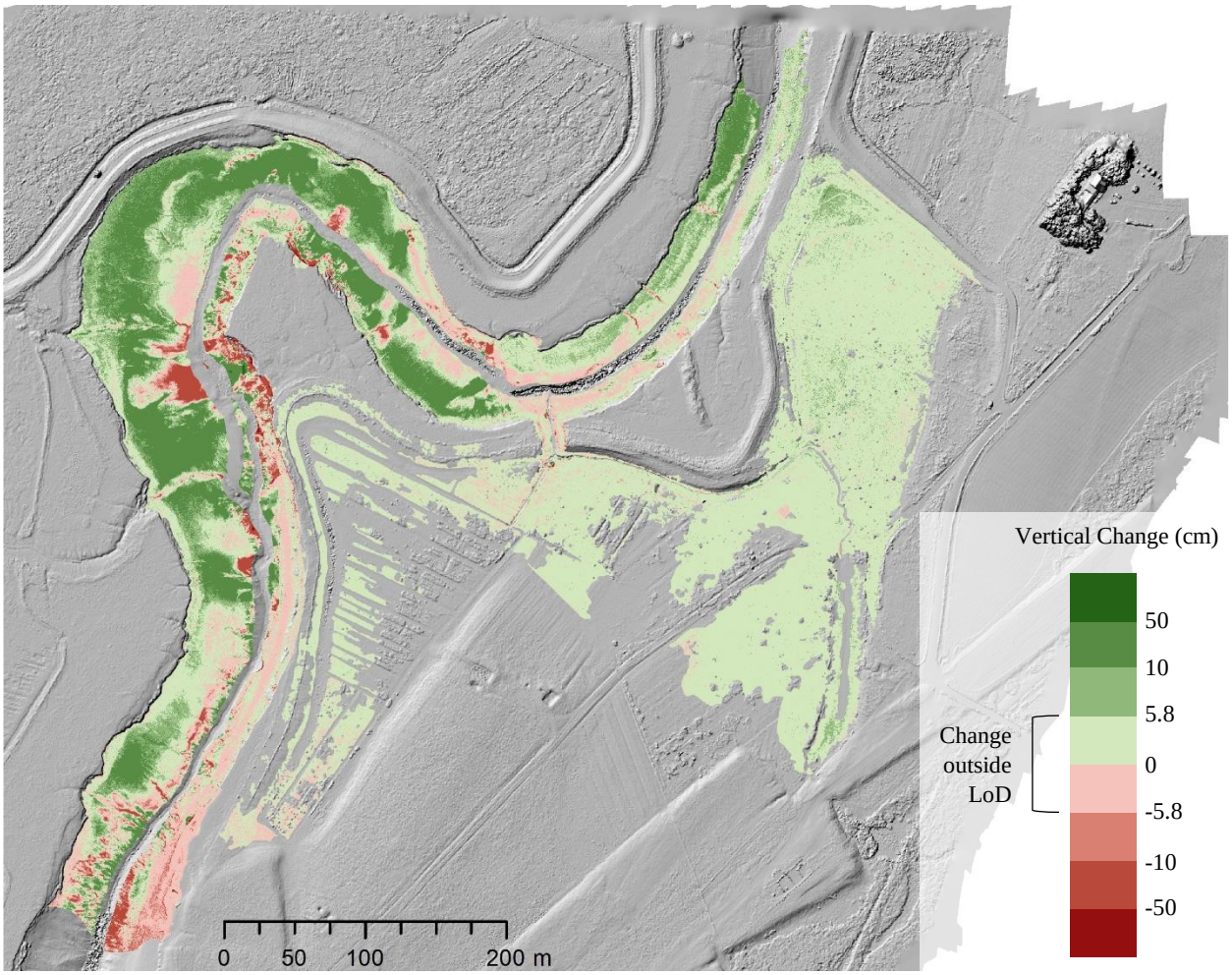

Figure H-9. DEM of Difference raster showing Full Site surface elevation change from August 21, 2020 to October 5, 2020 (summer-fall). LoD was calculated using a 95% confidence interval. Background is a hillshade of the October 5, 2020 DSM. Percentage of pixels in the site area and river area within LoD are 3% and 49% respectively.

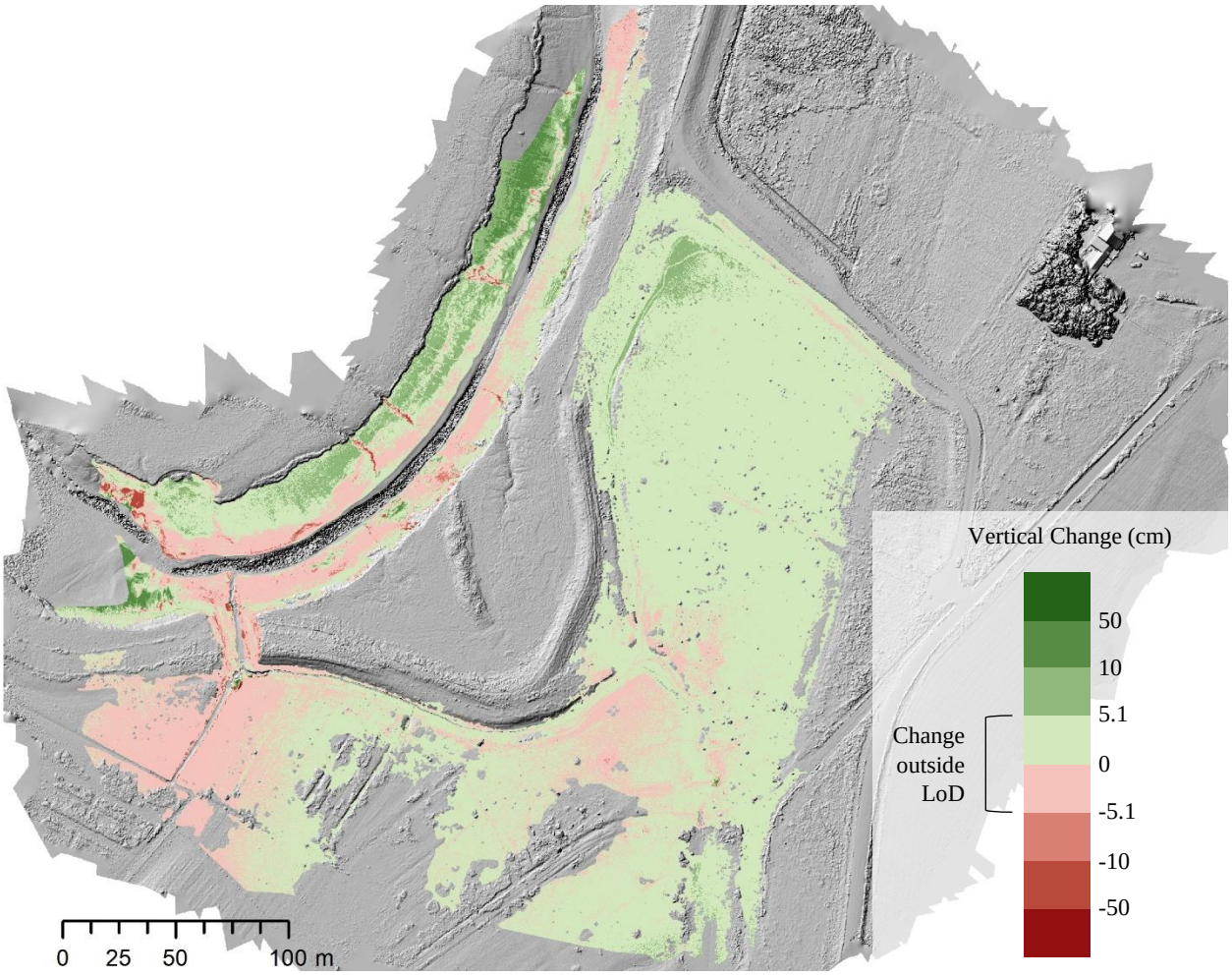

Figure H-10. DEM of Difference raster showing Target Area surface elevation change from August 21, 2020 to October 5, 2020 (summer-fall). LoD was calculated using a 95% confidence interval. Background is a hillshade of the October 5, 2020 DSM. Percentage of pixels in the site area and river area within LoD are 2% and 25% respectively.

Appendix I - Multiple Linear Regression Partition of Variance Results

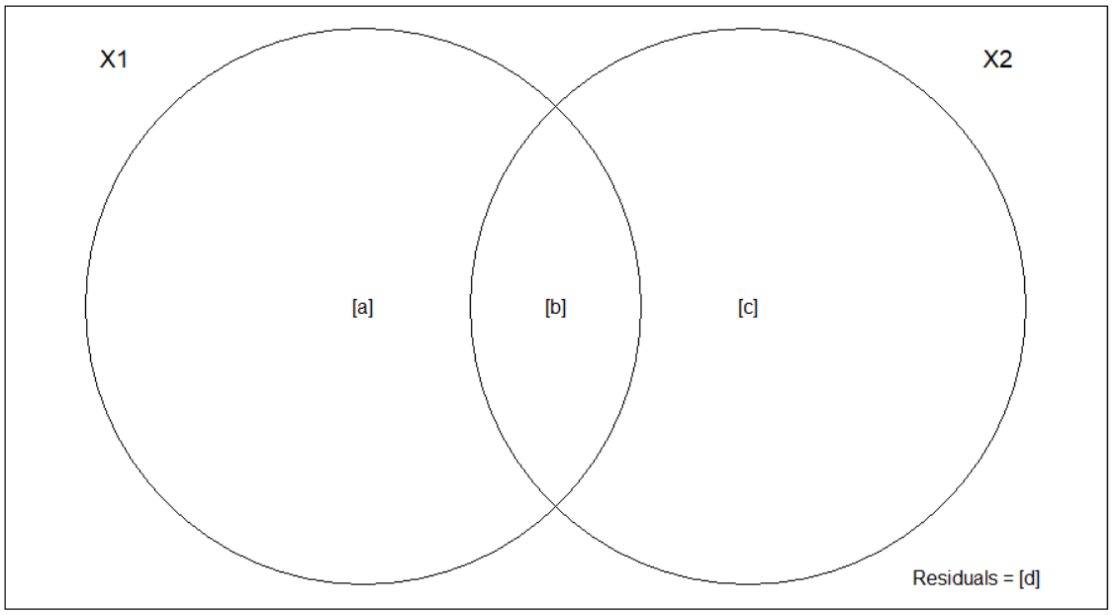

Figure I-1. Variance partitioning variables for calculated multiple linear regression models, where [a] = pure environmental variation, [b] = spatially autocorrelated environmental variation, [c] = pure spatial variation, and [d] = model residuals.

Table I-1. Partition of variance results for the unscaled multiple linear regression model of surface elevation change within the borrow pit from November 24, 2019 to October 5, 2020 (1-year, Target Area dataset).

	Df	Adjusted R^2
[a] + [b] = X1	3	0.50656
[b] + [c] = X2	6192	0.73953
[a] + [b] + [c] = X1 + X2	6195	0.79475
Individual Fractions		
[a] = X1 | X2	3	0.05522
[b]	0	0.45134
[c] = X2 | X1	6192	0.28819
[d] = Residuals		0.20525

Table I-2. Partition of variance results for the unscaled multiple linear regression model of surface elevation change within the study site but excluding main channel mouth, drainage ditches and borrow pit from November 24, 2019 to October 5, 2020 (1-year, Full Site dataset).

	Df	Adjusted R^2
[a] + [b] = X1	3	0.22708
[b] + [c] = X2	6627	0.49419
[a] + [b] + [c] = X1 + X2	6630	0.52561
Individual Fractions		
[a] = X1 | X2	3	0.03142
[b]	0	0.19567
[c] = X2 | X1	6627	0.29852
[d] = Residuals		0.47439

Table I-3. Partition of variance results for the unscaled multiple linear regression model of surface elevation change within the borrow pit from November 24, 2019 to June 1, 2020 (winter, Target Area dataset).

	Df	Adjusted R^2
[a] + [b] = X1	3	0.36725
[b] + [c] = X2	6192	0.68936
[a] + [b] + [c] = X1 + X2	6195	0.74298
Individual Fractions		
[a] = X1 | X2	3	0.05362
[b]	0	0.31363
[c] = X2 | X1	6192	0.37573
[d] = Residuals		0.25702

Table I-4. Partition of variance results for the unscaled multiple linear regression model of surface elevation change within the study site but excluding main channel mouth, drainage ditches and borrow pit from November 24, 2019 to June 1, 2020 (winter, Full Site dataset).

	Df	Adjusted R^2
[a] + [b] = X1	3	0.20406
[b] + [c] = X2	6627	0.53465
[a] + [b] + [c] = X1 + X2	6630	0.55212
Individual Fractions		
[a] = X1 | X2	3	0.01747
[b]	0	0.18659
[c] = X2 | X1	6627	0.34806
[d] = Residuals		0.44788

Table I-5. Partition of variance results for the unscaled multiple linear regression model of surface elevation change within the borrow pit from June 1, 2020 to October 5, 2020 (growing season, Target Area dataset).

	Df	Adjusted R^2
[a] + [b] = X1	3	0.28763
[b] + [c] = X2	6192	0.59471
[a] + [b] + [c] = X1 + X2	6195	0.61320
Individual Fractions		
[a] = X1 | X2	3	0.01850
[b]	0	0.26913
[c] = X2 | X1	6192	0.32558
[d] = Residuals		0.38680

Table I-6. Partition of variance results for the unscaled multiple linear regression model of surface elevation change within the study site but excluding main channel mouth, drainage ditches and borrow pit from June 1, 2020 to October 5, 2020 (growing season, Full Site dataset).

	Df	Adjusted R^2
[a] + [b] = X1	3	0.01284
[b] + [c] = X2	6627	0.21234
[a] + [b] + [c] = X1 + X2	6630	0.23535
Individual Fractions		
[a] = X1 | X2	3	0.02301
[b]	0	-0.01017
[c] = X2 | X1	6627	0.22251
[d] = Residuals		0.76465

Appendix J - Supplementary Data Products

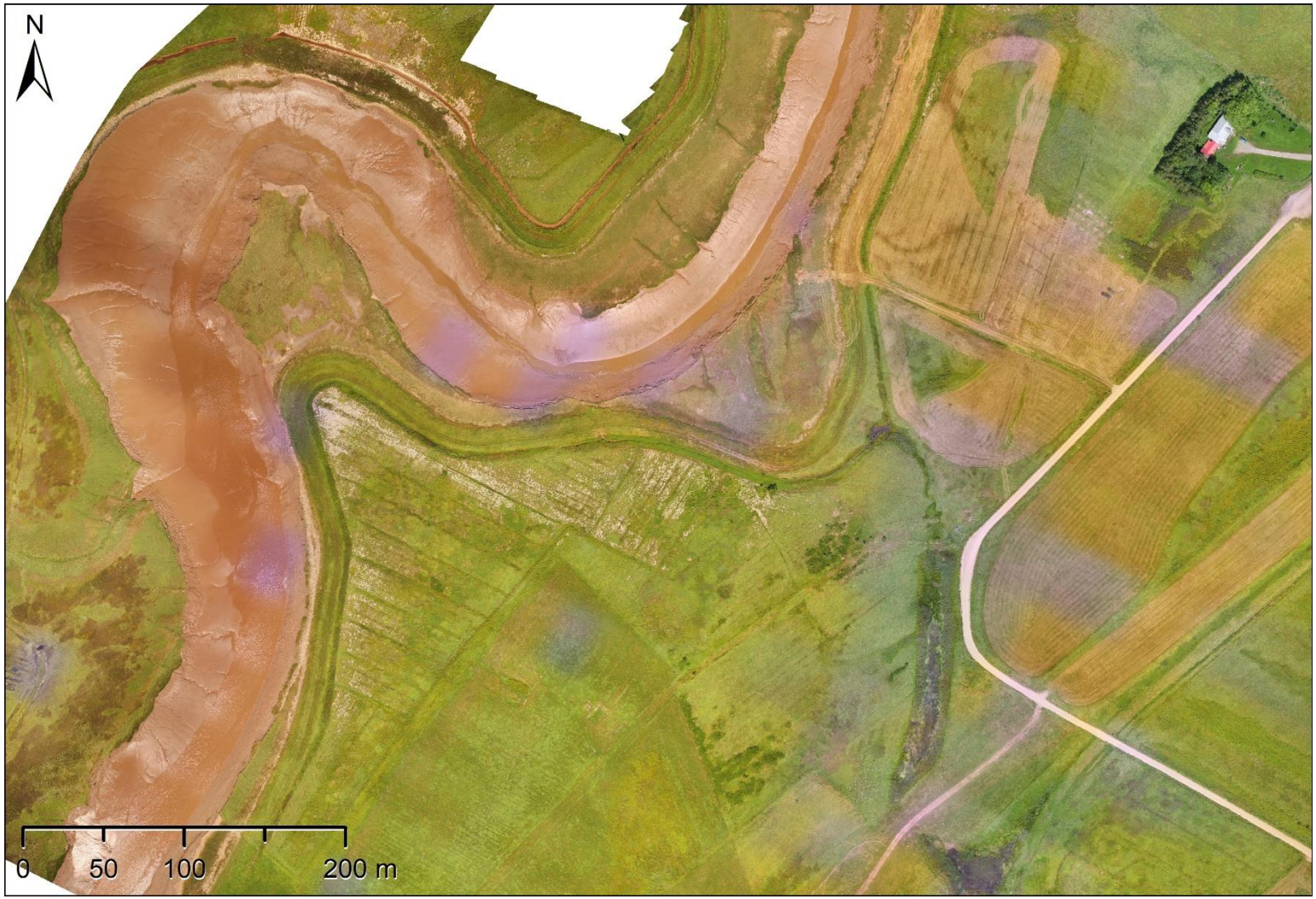

Figure J-1. RGB orthomosaic produced by Pix4D Mapper. Imagery data collected with a DJI Phantom 3 Professional RPAS during a full site survey of Converse, August 1, 2018, pre-breach. Orthomosaic resolution of 4 cm, and horizontal RMSE expected to be less than the resolution.

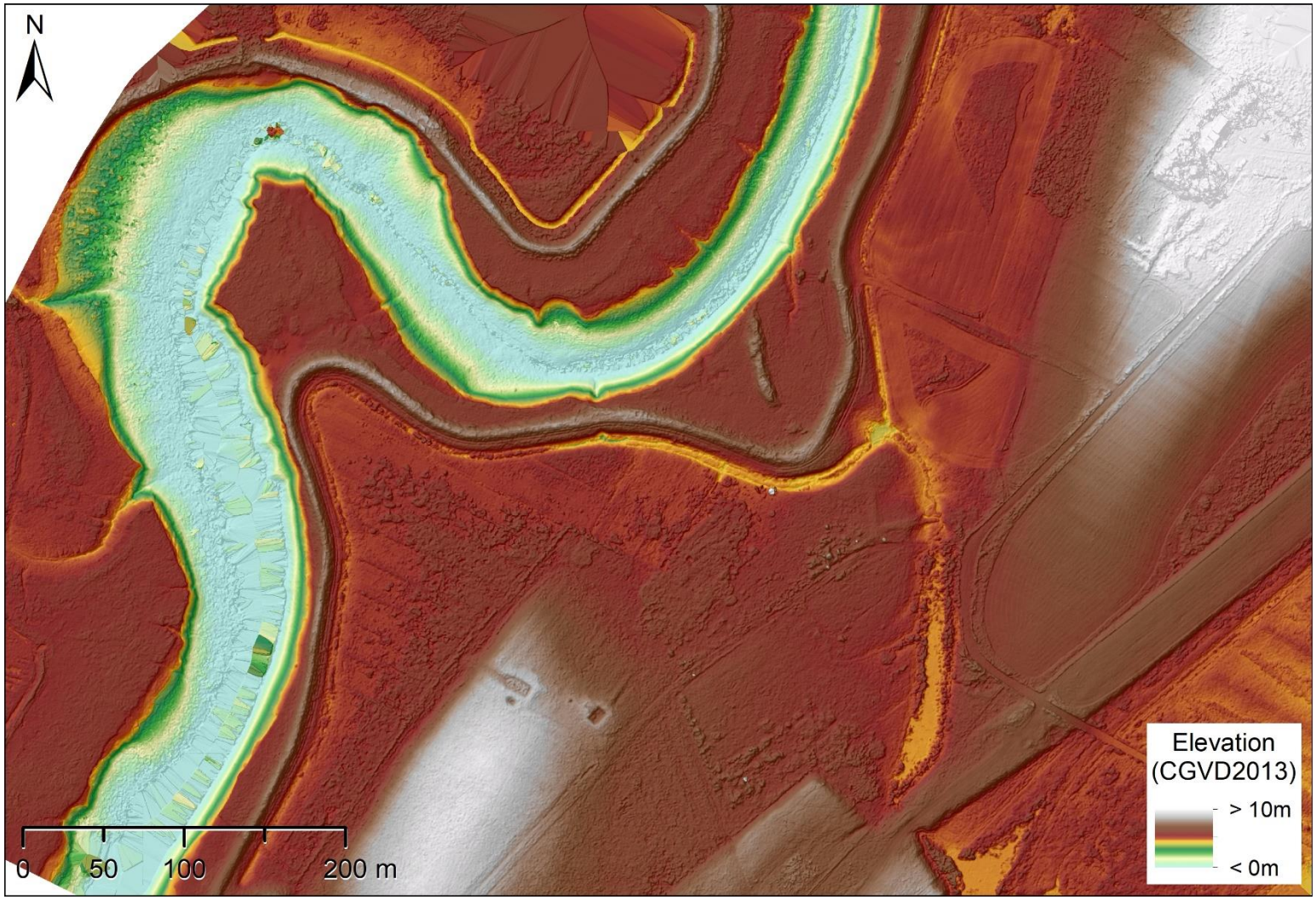

Figure J-2. Elevation model produced by Pix4D Mapper. Imagery data collected with a DJI Phantom 3 Professional RPAS during a full site survey of Converse, August 1, 2018, pre-breach. Elevation model resolution of 4 cm, and vertical RMSE unknown.

Figure J-3. RGB orthomosaic produced by Pix4D Mapper. Imagery data collected with a DJI Phantom 3 Professional RPAS during a full site survey of Converse, September 24, 2018, pre-breach. Orthomosaic resolution of 4 cm, and horizontal RMSE expected to be less than the resolution.

Figure J-4. Elevation model produced by Pix4D Mapper. Imagery data collected with a DJI Phantom 3 Professional RPAS during a full site survey of Converse, September 24, 2018, pre-breach. Elevation model resolution of 4 cm, and vertical RMSE of 15.7 cm.

Figure J-5. RGB orthomosaic produced by Pix4DMapper. Imagery data collected with a WingtraOne PPK RPAS during a full site survey of Converse, May 5, 2019. Orthomosaic resolution of 4 cm, and horizontal RMSE expected to be less than the resolution.

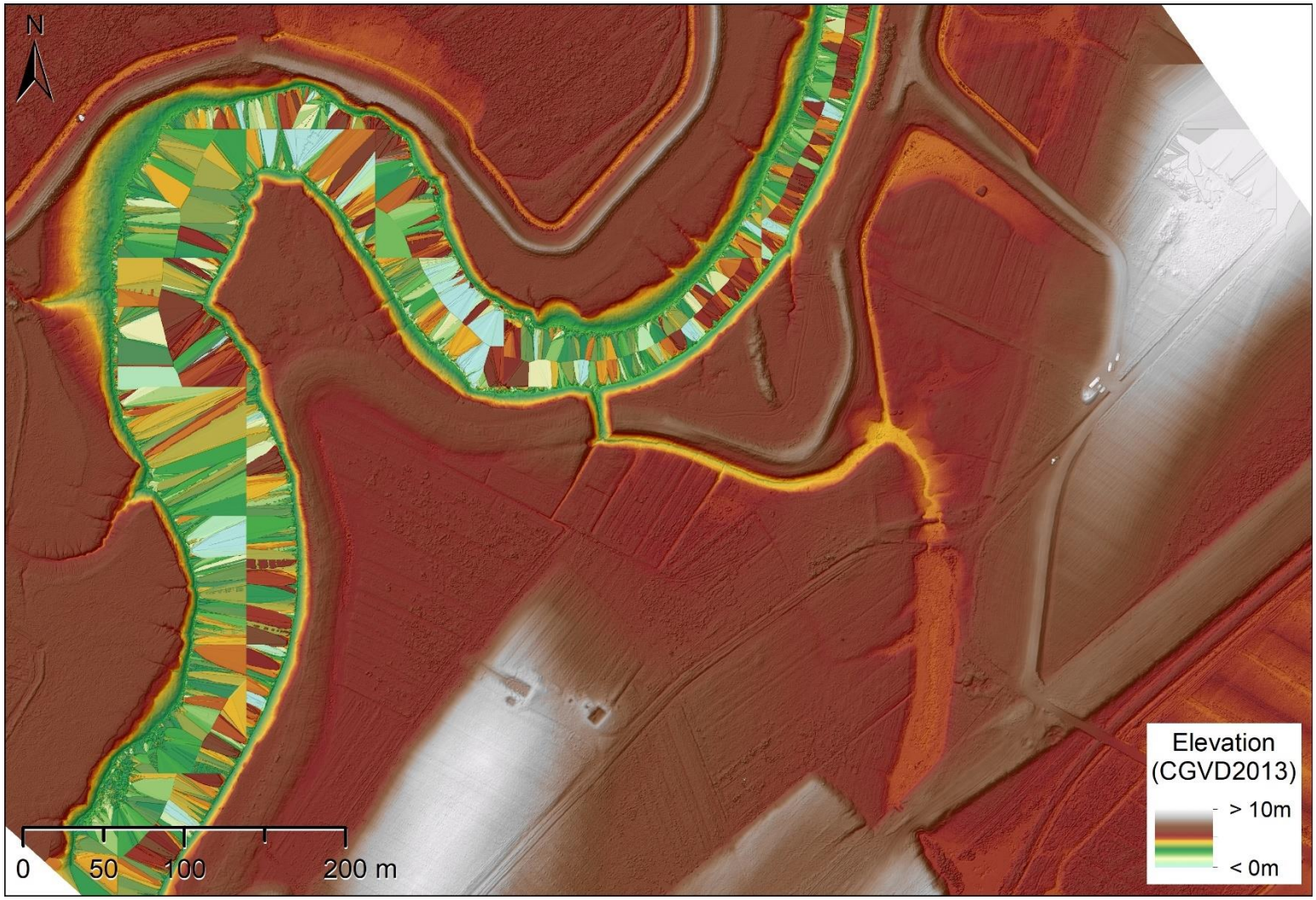

Figure J-6. Elevation model produced by Pix4D Mapper. Imagery data collected with a DJI Phantom 4 RTK RPAS during a full site survey of Converse, May 5, 2019. Elevation model resolution of 4 cm, and vertical RMSE of 6.8 cm.

Figure J-7. RGB orthomosaic produced by Agisoft Metashape. Imagery data collected with a WingtraOne PPK RPAS during a full site survey of Converse, August 2, 2019. Orthomosaic resolution of 2.5 cm, and horizontal RMSE expected to be less than the resolution.

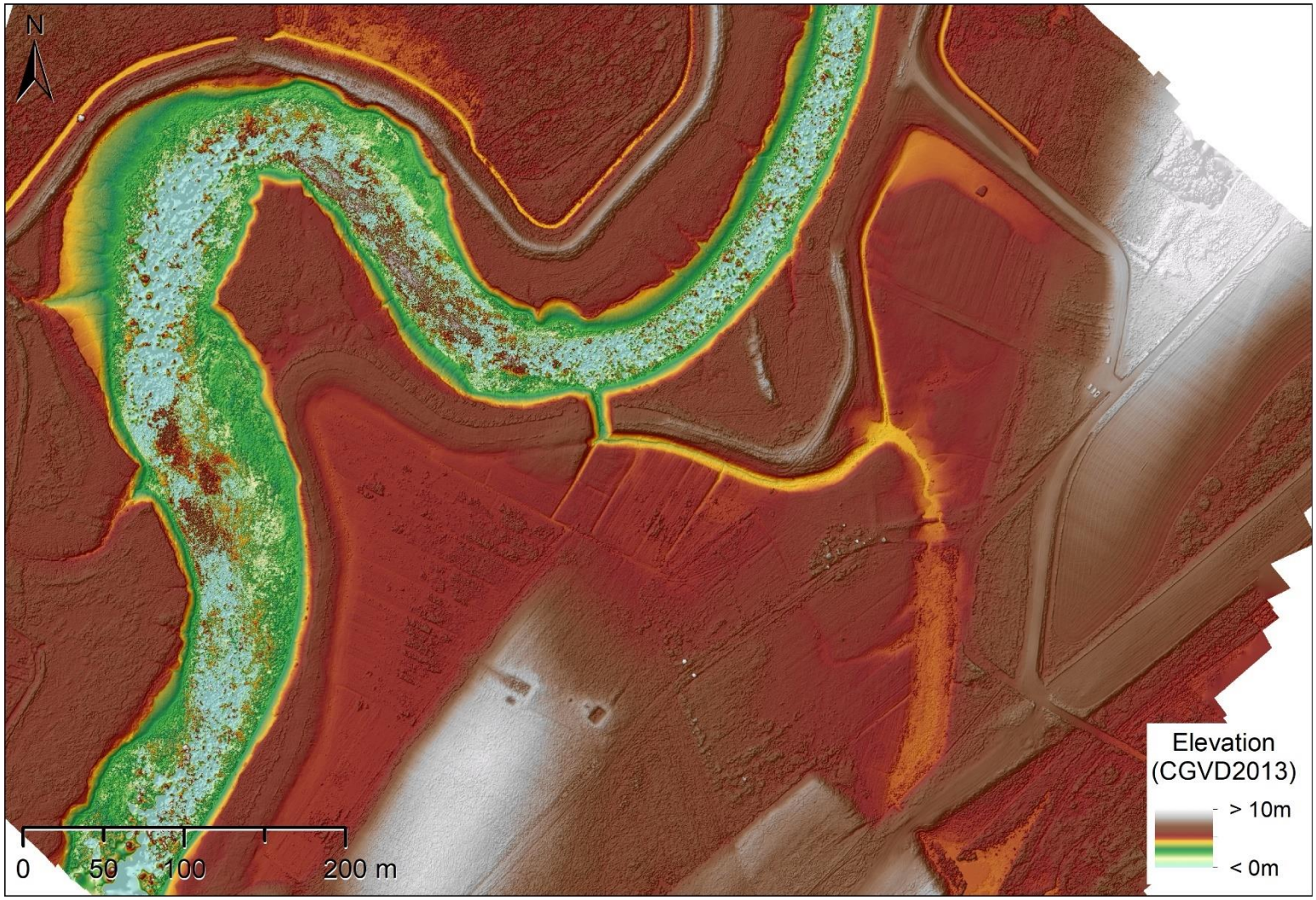

Figure J-8. Elevation model produced by Agisoft Metashape. Imagery data collected with a WingtraOne PPK RPAS during a full site survey of Converse, August 2, 2019. Elevation model resolution of 2.5 cm, and vertical RMSE of 3.1 cm.